Design, Analysis and Optimization of Line-Start Permanent-Magnet Synchronous Motors: Simultaneous Electromagnetic and Thermal Analysis

By

Mousalreza Faramarzi Palangar

Thesis

Submitted to Flinders University

for the degree of

Doctor of Philosophy in Electrical Engineering

College of Science and Engineering at Flinders University

May. 2021

DECLARATIONS

By submitting this thesis, I declare that this thesis does not incorporate without acknowledgement any material previously submitted for obtaining any degree or qualification in any university; and that to the best of my knowledge and belief, it does not contain any material previously published or written by another person except where due reference is made in the text, that the whole of the study within it is my own original work, that I am the sole author of it (except to the degree expressly specified otherwise), that no interests of third parties would be infringed by duplication and publishing thereof by Flinders University.

Signature: Mousalreza Faramarzi Palangar

Date: February 2021

ABSTRACT

Future energy concerns and global economic challenges are encouraging the world to undertake energy conservation projects. A significant way to address these concerns is to increase the energy efficiency of electric appliances. Since electric machines account for roughly 45% of all industrial electricity usage, an immense amount of energy saving can be accomplished by increasing the efficiency of electric motors. Induction motors are used in industry because of advantages like self-starting capability, affordable manufacturing cost and maintenance. However, intrinsic drawbacks of induction motors like comparatively low efficiency and power factor are not easy to overcome, even though induction motor performance has improved dramatically over the years.

Manufacturers of electric motors worldwide are gradually focusing on alternative electric machine technology to meet more rigorous energy efficiency requirements. Hence, line-start permanent magnet synchronous motor (LSPMSM) machinery has gained substantial recognition in comparison with other motor types. This type of motor has been made very appealing by significant benefits like self-starting, high efficiency and power factor. Extensive literature research on LSPMSMs has been undertaken, concentrating primarily on the development of rotor configurations, developing the steady-state analytical model, and using the transient time-step finite element (FE) approach for synchronization evaluation. Due to a hybrid LSPMSM rotor including both an induction cage and a permanent magnet, torque mechanisms in transient starting and steady-state operating conditions vary. Finite-element analysis (FEA) is commonly used to determine the LSPMSM's synchronization capability. However, this form of verification strategy is costly in terms of calculation. Hence, motor designers and engineers are interested in using a fast and reliable alternative design and optimization approach like analytical methods. Hence, it would be of great significance to develop a design and optimization methodology that allows motor designers to study transient and steady-state performance with high accuracy and low computation time.

This study presents a strategy to design an optimum line-start permanent magnet synchronous motor (LSPMSM) with improved performance in both transient (dynamic operation to reach synchronous speed) and steady-state (operating with constant synchronous speed). A mathematical design and optimization method, based on the developed machine sizing equations of induction motors (IMs) and permanent magnet (PM) motors, is proposed for the design of an optimum LSPMSM. The rotors of the IM and IPM are combined to create a hybrid rotor including an induction cage and permanent magnet for a LSPMSM. To verify the proposed mathematical method, a three-phase, 4-pole 4-kW LSPMSM is selected as a case study. A second case study of a three-phase, 1-kW, 8-pole LSPMSM is studied for further verification. The initial designs of the IM, IPM motor and LSPMSM are analyzed using FEM to verify the proposed analytical design and analysis method. The

IM and IPM are then analytically optimised using a genetic algorithm (GA) for the transient improvement (through maximizing the starting torque) and the steady-state performance improvement (via maximizing efficiency), respectively. The rotor cage bar dimensions and PM size are selected as optimisation variables in optimizing the IM and the IPM. Combining the rotors of the optimised IM and IPM yields the optimum hybrid rotor for the LSPMSM. To present a comparative study between the proposed optimisation method and FEM optimisation, the 2D design of an initial LSPMSM design is optimised based on FEM in Ansys/Maxwell. The designed LSPMSM meets the super-premium efficiency (IE4) standards, which outperforms the benchmark IM standard of premium efficiency (IE3). Also, the designed LSPMSM has the capability of starting directly whilst the benchmark PM motor requires an external driver to start.

In addition, this study presents a novel analytical thermal analysis model based on a lumped-parameter model of the LSPMSMs. Hence, a lumped-parameter thermal circuit is proposed for LSPMSMs based on the developed thermal model of an IM. To verify the proposed analytical thermal model, a 3-phase, 4-pole 3-kW IM is selected as a case study incorporated with thermal experimental test results from a 3-kW commercial IM to validate the results of the proposed thermal model. The performance of the proposed thermal model of the LSPMSM is verified using 3D FEM-based thermal analysis. In this section of the thesis (thermal analysis and modeling), the LSPMSMs are researched to discover the achievable maximum output power in the same frame size (3-kW and 4-kW commercial induction motors) with successful synchronization and safe operation in terms of temperature rise.

In summary, the imperative of this study proposes a novel analytical electromagnetic and thermal design, analysis and optimization platform of line-start permanent magnet synchronous motors (LSPMSMs). The main contributions made in this thesis are: (a) simultaneous starting torque and efficiency improvements of the LSPMSM designed based on the commercial IM via implementing optimization using FEM techniques; (b) comparing the performance of two different optimization approaches (gradient-free and gradient-based approaches) in the context of electric machines with a focus on the IMs and LSPMSMs; (c) developing an analytical design, analysis and optimization platform for the LSPMSMs using machine sizing techniques of IMs and permanent magnet (PM) motors; (d) proposing an analytical thermal model and analysis of the LSPMSMs based on lumped-parameter network.

ACKNOWLEDGEMENTS

Contents

Figure Contents

Table Contents

Published Outcomes of the Research

Parts of this thesis have been accepted/under revision/under preparation in the following conferences/journals based on the chapters:

Chapter 2:

[1] M. F. Palangar, Wen. Soong, Nicola Bianchi, Rong-Jie Wang., "Design and Optimisation Techniques in Performance Improvement of Line-Start Permanent Magnet Synchronous Motors: A Review", Submitted to IEEE Transaction on Magnetics, Under Review.

Chapter 3:

M. F. Palangar, A. Mahmoudi, S. Kahourzade, W. Soong., "Simultaneous Efficiency and Starting Torque Optimization of Line-Start Permanent-Magnet Synchronous Motor", *Arabian Journal for Science and Engineering*, *20 April 2021, https://doi.org/10.1007/s13369-021-05659-8*.

Chapter 4:

[3] **M. F. Palangar,** A. Mahmoudi, S. Kahourzade, W. Soong., "Optimum Design of Line-Start Permanent-Magnet Synchronous Motor Using Mathematical Method", **IEEE- ECCE 2020, October 2020, Detroit, Michigan, USA**.

[4] **M. F. Palangar,** A. Mahmoudi, S. Kahourzade, W. Soong., "Design Optimisation of an 8-Pole Line-Start Permanent-Magnet Synchronous Motor", **IEEE International Conference on Electrical, Control and Instrumentation Engineering (ICECIE2020), November 28, 2020, Kuala Lumpur, Malaysia**.

Chapter 5:

[5] **M. F. Palangar,** A. Mahmoudi, S. Kahourzade, W. Soong., "Electromagnetic and Thermal Analysis of a Line-Start Permanent-Magnet Synchronous Motor Designed based on a Commercial Induction Motor", **IEEE- ECCE 2020, October 2020, Detroit, Michigan, USA.**

[6] **M. F. Palangar**, W. Soong, Nicola Bianchi, Rong-Jie Wang, A. Mahmoudi, "Analytical Electromagnetic and Thermal Platform for a Line-Start Permanent Magnet Synchronous Motor", *Submitted to IEEE Transaction on Energy Conversion*, *Under Review*.

[7] **M. F. Palangar,** A. Mahmoudi, W. Soong, "Outer and Inner Rotor Line-Start permanent-Magnet Synchronous Motors: An Electromagnetic and Thermal Comparison", **Accepted** in IEEE- ECCE 2021, October 2021, Vancouver, Canada.

1. **CHAPTER** 1

1. INTRODUCTION

1.1 Motivation

Generally, energy is produced via non-renewable and renewable resources. Non-renewable resources, such as oil and coal, are diminishing at an increasing rate due to growth of the world's population. In addition to the inherent limit in the availability of non-renewable natural resources, the use of fossil fuels has raised serious environmental issues. Therefore, for the sake of humanity, it is important to make efficient use of these resources. One way of improving efficiency is to design highly energy efficient electric machines.

Electrical machines are known as high-usable types of electrical appliances that need more attention to increase their efficiency. They are divided into two different operational types: generators and motors. Electrical generators produce electricity using an external mechanical force applied to the shaft. In contrast, electrical motors generate mechanical power using input electric power. Every day we use many appliances that work using electrical motors such as lifts, escalators, and pumps. In fact, electrical motors have many applications and consume approximately 45% of electrical energy. Thus, a way of saving more energy is increase the use of high efficiency motors.

Electrical motors are generally divided into two types: direct current (DC) and alternating current (AC). The focus is more on AC supply motors, which are divided into two categories: induction motors (IM) and synchronous machines. Permanent-magnet (PM) motors are more efficient than IMs but need an external inverter to run and are expensive. These reasons have resulted in low interest for PM motors compared with IMs, which are self-starting and affordable, particularly for industrial applications. Low efficiency is known as a key disadvantage of IMs, which increases cost of energy during their lifetime.

Line-start permanent magnet synchronous motors (LSPMSMs) can be designed to deal with these short comings. The use a hybrid rotor that is a combination of an IM rotor and an interior PM. For commercializing any technology, it is of the great importance to be low cost and highly efficient. LSPMSMs include the advantages of IMs and PM motors such as self-starting capability and high efficiency and power factor. The following section discusses the challenges present in LSPMSMs electromagnetic and thermal analysis.

1.2 LSPMSM Challenges

1.1.1   LSPMSM Design Challenges

LSPMSM electromagnetic design is a multi-level and multi-disciplinary procedure. The design process is divided into three stages: (a) design topology choice including design modeling method choice, (b) design optimization implementation, and (c) thermal analysis.

1.1.1.1 Design Topologies

Various LSPMSM topologies have been extensively studied in the literature. An LSPMSM has a hybrid rotor including cage and PM. This makes the design process complicated. In design topology selection there are several factors that should be considered such as an appropriate induction cage model, proper PM volume and configuration, and manufacturing limitations to achieve a feasible design. The main design challenges that should be taken into account are:

a) PM demagnetization due to overheat (see Figure **1-1** showing temperature effect on intrinsic PM characteristic [1]), over-induced current in the stator winding and rotor bars, and inappropriate PM thickness due to rotor topology limitation.

b) Braking torque, due to the presence of a PM, that affects the starting capability of the LSPMSM through producing negative torque in the transient state.

c) Torque oscillation or cogging torque due to the interaction between PM and stator slots. There have been various methods to minimize the cogging torque for different configurations such as interior-PM (IPM) and surface-PM (SPM). SPM Machines suffer high cogging torque in comparison with IPM [2]-[3] (see Figure **1-2**).

d) Efficiency and power factor are the most important factor in designing an LSPMSM and the selected topology should provide a high efficiency and power factor to compensate for the cost of using PM.

A performance comparison of different LSPMSM topologies (illustrated in Figure **1-3**) for a fixed PM volume and material was studied in [3]-[6]. The radial-flux rotor topology (series-type) and W-type have better performance amongst other topologies [3]-[5]. However, the W-type configuration is too complicated, which makes it difficult and costly to manufacture [3]-[5]. Therefore, the series-type topology is considered an appropriate topology for this study because of good performance and simple structure in terms of fabrication.

1.1.1.2 Design Modeling Methods

Generally, there are three methods for the design and analysis of electromagnetic characteristics of electric machines: numerical (Maxwell's equations), analytical (magnetic equations), and machine sizing (sizing equations). Although numerical methods (like finite-element method) are accurate, they are computationally intensive and require high performance computing [6].

Figure 1-1. B-H demagnetization curve variation versus temperature for Sm_2Co_{17}, XG 26/60 PMs [1].

Figure 1-2. Performance parameters comparison of two different LSPMSM topologies, IPM and SPM [3].

a. Spoke-type	Series-type	U-type
V-type	W-type	Swastika-type
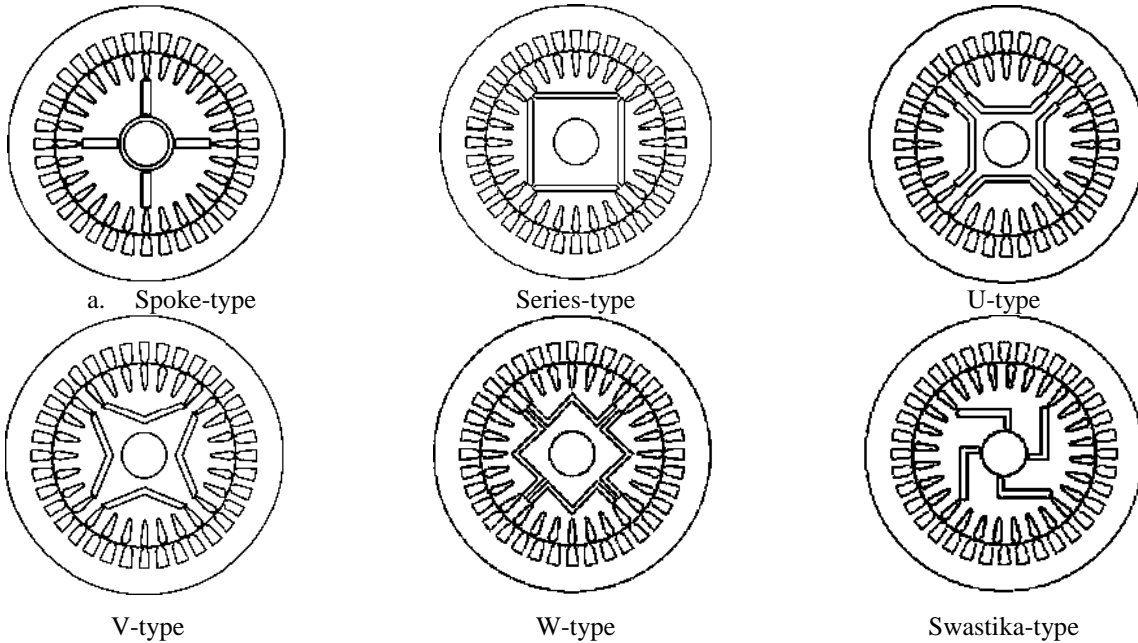
Figure 1-3. Different LSPMSM topologies based on PM configuration for LSPMSM [3]-[5].

Using these methods for the technical verification of developed solutions is a common practice, although implementing an optimization problem employing them is a lengthy process and, in certain cases involving multiple disciplines like electromagnetic and thermal characteristics, may not be applicable [6]. The analytical methods solve magnetic equations based on the assumptions made in geometric and material characteristics. These methods are less accurate than numerical methods and rely on a large number of assumptions. Designers should update assumptions for each design structure. Hence, if the design is not a conventional machine, the developed analytical model must be completely remodeled [6].

Machine sizing is a well-known design technique that solves sizing equations with a focus on electrical performance of machines. Two popular machine sizing techniques were studied in [7]-[8]. Recently, there have been developments in machine sizing equations to improve accuracy [9]-[11]. Sizing equation methods are very fast, though their accuracy is not as good as numerical methods. These techniques are generally categorized as analytical methods that solve sizing equations instead of magnetic equations. Estimating performance parameters (mainly steady-state) of a machine is straightforward via this method and, hence, computing it in an optimization problem is simple even for multi-disciplinary studies. There are independent sizing equations for induction motors and PM motors, whilst there is not a machine sizing strategy for the design and analysis of an LSPMSM due to its complex rotor topology inclusive of an induction cage and PM.

After selecting the design topology, it is time to consider the design modeling technique, which allows us to implement this thesis's aim of developing a multi-disciplinary design platform. This platform enables designers to calculate the main dimensions of the motor, estimate/predict key electromagnetic and thermal performance parameters of the motor, and provide a capability for optimization implementation. The design method must be fast to support rapid performance analysis and improvement. As the LSPMSM behavior in start-up is like induction motors and in steady-state is like PM motors, there is the possibility of developing an analytical design strategy based on sizing equations of IM and PM motors. This design modeling method is developed in this study for electromagnetic design and analysis of LSPMSM.

1.1.2 LSPMSM Optimization Challenges

LSPMSMs have been studied in the literature, with emphases on PM-assisted rotor topological development, steady-state performance improvement using analytical models, transient (synchronisation process to reach synchronous speed) performance improvements using finite-element methods (FEM). There have been two strategies to develop better LSPMSM performance in both the transient (dynamic operation to reach synchronous speed) and the steady-state (operating with constant synchronous speed): (a) design methodologies and (b) optimisation techniques using time-step finite element analysis (FEA). Design methodology studies present new methods for performance improvement of LSPMSM in the transient and the steady-state operation. These techniques are chiefly limited to either the transient performance improvement or the steady-state performance improvement. A focus on only the transient performance improvement may degrade the steady-state performance of the LSPMSM, and vice versa. There have been limited design strategies to simultaneously improve both transient and steady-state. Conversely, employing FEM to verify LSPMSMs performance is a time-consuming process that results in in less attention from designers

to implement FEM-based optimisation procedures. Note that a comprehensive discussion of LSPMSM performance improvement and optimization is presented in Chapter 2.

Simultaneous performance improvement of the LSPMSM is possible using developed analytical design methods given the fact that LSPMSM transient performance is mainly dependent on induction cage features (like IMs) and LSPMSM's steady-state performance is mainly dependent on PM characteristics (like PM motors). Hence, an optimum hybrid rotor is possible via combination of an optimized rotor from IM (with a focus on transient performance improvement) and an optimized rotor from PM (with a focused on steady-state performance improvement). Optimization study in this thesis is aimed to simultaneously improve the transient and steady-state performance of LSPMSM. It is divided in two studies: (a) optimizing LSPMSM based only on FEM optimization techniques including two different approaches; (b) optimizing LSPMSM based on the developed analytical design method and FEM individually for the same case study. The aim of the first study is to indicate how a FEM optimization is implemented and to compare the performance of two different optimization approaches in this field (Chapter 3). The second study is aimed at presenting an electromagnetic design, analysis and optimization platform for LSPMSM (Chapter 4).

1.1.3 LSPMSM Thermal Challenges

Overheating in electric machines is a serious problem causing machine failure in some cases due to extreme temperatures of the stator winding and rotor end ring for induction motors and PM demagnetization for permanent magnet machines. There are three strategies to analyze temperature distribution of motors: (a) analytical method; (b) numerical method; (c) experimental tests.

Thermal analysis and modeling of the LSPMSMs have been studied in a limited number of works, whereas thermal analysis and modelling of IMs and PM motors have been extensively studied in the literature (detailed discussion is presented in Chapter 5). FEM-based and experimental-based thermal analysis of an electric machine are time-consuming and computationally intensive. Analytical thermal analysis methods, mainly based on lumped-parameter networks, are fast and accurate enough and this enables the possibility of coupling them in optimization problems with electromagnetic analysis. There are extensive analytical thermal models in the literature for IMs and PM motors whilst there is a lack of an analytical thermal model of the LSPMSMs. A comprehensive thermal modeling and analysis study of LSPMSM will be discussed in Chapter 5.

1.3 Thesis Organization

This thesis develops an electromagnetic and thermal design, analysis and optimization of line-start permanent magnet synchronous motors. The organization and framework of the thesis is described as follows:

- Chapter 2 presents a comprehensive literature review of research mainly focused on design and optimisation techniques in performance improvement of line-start permanent magnet synchronous motors. It starts with a brief overview of energy production and consumption due to the world population growth and human beings needs to use electricity energy caused to global warming and CO_2 emissions. International viewpoints regarding to climate change as results of global warming are discussed briefly in this chapter to show the consequence of the energy production growth. Next, it introduces the line-start permanent magnet motors (LSPMSMs) as production of induction motor (IM) and interior permanent magnet (IPM) combination. Also, available international efficiency standards are studied in this chapter. A detailed comparison between LSPMSMs and IMs in terms of performance is presented. In second part of this chapter, recent developments of LSPMSMs performance improvement including design techniques and optimization strategies are discussed in depth. Conclusion and research gaps are discussed at the end of this chapter. Based on this chapter and recognized research gaps in this field, the thesis aims are framed and presented in the next chapters.

- Chapter 3 provides a comprehensive FEM-based optimization study. In this chapter the rotor of the benchmark IM (4-pole, 3-phase, 4-kW) is replaced with a hybrid rotor including a squirrel cage and PM to provide an LSPMSM. To have a design with the lowest manufacturing cost, the LSPMSM design should have same stator, winding and housing with only the rotor replaced. The hybrid rotor is designed based on some modifications to the rotor of the IM. After finalizing the initial design, the design is optimised to improve transient and steady-state performance. The optimisation is divided in three scenarios: 1) transient optimisation, 2) steady-state optimisation, and 3) transient and steady-state optimisation simultaneously. The first two scenarios are implemented under a single-objective function while the third scenario is a multi-objective optimisation. To present a comprehensive comparative optimization study in the context of electric machines particularly LSPMSMs the designs in this chapter are optimised using two different optimization approaches: 1) gradient-free, and 2) gradient-based approaches. Both approaches are compared in terms of two main factors: 1) performance of the optimum designs, and 2) time of optimisation. The study is enriched with 3D finite-element analysis (FEA).

- Chapter 4 proposes an analytical design, analysis and optimization approach for LSPMSMs to get a reliable optimum design in a time shorter than FEM-based optimization. It begins with a proposed analytical design method based on the machine sizing techniques of IMs and PM motors. The motor performance parameters are estimated analytically based on the

proposed analytical equations. To verify the proposed design and analysis, a finite-element method (FEM)-based study is employed to analyze the LSPMSMs designed by the proposed analytical method. Next, an analytical optimization strategy is developed to generate an optimum design of the LSPMSM. The purpose of the optimization is improving the transient and the steady-state performance of the LSPMSM. Likewise, to verify the performance of the proposed optimization strategy, the initial LSPMSM design is optimized based on FEM optimization under the same optimization conditions using a genetic algorithm (GA) and similar variables and objective functions. The proposed methodology is clearly discussed and verified with FEM for a 4-pole 4-kW LSPMSM as a case study. As further verification, the results and discussions are presented for a second case study of an 8-pole 1-kW LSPMSM designed based on the proposed method.

- Chapter 5 presents a thermal study of the LSPMSMs. In this chapter, a novel lumped-parameter thermal model is proposed to estimate steady-state temperature of the LSPMSM's main parts. In fact, the proposed method is aimed to be a reliable substitute for FEM-based thermal analysis, which is a time-consuming process. The proposed lumped-parameter thermal circuit model of the LSPMSM is based on a developed lumped-parameter network of the induction motors. Indeed, the thermal model of the IM is tuned to the LSPMSM model with consideration for the updated rotor inclusive of a PM and modified rotor cage. To clearly present the performance of the proposed method, a case study (3-kW, 3-phase) is studied against available experimental data for the IM benchmark. To present a comprehensive thermal study, the performance of the proposed method is verified using 3D FEM-based thermal analysis, and all simulation results are validated with experimental data of the 3-kW IM benchmark. Then, performance of the proposed thermal model of the LSPMSM is verified with 3D FEM-based thermal analysis for this motor. In a dedicated part of this chapter (Section 5.7), the discussions and thermal results of the 4-kW 4-pole LSPMSM and IM are presented. The proposed lumped-parameter thermal method performance for these case studies are verified with the 3D FEM-based steady-state thermal analysis.

  - Chapter 6 presents the thesis conclusion and recommendations for future studies in LSPMSM electromagnetic and thermal studies. In this chapter, the overall conclusion is presented with a viewpoint to future usage, improvement and development of delivered models and methods. The key outcomes of the study are presented in this chapter.

This thesis is an industry-framed project aimed at replacing conventional IMs with LSPMSMs to meet high level efficiency standards. A prototype of the final, optimum LSPMSM was intended in order to do more verification of the study, but due to tough circumstances caused by Covid-19,

prototyping the LSPMSM was impossible. However, the study is enriched with extensive 2D and 3D FEM simulations and, in some cases (for the benchmark IM), available experimental data validates simulations and proposed analytical method performance. In addition, in thermal analysis, extensive experimental tests conducted for a benchmark IM were used to verify the proposed analytical method performance and simulations.

2. CHAPTER 2

2. DESIGN AND OPTIMISATION TECHNIQUES IN PERFORMANCE IMPROVEMENT OF LINE-START PERMANENT MAGNET SYNCHRONOUS MOTORS: A REVIEW

In this chapter, an extensive literature review is presented for LSPMSM performance improvement approaches to understand recent trends in the design and technology as well as the significance of the current study. Generally, LSPMSM performance improvement techniques are divided into two strategies: 1) design methodologies, and 2) optimisation techniques. This chapter is divided in six sections: A summary of the chapter is presented in Section 2.1. Section 2.2 provides an introduction, and LSPMSM background is discussed in Section 2.3. Performance improvement of LSPMSM using design methodologies is discussed in Section 2.4 and optimization techniques are presented in Section 2.5. Lastly, Section 2.6 includes suggestions and recommendations for further investigations in future research work.

2.1 Summary

This chapter covers the design methodologies and optimisation techniques studied in the performance improvement of LSPMSMs. LSPMSM performance improvement using design techniques is chiefly limited to either transient or steady-state performance improvement, and a focus on only the transient performance improvement may degrade the steady-state performance of the LSPMSM and vice versa. Optimisation studies of LSPMSMs are categorized in terms of three optimisation aims: transient performance improvement, steady-state performance improvement, and simultaneous improvement of the transient and the steady-state performance. This study indicates the impact of various variables on LSPMSM performance improvement. The optimisation review shows that starting cage optimisation without considering the steady-state characteristics as constraints results in synchronous performance degradation. In steady-state performance optimization, considering transient characteristics as constraints results in a slight synchronous performance improvement and it contributes to avoiding transient performance degradation. Multi-objective optimization including a transient and a steady-state characteristic as individual objectives results in a more optimum LSPMSM with overall performance improvement. Finally, research gaps in design and optimisation of LSPMSMs are presented.

2.2 Introduction

Nowadays, electricity consumes 19% of total energy and demand is growing significantly in comparison with all other fuels [12]. Electrical machines are devices that use electrical energy to produce mechanical power. Therefore, more focus on increasing their efficiency can save energy.

Electrical motors, particularly alternating current (AC) motors, are used across an enormous range of applications (lifts, escalators, pump, etc.) and consume around forty-five percent (45%) of the total electricity generated worldwide [12]. As an example, in the UK, three phase induction motors released a massive amount of CO_2 emissions, around 97 million Ton, which was approximately 17% of the entire CO_2 release for the country [12].

Emissions of CO_2, and other greenhouse gases, increase average temperatures in the atmosphere and the oceans. This is known as "global warming" and is a result of climate change. The clues of global warming are indicated in all over the world such as ice floes melting, polar ice mass drop, rising sea levels, ecological systems change, and frequent heat waves [13]. The climate change has seriously affected the lives of human beings with some consequences visible and others non-obvious. We can point to some of these consequences such as heat waves affecting vulnerable people (children, elderly people), degraded air quality, falls in farm production, floods, tsunamis, and insects' migration resulting in epidemics (malaria) [13]. With electric motors such a large contributing factor to CO_2 emissions, it is important that they be as efficient as possible to reduce electric energy consumption. Using high-energy permanent magnets and optimizing machine designs are important means to the design of high-efficiency electric motors [14].

AC motors are divided into two categories induction motors (IMs) and permanent magnet (PM) motors. IMs are widely used in numerous industries as actuators or drives to provide mechanical motions and forces (including factories, industrial sectors, air compressors, fans, railway tractions, pumps, blowers, cranes, textile mills, electrical home appliances, vehicles, modes of transportation, and wind power systems). Maintenance of IMs is easy because of their simple structure, dependability, high efficiency, and low value [12]. However, this type of motor suffers low efficiency resulting in the consumption of a considerable amount of electricity. Hence, optimisation studies to improve efficiency of IMs have been implemented and a limited level of success has been gained [12].

PM motors are more efficient than IMs but need an external invertor to run them and are expensive. These disadvantages have resulted in low interest in this type of motor in comparison with IMs, which are self-starting and affordable, particularly for industrial applications. Line-start permanent magnet synchronous motors (LSPMSM) are a recently introduced generation of electric motors that can start direct on-line like IMs, which avoids the need for drives (inverters), and can provide high efficiency like PM motors. The trade-off between starting/synchronization capability (transient performance) and higher efficiency and power factor (steady state performance) is a key challenge for LSPMSMs.

2.3 LSPMSMs Background

2.3.1 **LSPMSM Description**

The International Electro-Technical Commission (IEC) standard IEC 60034-30-1:2014 [15] defines classifications of international efficiency (IE) for single- and three-phase direct-on-line motors. These classifications are listed in Table **2-1**.

Induction machines (IM) are widely used but only have medium levels of efficiency, e.g., IE2 [16]. Permanent magnet synchronous machines (PMSM) offer higher efficiency at a higher cost but generally also require a drive (inverter), which is an additional cost to the machine. For applications that require only constant speed operation, a line-start permanent magnet synchronous motor (LSPMSM) is an option that avoids the need for a drive. LSPMSM machines have a rotor that has both a squirrel-cage, for direct-on-line starting, and permanent magnets. The latter allows for higher efficiency steady-state operation due to the reduction in rotor cage losses [17]. Using the high-energy permanent magnets has allowed LSPMSMs to reach the super-premium efficiency (IE4) standard. The highest efficiency levels in the power output range of 0.55-kW to 4-kW are achieved by LSPMSMs [18]-[19].

Table 2-1. Classifications in international efficiency (IE) [15].

IE Code	Description
IE1	Standard Efficiency
IE2	High Efficiency
IE3	Premium Efficiency
IE4	Super Premium Efficiency
IE5	Ultra-Premium Efficiency

The modelling of LSPMSMs is based on the stationary *d-q* reference frame as described in [19]-[21] and is given by the following equations:

$$v_{sq} = R_s i_{sq} + \omega_r \Psi_{sd} + \frac{d\Psi_{sq}}{dt} \tag{2.1}$$

$$v_{sd} = R_s i_{sd} - \omega_r \Psi_{sq} + \frac{d\Psi_{sd}}{dt} \tag{2.2}$$

$$v_{rq} = R_{rq} i_{rq} + \frac{d\Psi_{rq}}{dt} = 0 \tag{2.3}$$

$$v_{rd} = R_{rd} i_{rd} + \frac{d\Psi_{rd}}{dt} = 0 \tag{2.4}$$

$$\Psi_{sq} = L_{sq} i_{sq} + L_{mq} i_{rq} \tag{2.5}$$

$$\Psi_{sd} = L_{sd} i_{sd} + L_{md} i_{rd} + \Psi_m \tag{2.6}$$

$$\Psi_{rq} = L_{rq} i_{rq} + L_{mq} i_{sq} \tag{2.7}$$

$$\Psi_{rd} = L_{rd} i_{rd} + L_{md} i_{sd} + \Psi_m \tag{2.8}$$

where v_{sq}, v_{sd}, v_{rq}, v_{rd}, i_{sq}, i_{sd}, i_{rq} and i_{rd} are the *d-q* axis voltages and currents in the stator and rotor, and Ψ_{sq}, Ψ_{sd}, Ψ_{rq}, and Ψ_{rq} represent the flux linkage of the stator and rotor, respectively. The parameters ω_r, R_s, R_{rd} and R_{rq} are the angular speed of the rotor, resistance of stator and rotor resistances referred to stator, respectively. The calculation of the stator and rotor fluxes linkage are described by Equations 2.5-2.8. In these equations L_{sq}, L_{sd}, L_{rq}, L_{rd} are the inductances of the stator and rotor and L_{mq}, L_{md} and Ψ_m are the mutual inductances and the permanent magnet flux-linkage. Dynamic torque is as follows, with three terms being the reluctance, cage and PM synchronous torque, respectively [19]-[21],

$$T_{ind} = \frac{3P}{2}[(L_{sd}-L_{sq})i_{sd}i_{sq} + (L_{md}i_{sq}i_{rd} - L_{mq}i_{sd}i_{rq}) + \Psi_m i_{sq}] \tag{2.9}$$

Figure **2-1** shows the *d-q* equivalent circuits for LSPMSMs.
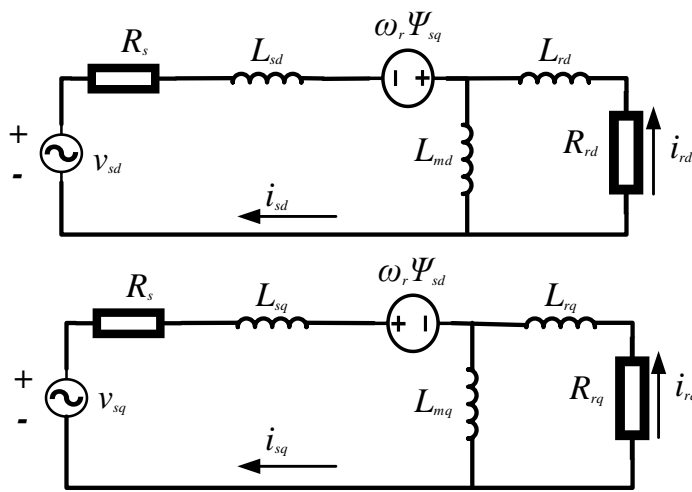
Figure 2-1. The d-q equivalent circuits of LSPMSMs.

```
                    ┌─────────────────────┐
                    │   Design Procedure  │
                    └─────────────────────┘
                    ┌─────────────────────┐
                    │   Inputs (Design    │
                    │    Parameters)      │
                    └─────────────────────┘
                       ┌──────────────┐
                       │ Stator Design│
                       └──────────────┘
        ┌─────────────┐              ┌─────────────┐
        │  PM Design  │              │ Cage Design │
        └─────────────┘              └─────────────┘
        ┌─────────────┐              ┌─────────────┐
        │  IPM Rotor  │              │  IM Rotor   │
        │   Design    │              │   Design    │
        └─────────────┘              └─────────────┘
                    ┌─────────────────────┐
                    │     Combination     │
                    └─────────────────────┘
                       ┌──────────────┐
                       │    LSPMSM    │
                       │    Design    │
                       └──────────────┘
```
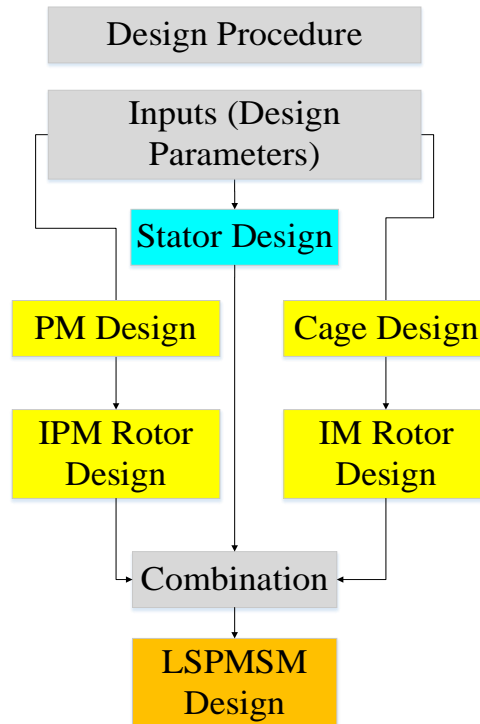
Figure 2-2. Analytical LSPMSM design procedure flowchart [30].

2.3.2   LSPMSM Design Methods

Over the last few decades, LSPMSM designs have traditionally designed starting from a benchmark squirrel-cage IM design and adding a PM to the rotor and then performing a comparative study between the starting and the steady-state performance of the IM and LSPMSM [22]-[28].

In contrast to this, an analytical design procedure for an LSPMSM based on classical machine sizing methods was presented in [29]-[30]. Figure **2-2** illustrates an LSPMSM design procedure based on the combination of an interior PMSM and an IM designed analytically based on machine sizing techniques [31]-[32]. The same stator and winding were used for the two machines and there is a trade-off between the rotors of IM and interior permanent magnet (IPM) motor to produce the hybrid rotor for the LSPMSM. When adding the PM to the IM rotor, there is a post processing step to re-design the squirrel cage to achieve an appropriate balance between successful starting and high efficiency.

Similar to IMs and PMSMs, LSPMSMs can be designed in radial and axial-flux configurations. An axial-flux LSPMSM (AFLSPMSM) was obtained by adding a squirrel-cage to the rotor of an AF-PMSM and was shown to have a higher efficiency than the induction motor of the same power rating [33]. The axial-flux LSPMSM has potentially higher power density, and in some applications it has higher efficiency than radial-flux LSPMSMs [34].

2.3.3   LSPMSMs vs. IMs

The following subsections compare LSPMSM performance with IMs across several features.

2.3.3.1 Starting and synchronization capability

LSPMSMs use the starting torque produced by the rotor induction cage to bring the load up to near synchronous speed at which point, if the load torque and inertia are within allowable bounds, the rotor PM torque is sufficient to cause synchronization to occur. A successful synchronisation requires the motor starting torque to be higher than the load torque at all speeds as well as a sufficiently low value of load inertia to allow the final synchronisation stage.

Figure **2-3** shows the steady-state torque-speed curve of a 4-kW LSPMSM in comparison with its baseline IM. This shows the net LSPMSM torque as well the LSPMSM torque when the magnets are removed. The difference between these is the PM braking torque [28]. The torque versus speed curve of an LSPMSM is generally lower than that of the baseline induction machine. Firstly, due to the presence of the rotor magnets, the cross-sectional area of the rotor squirrel-cage bars is normally lower, which mainly affects the performance at higher speeds. Secondly, the rotor magnets produce a magnet braking torque that peaks at relatively low speeds [35]-[38] and reduces the net output torque. The steady-state torque of a LSPMSM is calculated as follows [19]:

$$T_{tot} = T_{mag} + T_{cage} \tag{2.10}$$

where T_{mag}, T_{cage} and T_{tot} are the magnet-generated torque (braking torque), asynchronous torque developed by winding (induction torque) and the total resultant torque (LSPMSM torque), respectively. This is shown in Figure **2-3**. The load torque must be less than the LSPMSM torque generated by the motor for a successful start-up. The magnet torque (braking torque) is directly related to the electromotive force (EMF) and stator resistance [19]-[21]:

$$T_{mag} = -\frac{3P}{\omega_s}(1-s)E_0^2 R_s \frac{R_s^2 + X_q^2(1-s)}{[R_s^2 + X_d X_q(1-s)]^2} \tag{2.11}$$

where s, P, R_s and ω_s are the slip, number of poles, stator resistance and synchronous electrical speed, respectively, E_0 is the no-load EMF, and X_d, X_q are the synchronous reactance in the d- and q-axes.

A convenient way of describing the starting performance of a LSPMSM is to show the envelope of its starting capability on a plane with axes of load torque and load inertia. The load torque is given as the load torque at rated speed with some stated assumption of its speed variation such a constant torque or a fan-type load. The load inertia is normally expressed relative to the rotor inertia.

Considering a constant load torque versus speed curve, for the baseline induction machine the starting capability would be limited by the "pull-up" torque of its torque-speed curve, but there would be no limit on load inertia. For the corresponding LSPMSM, the maximum allowable load torque is generally lower due to the two effects described above and there is a finite limit on the maximum load inertia, typically 5 to 15 times the rotor inertia. Beyond these limits, the LSPMSM will fail to reach synchronous speed, which results in large oscillatory output torque and poor steady-state

performance. Figure **2-4** shows an example of the boundary of the successful starting and synchronisation of a 4-kW LSPMSM and its baseline IM for different inertia ratios and load torques. The impact of braking torque on LSPMSM starting capability is shown in Figure **2-5** [36]. It shows unsuccessful starting (synchronization) of a LSPMSM. In Case 1 this is due to high braking torque, which degrades the normal operation of the motor at low speeds compared to an IM and the machine effectively stalls. In Case 2 this is due to too high a load torque and/or inertia, which prevents final synchronisation.

There is an overshoot in the dynamic speed-time graph for a LSPMSM which can reach synchronous speed and the settling time is longer in comparison with an IM starting [37]-[38]. The synchronisation capability of a 4-kW LSPMSM is compared with a baseline IM in terms of settling time in Figure 2-6. It shows that the IM reaches the steady-state speed roughly three times faster than the LSPMSM. Initial rotor position influences the LSPMSM synchronization performance, as is seen in Figure 2-6b. This indicates that the LSPMSM with initial rotor position forced at 75 and 90 mechanical degrees reached synchronous speed faster than other positions. Analysis indicates that the steady-state performance of the LSPMSM is not affected by the initial rotor position while the synchronization is more sensitive to this factor.
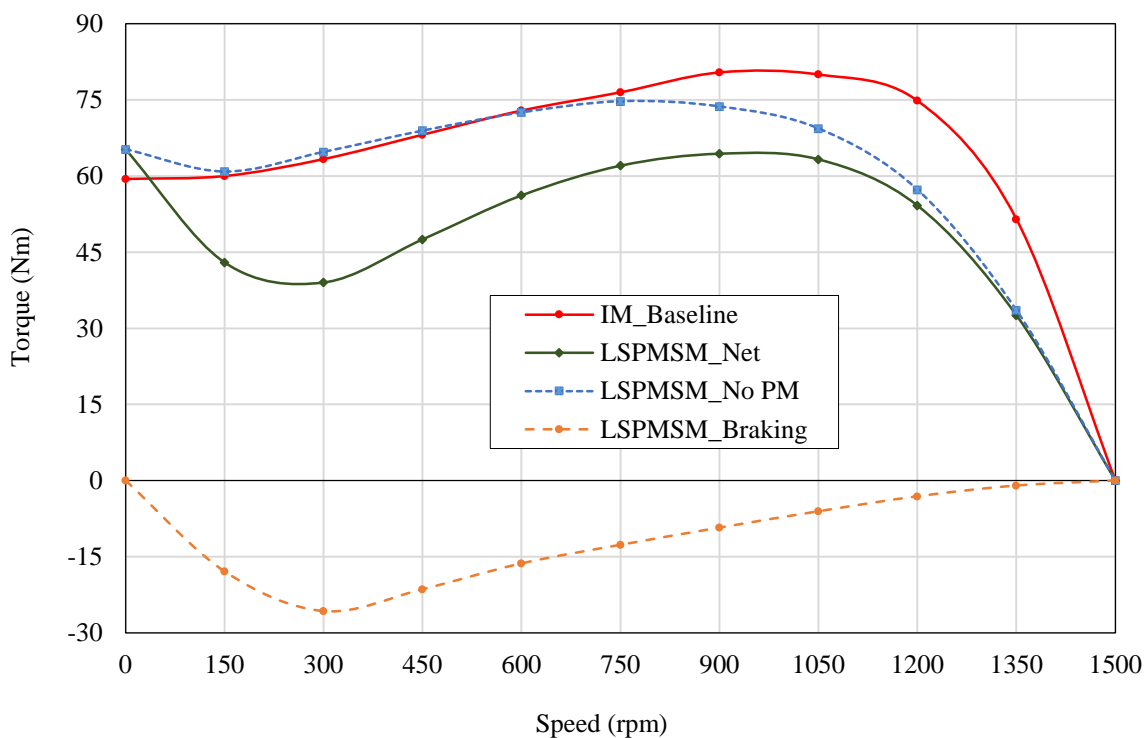
Figure 2-3. Steady-state torque-speed curve of a 4-kW IM and LSPMSM [28].
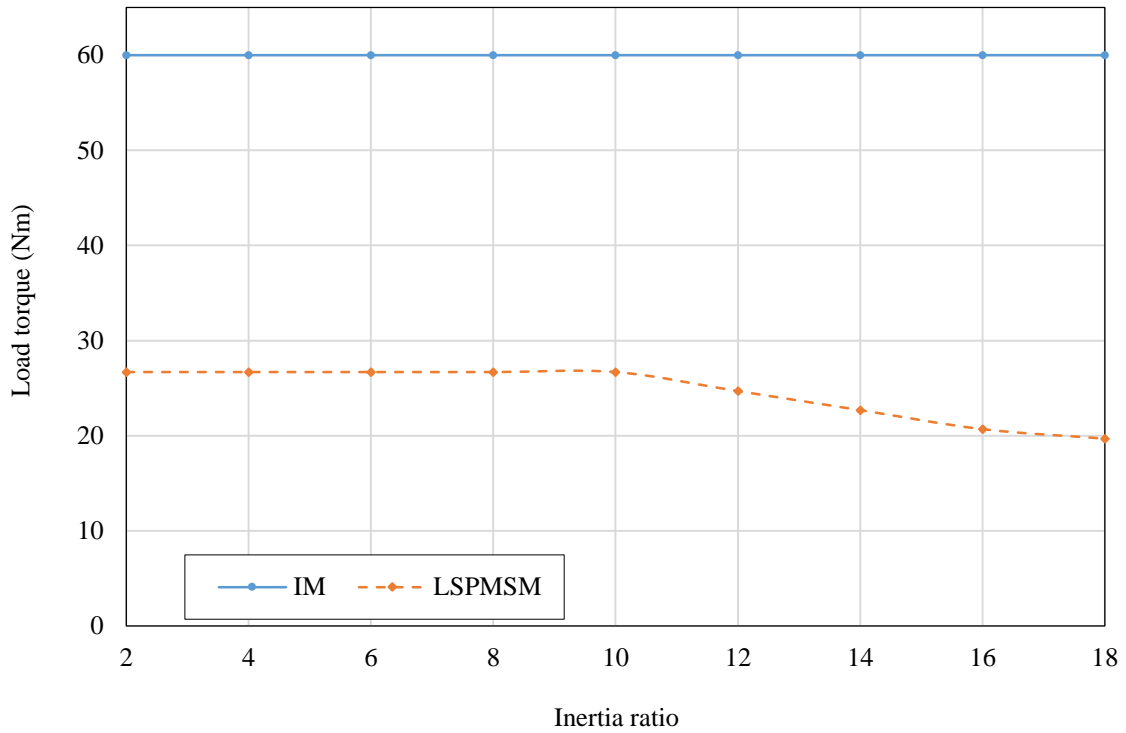
Figure 2-4. Boundaries of successful synchronisation in the plane of load torque versus inertia ratio for a 4-kW LSPMSMs and an IM.
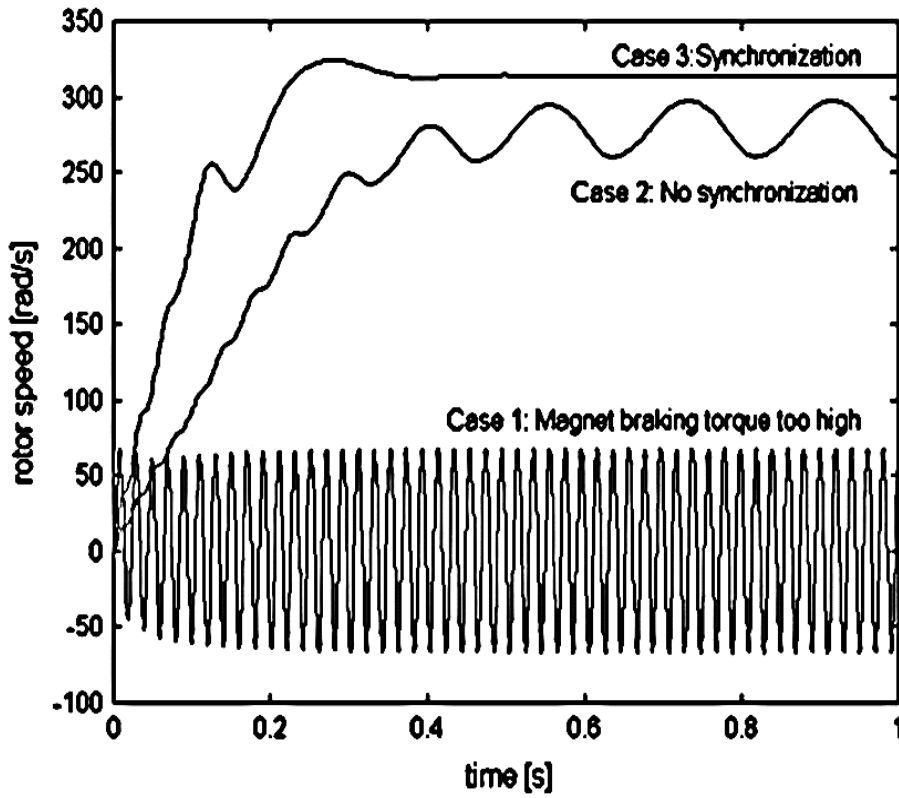
Figure 2-5.Unsuccessful synchronisation [36].
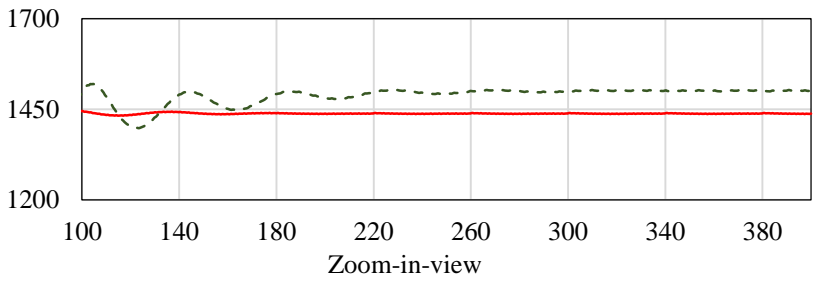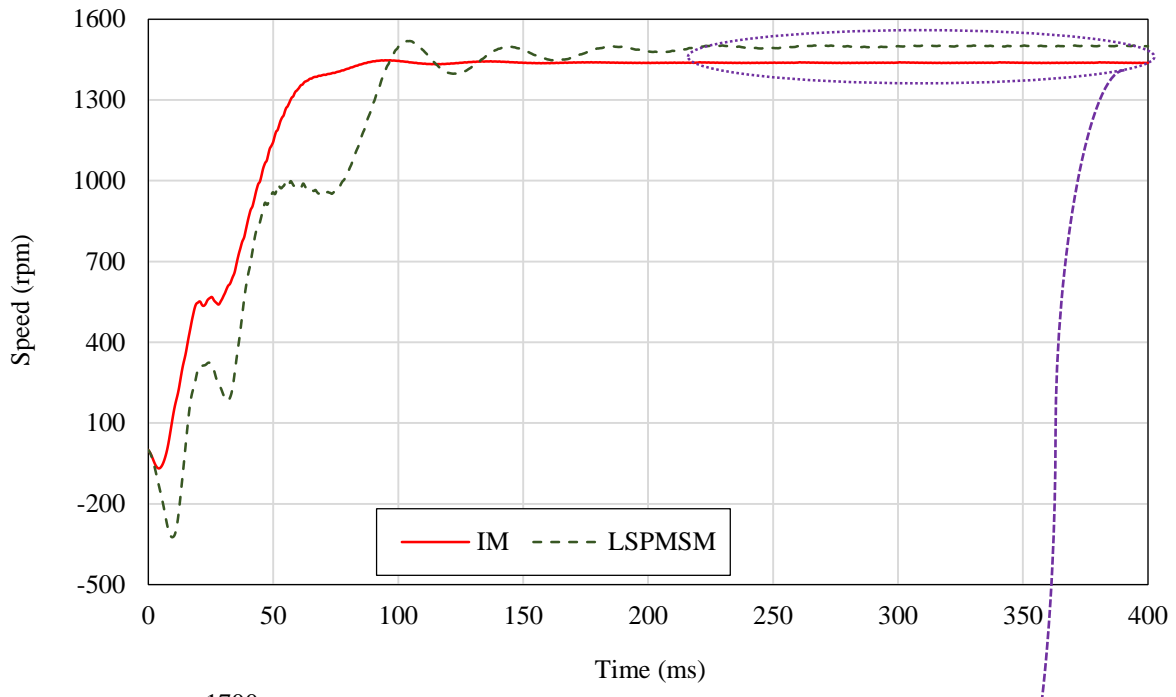
a. Speed-time responses of a 4-kW LSPMSM and the baseline IM
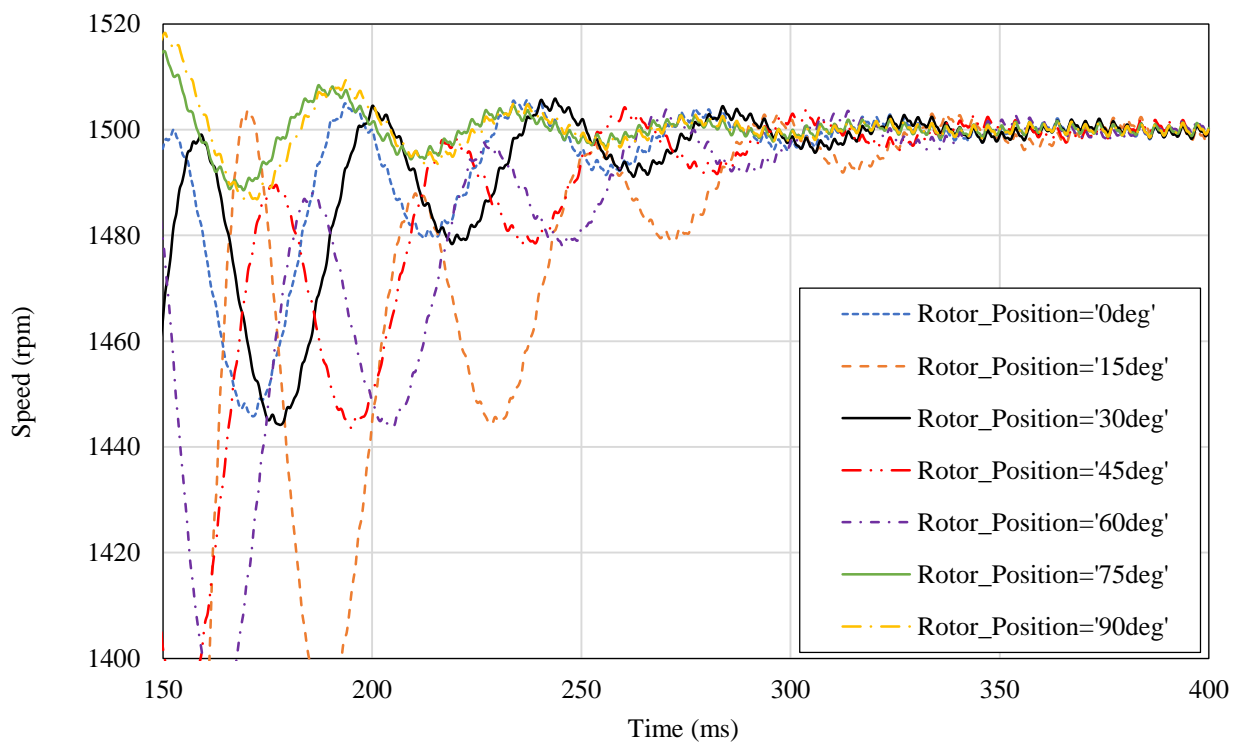
b. Speed-time responses of a 4-kW LSPMSM with various initial rotor position
Figure 2-6. 4-kW LSPMSM performance.

17

2.3.3.2 Steady-state efficiency and power factor

Figure **2-7** shows five current motor efficiency standards [39]-[40] for machines with ratings between 0.75 and 160-kW. Approximately a quarter of the total loss of four-pole induction motors is due to rotor cage losses that are associated with the slip of the rotor. LSPMSMs operate at synchronous speed and so have only low rotor cage losses due to high-order harmonics [41].

Figure 2-8 shows the calculated full-load loss contributions (Figure 2-8a) and other performance metrics (Figure 2-8b) of a 2.2-kW LSPMSM and the baseline IM (excluding the mechanical loss). The LSPMSM total loss is about one-third less than the IM at full-load operation resulting in a substantially improved efficiency [42]. This reduction in total losses is due to a reduction in rotor cage loss (29% of total loss in IM, 7% in LSPMSM) and reduction of the stator copper loss due to the lower input current resulting from the significant decline in magnetizing current in the LSPMSM. Figure 2-8b compares the full-load power factor of the machines. The LSPMSM shows a significantly higher power-factor due to the permanent magnet excitation. A low power-factor causes additional stator winding copper losses and can result in extra supply charges by electrical utilities [43]. Figure **2-9** compares the efficiency of the two designs as a function of output power and includes the NEMA standards of 4-pole, 50 Hz electric motors. It shows that the calculated full-load efficiency without mechanical loss of the LSPMSM exceeds the IE4 standard while the corresponding IM efficiency is just above the IE3 level.
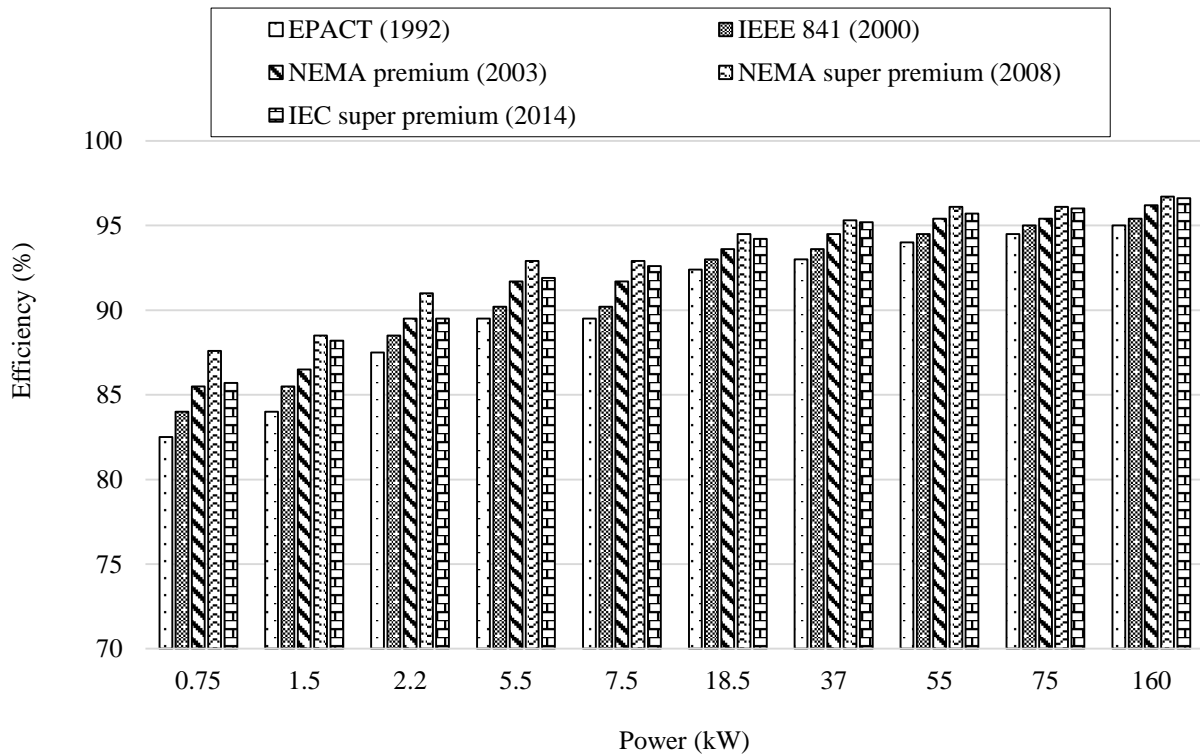
Figure 2-7. Comparison of the five efficiency standards versus output power of 3-phase, 4-pole motors [12].
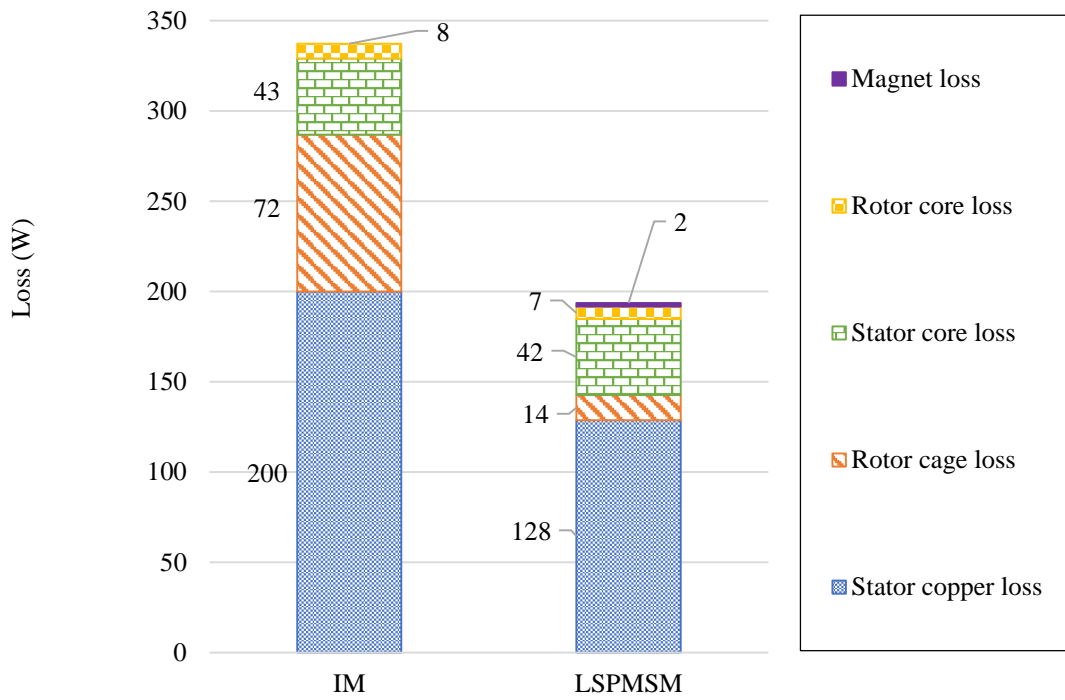
a. Calculated loss component comparison neglecting mechanical losses.
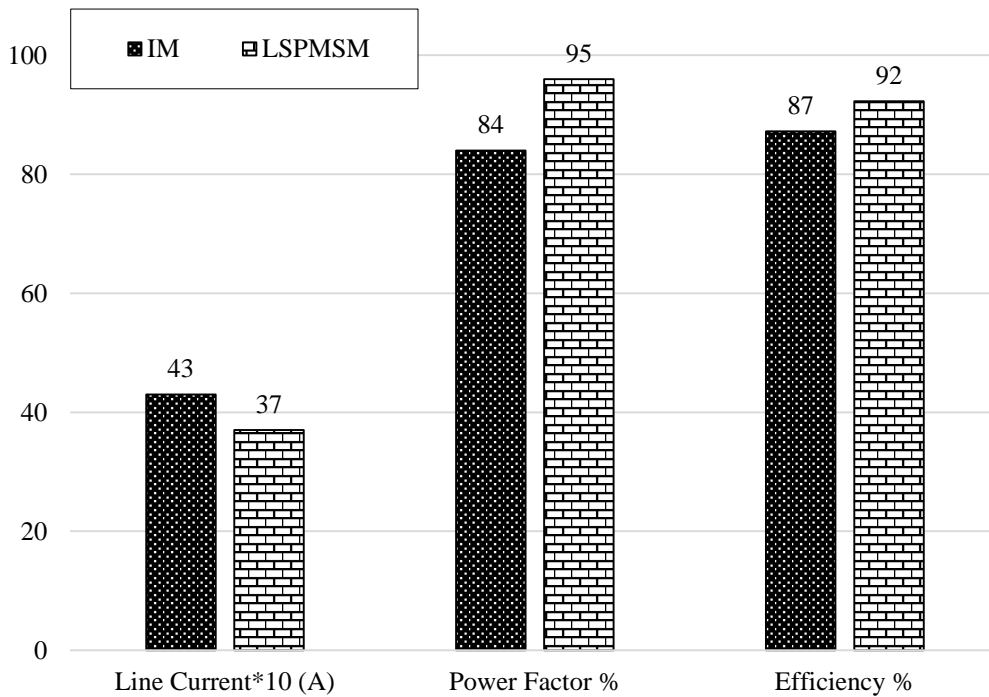
b. Calculated efficiency, power factor and phase current.
Figure 2-8. Steady-state performance parameters of a 2.2-kW IM and LSPMSM.
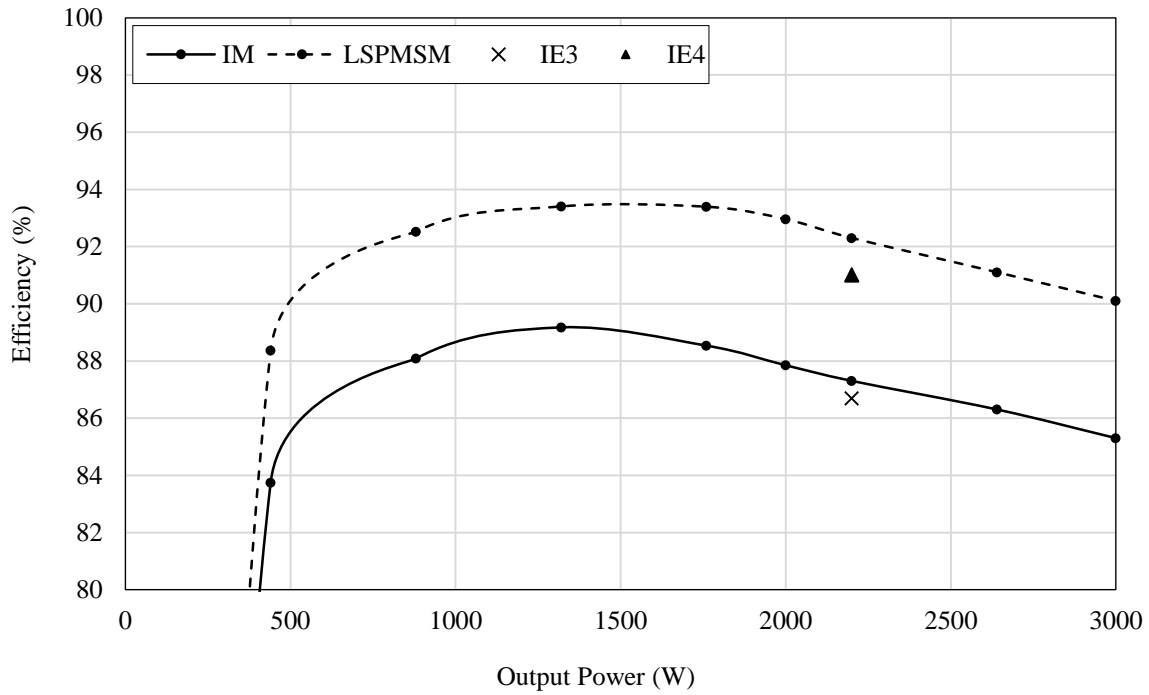
Figure 2-9. Calculated efficiency variations of a 2.2-kW IM and LSPMSM vs output power including NEMA efficiency standards.

2.4 Design Techniques for LSPMSM Performance Improvement

2.4.1   Transient Performance Improvement

A d-q model of a LSPMSM was proposed to study the starting torque and synchronisation capability of a LSPMSM under high inertia loads [44]. Possible PM demagnetization due to the large starting current was minimized through reducing the rotor bar size by 40%. This resulted in an increase in rotor resistance that led to a starting torque increase and a starting current reduction.

An innovative approach of using a 6- to 8-pole changing stator winding improved the starting performance of the LSPMSM by reducing the magnet braking torque by having a different number of stator winding and rotor PM poles during starting. The pole changing method was based on using a slot-number phase diagram [45]. The starting performance was significantly improved in comparison with a 2/4 pole changing winding method studied in [46] based on the Dahlander connection method. However, 2/4 pole changing is more practical as the stator winding is not changed, and in 8-pole changing method the synchronous torque is low, which is not proper for applications like pumps and fans. Figure 2-10a and Figure 2-10b compare the calculated LSPMSM braking torque and torque ripple versus speed using the proposed 6/8 pole shifting method with the conventional motor. It shows that the start-up capability of the LSPMSM was essentially improved.

The starting torque improvement of LSPMSMs was studied in [47]-[52] and covered aspects like: composite solid rotors [47], slotted solid rotors [48]-[49], influence of space harmonics [50], optimal skew angle [51] and the magnetizing inductance effect [52]. Figure **2-11** shows the improvement of a slotted solid rotor of a LSPMSM in comparison with a smooth solid rotor and a squirrel-cage

20

LSPMSM rotor. It shows that for the designs, when considering loading and rotor inertia, only the slotted solid rotor can reach synchronous speed. The maximum braking torque of LSPMSMs is affected by the magnetizing inductance, and higher magnetizing inductance leads to lower maximum braking torque and better start-up performance, but lower synchronization capability [52]. An analytical method including the mutual effect of fields due to cage bar currents, permanent magnets and armature currents was proposed to clarify the asynchronous torque specification impact on torque oscillations.

Figure **2-12**a and Figure **2-12**b compare the cage torque and magnet torque of the proposed method and conventional method as a function of slip. It is seen that the calculated cage torque and magnet torque using the proposed method is larger than conventional method. The coupling effect between cage bar flux and the magnet flux produces a significant negative dc component on the magnet torque [53].

a.   braking torque versus speed

b.   torque ripple versus speed
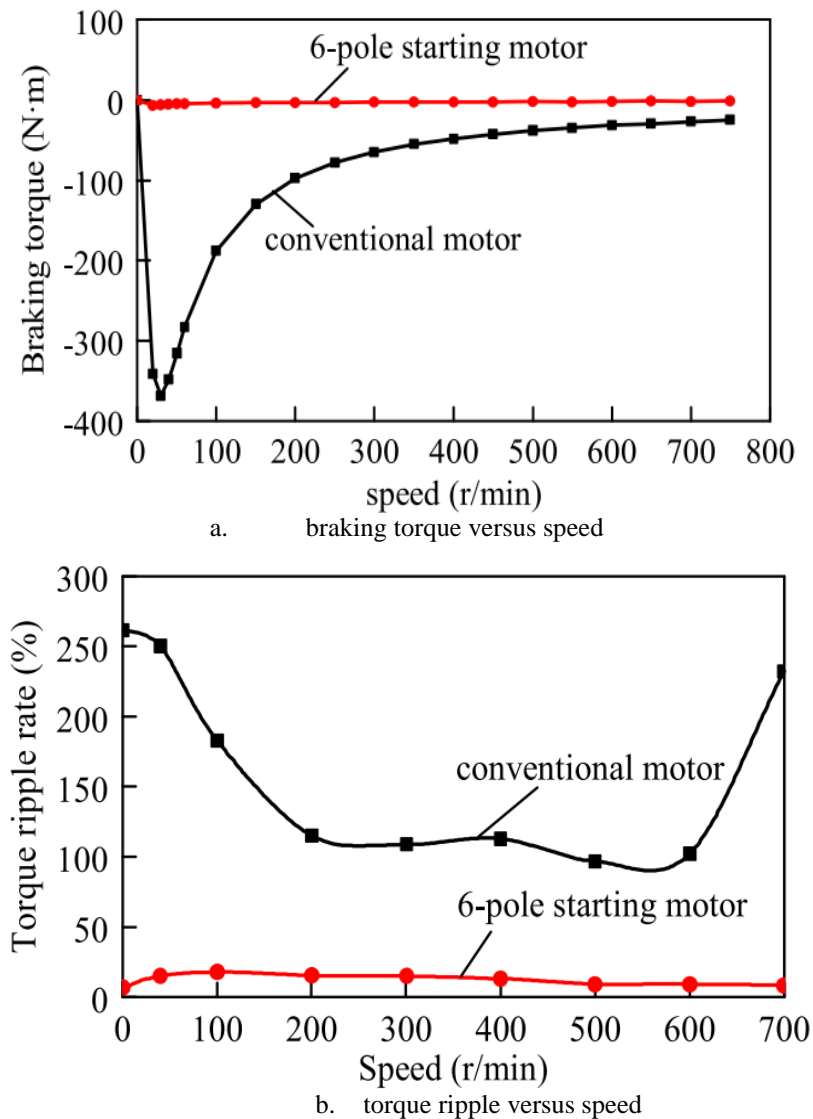
Figure 2-10. 6/8 pole changing braking torque and torque ripple versus speed [45].

21
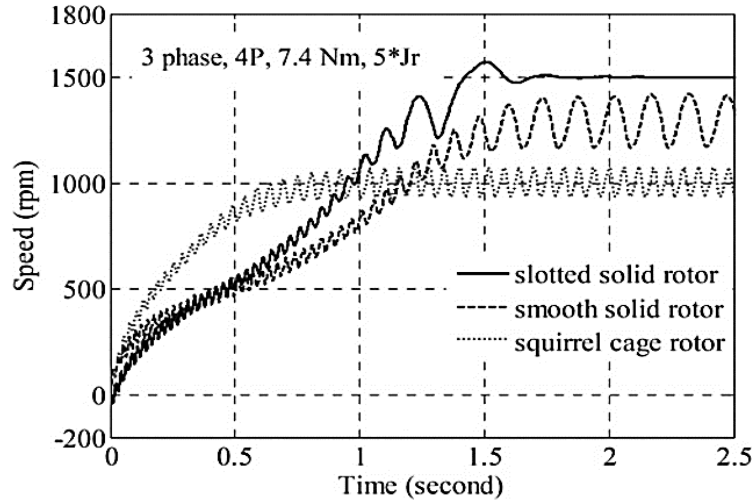
Figure 2-11. Synchronization comparison of slotted solid, solid and squirrel-cage LSPM rotors for 5 × Jr [48].

a.   Cage torque   b.   Magnet torque
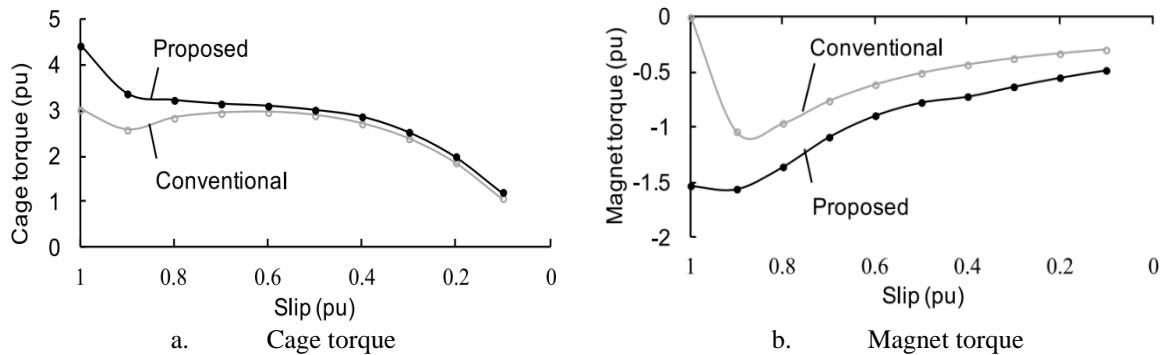
Figure 2-12. Analyzed slip characteristics of cage and magnet torque [53].

2.4.2   Steady-State Performance Improvement

The ideal steady-state performance of a LSPMSM is to have high efficiency and power factor, and low torque ripple and cogging torque. In LSPMSMs, the area and configuration of the PMs has a considerable effect on the efficiency and power factor but also affects the transient performance of these motors. Figure **2-13** shows the calculated effect of PM area on the steady-state and transient performance of a 2.2-kW LSPMSM. A minimum of 60 mm^2 of PM was found necessary to synchronize. Increased PM area results in improved efficiency and power-factor but degrades starting and settling time.

Cogging torque in LSPMSMs causes speed ripple and vibration and there have been efforts to reduce this [54]-[56]. These include: dividing the PMs into segments [54], optimizing the magnet shape [55] and using flux barriers on the rotor [56].These techniques are chiefly limited to either transient improvement or steady-state performance improvement. Thus, a focus on only transient performance improvement may degrade the steady-state performance of the LSPMSM and vice versa.

22
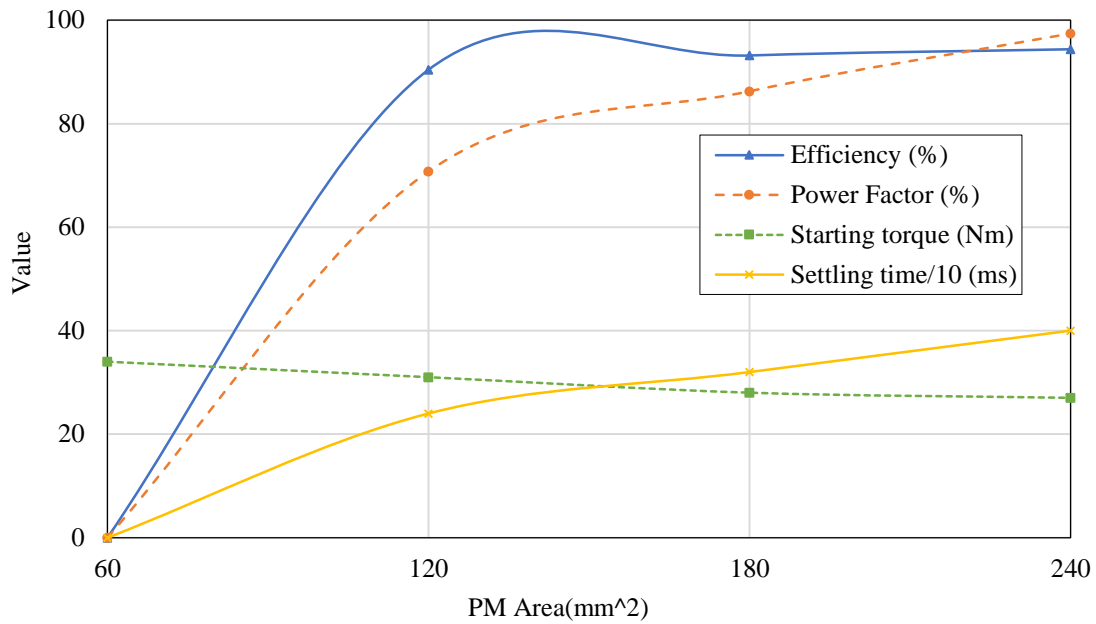
a. Variation of performance parameters versus PM area
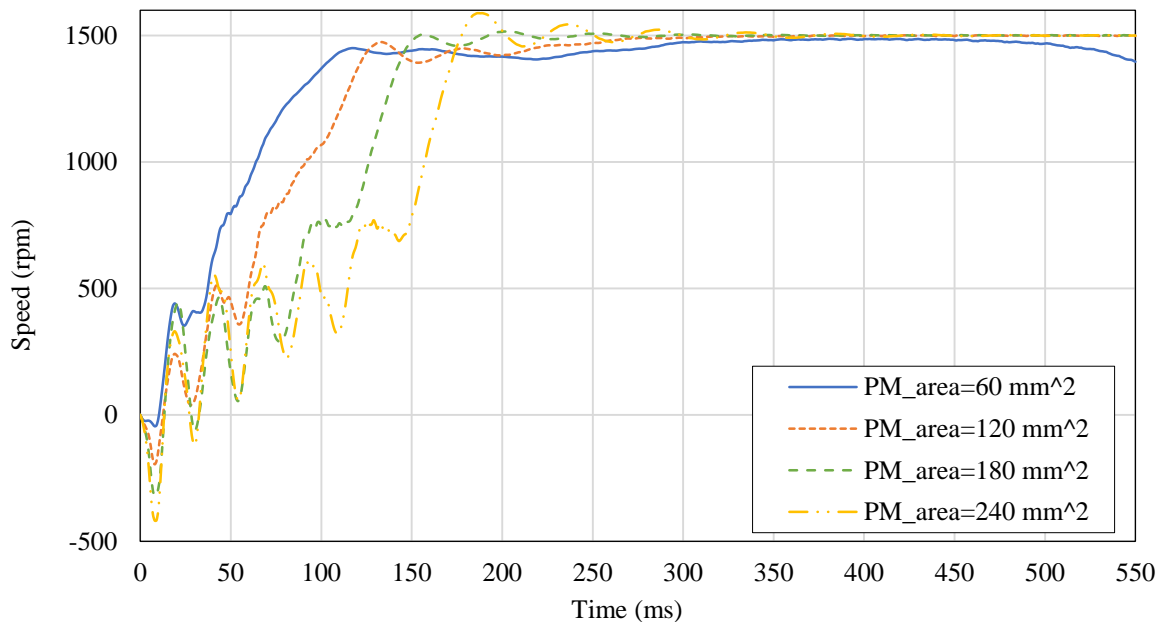
b. Speed-time responses

Figure 2-13. Effect of PM area on the transient and the steady-state performance parameters of a 2.2-kW LSPMSM.

2.5 LSPMSM Performance Improvement Using Optimization Techniques

Studies on the performance improvement of LSPMSMs are divided in two categories. Firstly, design methodology studies presenting new methods for performance improvement of the LSPMSMs were discussed in the previous section. Optimization implementation is the second category of LSPMSM performance improvement. Although optimization of induction and permanent magnet motors are common practice, there is limited optimization studies on LSPMSMs. Optimization studies for LSPMSMs can be divided in three categories based on the optimization aim: 1) transient performance improvement, 2) steady-state performance improvement, and 3) simultaneous improvement of the transient and the steady-state performance.

Most optimisation studies in the context of electric machines have been conducted using gradient-free optimization approaches, and no significant differences were observed in optimizing an electrical machine with various alternative gradient-free approaches like genetic algorithms, particle swarm optimization (PSO), evolutionary algorithms (EAs), and differential evolution algorithms (DEAs). [57]. However, the differential evolution (DE) algorithm was found to generally give the best results in terms of convergence time and repeatability of results [58]. A literature review of optimization studies was categorized as follows.

2.5.1 Transient Performance Improvement

The starting torque, settling time and synchronization capability are considered to be important factors of LSPMSM transient performance. The transient performance can be improved through maximizing starting torque, minimizing braking torque, and maximizing the allowable moment of inertia of the load. Maximizing starting torque and minimizing braking torque results in faster starting and torque improvement at low speeds. Maximizing the allowable moment of inertia of the load leads to synchronization capability improvement for high inertia loads, although it takes a longer time to reach synchronous speed. In transient performance improvement, the rotor bar and end ring dimensions play a key role and are considered to be optimization variables for this purpose [59]-[63].

To avoid steady-state performance degradation in an optimization study with a focus on transient improvement, there are two options: 1) considering both the transient and the steady-state performance parameters in the cost function, or 2) considering the steady-state performance parameters as constraints in an optimization function formed by only transient performance parameters. In fact, in a transient optimization, considering only the rotor bars and end ring dimensions as variables to improve the transient performance, using the steady-state performance parameters as optimization objectives or constraints are effective to avoid steady-state performance degradation. This is supported as follows.

2.5.1.1 Transient improvement without considering the steady-state characteristics

The starting performance and synchronization capability of an LSPMSM was improved by optimizing the rotor bar dimensions without considering steady-state performance parameters in the optimisation implementation [59]. Hence, although the starting performance was improved, there was degradation in efficiency. It is due to reduction happened in PM size and increase in rotor copper loss at steady sate due to the impact of harmonic in the airgap field and rotor resistance increase.

Synchronization capability and starting performance of a slotted, solid-rotor LSPMSM was optimised through maximizing the starting torque (T_{st}) and the torque near synchronous speed (T_{end}), with the slot depth and width selected as the main optimisation variables [60]. As above discussed, the solid-rotor construction improves the starting performance, but there is a degradation in the

steady-state efficiency in comparison with a laminated slotted-rotor. Although the efficiency of the optimum LSPMSM is higher than the benchmark IM, it only meets the IE2 standard, which is not an acceptable development.

2.5.1.2 Transient improvement involving both transient and steady-state characteristics in a cost function

The steady-state performance parameters of a LSPMSM were used in an objective function of an optimization with a focus on synchronization improvement through optimizing rotor bar dimensions [61]. The objective function was made based on the combination of the three performance parameters as follows:

$$f(x) = \left(\frac{\eta(x)}{\eta_0}\right)^{q1} \times \left(\frac{PF(x)}{PF_0}\right)^{q2} \times \left(\frac{T_{80}(x)}{T_0}\right)^{q3} \tag{2.12}$$

where η, PF and T_{80} are the steady-state efficiency, power factor and the torque generated at 80% of synchronous speed, and η_0, PF_0 and T_0 are the initial values of the same parameters. The exponents $q1$, $q2$, and $q3$ were assigned to be weighting coefficients and all their values were assumed to be unity. The efficiency and power factor represented the steady-state performance and T_{80} represented the synchronization performance. Figure 2-14a shows the cross-sections of the initial and optimised LSPMSM designs. It is seen that the optimisation approach increased the area of some of the rotor bars to improve the synchronisation capability of the LSPMSM for a fixed PM area. Speed-time response of the initial and optimized LSPMSM is shown in Figure 2-14b. The optimised LSPMSM has successful start-up for higher inertia ratios (75% increase in the maximum load inertia) and had not the steady-state performance reduction in comparison with the initial LSPMSM design. The steady-state performance parameters were not improved while they were included in the objective function. The value of the rotor resistance of the optimum cage decreased due to the increased bar section area, and this affected the steady-state torque-speed characteristic.

Synchronization capability improvement for high inertia loads of a LSPMSM was studied through rotor slot optimization [62]. The asynchronous torque at 80% of the synchronous speed and the maximum synchronous torque at the rated condition were selected as the two objectives, corresponding to synchronization and steady-state performance, respectively [62]. The optimum motor design was able to synchronize a load with a maximum of 12 times the rotor inertia compared to 7 times for the initial design. The efficiency of the optimum design was only slightly less than the initial design. The optimization was not successful in improving both the transient and the steady-state performance as the selected variables in this optimization only included the starting performance and did not consider the impact on steady-state performance.
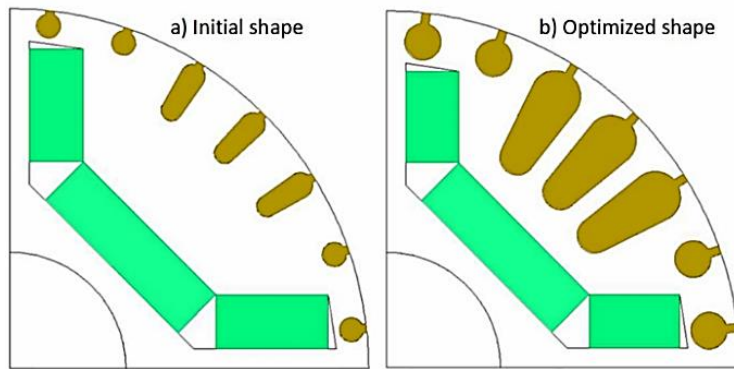
a.　Cross sections of the initial LSPMSM and optimised LSPMSM.

Initial LSPMSM
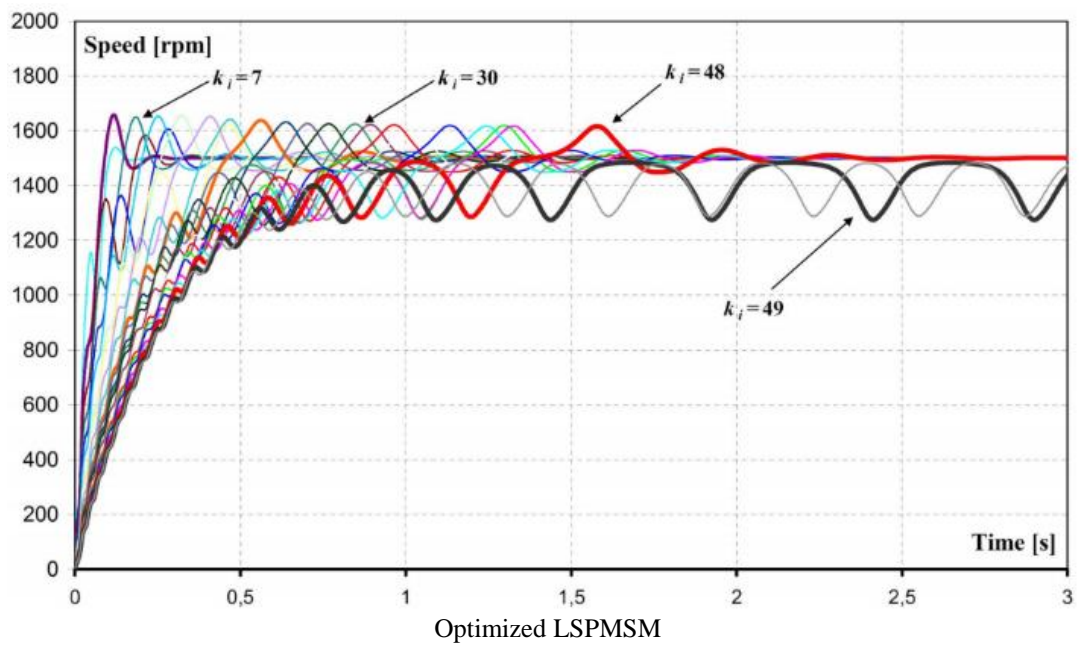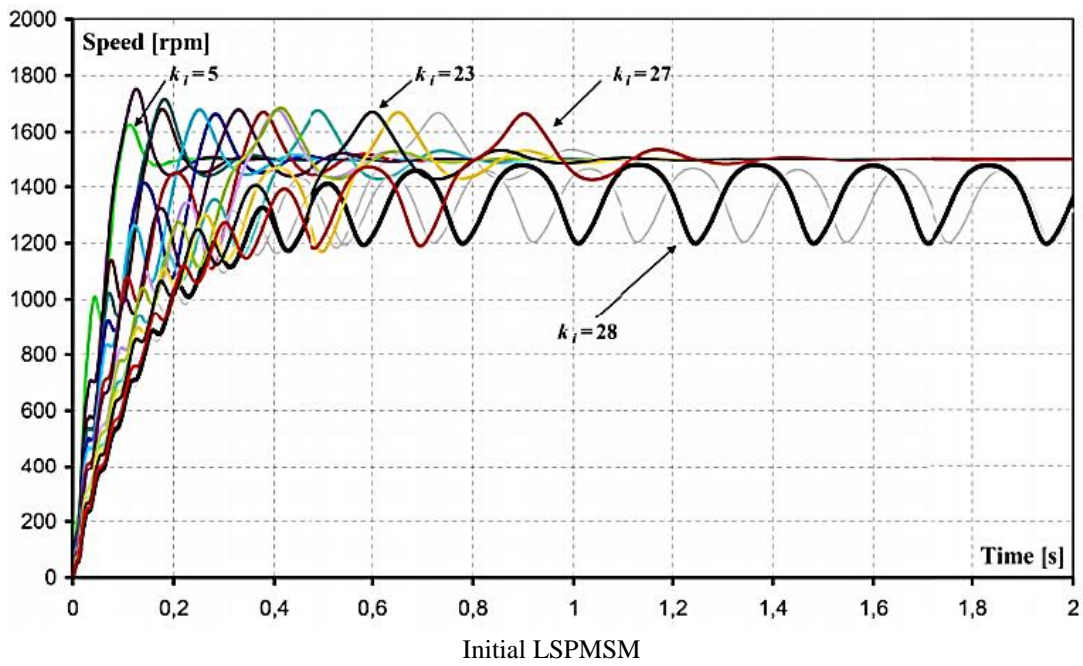
Optimized LSPMSM

a.　Speed-time responses

Figure 2-14. Cross-sections and speed-time response of the initial and optimised LSPMSMs [61].

A. *Transient improvement considering starting characteristics in constraint functions and synchronous characteristics in objective function*

The starting characteristic of a single-phase LSPMSM was improved through optimizing the rotor bar and end-ring dimensions. To avoid significant steady-state degradation, efficiency maximization was the objective function and the transient characteristic was controlled via the constraint function. The rotor bar and end-ring sizes were reduced in the optimum design (see Figure 2-15). The efficiency of the optimum design calculated by FEA was not improved in comparison with the initial design while the starting performance was improved significantly. The superiority of the optimum design in its start-up and synchronisation capability compared to the initial design is shown in Figure 2-16a and Figure 2-16b [63].
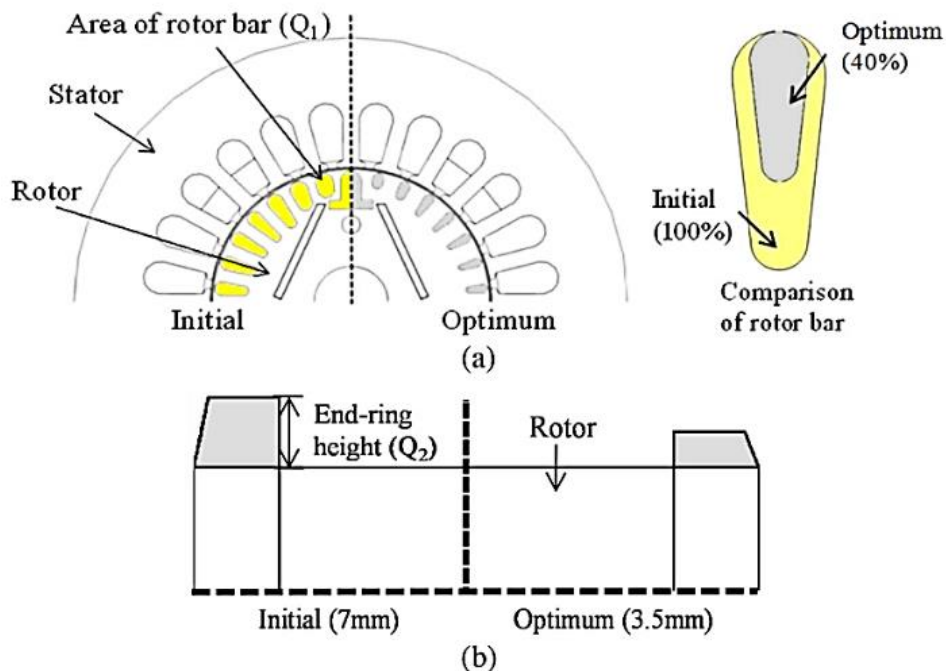
Figure 2-15. Initial and optimum designs (a) shape, (b) end-ring [63].
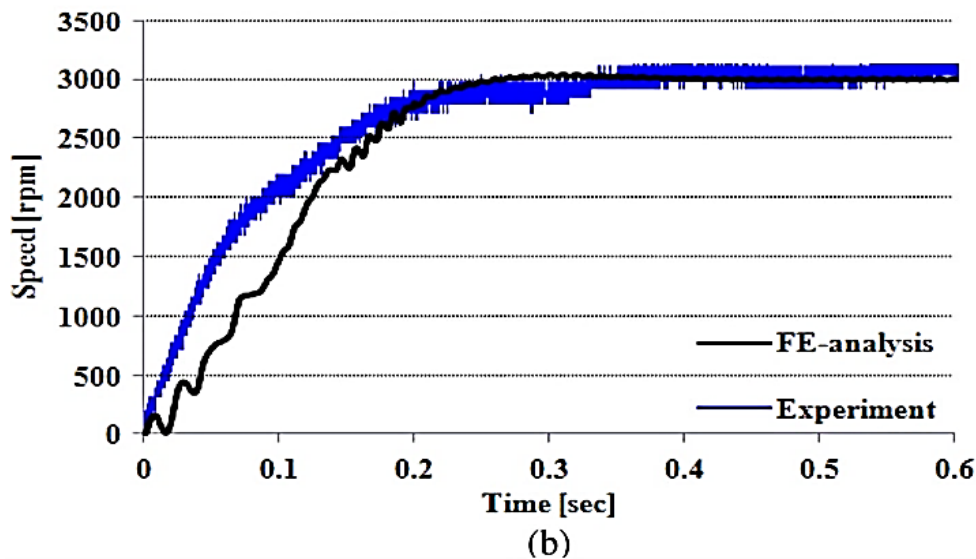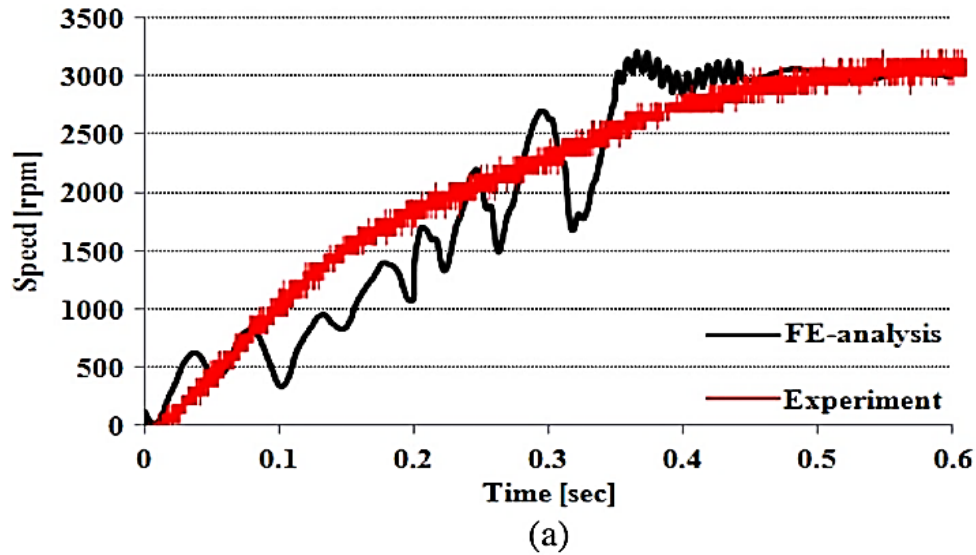
Figure 2-16. Speed-time response comparison (a) initial design, (b) optimum design [63].

2.5.2 Steady-State Performance Improvement

The steady-state performance of LSPMSMs can be improved through optimizing the steady-state performance parameters such as efficiency and power factor. In fact, a focus on the synchronous improvement will affect the transient performance of the LSPMSM. Hence, considering constraint functions that contain the starting characteristics is an effective strategy for avoiding substantial transient performance degradation [64]-[65]. The steady-state improvement of LSPMSMs were studied in four categories as follows.

2.5.2.1 Steady-state performance improvement without considering PM

There is no significant improvement in the steady-state performance of a LSPMSM without considering the PM dimensions as optimization variables. As an example, the efficiency of a 4-pole 7.5-kW LSPMSM was maximized and the rotor slot, core length and winding were optimization variables. The optimization included five constraints: efficiency (g_1), power factor (g_2), the starting torque multiplier (g_3), the starting current multiplier (g_4) and the minimum starting torque multiplier

28

(g$_5$) to minimize the transient performance degradation (see Table **2-2**)[64]. There was only a 0.4% and 0.6% improvement in the efficiency and the power factor, respectively, and this level of improvement was not considered significant.

2.5.2.2 Steady-state performance improvement with considering PM

PM dimensions and configurations play a key role in the steady-state improvement but, on the other hand, the braking torque produced by the PM is changed with PM dimensions. Therefore, to avoid transient degradation due to braking torque variations, it is useful to consider constraint functions that include the starting characteristics. The steady-state performance optimization of a LSPMSM was implemented through PM dimension optimization (see Table **2-2**). The bat algorithm (BA), an optimisation algorithm, may be an effective method to optimize complex design problems with non-linear constraints in comparison with other artificial intelligence approaches [64]. The efficiency and the power factor of a two-pole, 3.7-kW LSPMSM was maximized by PM configuration optimization. The details of the constraints are presented in Table **2-2**, and the cross-section and optimization variables (*L, Θ, Rib*) are shown in Figure **2-17** [65]. The efficiency and power factor were increased by 1.4% and 5%, respectively. This indicates how only the PM dimensions have an impact on the steady-state performance improvement.

2.5.2.3 Steady-state performance improvement including cost reduction

Efficiency maximization of LSPMSMs is possible through increasing PM volume but it causes material cost increases, which are not desirable. Hence, the material cost (mainly the PM cost) should be included in the objective function together with the steady-state performance parameters [67]-[68]. Considering the cost minimization, efficiency maximization and avoiding transient performance degradation via constraints makes the optimization more complex and there may be no significant improvement in optimization goals. For example, a LSPMSM was designed based on a squirrel-cage IM and was optimized to obtain higher efficiency and lower cost [67]. The rotor length and diameter were assumed equal based on torque per volume considerations. The efficiency and the volume of PM was selected as sub-objectives while having minimum cost as the main objective. Therefore, a single-objective optimization was defined to optimize the PM dimensions as follows:

$$f = 1 + 9 \times (1 - \eta) \tag{2.13}$$

$$g = \left(1 + \frac{9}{(S_{max} - S_{min})}\right) \times (S_{nc} - S_{min}) \tag{2.14}$$

$$Cost = (f - 1) \times 0.8 + (g - 1) \times 0.2 \tag{2.15}$$

where η, S_{max}, S_{min} and S_{nc} are efficiency, maximum, minimum and selected cross-sections of the PM, respectively. Although the cost was minimized due to PM volume reduction, the efficiency and power factor of the optimum design were lower than the initial design.

A line-start permanent magnet synchronous shaded-pole motor in Figure **2-18** [68] was optimized to minimize the total cost formulated as follows:

$$raw\ material\ cost = \sum_{i=1}^{4} weight\ of\ material(i) \times PU\ cost\ of\ material(i) \qquad (2.16)$$

$$Operating\ cost\ (\$) = \frac{P_{in}}{1000} \times 0.08 \times 10000 = 0.8 \times P_{in} = 0.8 \times \frac{P_{out}}{\eta} \qquad (2.17)$$

$$total\ cost = raw\ material + operating\ cost + power\ factor\ correction\ cost\ (\$) \qquad (2.18)$$

$$f(x) = \begin{cases} minimizing\ (total\ cost)\ , \\ all\ the\ constraints\ are\ satisfied \end{cases} \quad (see\ table\ 3) \Big\} \qquad (2.19)$$

where *material(i)* is the material types of iron, PM, copper and aluminium; P_{in}, P_{out} and η are the rated input power, output power and the efficiency, and the power-factor correction cost is assumed to be \$10/kVAr. Although the optimisation improved the efficiency and reduced the total cost, the synchronisation and the starting performance were still a challenge.
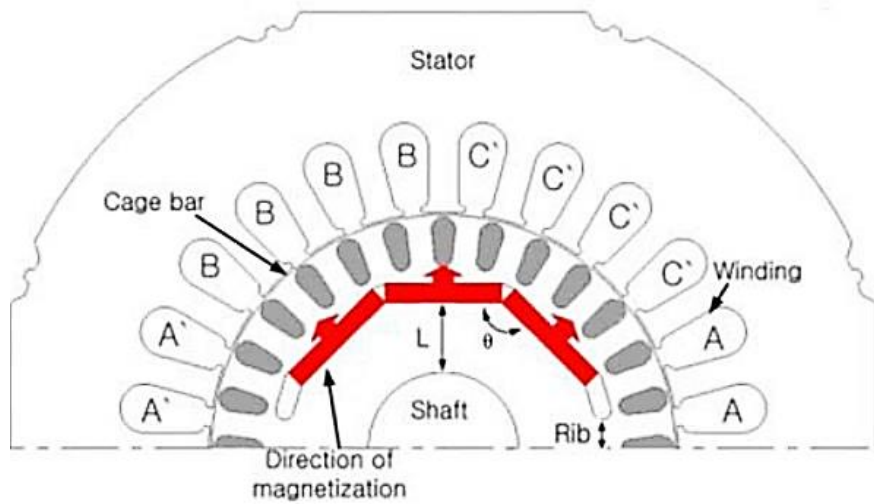
Figure 2-17. Cross-section of the LSPMSM and optimization variables [66].
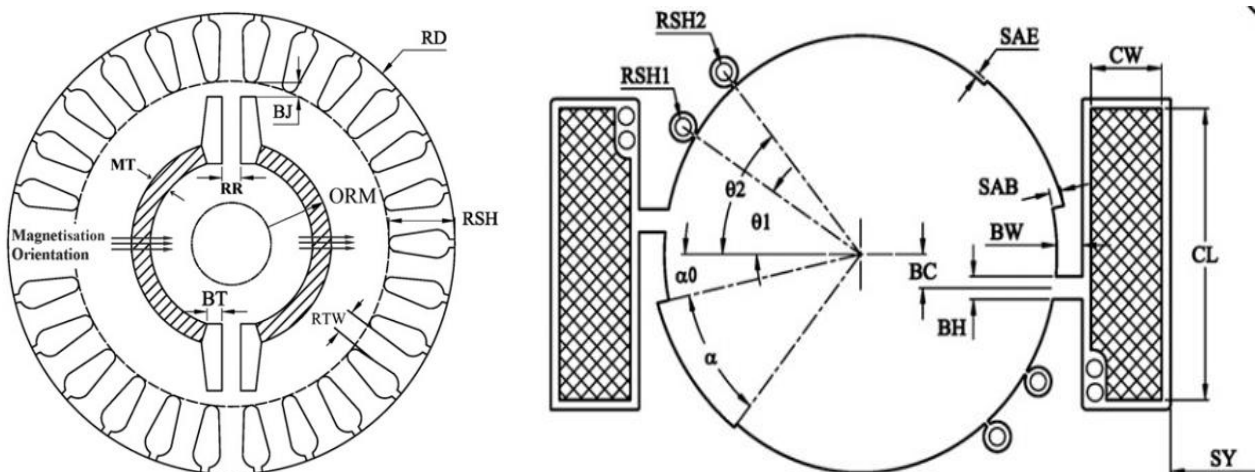
Figure 2-18. Rotor and stator schematic views including variables [68].

2.5.2.4 Steady-state performance improvement based on an optimized IM

30

A LSPMSM was designed to optimize the steady-state performance (efficiency) based on an optimized induction motor. The designed LSPMSM offered a 50% reduction in total loss compared to the original IM [69]. However, it is not necessarily true that the performance of a LSPMSM designed based on an optimized IM is better than a LSPMSM designed based on the non-optimized IM [70].

In all the above work, the optimization could only improve either the transient performance (synchronization) or the steady-state performance. Involving both the transient and steady-state characteristics in the objective function and considering constraints in the optimisation may be able to control the degradation of other performance parameters that were not included in the optimization goal or constraints. However, they were not able to propose an optimum LSPMSM with simultaneous improvement in both the transient and the steady-state performance.

2.5.3 Simultaneous Improvement of Steady-State and Transient Performance

Improving both the transient and the steady-state performance is possible through introducing a multi-objective function (MOF) optimization including a representative of both transient performance and steady-state performance in the optimization variables and objectives. In a MOF, both objectives are optimised individually and then the optimum design is extracted based on a Pareto front of the objectives. In the previous sections (2.5.2 and 2.5.1) there were optimizations with several objectives, but they were merged in a complex cost function and hence it was not possible to show a Pareto front. In a multi-objective optimization where either the optimization variables or objectives are not covering both transient and steady-state performance, the optimum design is not considered as the best feasible optimum design. Hence, multi-objective optimization studies are divided in two classes as follows.

2.5.3.1 Multi-objective optimization with objectives and variables not covering both transient and steady-state performance

A stochastic optimization was employed to optimize the rotor lamination design of a LSPMSM under a multi-objective optimisation coupled with magnetostatic FE analysis [71]. The maximization of the torque per Joule loss ratio and the reduction of the torque ripple were selected as two objectives, and the design variables are shown in Figure **2-19**. Figure **2-20** illustrates a Pareto front of the objectives after 18 generations. The final optimum design exhibited T_{ripple}=18% and T_{avg}= -6.24 Nm (see Figure **2-19**). There was a considerable improvement in the steady-state performance parameters while the synchronization performance with the full PM size was inferior compared to the 70% PM size but still acceptable. The reason why the starting improvement was not large is that the optimization objectives were both synchronous performance parameters and there were no starting performance parameters in the optimization objectives.

2.5.3.2 Multi-objective optimization with objectives and variables covering both transient and steady-state performance

A multi-objective optimisation using the Taguchi method was employed to improve the transient and steady-state performance of a LSPMSM. An upgraded regression rate technique and a weighted factor multi-objective method were incorporated to create an improved Taguchi method, which addressed the inherent limitations of the original Taguchi method in multi-response optimisation problems [72]. The rotor shape and design parameters (optimization variables) of the LSPMSM are shown in Figure 2-21. The power factor (PF) of LSPMSMs correlates with the efficiency and thus PF maximization was selected as the optimization objective corresponding to the steady-state performance.
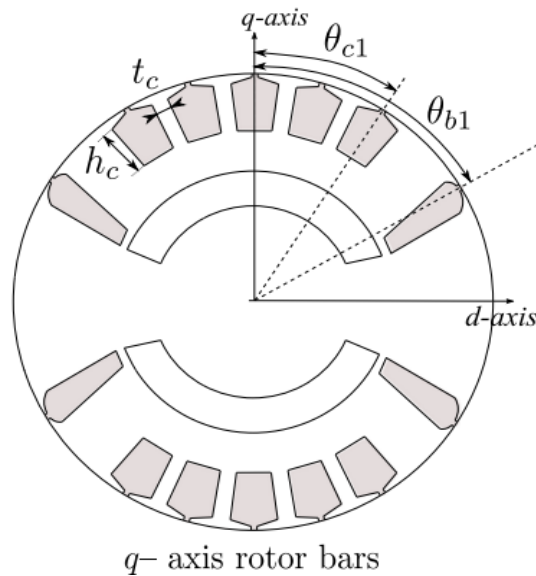
Figure 2-19. Description of the parameters used for the automatic LSSM design [71].
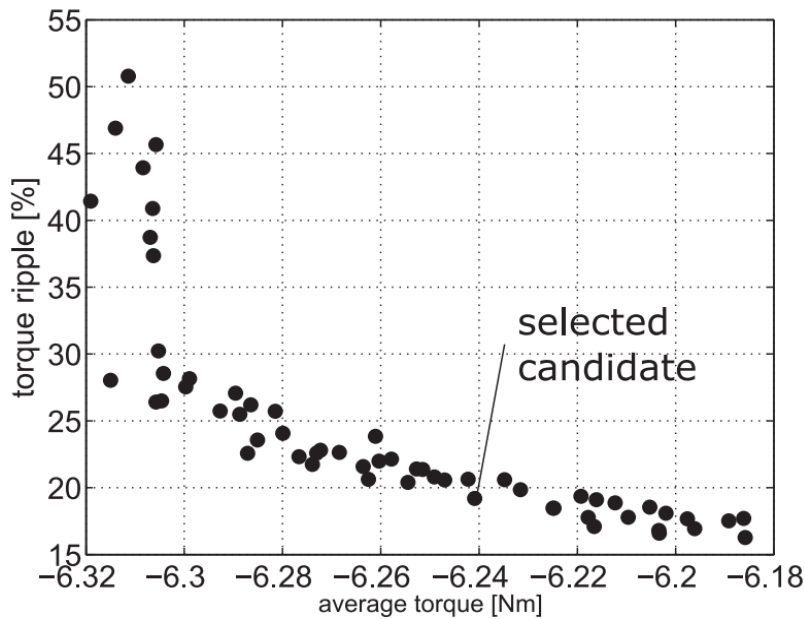
Figure 2-20. Pareto front after 18 generations [71].

The start-up capabilities are strongly associated with the maximum allowable load inertia and maximizing this was considered as the second optimization objective (transient performance). The Pareto optimum of the overall evaluation criterion (OEC) was described as following to present a judicious trade-off of the two objectives:

$$OEC = f(w_1, w_2) = w_1 \frac{PF}{PF_{max}} + w_2 \frac{x_{cr}}{x_{cr\,max}} \tag{2.20}$$

where w_1 and w_2 are the weighting factors for the objectives and they are related by $w_1 + w_2 = 1$. The PF and x_{cr} are the full-load power factor and the maximum allowed load inertia coefficient. Figure 2-22 shows the Pareto front of the objectives for a range of weighting factors. The final optimum design was a robust design with the lowest sensitivity to uncontrollable manufacturing factors that are not predictable during the design procedure (like material property variations). The robust optimum design presented a PF of 0.98, efficiency of 89.2%, and critical inertia J_{cr} of 22 times rated inertia.

(a)

(b)
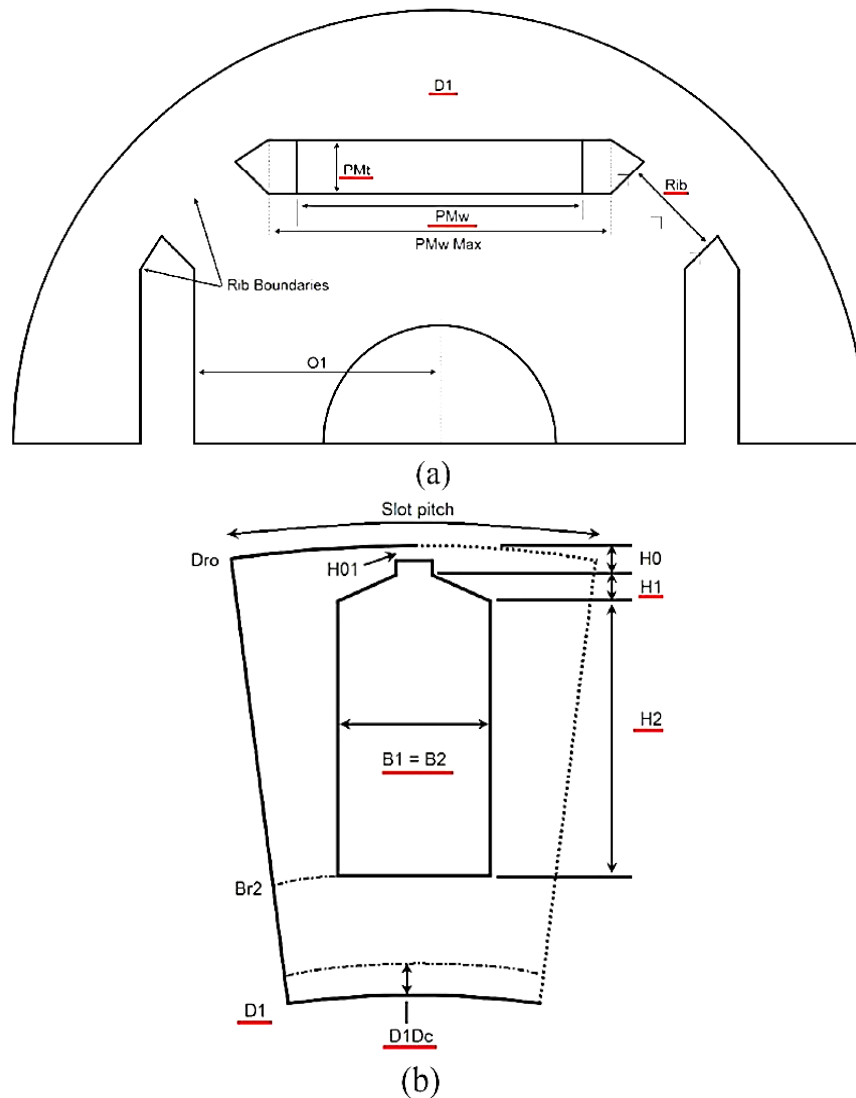
Figure 2-21. LSPMSM rotor shape and design parameters (a). Radial flux PM topology, (b). Blocked-type rotor slot [72].
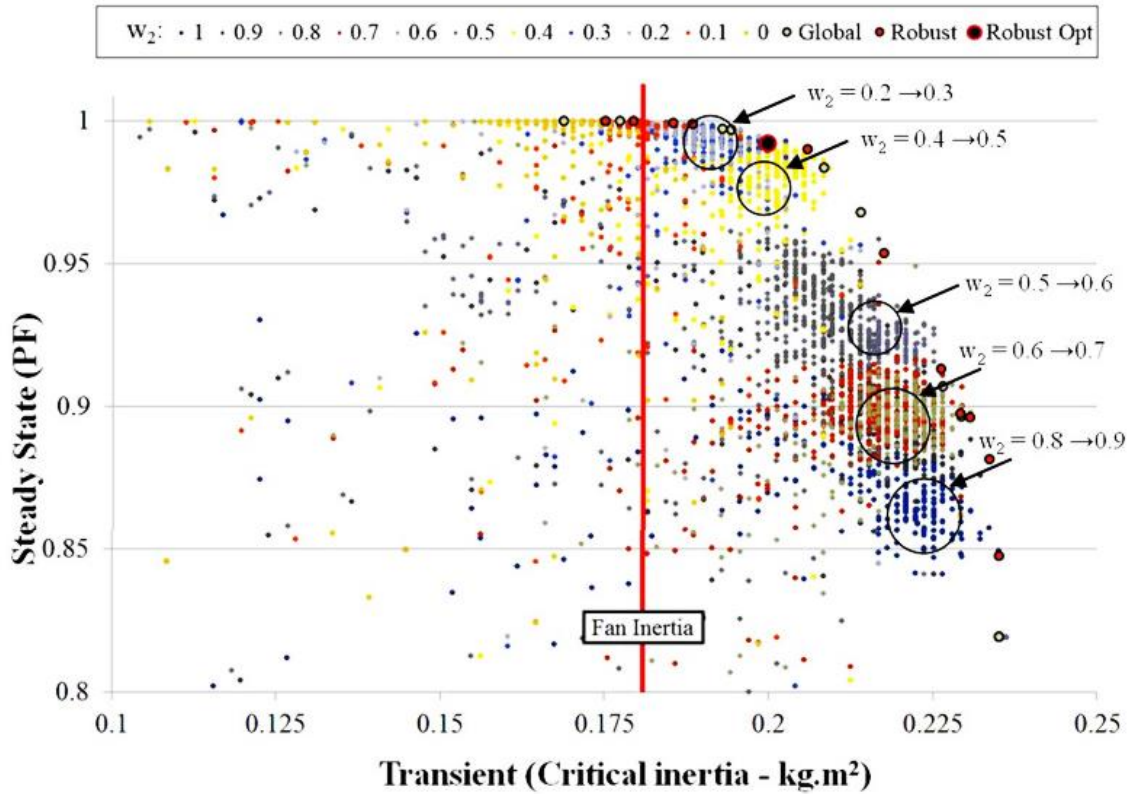
Figure 2-22. Pareto front using OA trial, optimum, and robust design results [72].

Optimisation guidelines to improve steady-state and transient performance of a LSPMSM was studied in [73]. An optimal design methodology was proposed to improve the steady-state and the transient performance for LSPMSMs. The transient improvement was conducted through minimizing the peak braking torque and maximizing the allowable moment of inertia, which were defined as a function of the d- and q axis reactances and the back EMF. Because the motor efficiency is correlated to the power factor [73], the power factor was selected as the objective for the steady-state performance improvement. With respect to the fact that there is an overall settlement between the transient and the steady state characteristics in critical slips, the optimum d- and q-axis reactances (X_d, X_q) values and optimum back EMF (E) are estimated based on the design guidelines as follows:

1) when E increased, the value of PF, J_{cr} and T_{mag} will be boosted.

2) With X_d reduction the values of J_{cr} and T_{mag} increased and it does not affect the power factor value.

3) The PF and T_{mag} are dependent on the saliency ratio whereas its relationship with J_{cr} may be variant (direct, inverse, or even neutral).

A flowchart of the proposed design guidelines is presented in Figure **2-23**. It indicates the calculation technique of the optimized design parameters based on the design guidelines proposed in Figure **2-23**.

2.6 Discussion of Literature Review

Table **2-2** and Table **2-3** summarize the literature review of the optimisation and design techniques employed in LSPMSM performance improvement. In Table **2-2** the details of the optimization studies including the variables, the optimization objectives, constraints and optimization algorithm are listed. It shows there is limited optimization studies considering MOF to improve LSPMSM transient and steady-state performance simultaneously. A MOF that considers one parameter of the transient performance and one parameter from the steady-state performance can be a good optimization implementation of LSPMSMs. Based on the information in Table **2-2**, it is clear that in previous studies, the rotor cage and PM dimensions were considered to be variables in the LSPMSM optimization studies and the stator parameters like stator slot dimensions and number of conductors per slot were generally not used as variables.

Table **2-3** shows that significant performance improvement can be possible with optimisation. It indicates that there are limited studies considering improvement in the starting torque, synchronous torque, cogging torque and manufacturing cost minimization while considering improvement of the synchronization capability and efficiency for LSPMSMs. In addition, there is a lack of optimization studies using gradient-based approaches in the electric machines, particularly in LSPMSMs optimization, whereas employing gradient-free optimisation approaches is common.
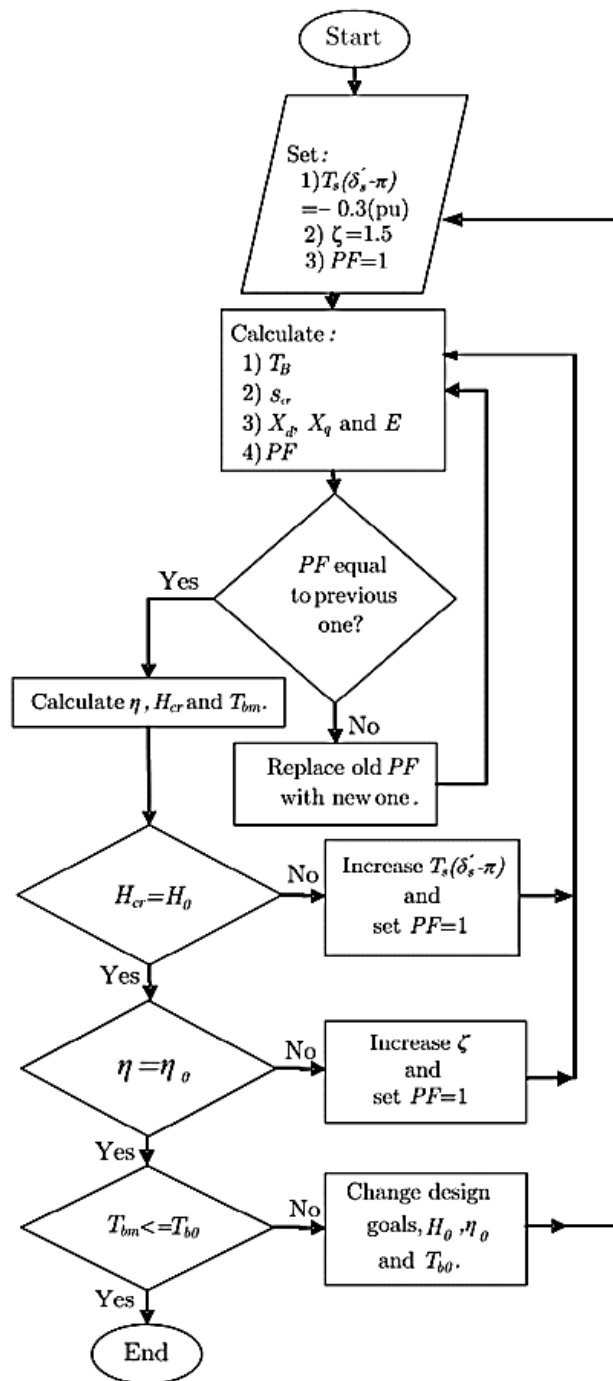
Figure 2-23. The proposed optimal design technique flowchart [73].

2.7 Conclusion

Recent developments in LSPMSM performance improvement were reviewed in this chapter. LSPMSMs have superior steady-state performance compared to IMs and can be used in relatively constant speed applications such as pumps and fans. In LSPMSMs the starting and synchronisation performance are significant challenges in comparison with IMs and hence researchers have sought to improve the transient performance through design techniques or the use of optimization. Based on a literature review, an effective transient optimization is: 1) a single-objective function including a transient characteristic (recommended to use either starting torque or maximum allowable moment of inertia) constrained with the steady-state characteristics to avoid steady-state performance degradation, 2) a multi-objective optimization containing both the transient and the steady-state characteristics and corresponding variables.

Research gaps in LSPMSM optimization were identified as:

- Limited optimization studies considering the stator and winding parameters as optimization variables,

- Limited analytical design and optimization techniques of the LSPMSMs,

- Limited MOF optimization for the LSPMSM performance improvement,

- Limited MOF optimization considering cost minimization,

- Lack of comparative studies in the performance of gradient-based and gradient-free optimization approaches in the context of electric machines,

- Lack of optimization studies considering thermal performance of the LSPMSM as either objective or constraints.

In this chapter, the research gaps corresponding to the LSPMSMs were realized, and this thesis aims to cover some of these gaps. In next chapter (Chapter 3), an LSPMSM is designed based on a commercial IM and, using FEM-based optimization techniques, the starting torque and efficiency of the LSPMSM are simultaneously optimised. Two different optimization approaches (gradient-free and gradient-based) are studied to compare their performance. This optimization study covers the gaps corresponding to limited MOF optimization highlighted in this chapter.

Table 2-2. Review summary of LSPMSMs optimization techniques.

Ref.	Optimization Algorithm	Variables	Objective functions	Constraints	Happened performance Improvement	
					Transient	Steady-state
[59]	• GA	• Rotor slot dimensions	• Minimizing rotor bar resistance	• No constraint	✓	✗
[60]	• Neural network and imperialist competitive algorithm	• Rotor slot dimensions	• Maximizing the starting torque • Maximizing the T_{80}	• No constraint	✓	✗
[61]	• Modified PSO	• Rotor slot dimensions	• Maximizing efficiency and PF • Maximizing T_{80}	• No constraint	✓	✗
[62]	• PSO	• Rotor slot dimensions	• Maximizing torque in 80% of synchronous speed T_{80} • Maximizing synchronous torque	• No constraint	✓	✗
[63]	• GA	• Rotor bar and end-ring dimensions	• Maximize efficiency	• Starting torque>1.1 Nm & Maximum torque>1.2 Nm	✓	✗
[64]	• Ant Colony Algorithm	• Rotor slot width, • Core length, • Number of conductors per slot • Wire diameter	• Maximizing efficiency	• $g_1(x) = \left(\frac{\eta - \eta_0}{\eta_0}\right) > 0$ • $g_2(x) = \left(\frac{PF - PF_0}{PF_0}\right) > 0$ • $g_3(x) = \left(\frac{T_{st\,min0} - T_{st\,min}}{T_{st\,min0}}\right) > 0$ [*] • $g_4(x) = \left(\frac{I_{st0} - I_{st}}{I_{st0}}\right) > 0$ [**] • $g_5(x) = \left(\frac{T_{st} - T_{st0}}{T_{st0}}\right) > 0$	✗	✓
[65]	• Bat Algorithm (BA)	• PM width and length	• Maximizing efficiency and power factor	• $g_1(x) = \left(1 - {T_{80}(x)}/{T_z}\right) \le 0$ [***] • $g_2(x) = \left({m_{m(x)}}/{m_z}\right) \le 0$ [****]	✗	✓
[66]	• Response surface methodology (RSM)	• See Figure **2-17**	• Maximizing efficiency and power factor	• No constraint	✗	✓
[67]	• GA	• PM dimensions	• Maximizing efficiency, • Minimizing PM Volume (cost)	• No constraint	✓	✗
[68]	• GA	• See Figure **2-18**	• Material and power factor correction cost minimization • Efficiency Maximization	• Nominal torque Nm $0.035 < T_n < 0.045$ • Starting torque Nm $T_{st} > 0.015$ • Average flux density in yokes $0.7 < B_{yoke} < 1.25$	✗	✓
[69]	• Using a combination of formal optimization techniques and standard design methods	• Rotor slot dimensions	• Maximizing Efficiency	• No constraint	✗	✓
[70]	• GA	• Rotor slot and PM dimensions	• Starting torque and efficiency maximization	• No constraint	✓	✓
[71]	• Stochastic optimization (Pareto dominance criterion)	• L, Ө, Rib (see Figure **2-19**)	• Maximizing torque per Joule loss ratio • Minimizing of the torque ripple.	• No constraint	✓	✓
[72]	• Improved Taguchi method based on regression rate (TBRR) optimization framework	• Rotor slot and PM dimensions	• Maximizing power factor and moment inertia	• No constraint	✓	✓
[73]	• New optimization guideline	• Not available	• Maximizing power factor, inertia, and minimizing braking torque	• Braking torque (BT) less than allowable BT	✓	✓
Symbols	[*] Starting torque multiplier	[**] Starting current multiplier	[***] T_z: initial value of T_{80}	[****] m_m and m_z: total and initial mass of PM		

Table 2-3. LSPMSMs main performance parameters improvement using design and optimization techniques.

Improvement focus / Techniques	Ref.	Applied Technique	Improvement happened in main performance characteristic under employed technique stated by literature					
			Starting Torque	Synchronization	Cogging Torque	Synchronous Torque	Efficiency & PF	Cost ($)
Design Methodologies	[44]	• A d-q model including cage bar reduction to PM demagnetization reduction	✗	✓	✗	✗	✗	✗
	[45]	• innovative approach 6- to 8-pole shifting stator windings	✗	✓	✗	✗	✗	✗
	[46]	• 2-to4-pole changing at starting	✗	✓	✗	✗	✗	✗
	[47]-[49]	• Slotted Solid rotor technique	✗	✓	✗	✗	✗	✗
	[50]	• dq-model based on a space harmonic	✗	✓	✗	✗	✗	✗
	[51]	• Optimal skew angle	✓	✓	✗	✗	✗	✗
	[52]	• Magnetizing inductance impact on start-up	✓	✗	✗	✗	✗	✗
	[53]	• Mutual effect among the fields due to armature current, cage-bar current, and PMs	✗	✓	✗	✓	✗	✗
	[54]-[56]	• Cogging torque reduction	✗	✗	✓	✓	✗	✗
Optimisation Methods	[59]	• Optimizing rotor bar resistance	✗	✓	✗	✗	✗	✗
	[60]	• Maximizing the starting torque • Maximizing the T_{end}	✓	✓	✗	✗	✗	✗
	[61]	• Maximizing efficiency and PF • Maximizing T_{80}	✗	✓	✗	✗	✗	✗
	[62]	• Maximizing torque in 80% of synchronous speed T_{80} • Maximizing synchronous torque	✗	✓	✗	✓	✗	✗
	[63]	• Maximize efficiency • Improving starting characteristic	✓	✓	✗	✗	✓	✗
	[64]	• Maximizing efficiency	✗	✗	✗	✗	✓	✗
	[65]	• Maximizing efficiency and power factor	✗	✗	✗	✗	✓	✗
	[66]	• Maximizing efficiency and power factor	✗	✗	✗	✗	✓	✗
	[67]	• Maximizing efficiency, • Minimizing PM Volume	✓	✗	✗	✗	✗	✓
	[68]	• Total cost minimization • Efficiency maximization	✗	✗	✗	✗	✓	✓
	[69]	• Maximizing Efficiency of the baseline IM	✗	✗	✗	✗	✓	✗
	[70]	• Starting torque and efficiency maximization	✓	✓	✗	✗	✓	✗
	[71]	• Maximizing torque per Joule loss ratio • Minimizing of the torque ripple.	✗	✓	✗	✓	✓	✗
	[72]	• Maximizing power factor • Maximizing moment inertia	✗	✓	✗	✗	✓	✗
	[73]	• Maximizing power factor, inertia, • Minimizing braking torque	✓	✓	✗	✗	✓	✗
Influential factors			Rotor resistance, PM flux	Braking torque, rotor resistance, T_{80} and inertia	Average torque, synchronous torque		Losses	Material price
Geometric components			Rotor slots dimensions	PM and rotor slots dimensions	PM, flux barrier and stator slots dimensions		PM dimensions, Coil number	PM and motor sizes

3. CHAPTER 3

3. SIMULTANEOUS EFFICIENCY AND STARTING TORQUE IMPROVEMENT OF LINE-START PERMANENT MAGNET SYNCHRONOUS MOTORS BASED ON FEM OPTIMIZATION

This chapter presents a FEM-based optimisation study to improve efficiency and starting torque of a 4-kW, 3-phase LSPMSM design based on a commercial IM. The chapter is divided in six sections: Section 3.1 presents the summary of the chapter. Section 3.2 is an overall introduction, while the machine under study is introduced in Section 3.3. Optimisation implementation based on FEM and optimization results are studied in Section 3.4. A comparison of the performance of optimisation approaches is discussed in Section 3.5. A conclusion is presented in Section 3.6.

3.1 Summary

Simultaneous steady-state and transient performance optimization of a 4-kW line-start permanent magnet synchronous motor (LSPMSM) under a multi-objective function is examined in this study. Efficiency maximization (representing steady-state performance) and starting torque maximization (representing transient performance) are nominated as objective functions. Two different optimization algorithms, gradient-based algorithm (GBA) and gradient-free algorithm (GFA), are employed to optimize the LSPMSM. Sequential nonlinear programming (SNLP) is the gradient-based algorithm in this study and the gradient-free algorithm under study is a genetic algorithm (GA). A comparative study of the algorithms' performance is presented. To provide an inclusive comparison of both algorithms' performance, a similar optimization study is implemented for the baseline induction motor. The optimization results demonstrate that the multi-objective optimization studies present optimum designs with optimized steady-state (using efficiency maximization) and start-up (using starting torque improvement) performance of both motors. Results indicate that both algorithms converge reliably to almost the same optimum (objective) value. Depending on the nature of the optimisation problem, number of design variables, and degree of convergence, the genetic algorithm requires many more evaluations than the gradient-based algorithm. Accordingly, optimization time required by the GA is more than the gradient-based algorithm under similar optimization conditions.

3.2 Introduction

Due to the high efficiency and power factor of LSPMSMs and their ability to rotate at synchronous speed, they are serious competitors for squirrel-cage induction motors (SCIMs) in industrial applications (fans, pumps, etc.) [74]-[75]. Although the LSPMSMs do not have smooth start-up like

induction motors, they benefit from avoiding the need for drives (inverters) and associated costs as well as having higher efficiency. These motors can be designed by modifying the rotor of induction motors. However, selection of the permanent magnets (PMs) needs careful consideration to achieve a balance between starting and synchronisation [76].

Improving electric machine performance and cost reduction have been the subject of many studies for researchers and engineers. Optimization implementation is a well-known strategy for the performance improvement of electric machines. While there is no set method in the design optimization of electrical machines, there are some important stages to be considered [57]. The stages are listed as follows:

Stage 1: Design the model of optimization based on the initial design of the case study. In any type of optimization method, optimization variables, constraints, objective(s), and types of them, such as linear or non-linear, should be clarified. A recently introduced optimization model, called robust optimization, may be developed as a replacement for traditional optimization methods when considering manufacturing limitations in designing a real production system [77]-[88].

Stage 2: Implement the optimization method using an optimization algorithm and gain an optimal design. The optimization techniques are categorised in various ways such as multi-level and multi-disciplinary [89], [90], [91]-[102].

Stage 3: Validation of the optimum design using prototyping and experimental tests or a finite-element analysis. The optimization should be re-designed if there is not an agreement between simulation results and experimental tests.

While performance improvement of the induction and PM machines is common practice [103]-[105], there are limited development studies on the LSPMSM. Recent developments including design methodologies and optimizations of the LSPMSMs were extensively discussed in the previous chapter. For example, d-q model for synchronisation improvement [106] and digital observer controller technique for torque ripple minimization [107] were design methodologies studied to improve the LSPMSM performance. Regarding design methodologies, it was understood that these techniques are chiefly limited to either transient or steady-state performance improvement. A focus on only transient performance improvement may degrade the steady-state performance of the LSPMSM and vice-versa.

Optimization studies for LSPMSMs are divided in two categories: single-objective or multi-objective optimization. Single-objective optimization focusses on either the transient performance or the steady-state performance. For example, cogging torque and torque ripple minimization [108]-[112] were studied to improve the steady-state performance based on a single-objective optimization. Recently, a few optimization studies have focused on simultaneous improvement of the transient and the steady-state performance of LSPMSM using multi-objective optimization. There are several well-

known multi-objective optimization algorithms like non-dominated sorting genetic algorithm (NSGA and NSGA-II), and multi-objective particle swarm optimization (PSO) algorithm [113]-[120].

There are two main approaches for optimization algorithms: conventional (gradient-based) and modern intelligent (gradient-free) approaches. All the studies mentioned previously chiefly made use of gradient-free optimizations (e.g., evolutionary algorithms) like genetic algorithms [121], particle swarm optimization (PSO) [122], evolutionary algorithms (EAs) [123], and differential evolution algorithms (DEAs) [124] No significant differences were observed when optimizing an electrical machine with various gradient-free algorithms [57]. Limited conventional gradient-based optimization approaches have been studied in the performance optimization of electric machines though they are simple in implementation [57]. For instance, they can be used to optimize a motor and estimate its performances according to a magnetic circuit model [125]-[127]. A comparative study on performance of two different optimization approaches (gradient-based and gradient-free) was conducted on an aerodynamics problem in [128]. The Adjoint algorithm was the gradient-based algorithm and the genetic algorithm was used as the gradient-free algorithm [128]. It was concluded that the gradient-based algorithm was more beneficial than gradient-free for detailed designs that seek tighter convergence and high-fidelity simulations. However, there is a lack of a similar comparative study in the context of the electrical machines.

This chapter tries to address three main shortcomings of the previously published works. Firstly, there are few comprehensive optimization studies on the LSPMSM despite the existence of numerous optimization studies of other motor types. Secondly, a lack of gradient-based optimization study in the context of electrical machines, and comparative studies between performance of GBA and GFA in electrical machine optimization. Thirdly, a lack of clear information about the other key performance parameter variations not included in the optimization objective functions. For example, it should be investigated how, in an efficiency optimization study, the other key parameters like power factor and cogging torque are affected.

In this chapter, a LSPMSM is designed based on a 4-kW commercial IM. The LSPMSM performance in both transient and steady state are simultaneously improved using multi-objective optimization. Two different approaches, gradient-free and gradient-based, are employed to achieve this aim and a comprehensive comparison of the performance of these two different algorithms is presented in the context of electrical machines. The gradient-based algorithm considered in this study is sequential nonlinear programming (SNLP) and the genetic algorithm (GA) is the gradient-free algorithm. Firstly, the transient and the steady-state performance are separately improved under two single-objective functions (SOFs). Then, a multi-objective function (MOF) is formulated for simultaneous improvement of the steady-state and transient performance of the LSPMSM. An optimum design of LSPMSM with superior performance in both transient and steady-state is

produced. To present a wider comparative study on the performance of optimization algorithms, the same analysis is implemented on the IM. It is found that the number of function evaluations required in the GA is many more than the SNLP algorithm and, hence, has a longer execution time than the SNLP algorithm.

3.3 Problem Definition and Machines Under the Study

According to the international efficiency standard [129], the efficiency of direct-on-line motors are categorized as: standard efficiency (IE1), high efficiency (IE2), premium efficiency (IE3) and super premium efficiency (IE4). According to the IEC, for 4-kW, 50-Hz 4-pole electric motors the values for IE2 and IE4 are 86.6% and 92.1%, respectively. The benchmark is a commercial 4-kW IM which meets the IE2 standard. To achieve the IE4 standard for a fixed frame size (without changing the rotor and stator diameters) a hybrid rotor is presented as a solution that includes changing the rotor cage design and inserting a PM in the rotor of the IM. Four-pole commercial super premium (IE4) LSPMSMs are designed to be exchangeable with current commercial IMs (IE2). Standard frame sizes used for LSPMSMs are similar to IMs. Typically, the IE4 LSPMSM has a greater power density (kW/kg) than the IE2 IM [130]. The presence of permanent magnets in the LSPMSMs facilitates a higher power density than the squirrel cage IMs but increases the motor material cost.

The starting torque of LSPMSMs is generated in the same way as induction motors through the interaction between the rotating electromagnetic field produced in the air gap by the stator excitation currents and the induced currents in cage bars. When the rotor starts to rotate, EMF and current at slip frequency is induced in the stator windings by the PM flux. This produces a magnet braking torque that opposes the induction motor acceleration (cage) torque during the acceleration, and it causes the LSPMSM torque in the transient operation area to be lower than the induction (cage) torque because of the magnet generated torque. The cage torque disappears after synchronization and only the magnet torque remains.

In this section, the commercial 4-kW IM is analyzed using FEA and the simulation results are validated using experimental data. Then the rotor of the IM is changed to a hybrid rotor including a PM. In the LSPMSM design process, firstly, with modification of the rotor of the IM and inserting a PM in the rotor, the initial design of the LSPMSM is created. Then, its performance is analyzed using FEM and compared with the benchmark IM. The temperature rise in the design process is considered 65°C and 85°C in winding and PM, respectively, to present a more realistic design and precise result.

<div align="center">Commercial motor</div>

<div align="center">Stator and winding</div>

<div align="center">Rotor and bearing</div>
<div align="center">Figure 3-1. View of the 4-kW commercial IM.</div>

3.3.1 IM Structure

The present study considers a 4-kW, 3-phase commercial IM. Typical values of efficiency and power factor for 4-kW IMs are approximately 87% and 0.84, respectively. A 2D model of the commercial IM is developed using the motor dimensions. The stator and rotor magnetic material have been chosen as non-oriented steel (M470-50A). The main specifications of the motor are determined depending on the values given in Table **3-1**. Figure 3-1 illustrates some views of the commercial IM under study.

3.3.2 LSPMSM Structure

The initial LSPMSM is designed by applying changes in the rotor of the IM. Stator and winding for both are the same and the same input source 415V-Delta, 50 Hz is used for them. The configuration of the permanent-magnet locations and volume and rotor bar shape are calculated based on sizing equations to reach a balance between starting and synchronization performance. So, the minimum PM volume that generates the required air gap flux density is determined. Table **3-2** lists the magnetic properties of the permanent-magnet (NdFe35) used in this study. This initial motor design is then put through optimization to achieve various objective functions. It is to be noted that the stator and winding configurations are subject to no change and kept like that of the commercial IM. It is expected that both motors operate with the same power supply (3-phase 415-V, 50-Hz).

Table 3-1. Design parameters of the studied 4-kW IM.

Parameters	Value
Power	4-kW
Voltage	415 V-delta
Poles	4
Frequency	50 Hz
Number of Stator Slots	36
Number of Rotor Slots	28
Conductor per slot	56
Winding Material	Copper
Bars and End Ring Material	Aluminum
Insulation class	F

Table 3-2. Permanent Magnet Properties at 20 °C.

NdFe35 PM Properties	Value	Unit
Residual flux density (B_r)	1.23	Tesla
Coercive force (H_c)	890.00	kA/m
Maximum energy density	273.00	kJ/m^3
Relative permeability	1.10	-
Mass density	7400.00	kg/m^3
Conductivity	625000.00	S/m
Max Temperature	225	°C
Curie temperature	460	°C

3.3.3 Electromagnetic Performance Analysis (FEM)

Electromagnetic analyses of the designed motors are performed using the Maxwell software package. The experimental data of the IM is used to verify the FEA simulation results of the IM. This shows the FEA simulation process is accurate and reliable and that the FEA simulation results for the baseline LSPMSM design can be considered reliable. The studies and simulation results are based on operation at rated torque (26.7 Nm). The performance of the LSPMSM, in both steady-state and starting, is tested with different loading conditions using FEM.

3.3.3.1 Magnetic analysis

The computed time domain magnetic fields are plotted as field overlays, which represent the field quantities on the surface of the motor at a specific time in the simulation. Field overlays are presented to show the magnetic flux density magnitude and the magnetic field lines for the motor. The magnetic flux density of 2D and 3D designs is given in Figure **3-2** and shows the maximum flux density value is approximately 1.87~2T. The magnetic flux density is measured in units of Tesla (T). It indicates the level of magnetic saturation in the electrical steel of each design. Red areas indicate the location of any magnetic saturation and are associated with increased core losses. Saturation occurs in the electrical steel if the magnetic flux density exceeds 1.8 T. This figure indicates that both motors safely operate under full constant load with the LSPMSM having a slightly lower peak flux density than the IM.

3.3.3.2 Steady-state analysis

LSPMSMs in the steady-state operate with synchronous speed (slip=0) and, hence, they avoid rotor losses and eliminate all problems related to slip, resulting in efficiency and power factor

improvement, reducing stator current and increasing torque density. Also, this reduction in stator current, which is due to magnetizing current reduction, also reduces the copper loss of the LSPMSM. Figure 3-3 shows the loss contributions of two studied motors (excluding the mechanical loss). The LSPMSM loss is 150 W less than the IM at full-load operation due particularly to the significantly decreased rotor cage loss in the LSPMSM. The rotor cage loss is roughly 30% of the total loss in the IM, while it is 12% of the total loss for the LSPMSM. The stator copper loss is also reduced in the LSPMSM due to the increase efficiency and power factor because of stator current reduction.

Figure 3-4 compares the motor steady-state performance under full-load conditions. Figure 3-4a shows the motors efficiencies versus output power (including mechanical losses) and compares their values with the IE standards (IE2, IE4) for 4-kW, 4-pole motors. It includes the experimental results of the commercial IM at some points. The IM meets the IE2 standard while the initial LSPMSM design meets the IE3, but not the IE4 standard. Therefore, the initial LSPMSM should be optimized to reach the IE4 standard. Figure 3-4b shows the power factor comparison of the two motors versus output power including some experimental data of the commercial IM. It shows the LSPMSM has better power factor than the IM. There is acceptable difference between experimental and simulation results for power factor at rating lower than rated output power due to effect of operating temperature on stator current and input power. The comparison between the FEM results and the experimental values of the commercial IM validates the accuracy of the simulation. The slip causes joule losses in the rotor of the IMs during steady-state that is proportional to the slip times the output power of the motor.
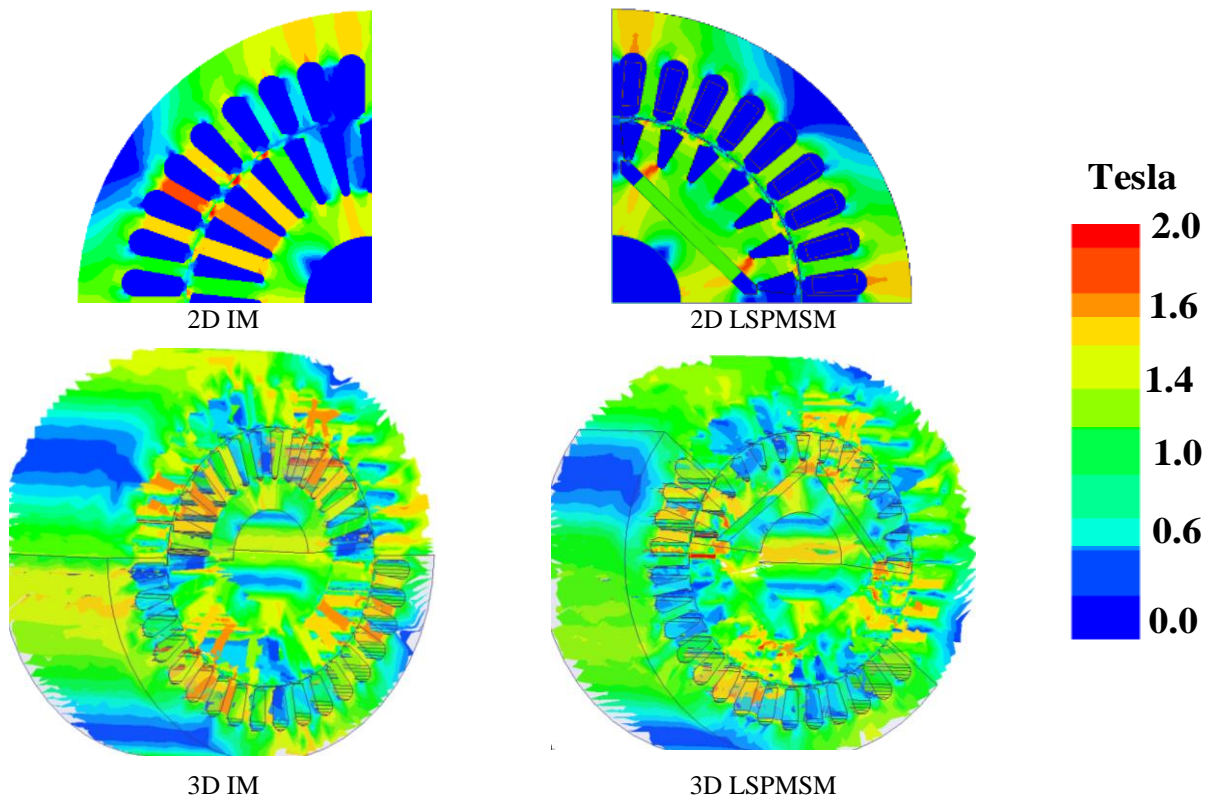
Figure 3-2. Flux density distribution comparison of 2D and 3D IM and LSPMSM designs.
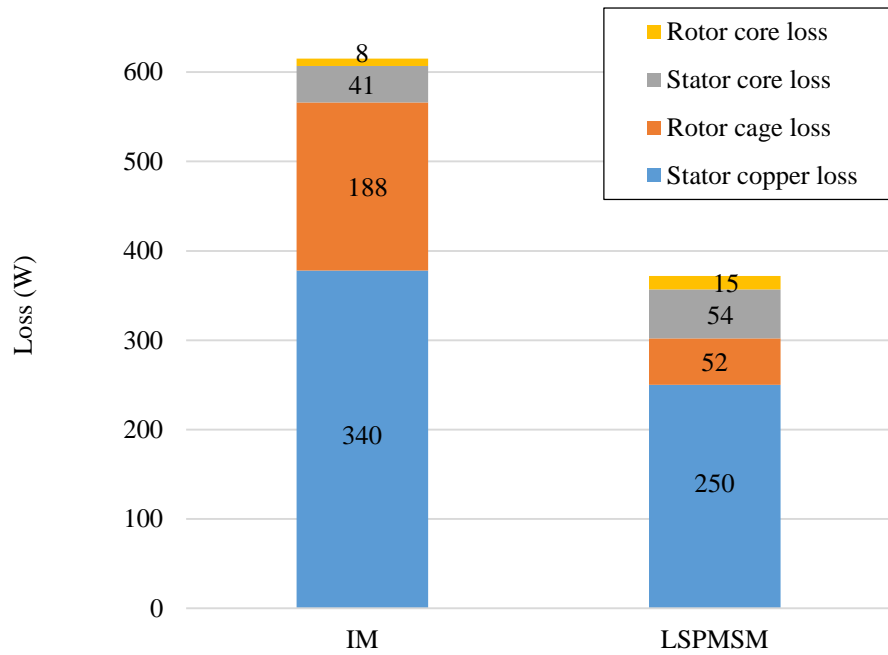
Figure 3-3. Loss components comparison of the studied motors including core losses, copper loss, cage loss and magnet loss.
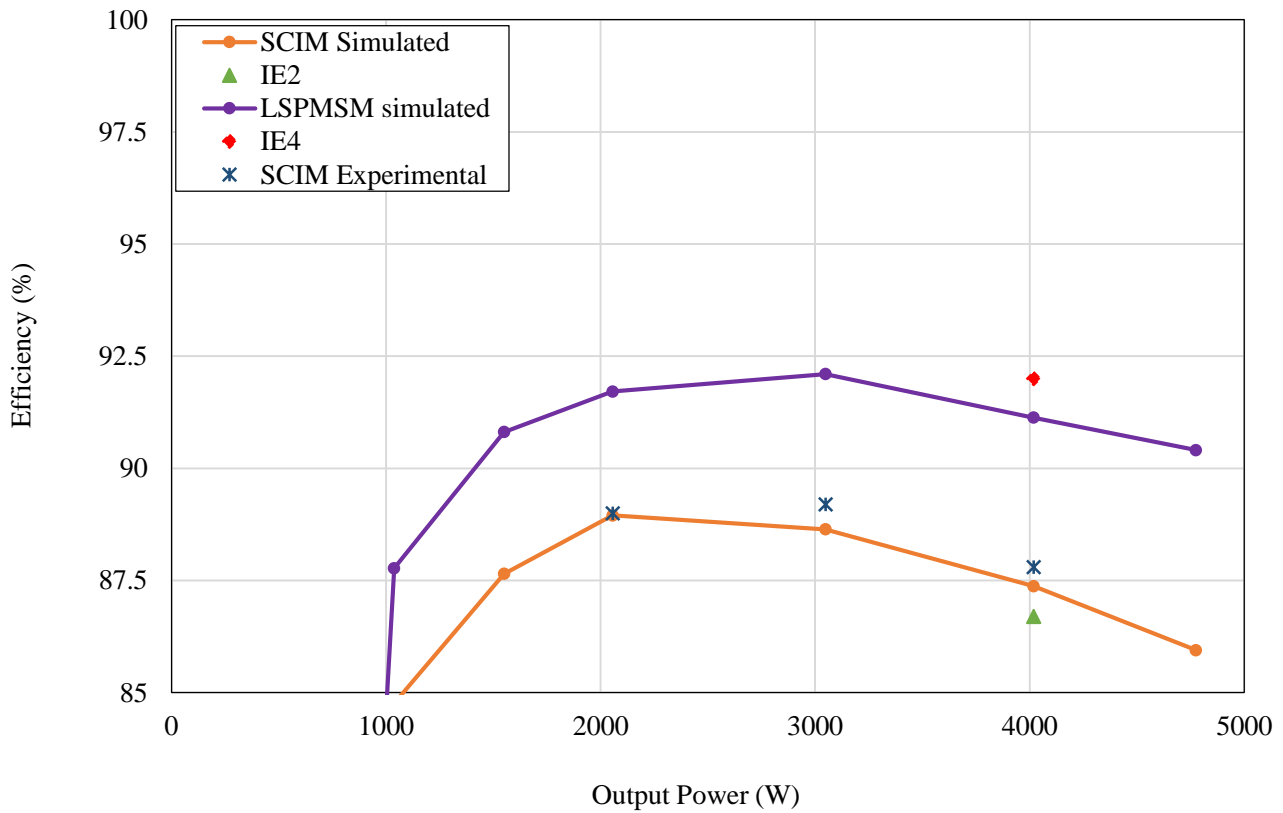
a. Efficiency variations of both IM and LSPMSM designs as function of output power including IE2, IE4 standards and experimental data for the commercial IM
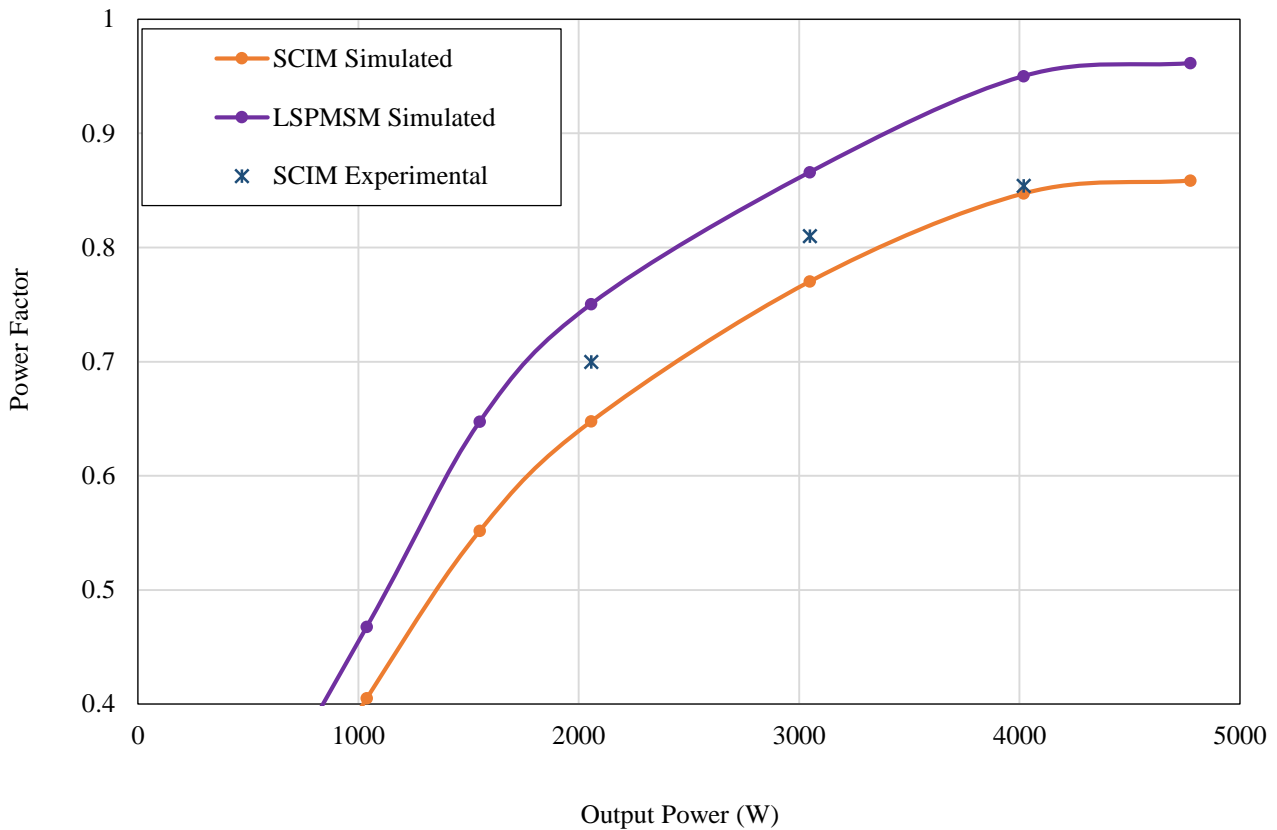
b. Power factor variations of both IM and LSPMSM designs as function of output power including experimental data for the commercial IM

Figure 3-4. Steady-state performance comparison of the IM and the LSPMSM.

3.3.3.3 Transient analysis

The steady-state torque versus speed performance of the IM and the LSPMSM is shown in Figure **3-5**a. This shows the net LSPMSM torque as well the LSPMSM torque when the magnets are removed. The difference between these is the PM braking torque. The net LSPMSM torque is significantly degraded due to the braking torque generated by the PM, particularly at low speeds. Figure **3-5**b represents the FE calculated torque-time response of 2D designs for both motors under constant full-load. The overshoot in the torque response curve of the LSPMSM is higher than that of the IM during the start-up because of magnet generated torque of LSPMSM at the starting instant. The speed-time response of both motors are compared in Figure **3-5**c. As expected, the start-up of the IM is smoother and faster than the LSPMSM due to the lack of PM braking torque (for the same frame size and weight).
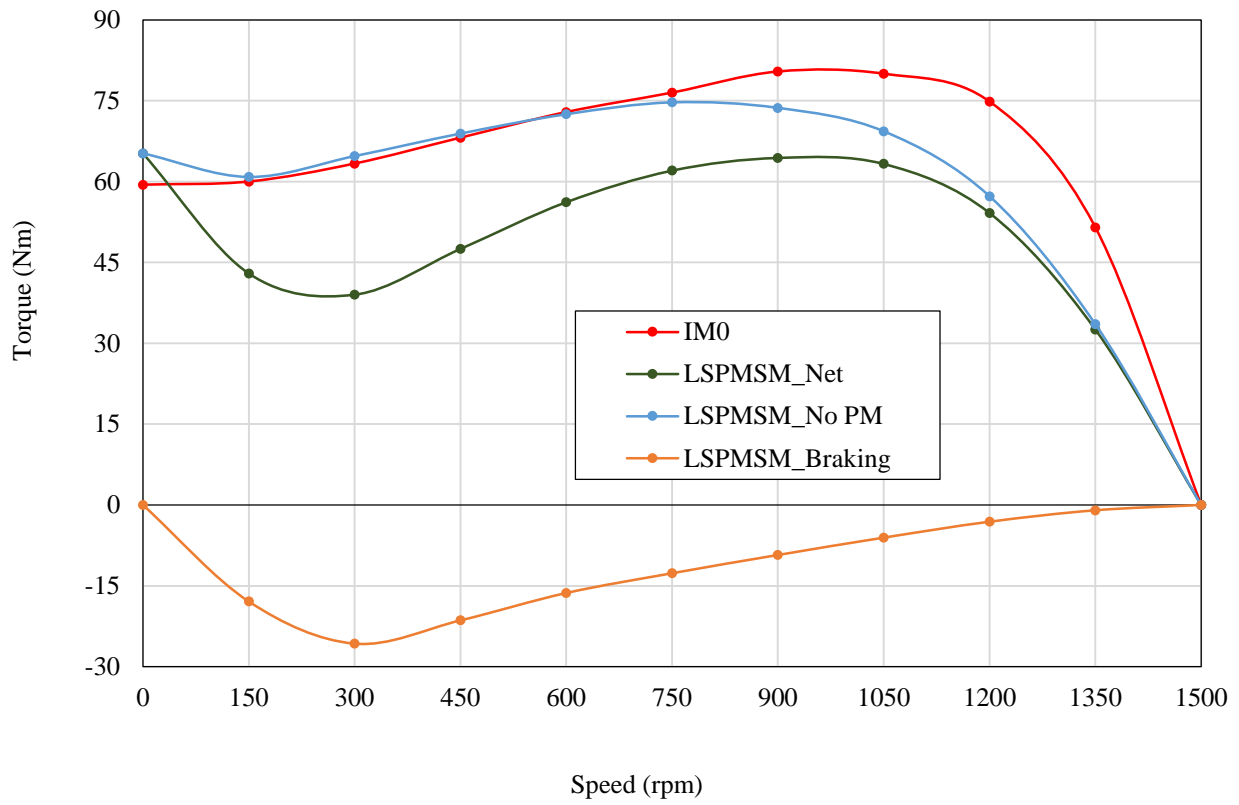
a. Steady-state torque versus speed curve of the IM and LSPMSM with and without PM
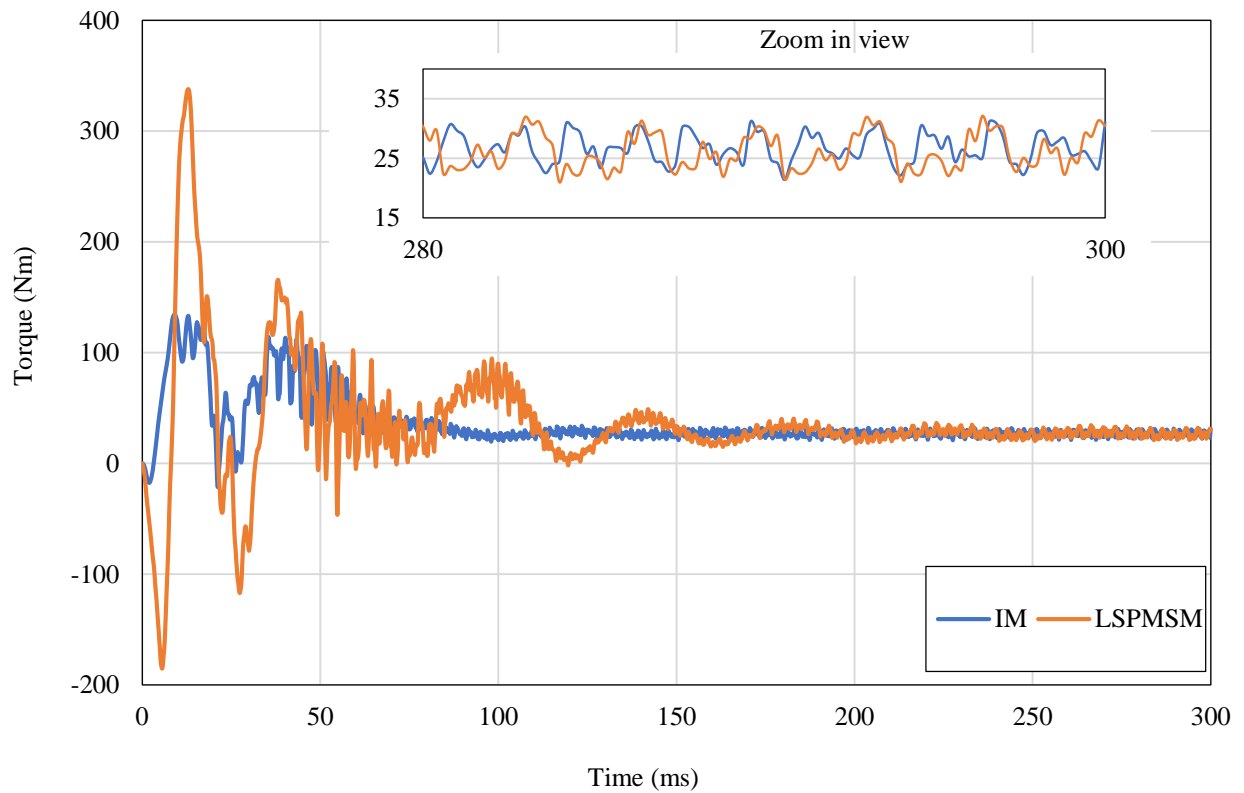
b. Torque-time response comparison of 2D designs for the IM and the LSPMSM

49
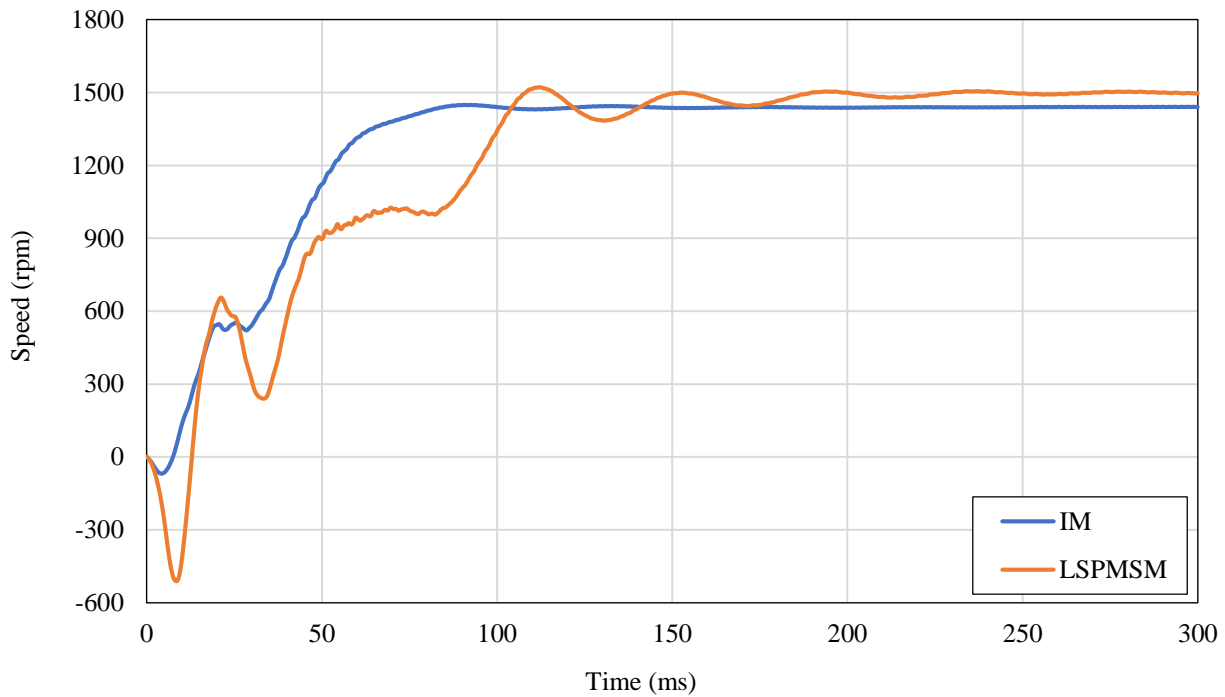
c. Speed-time comparison of 2D designs of the IM and the LSPMSM

Figure 3-5. Starting performance comparison of the 4-kW IM and the LSPMSM.

To investigate the effect of the stator end-winding and rotor end-connection on the performance of the motors and as verification of the 2D FEA simulation, the 2D and 3D torque-time and speed-time responses are compared in Figure 3-6a to Figure 3-6d, respectively. Figure 3-6a and Figure 3-6b show that the torque ripple in 3D is a bit less than 2D. The speed-time response graphs (Figure 3-6c and Figure 3-6d) indicate that there is good agreement between 2D and 3D FEA simulations. Note that as the 3D FEA simulation is time-consuming, the time step for 3D simulations is selected to be 0.6 ms. Hence, to provide a true comparison between 2D and 3D simulations, the 2D simulations are analysed under the same time-step (0.6 ms) in only these comparative graphs (Figure 3-6a to Figure 3-6d). The 3D FEA simulation has been implemented to analyse the motors performance comprehensively considering all components of the motors that directly influence the motors' performance. The 3D FEM model validates the accuracy of the 2D FEM model, which is considered in the optimization implementation study (this will be discussed in the next section).

In this study, the starting torque is estimated by averaging the torque values in the first cycle (20 ms for the source frequency of 50 Hz) from the dynamic 2D torque-time graph. Accordingly, this idea allows us to implement FEM-based transient optimization including consideration of the starting torque, which is a potential transient performance representative as objective optimisation. The accuracy of this assumption is extensively discussed in the following section. In Figure 3-13, it will be indicated the error between estimated starting torque in this method and locked-rotor torque (true starting torque) is in an acceptable range and it shows this has minimal impact on optimization process of starting torque.

50
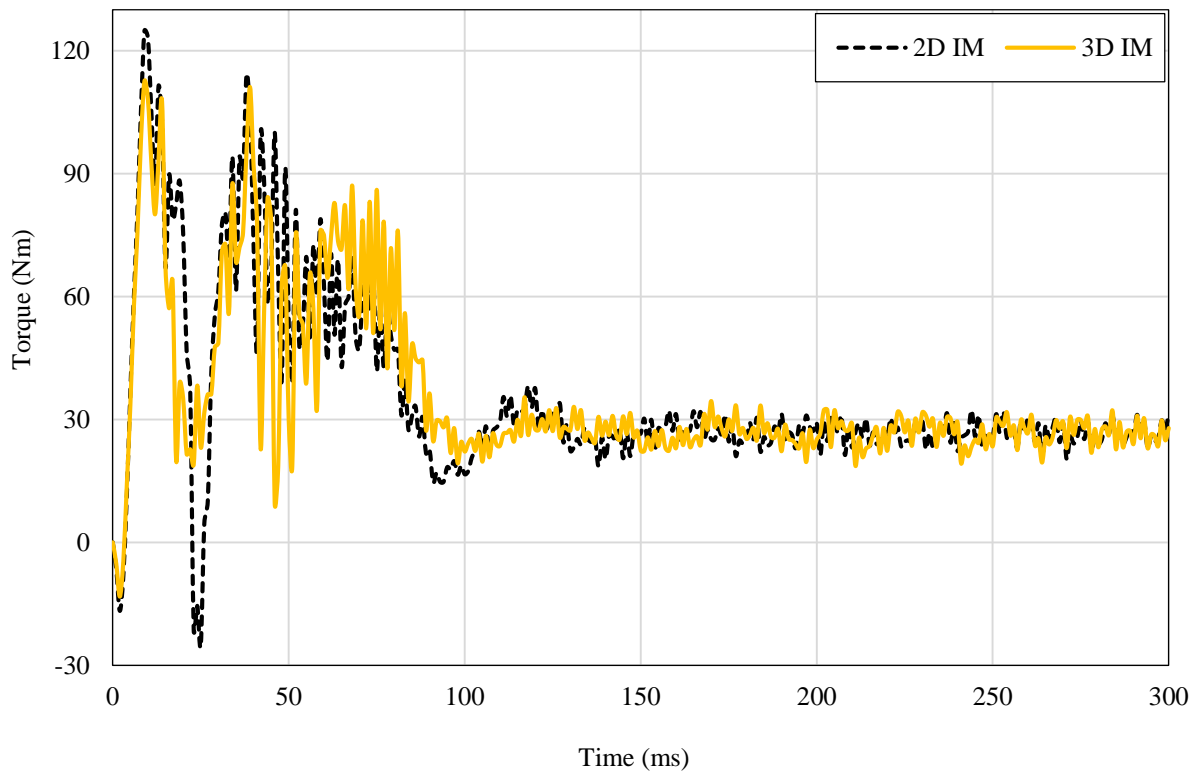
a.   Torque-time responses comparison of 2D and 3D designs for the IM
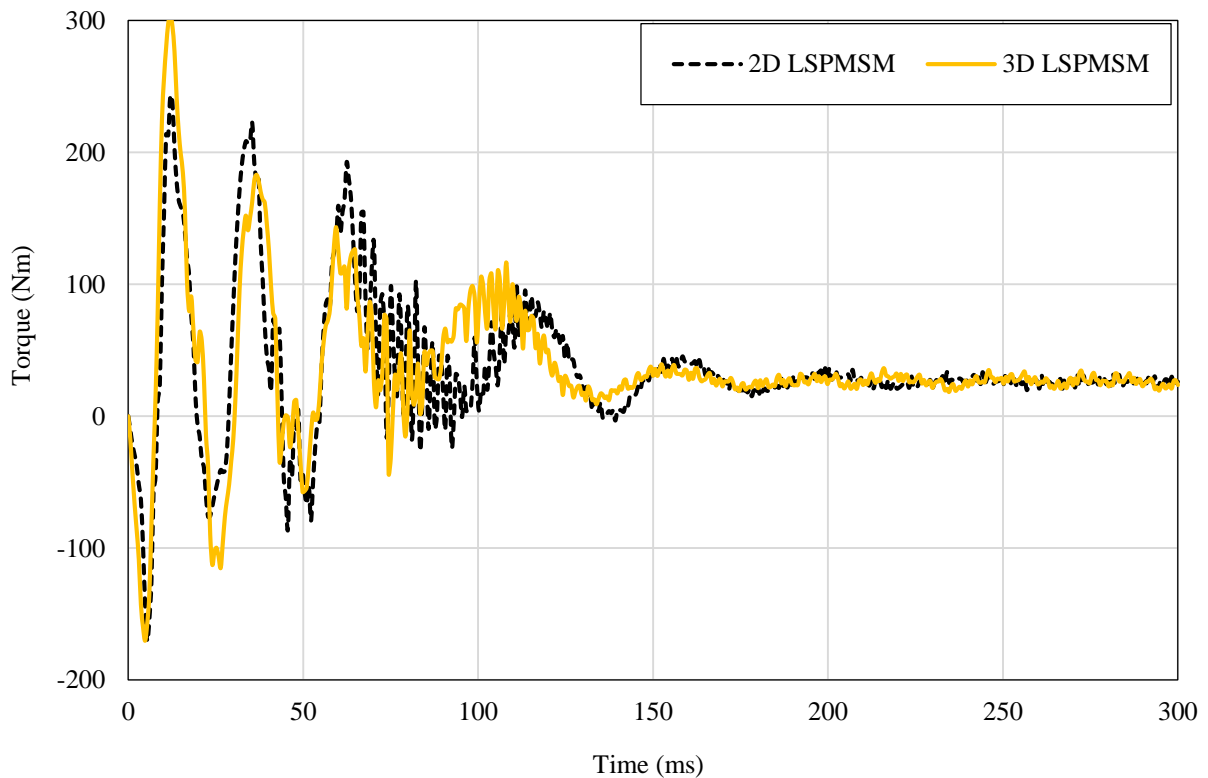
b.   Torque-time responses comparison of the 2D and 3D designs for the LSPMSM
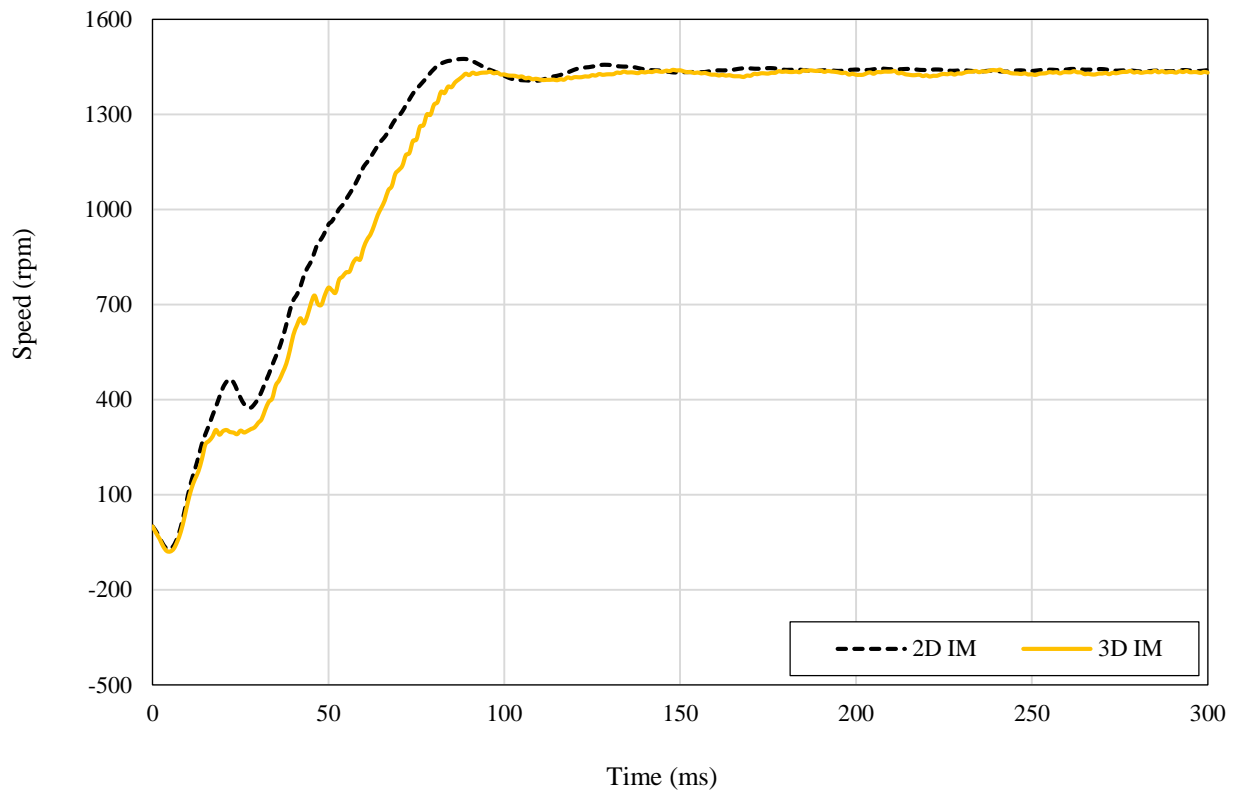
c.   Speed-time responses comparison of the 2D and 3D designs for the LSPMSM
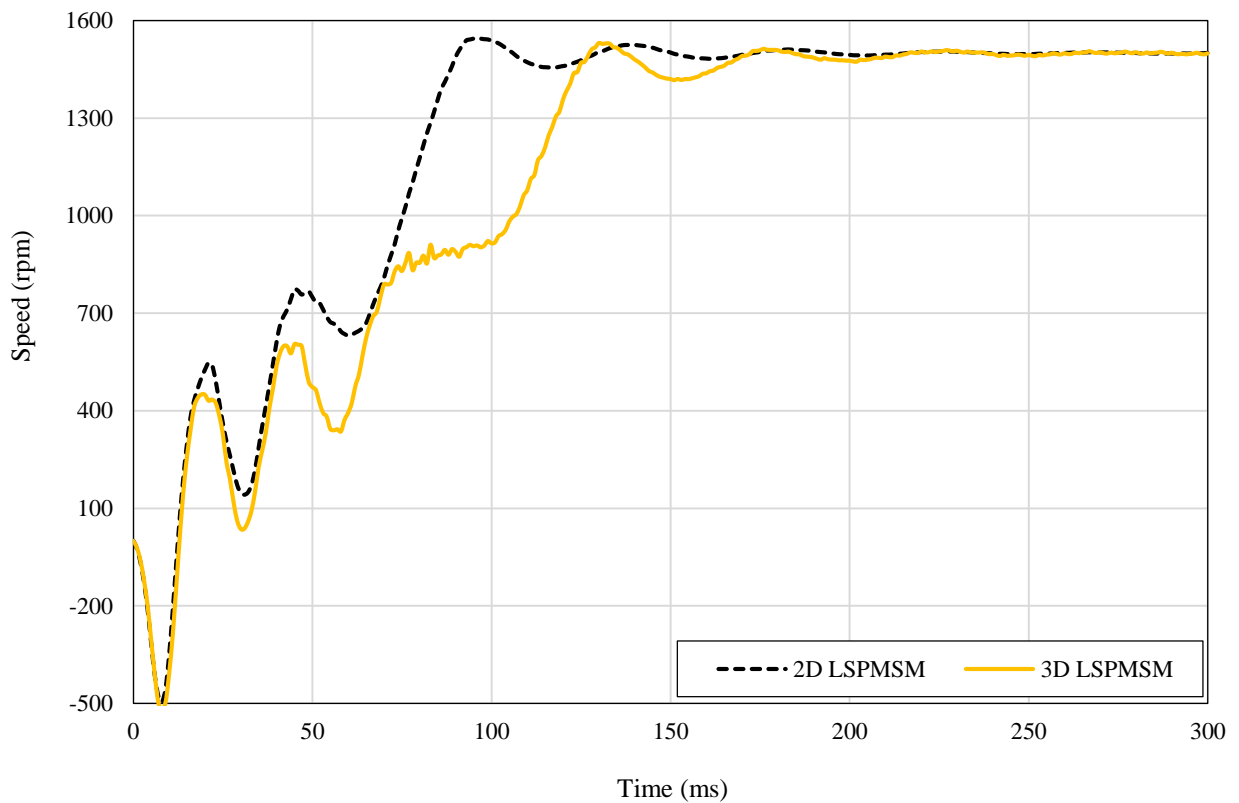
d.   Speed-time responses comparison of the 2D and 3D designs for the LSPMSM

Figure 3-6. Performance comparison of 2D and 3D designs for the 4-kW IM and the LSPMSM.

3.4 Optimization Implementation

3.4.1 Problem Definition

The designed LSPMSM should meet the IE4 standard in the steady-state and should have good start-up performance. Adding PMs within the rotor improves efficiency, but generally degrades the starting performance of the IM. So, the LSPMSM needs to be optimized to improve both the steady-state and the transient performance. Improving steady-state performance is implemented through maximizing efficiency. Transient performance improvement makes use of starting torque maximization as the objective function. Two different optimization approaches (GA and SNLP) are developed in this chapter to implement the optimization study and present a comparative study between gradient-free and gradient-based approaches in the context of electric machines. There are two scenarios: first, two single-objective functions (SOFs), which only individually focus on one objective function, are examined under the "maximize" condition. In this case, the final cost function is the same as the objective-function value. Second, a multi-objective function (MOF), which simultaneously optimizes two or more objectives, is defined. In this case the final cost function is the sum of the errors of each weighted sub-objective. The cost function procedures will be discussed in detail in the following section.

3.4.2 Cost Function Calculation Methodology

The optimizers adjust the variable values to a minimal position of the cost function. The minimum location of the cost function is the optimum value in a SOF optimization problem. In setting up a multi-objective optimization, a weight is assigned to each sub-objective and the optimizer gives more importance when calculating the cost function to the sub-objective with the greater weight. In this case, the sum of the weighted sub-objective errors is considered to be the total error function. At each iteration, each sub-objective is evaluated and contributes to a value that refers to positive error. This error value indicates the difference in the estimated values of the sub-objective and the reference (objective) value boundary. If the simulated value matches the goal value boundary, then the error value is 0. The function for error is [131]:

$$\sum_{j}^{G} \frac{W_j}{N_j} \sum_{i}^{N_j} e_i \tag{3.1}$$

where:

- G is the number of sub-goals;
- W_j is the weight coefficient for the jth sub-goal;
- N_j is the number of iterations for the jth sub-goal;
- e_i is the error contribution from the ith sub-goal.

The error value (e_i) is calculated based on the band characteristics, goal value, and the simulated value. There are three band characteristics $<=$, $=$, and $>=$ which we can select for any sub-objective [131].

Table 3-3. Optimization variables and the PM shape.

Optimization Variables Range (mm)				
b_{r1}	b_{sr}	h_{1r}	PM Thickness (*Th*)	PM Width (*W*)
3-10	1-4	4-9	2-7	19-42
PM Shape				
Rotor Slot Shape				

3.4.2.1 Variables

There are some constraints for the variable range based on manufacturing limitations (constant stator and rotor size). Table **3-3** lists the range of selected variables, their location on the rotor bar, and the PM shape in this study.

3.4.2.2 Objective functions and constraints

a) Single-objective Function (SOF) Optimization

A SOF optimisation problem is defined as:

$$f(k_1, k_2, \dots, k_2), i = 1,2, \dots, m \tag{3.2}$$

where (k_1, k_2... k_m) are the m design variables, $f(k_1, k_2, \dots, k_n)$ is the single-objective cost function. The objective to improve steady-state performance is defined:

$$f_1 = max\,(Efficiency) \tag{3.3}$$

The efficiency is averaged in the last cycle of simulation time (380-400 ms) when the motor reaches steady-state. The second objective (f_2) is related to maximizing the starting torque. In this function the aim is to maximise per unit starting torque (in nominal torque base) while keeping synchronization by defining steady-state speed as a constraint. To measure the starting torque, the first cycle (0-20 ms) of the dynamic torque is averaged (Figure **3-5**). The maxima of the averaged dynamic torque (Figure 3-5) was found to be a parameter that can be used in the optimization process to represent the maxima of steady-state starting torque.

$$f_2 = max\,(Per\,Unit\,Starting\,Torque) \tag{3.4}$$

b) Multi-Objective Function (MOF) Optimization

A multi-objective optimisation problem is expressed as follows:

$$f_i(k_1, k_2, \dots, k_m), i = 1,2, \dots, p \tag{3.5}$$

where $f_i(k_1, k_2, ..., k_m)$ are the objective functions. The objective functions of the problem in this study are efficiency and starting torque maximisation with a constraint on the steady-state speed. In this case, the cost function is normalized based on the defined characteristics, minimum desired values, and the norm type. Table **3-4** presents the optimization conditions under MOF. In a multi-objective optimization problem, where none of objectives use the "minimize" or "maximize" conditions, the optimizer normalizes the cost function. Thus, the error corresponding to each specific weighted sub-objective is merged in a technique that depends on the norm type selected. The normalization type (N_2), which is the cost function, is calculated as follows [131]:

✓ N_2 norm: the final cost function in MOF optimization is determined based on the weighted sum of the absolute values of the individual goal errors:

$$\text{Cos}\, t = \sum_{1}^{N} w_i . \varepsilon_i^2 \tag{3.6}$$

where N, w_i and ε_i are the number of exclusive objectives, weighting factor, and residual error, respectively. A residual or error is associated with each objective. These residuals are the proportional measures of how far we are from reaching the associated goal.

Table 3-4. Applied optimization conditions in MOF study.

Objectives	Band characteristics	Minimum desired values		Time (ms)
Efficiency	>=	SCIM	89%	380-400
		LSPM	93%	
Per unit Starting torque	>=	3		0-20
Per unit Speed	=	1		380-400

3.4.3 Optimizations Approaches and Implementation Strategy

In this study, optimization is the process of locating the minimum of a cost function. Optimizer's algorithms modify the variable vector until the minimum is reached with acceptable accuracy. Figure 3-7 and Figure 3-8 show the optimisation procedure flowchart of SOF and MOF implemented in this chapter. The optimization process of SOF and MOF is described in the following sections.

3.4.3.1 SOF optimization procedure

In the first step, the optimisation space takes the initial design and calculates the objective function using FEA making sure the constraints are satisfied. Then GA and SNLP (as the optimization approaches) update variable vectors at their own pace and calculate the objective function (Step 4 in Figure 3-7) in each evaluation. Noted that, in a SOF optimization that uses a "maximize" or "minimize" condition, the optimization is implemented for the number of required evaluations (which depends on the maximum iteration and type of approach) or its stopping criterion. Then, the best design variables that present the best objective-function results, with the constraints satisfied, are presented as optimum design variables.

3.4.3.2 MOF optimization procedure

In multi-objective optimisation, the optimizers determine each of the objectives as a sub-objective and try to improve them based on the desired value defined for them. The cost function calculation method is described extensively in the following sections. If the final error cost function is in the acceptable range and it meets the convergence factor, the optimization is stopped. If not, the next evaluation updates the variables and the procedure is repeated. When all evaluations are done, the optimum design is the one that yields the minimum error (best cost function). The ideal value for cost function is 0, which represents the value of the final error cost function. Hence, it is very important to define a reasonable desired value for each sub-objective. In this case, the Pareto Front of each multi-objective optimization is extracted to verify the performance of the proposed MOF optimization (results are discussed in the next section).

The search procedure used by each optimisation algorithm is presented as follows:

- Genetic Algorithm

Optimizers based on the Genetic Algorithm (GA) are part of a family of optimization approaches called stochastic optimizers. To decide where to further explore the design space, they do not use the data from the experiment, nor the cost function calculated in previous evaluation. They use a sort of random sorting instead and execute it in an organized way. The ability to arbitrarily select evaluations to progress in the next generation allows the optimizer to leap out of local minima, at the cost of several random options that do not improve the optimization objective. Consequently, the GA optimizer generally requires more iterations and could even be prohibitively long. In the GA, the search strategy is an iterative process that goes over many generations. New children (individuals) are produced in each generation and the growing population engages in a mechanism of selection (natural selection), which in turn decreases the population size to the optimal level (next generation). The GA chooses individuals from the original collection while a smaller set of individuals must be generated from a greater set. Better matched individuals (in comparison to the cost function) are favoured during this phase of optimization. An iterative approach begins to pick the individuals and fill in the resulting range, but instead of choosing the best of many, we use a roulette wheel that has been made proportional to the candidate's fitness level (relative to the cost function) for each selection-candidate division. It implies that the fitter the individual is, the greater the probability of its survival [131].

- Sequential Non-linear Programming (SNLP)

SNLP's key benefit is that it handles the issue of optimization in greater detail. This optimizer implies a continuous space is spanned by the optimization variables. Consequently, there is no minimum step size defined in this optimizer and any value can be taken by the variables within the permitted constraints and within the limits of the simulator's numerical precision. This decreases the influence of the noise, but the filtering of the noise is not solid. Using response surfaces (RS), the

SNLP approximates the FEA characterization. SNLP has a good approximation of the cost function in terms of the optimization variables with the FEA-based calculation and with light evaluation of the cost function. This estimation helps SNLP to predict the location of the improving point.
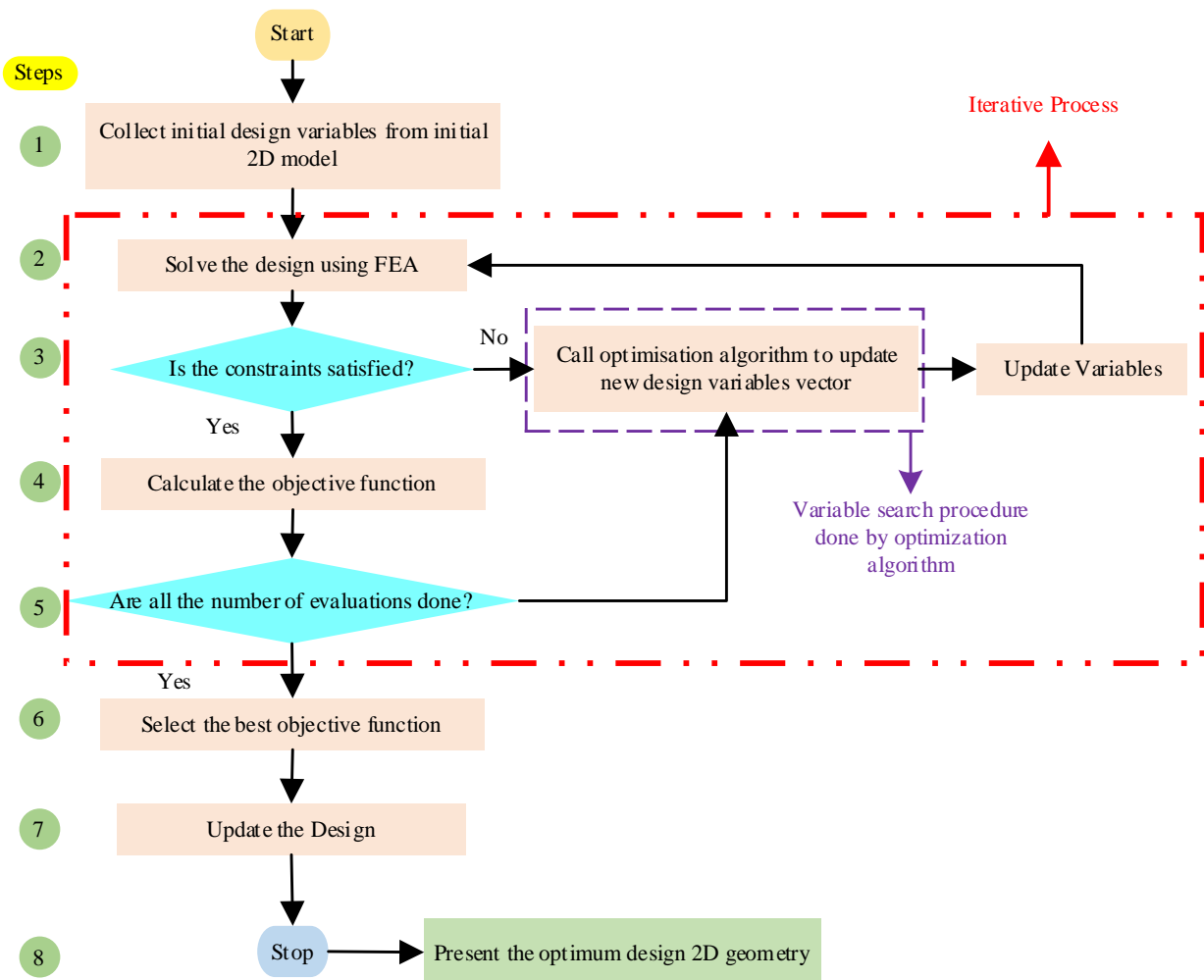
Figure 3-7. SOF Optimisation procedure flowchart in both methods.
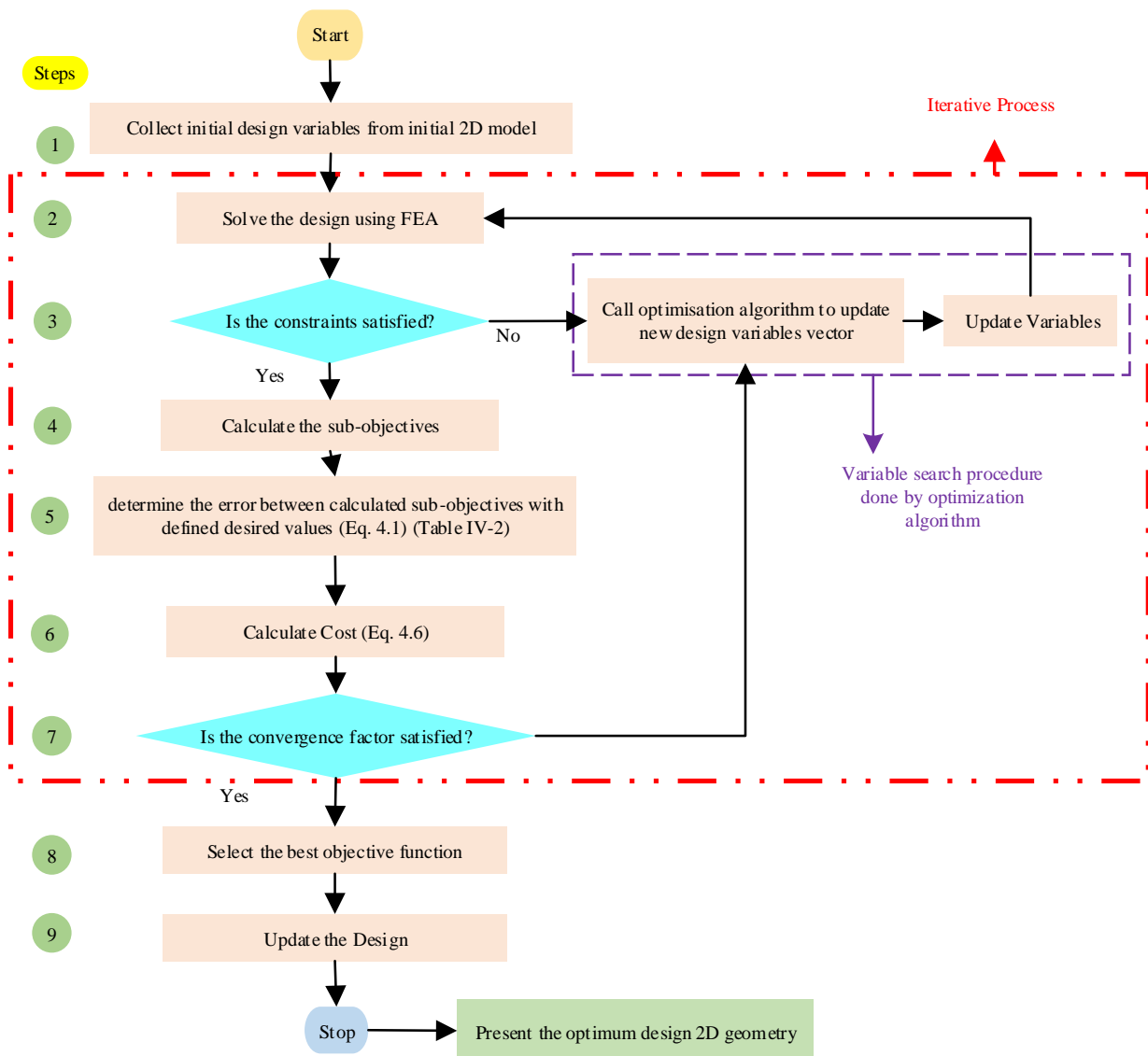
Figure 3-8. MOF Optimisation procedure flowchart in both methods.

The total cost-function calculation is more reliable. This achieves a higher functional convergence speed for the SNLP optimizer than for quasi-Newton. The SNLP generates the response surface using a Taylor Series approximation from the FEA simulation results available from past solutions. In the optimization loop, the response surface is used to estimate the gradients and determine the path and distance of the next step. The response surface serves as a surrogate for the FEA simulation, minimizing the amount of necessary FEA simulations and speeding up the problem considerably. If more FEA solutions are produced and the response surface approximation increases, convergence improves. The SNLP is iterative, changing the optimizer state and iterating from the current optimal value to the new optimum values. Successive optimization can be considered to be a step-by-step approach towards an optimal goal [131].

3.4.4 Optimization Results Discussion

The cost function is calculated in each evaluation, depending on the number of parameters optimised. Details of the optimisation procedures are presented in Table **3-5**. Scenarios 1 and 2 are under SOF optimization (efficiency maximization) using genetic algorithm (gradient-free representative) and SNLP (gradient-based representative), respectively. Scenarios 3 and 4 optimize the starting torque under SOF optimization using GA and SNLP, respectively. The steady-state speed is selected as a constraint only for the LSPMSM.

Scenarios 5 and 6 are MOF optimization (simultaneous efficiency and starting torque improvement) with synchronous speed as a constraint (only for LSPMSM) using GA and SNLP, respectively. The synchronous speed in the LSPMSM optimization process has been selected as a constraint to avoid an optimum LSPMSM design that is not able to reach synchronous speed. In scenarios 5 and 6, for LSPMSMs the weighting factors of synchronous speed (constraint) is twice the efficiency and the starting torque weighting factors and, hence, the optimizer considers it more important. The Pareto Front results of multi-objective optimization in scenarios 5 and 6 for the case studies are shown in Figure 3-9a to Figure 3-9d. Please note that the original induction motor is a commercial motor, and the commercial motors are considered to be optimum designs, particularly for efficiency. Hence, there is a slight improvement in efficiency of the optimum design in comparison with the original design. The black points correspond to the non-optimized design and the red points refer to the optimum design. As is seen, the extracted optimum design by the proposed MOF optimisation is the ideal optimum design according to Pareto Front results. This verifies the reliable performance of the MOF optimization.

Table 3-5. Objective functions, constraints, and number of evaluations for each optimized design.

Scenarios	Type	Objective Function	Constraint on Speed		Weighting factors		Optimization Type	Evaluations	
1	IM1-L2	Max. Efficiency	-		-		SOF GA	540	
2	IM2-L3	Max. Efficiency	-		-		SOF SNLP	50	
3	IM3-L4	Max. Starting Torque	IM	-	S. Torque	1	SOF GA	35	
			LSPM	1500	Speed	1			
4	IM4-L5	Max. Starting Torque	IM	-	S. Torque	1	SOF SNLP	10	
			LSPM	1500	Speed	1			
5	IM5-L6	Max. Efficiency and Starting Torque	IM	-	Efficiency	1	MOF GA	IM	136
			LSPM	1500	S. Torque	1			
					Speed	2		LSPM	90
6	IM6-L7	Max. Efficiency and Starting Torque	IM	-	Efficiency	1	MOF SNLP	40	
			LSPM	1500	S. Torque	1			
					Speed	2			
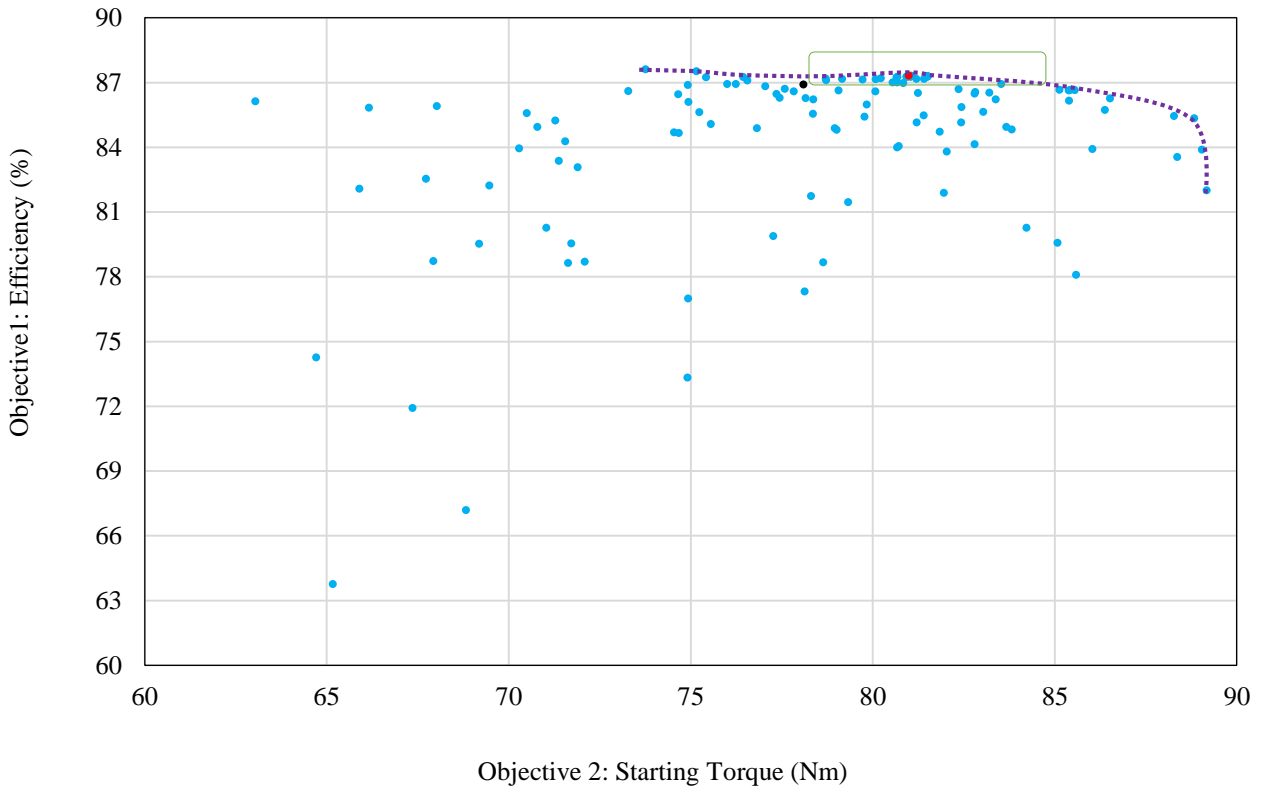
a. IM5 (Optimized by GA)
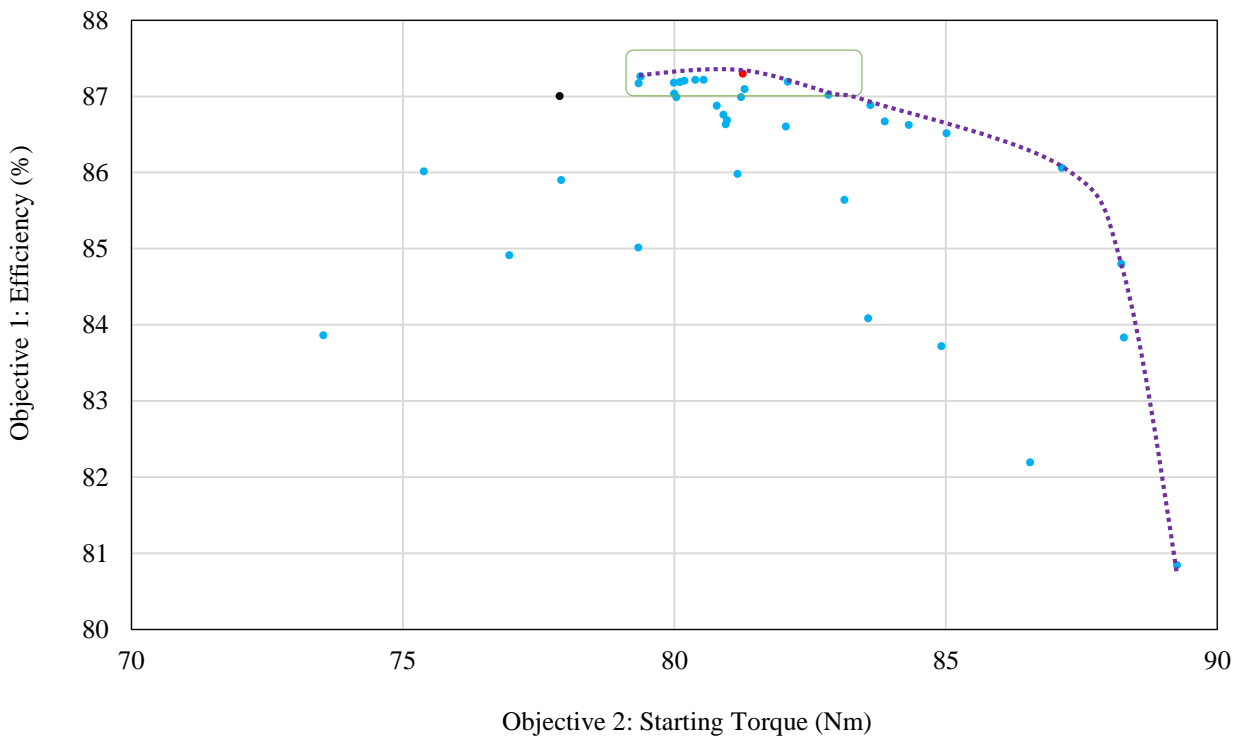
b. IM6 (Optimized by GRA)
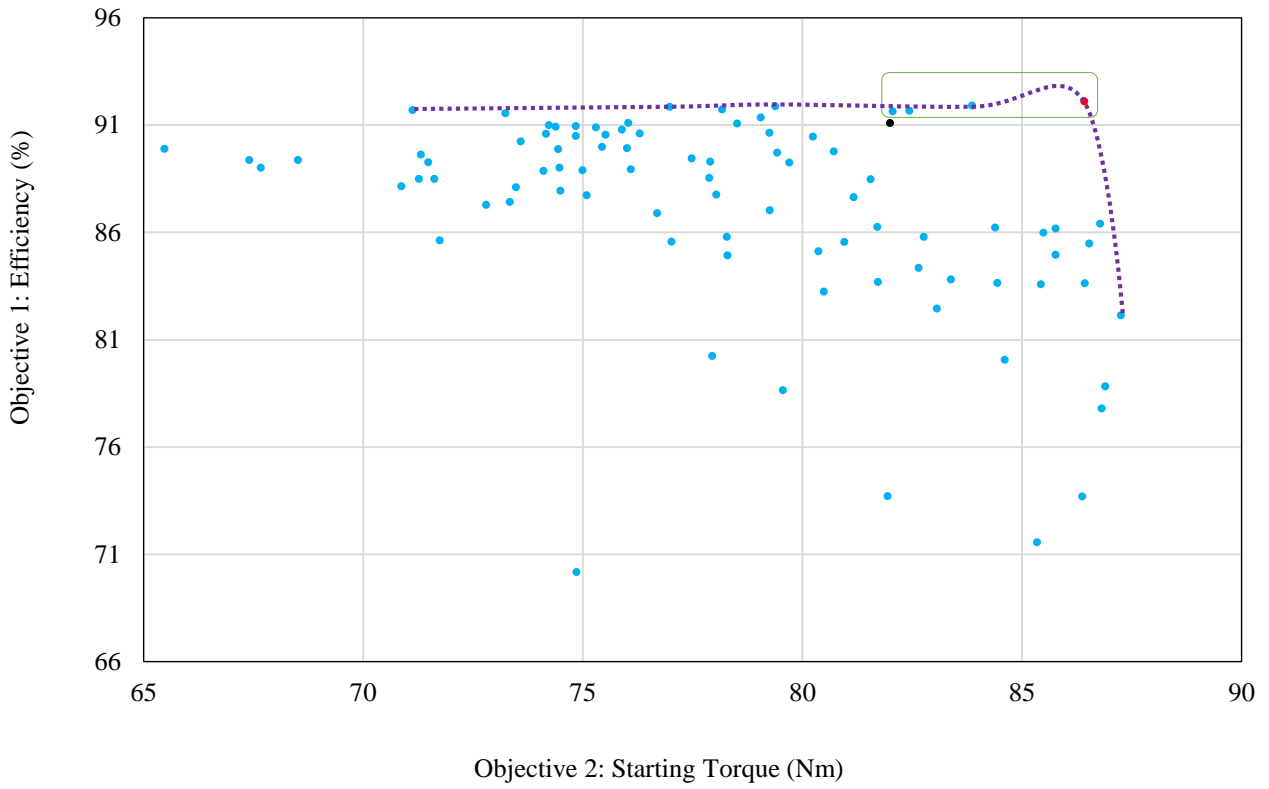
c. L6 (Optimized by GA)
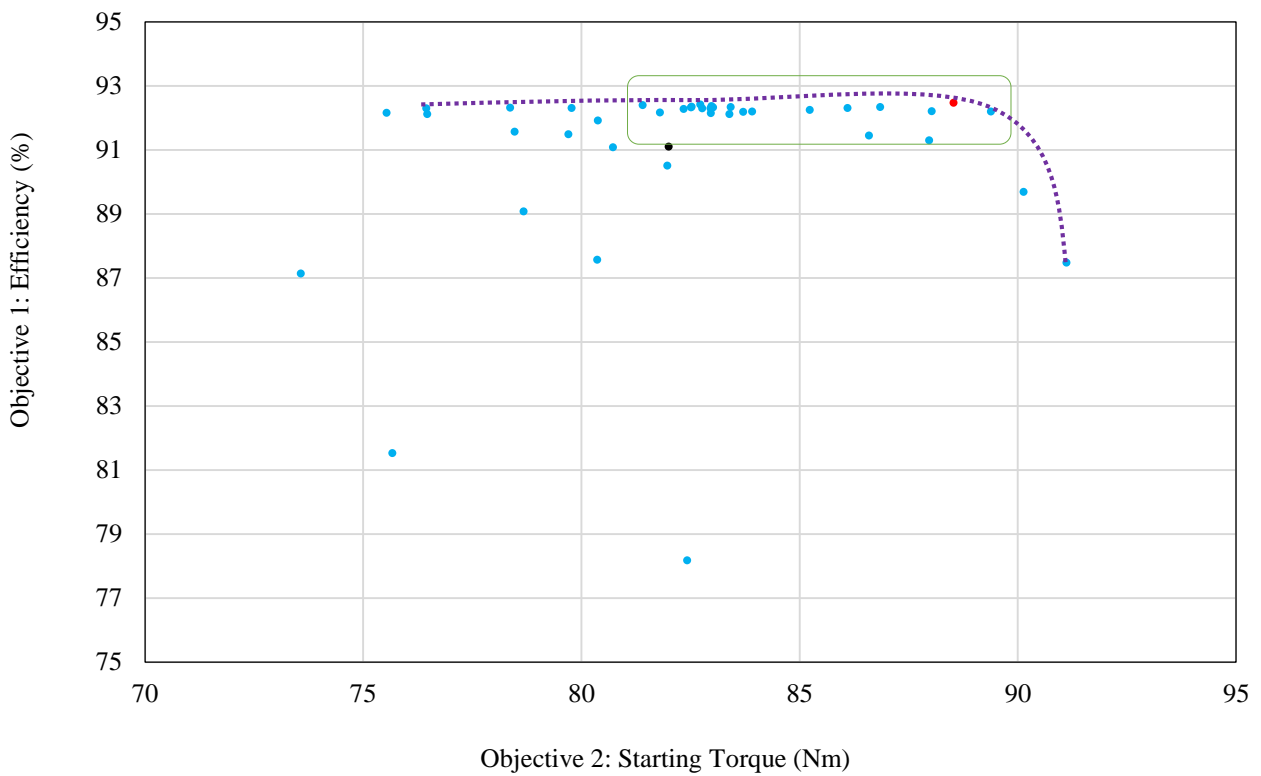
d. L7 (Optimized by GRA)

Figure 3-9. Pareto Front results of multi-objective optimizaation studied in scenarios 5 and 6.

It is seen that the number of optimization evaluations required to obtain a result using GA is much higher than when using SNLP. Table **3-6** presents the cross sections of the optimised motors and lists the optimized variables. The discussion on the cross section variations based on each scenario is as follows:

- Scenarios 1-2 (IM1, L2, IM2 and L3): these scenarios only focus on the steady-state improvement through efficiency maximization. The cross sections of the designs show that the slot depth of the rotor (h_{1r}) increased in the IM designs, but it decreased for the LSPMSM designs. Also, the slot widths (b_{r1} and b_{sr}) decreased for IM1 and IM2 and increased in the LSPMSM designs. In addition, the volume of PM for L2 decreased whereas it increased for L3 versus the baseline LSPMSM (L1).

- Scenarios 3-4 (IM3, L4, IM4 and L5): these scenarios optimize the transient performance via the starting torque maximization. In this case, the slot depth of the rotor (h_{1r}) decreased and the slot widths (b_{r1} and b_{sr}) increased in all designs. The PM volume in L4 decreased while it increased in L5 compared to L1.

- Scenarios 5-6 (IM5, L6, IM6 and L7): these scenarios focus on simultaneous improvement of the transient and steady-state performance under a MOF. The IM and LSPMSM designs have different behaviour in this case. In both IM5 and IM6 designs, the h_{1r} and b_{sr} decreased and b_{r1} increased. In contrast, in L6 and L7 designs, the h_{1r} and b_{sr} increased while b_{r1} for L6 increased and for L7 it decreased. The PM volume for LSPMSMs increased in both scenarios.

Table 3-6. Variables and cross-sections of the optimized designs for the SCIM and LSPMSM.
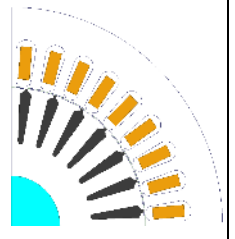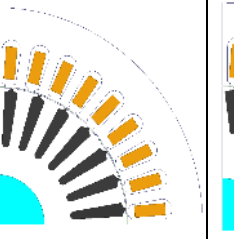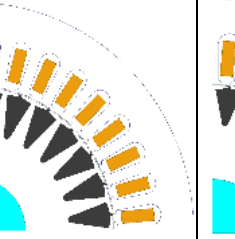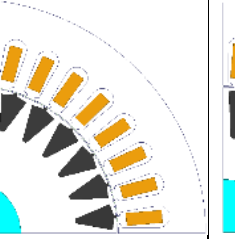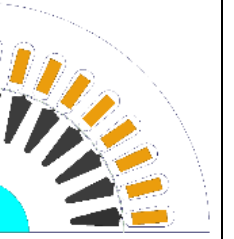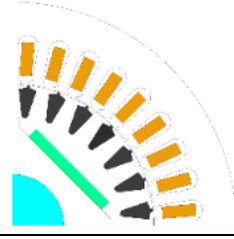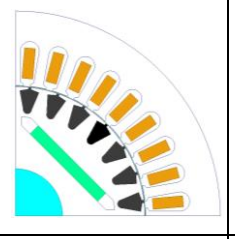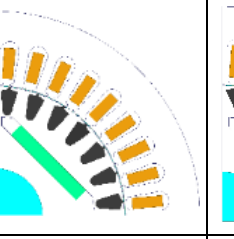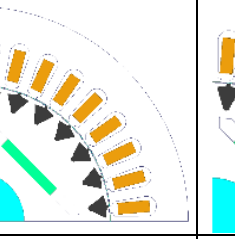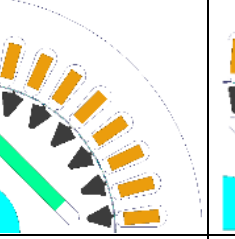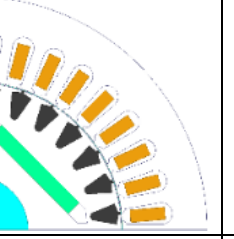
Motor Type		Original IM (IM0)	IM1	IM2	IM3	IM4	IM5	IM6
Cross Section								
Variables (mm)	h_{1r}	18.10	19.36	19.21	13.85	11.43	15.40	15.99
	b_{r1}	6.50	5.02	5.12	9.36	9.07	7.05	7.28
	b_{sr}	2.50	2.66	2.97	2.37	2.02	2.39	1.93
Motor Type		L1	L2	L3	L4	L5	L6	L7
Cross Section								
Variables (mm)	h_{1r}	9.00	7.26	7.73	5.35	6.44	7.48	7.53
	b_{r1}	6.50	7.71	6.66	8.56	7.85	7.29	5.82
	b_{sr}	2.50	3.37	3.69	1.92	2.47	2.98	2.61
	W	38.00	38.41	37.11	26.71	33.40	38.88	38.74
	Th	4.00	4.71	5.50	3.88	5.11	5.51	6.00

Figure. 3-10a and Figure. 3-10b summarize the steady-state and transient performance of the designs. All designs are compared on the axes of efficiency and starting torque in Figure. 3-10a. It is observed that designs IM5 and IM6 have good transient and steady-state performance among the IM designs. In the LSPMSM designs, L3 and L2 have the highest efficiency values however their start-up is poorer than the initial LSPMSM design (L1). In contrast, the L6 and L7 designs have efficiency and starting torque better than L1. Efficiency improvement of the final LSPMSM design, L7, is about 5% more than IM0, which brings the LSPMSM into the IE4 range while the commercial IM meets IE2. A 5% improvement in efficiency in electrical motors is a significant improvement for a similar frame size.
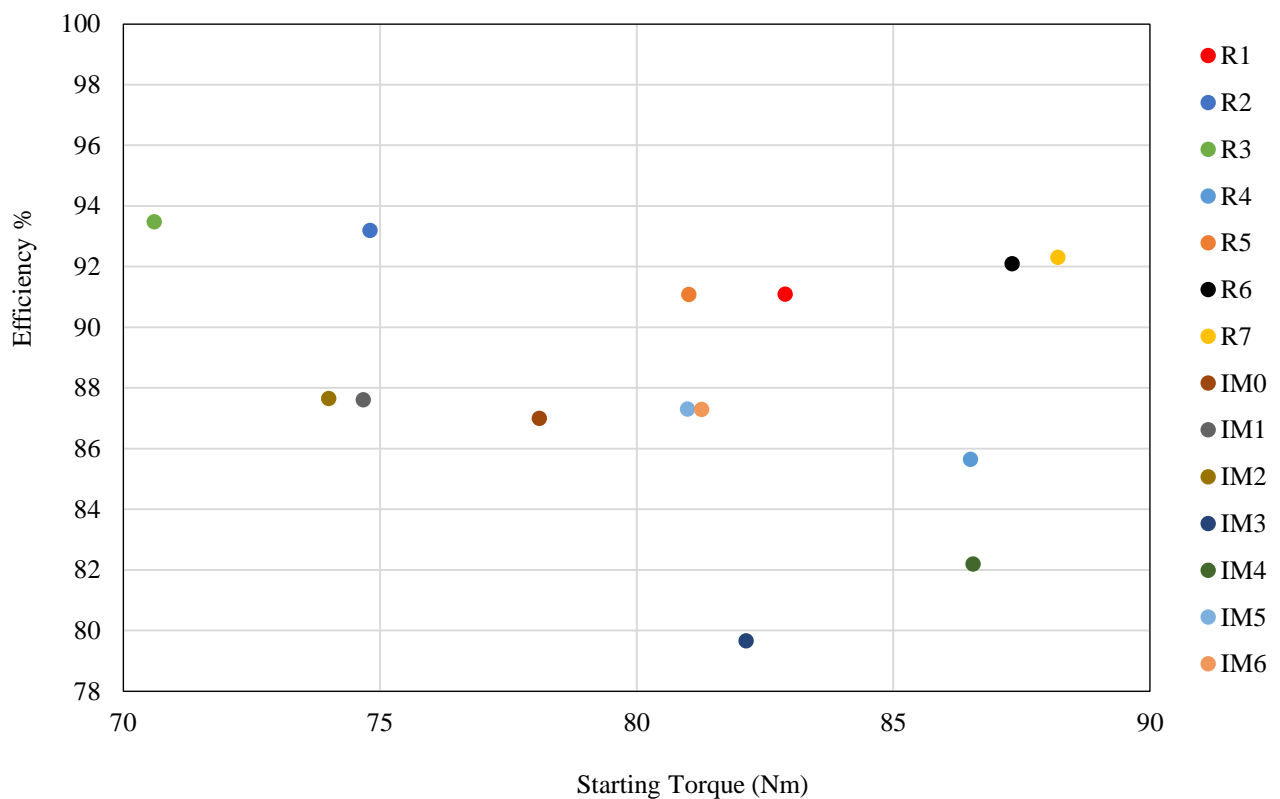
a. Location of the optimized designs in efficiency and starting torque plane.
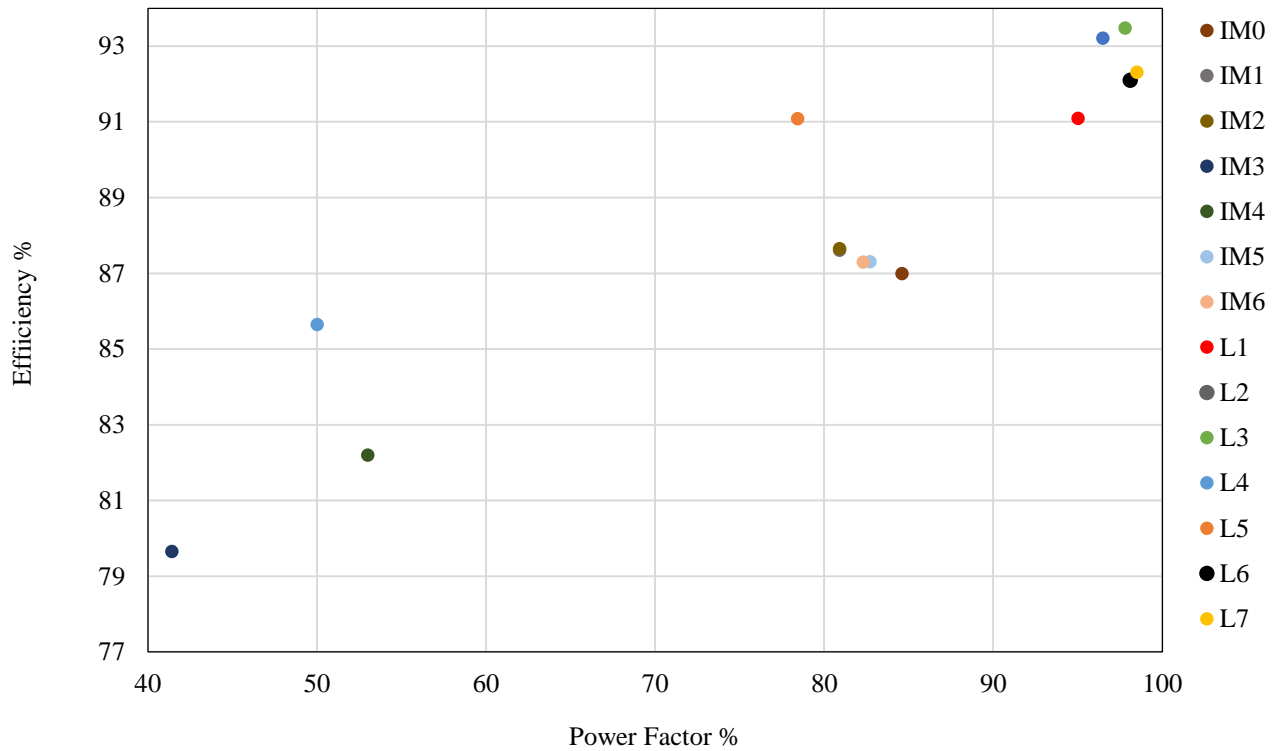
b. Location of the optimized designs in efficiency and power factor plane.
Figure. 3-10 Efficiency variation of optimized designs versus starting torque and power factor.

Figure. 3-10b shows the efficiency versus power factor results. This figure shows that the L6 and L7 designs have good power factor and they meet the IE4 efficiency standard. As it can be clearly seen, IM3 and IM4 have considerable growth in starting torque while the efficiency improvement in IM1 and IM2 is small, about 1% more than IM0. Accordingly, the slot dimensions influence the transient performance more than the steady-state performance in IMs. This is because of change in rotor resistance due to slot dimensions change. In fact, in transient improvement by maximizing starting torque the rotor resistance plays a key role in maximizing starting torque. In LSPMSMs, the PM volume affects the steady-state more than the slot dimensions and in transient improvement, the LSPMSMs prefer to reduce the PM size to maintain synchronization.

Cogging torque in PM motors is known to be a disadvantage and there have been attempts to reduce it through optimisation techniques. Figure 3-11a shows the cogging torque versus mechanical angle of the optimised LSPMSMs in comparison with the initial design. The peak to peak value of cogging torque in this figure shows that the cogging torque of the optimised designs have been improved and the cogging torque value of optimised designs are less than the cogging torque of the initial LSPMSM. The cogging torque versus torque ripple of the optimised LSPMSM designs is presented in Figure 3-11b. This figure indicates the initial design (L1) has maximum cogging torque and comparable with L4 it has maximum torque ripple while the optimized designs (L7 and L6) have cogging torque and torque ripple less than the initial LSPMSM. This shows that the optimised designs not only have

better efficiency and starting torque but they also have improved cogging torque and torque ripple in comparison with the initial LSPMSM.
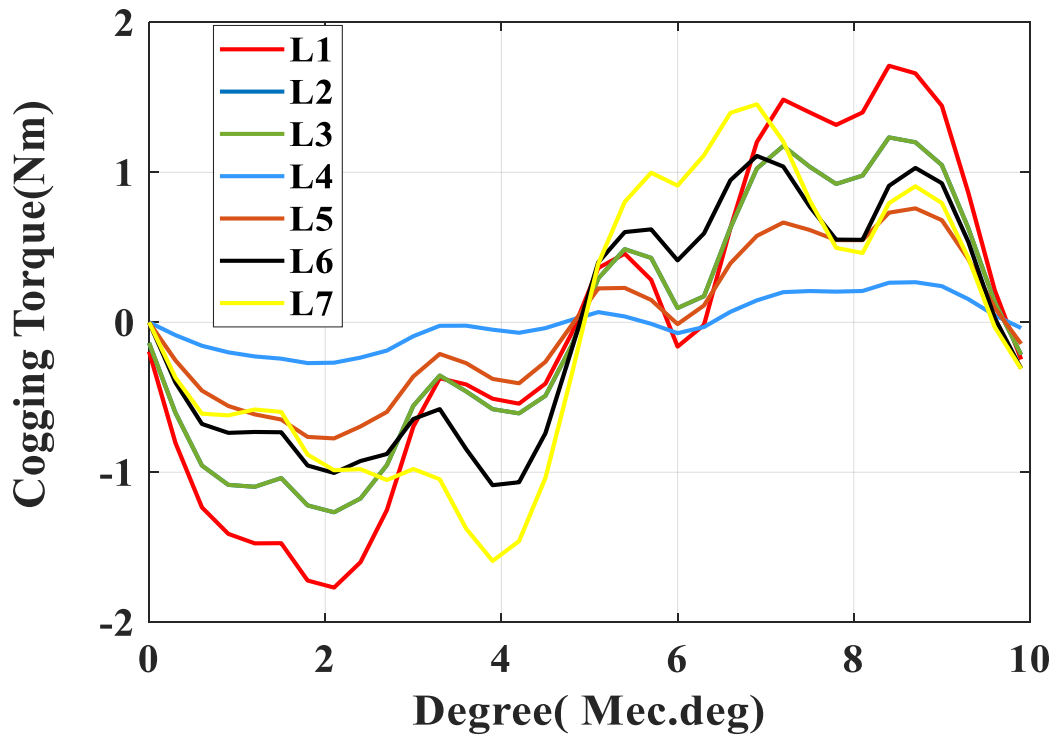
a. Cogging torque versus mechanical degree.
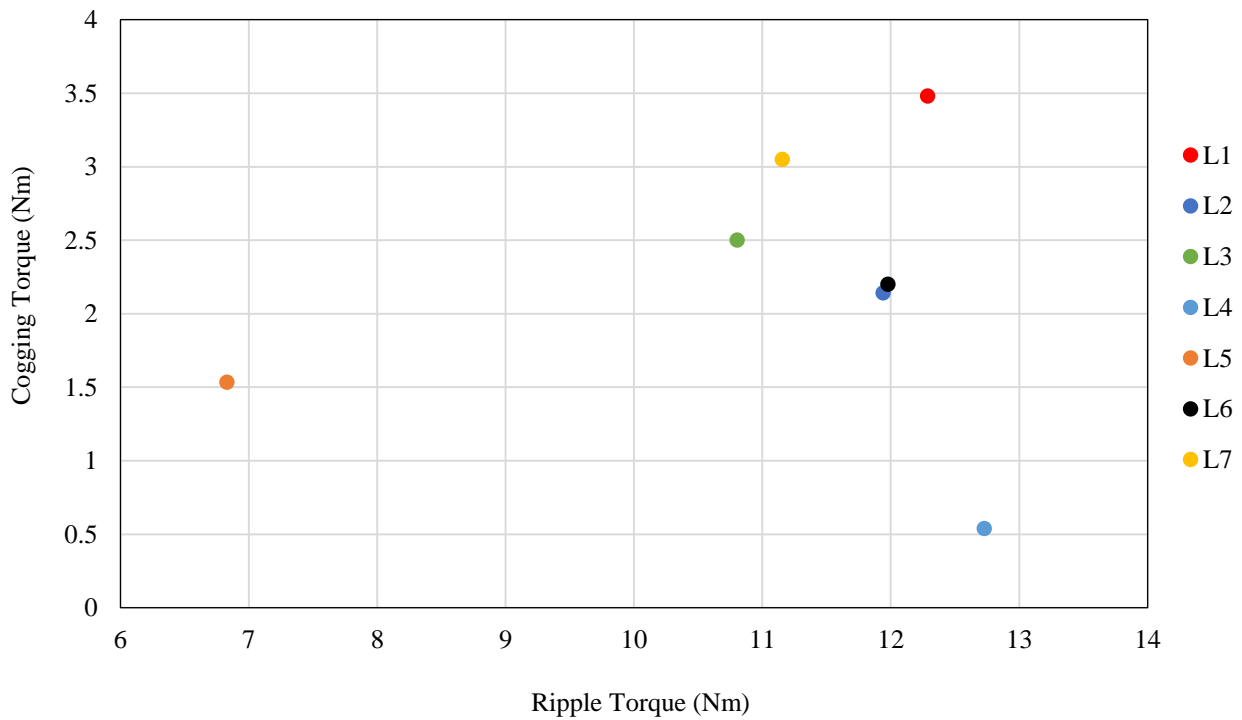
b. Cogging torque vesus torque ripple.

Figure 3-11. Cogging torque variations of the LSPMSMs.

The speed-time responses of all the designs are compared under full-load for normal inertia (Figure **3-12**). A magnified view of the speed-time graph during the steady-state is shown in this figure. All the LSPMSM designs reach synchronous speed under full load. However, the settling time of IMs are faster than LSPMSMs.

As mentioned in Section 3.4.2.2a, the average of the FE torque-time response in the first cycle (0-20 ms) can be used for the starting torque estimation. Figure **3-13** shows that this is an acceptable estimation compared to the measured FE locked-rotor torque and starting torque calculated by analytical equations. To calculate the locked-rotor torque the designs are run at zero speed at rated voltage. The maxima of the averaged dynamic torque (Figure 3-5) was found to be a parameter that can be used in the optimization process to represent the maxima of steady- state starting torque. Figure **3-14** and Figure **3-15** show the efficiency and the starting torque variation versus PM and aluminium mass for all the LSPMSM designs. It is indicated that efficiency and starting torque are generally in opposition with each other against PM and aluminium mass. Designs where efficiency is highest have the starting torque being lowest, and vice versa. As seen in the figure, L7 shows a good trade-off for the efficiency and starting torque (93% and 85 Nm, respectively), which are accessible for the reasonable material quantities.
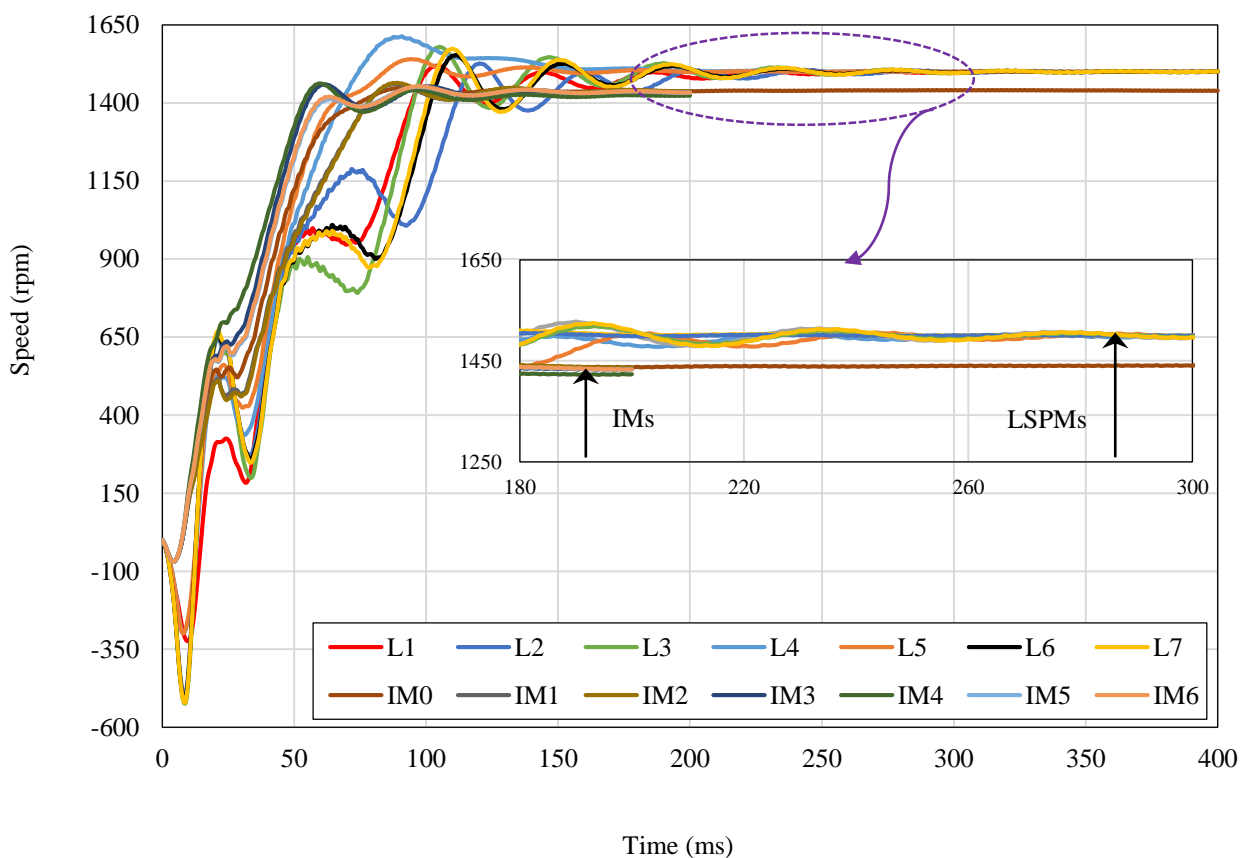
Figure 3-12. Transient comparison of optimized designs (speed response) at full-load.
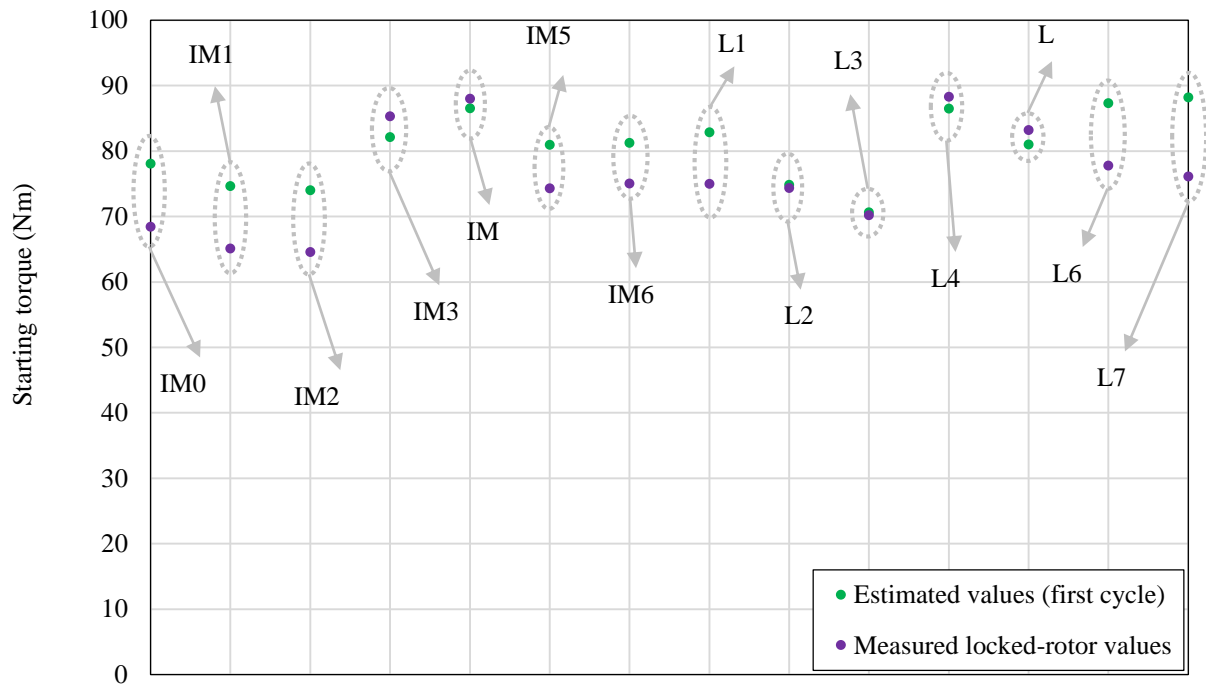
Figure 3-13. Validation of estimating starting torque by measured locked-rotor torque.

3.5 Optimization Approaches Performance

3.5.1 Background of Algorithms

This section presents the strengths and weaknesses of the gradient-based (SNLP) and gradient-free (GA) algorithms. The main advantage of the gradient-based algorithm is fast convergence. Convergence speed is dramatically boosted with appropriate utilization of a gradient-based algorithm rather than a gradient-free approach. Clear convergence criterion is another advantage of the gradient-based approach. Inaccurate gradients, noisy objective function spaces, categorical variables, and topology optimization are difficulties that make a gradient-based algorithm moderately intolerant and this is a drawback of this method. The principal disadvantages of the gradient-based approaches are also the strengths of genetic algorithms like greater ability to find the global optimum, ability to handle noisy objective functions, and categorical variables. However, slow convergence, particularly around an optimum, and unpredictable termination criterion are two key drawbacks of genetic algorithms.

3.5.2 Performance Discussion of Studied Algorithms

A performance comparison of the genetic and SNLP algorithms has been emphasized in this research for a specific optimization problem in the context of electrical machines. The key points of this comparison are an identical optimization problem, including the variables, objective functions, and constraints for both algorithms. The number of evaluations required to reach a desired level of convergence was calculated. The number of evaluations during optimisation for the SNLP algorithm depends directly on the maximum number of iterations. However, in GA it is related to the population

size (parents), maximum number of iterations (generation size), children and number of survivors chosen.

Figure **3-16** shows the algorithms' performance in terms of optimisation time under equal number of iterations for each scenario. It indicates that the gradient-based algorithm resulted in optimal designs (L7 and IM6) with better performance than GA ones (L6 and IM5) in much less time. The GA, like other evolutionary algorithms, is a global search optimizer. It has no knowledge of the trends of the performance parameters against variations of the input variables. It thus may choose candidates whose variables are too far from the ideal design since the selection process is random. This feature makes the GA advantageous for optimization problems where limited information about the behaviour of the case study is available. Conversely, the gradient-based algorithm is superior when higher accuracy and better convergence are necessary. The disadvantage of GA is that there is no guarantee of a better set of candidates (design points) based on the available population. It means that the next generation of candidates do not necessarily result in an improved design.
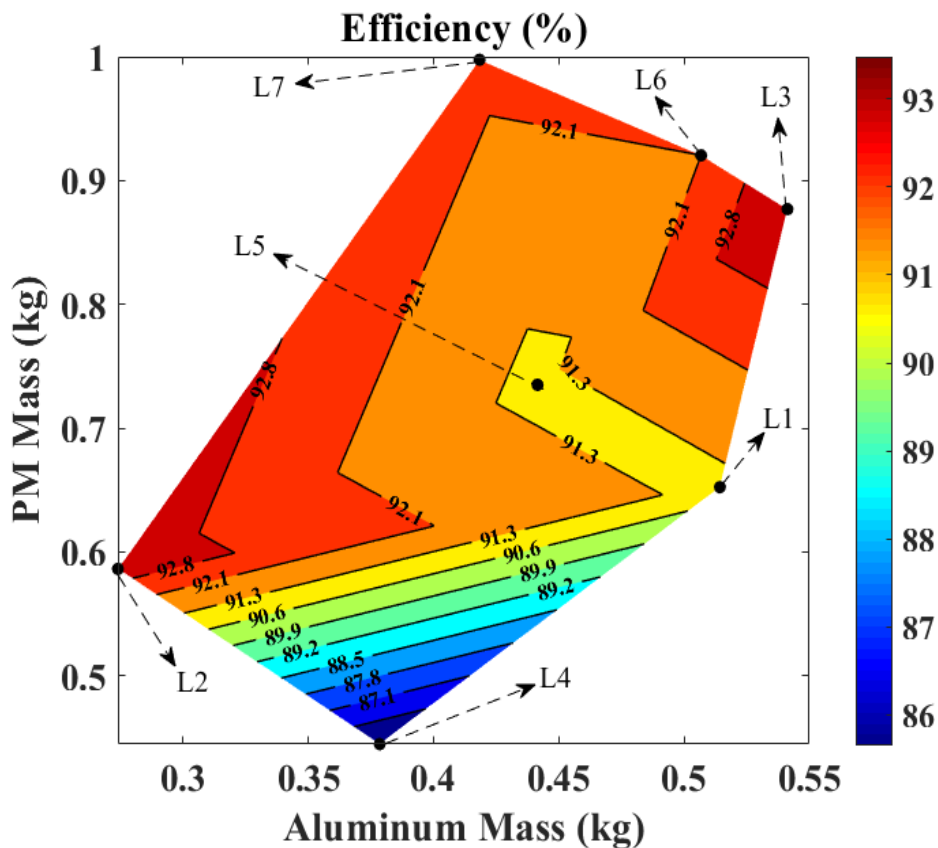
Figure 3-14. Efficiency variations in relation with PM and aluminium mass changes.

69
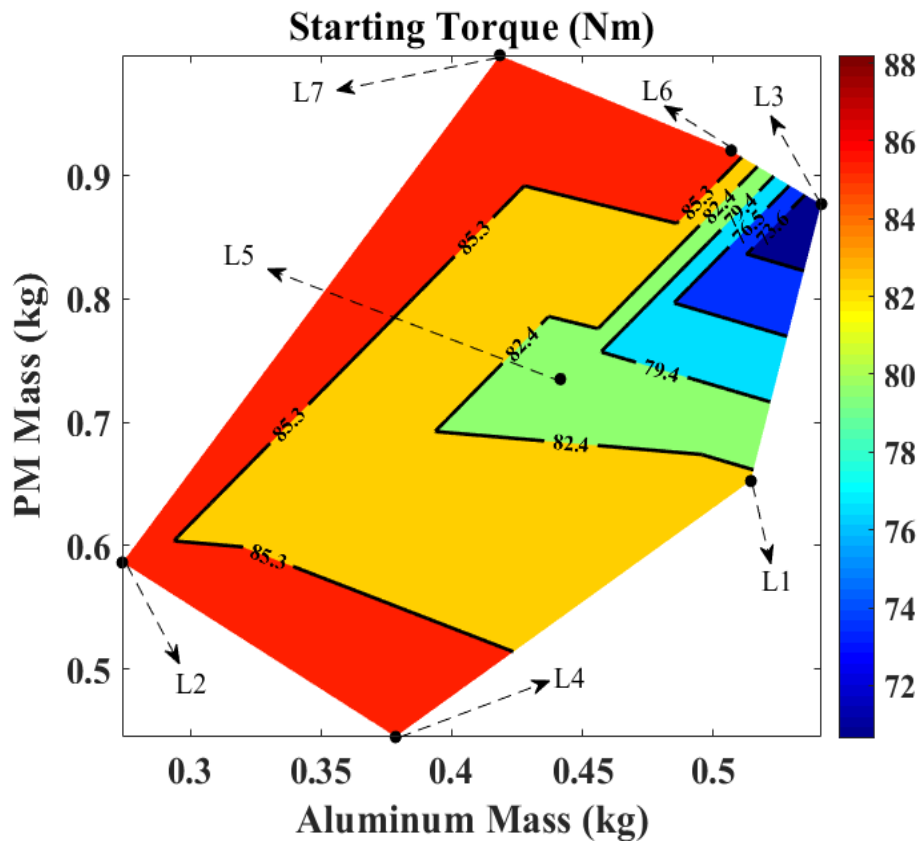
Figure 3-15. Starting torque variations in relation with PM and aluminium mass changes.
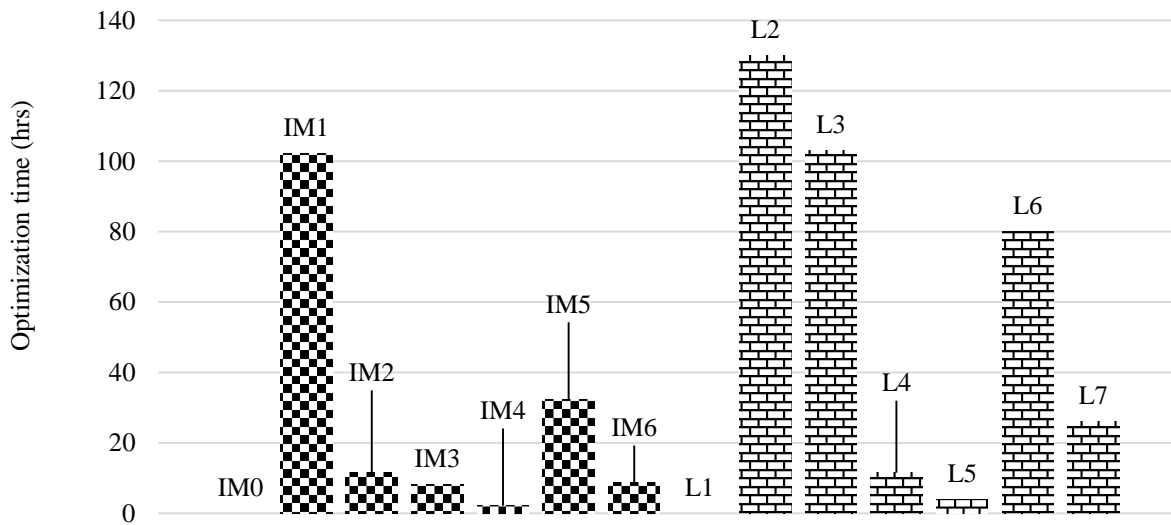
Designes optimised by gradient-free approach (GA): IM1, IM3, IM5, L2, L4, and L6.

Designes optimised by gradient-based approachec (SNLP): IM2, IM4, IM6, L3, L5, and L7.

Figure 3-16 Optimization time in each scenario (Note that the original IM and L1 were not optimized).

3.6 Conclusion

This chapter designed a LSPMSM based on a commercial 4-kW IM to meet the IE4 efficiency standard. The initial design of the LSPMSM was created using a hybrid rotor with the same stator and winding as the IM. The initial LSPMSM design has an efficiency (91%), which was more than the original IM (87%), but not meeting the IE4 requirement (92%). Hence, it was optimised to improve both the steady-state and the transient performance. Two different optimization approaches (GA and SNLP algorithms) were employed to reach this aim and to compare the performance of both algorithms in an electrical machine context. Based on the results, the following conclusions can be drawn:

- Multi-objective optimizations resulted in better overall designs than single-objective functions for both transient and steady-state performance. The optimal designs (IM6 and L7) not only meet the IE4 efficiency standard, but also have better start-up performance than their baseline designs.

- The number of evaluations in the SNLP algorithm (gradient-based) varies almost linearly with the number of variables and maximum iterations whereas, for the GA, it increases more rapidly compared to the number of design variables and is related to the number of children and survivors. Therefore, the GA (gradient-free) generally requires much more time to complete an optimization problem than SNLP (gradient-based) under similar conditions.

- In addition, the gradient-based algorithm presents the optimum designs for both motors (IM6 and L7) with superior overall performance in the transient and steady-state conditions.

In this chapter it was concluded that motor performance analysis and optimization implementation by FEM are time-consuming processes. Optimization by FEM requires a supercomputer and time to implement a study. Hence, in the next chapter, the aim is to present a strategy to design, analyse and optimize an LSPMSM analytically.

4. CHAPTER 4

4. AN ANALYTICAL DESIGN AND OPTIMIZATION PLATFORM OF LINE-START PERMANENT MAGNET SYNCHRONOUS MOTORS

This chapter proposes a design strategy of a LSPMSM based on the machine sizing techniques of the IMs and PM motors. The chapter is divided in six sections. A summary of the chapter is presented in Section 4.1. Section 4.2 is a brief introduction. Section 4.3 proposes a design methodology and a verification of the method using a 4-kW 4-pole case study. The proposed optimisation strategy and results of the case studies are discussed in Section 4.4. Further results, verification and discussion of the other case study (1-kW 8-pole LSPMSMs) are pointed out in Section 4.5. The chapter concludes in Section 4.6.

4.1 Summary

This chapter presents an analytical method for the design of an optimum Line-Start Permanent-Magnet Synchronous Motor (LSPMSM). An initial LSPMSM (L0) is designed by combining an induction motor (IM0) and an interior permanent magnet (IPM0) motor. The IM0 and IPM0 are designed analytically from sizing equations. The optimum LSPMSM is developed from IM cage optimization for starting torque and permanent magnet (PM) optimization of the IPM for efficiency. By combining the rotors of the optimised IM and IPM, an optimum hybrid rotor is obtained for the LSPMSM. The optimum motor has better performance in the transient and the steady state compared to initial LSPMSM. The proposed optimisation method based on a mathematical model is implemented using a genetic algorithm (GA). An optimization case study is implemented using FEM to verify the performance of the proposed optimisation strategy. The optimization results indicate that the optimum design found using the proposed mathematical method is obtained more rapidly and has comparable performance to that found using FEM optimization.

4.2 Introduction

Designing electric machines is a multi-physics procedure and, hence, analyses such as electromagnetic, thermal and structural mechanic need to be considered in the design process [132]-[138]. The key purpose of the design phase, before an optimization implementation stage, is to gain a feasible structure/design for a specified application using the investigations of various dimensions and materials, types of machine, and different types of analysis like electromagnetic and thermal analysis. The electromagnetic analysis of an initial design provides details for the development of the optimization model, which will be used in the next step, including motor parameter estimation and performance assessment. The main aim of the optimization phase is to use optimization algorithms

and strategies to improve the transient and steady-state performance of the initial motor designed in the design phase [57].

There are three methods for the electromagnetic design and analysis of an electrical machine: analytical methods (like subdomain or Fourier techniques), numerical (such as the finite-element method) and machine sizing (like sizing equations) [139]-[144]. The analytical method is simpler but less accurate. The numerical technique is accurate but time-consuming. The machine sizing method is a fast method although it is not as accurate as the numerical method.

Thermal and structural design are two main disciplines that are usually studied after the electromagnetic design [57]. The key purpose of thermal analysis is to study temperature distribution of the main parts of the machine as a result of the heat generated by losses estimated from the electromagnetic analysis. The two well-known thermal analysis models are lumped-parameter thermal network and finite-element method [145]-[147]. Thermal modelling and analysis of the LSPMSM will be discussed in depth in Chapter 5.

Generally, an LSPMSM can be designed by modifying the rotor of an induction motor. However, selection of the permanent magnets needs careful consideration to achieve a balance between starting and synchronisation performance. The well-known and popular LSPMSM design method is a retro-fit design (induction motor rotor "swap-out") using a direct replacement of the rotor of an induction motor (IM) with an LSPMSM rotor without machine sizing [148]-[150]. This method was used in the previous chapter to design a 4-kW LSPMSM based on a commercial IM. There are independent machine sizing methods to design IMs and interior permanent magnet (IPM) motors and hence there is the possibility to employ optimisation techniques in machine sizing to design an optimum machine. LSPMSMs include a squirrel cage and interior permanent magnet in its rotor and, hence, there is not an independent machine sizing design and, therefore, optimization technique for LSPMSMs.

In this chapter, a mathematical design and optimization method based on the developed machine sizing equations of induction motors and permanent magnet motors is proposed in order to design an optimum LSPMSM. The rotors of the IM and IPM are combined to create a hybrid rotor including induction cage and permanent magnets for a LSPMSM. To verify the proposed mathematical method, a three-phase 4-kW LSPMSM is selected as a case study. The initial designs of the IM, IPM motor and LSPMSM (L0) are analyzed using FEM to verify the sizing equation design. The IM and IPM are then analytically optimised using a genetic algorithm (GA) for the transient improvement (through maximizing the starting torque) and the steady-state improvement (via maximizing efficiency), respectively. The rotor cage bar dimensions and PM size are selected as optimisation variables in optimizing the IM and the IPM, respectively. Combining the rotors of the optimised IM and IPM, the optimum hybrid rotor of the LSPMSM is obtained. To present a comparative study between the proposed optimisation method and FEM optimisation, the 2D design of L0 is optimised using GA

based on FEM in Ansys/Maxwell. The results indicate that the proposed mathematical optimization method presents an optimum LSPMSM with comparable performance in both transient and steady-state in a much shorter time than the FEM optimization with reasonable accuracy.

4.3 Design Methodology

Because of the higher efficiency and higher power factor of LSPMSMs and their ability to run a set of fixed frequencies and speed adjust to zero-steady slip, they compete with cage induction motors in industrial applications. They operate with much higher power factor than IMs. LSPMSMs have a power factor near one in lots of applications and operating conditions. LSPMSMs with an inverter are already in use in a wide range of applications and is on the rise. The two reasons for this trend are first, the high power factor and efficiency of LSPMSMs, and second, permanent magnet price cuts. In addition, the LSPMSMs run up from zero speed with a static frequency and this has become an appealing scheme for senseless drives. Because of the existence of PM, the starting performance of the LSPMSM is not as good as the IM and the steady-state performance (efficiency) is not as good as the PM. Therefore, there is a significant need to design and optimize an LSPMSM covering these shortcomings.

4.3.1   Principles of Proposed Method

This study aims to develop a guideline for the design of an LSPMSM based on the machine sizing equations. LSPMSMs operate in starting like IMs and in the steady-state like an IPM. Figure 4-1a illustrates the steady-state torque-speed graph of an LSPMSM (4-pole, 50 Hz, 415 V, 4-kW). The curves are extracted from the equivalent circuit. The LSPMSM torque is lower than the induction (cage) torque because of the magnet braking torque. The LSPMSM torque is calculated according to Equation 2.10. The load torque must be lower than the LSPMSM torque generated by the motor for a successful start-up. The magnet torque is directly related to the electromotive force (EMF) and the q-axis reactance and has an inverse relation with the mutual d- and q-axis reactances as calculated by Equation 2.11. Figure 4-1b illustrates an example dynamic torque-speed graph of the LSPMSM. The behaviour of dynamic torque and the steady-state torque are not similar but the starting torque can be estimated from Figure 4-1b in the first cycle (20 ms, because the frequency of the source is 50 Hz) the very similar actual starting torque in Figure 4-1a.

Cage torque disappears after synchronization and magnetic torque, as the only source of torque, plays a reverse role. The contributions and effects of cage torque (induction) and magnet torque (braking torque) are seen in Figure 4-1b. The transient and the steady-state operation are highlighted in Figure 4-1b. The motor can run rated load (constant or fan type) at synchronous speed. The behaviour of the dynamic torque and the steady-state torque-speed are not exactly similar but can be

considered alike. Hence, the staring torque can be estimated from the electromagnetic torque versus time using FEA.

Cogging torque is produced by the cogging effect and this torque produces a speed ripple and creates vibration under low loads and speed levels. However, at high-speed levels, the effect of cogging torque is eradicated due to high inertia. Ways of omitting cogging torque are to 1) split the PM, 2) change the ratio of the arc phase to pole step, and 3) using a flux barrier on the rotor. Lack of joule losses from the rotor cage in the steady-state is one of the factors for why an LSPMSM has high efficiency. Copper loss of the stator is reduced because of low input current resulting from a significant decline in magnetizing current. The existence of magnet saliency in the rotor adds another torque component in comparison with a rotor surface that is smooth. Magnet volume determines the flux density level of the air gap. Induced EMF and torque in an LSPMSM depends on the flux density of the air gap, which is dependent on shaft material, magnet thickness and pole arc coefficient.
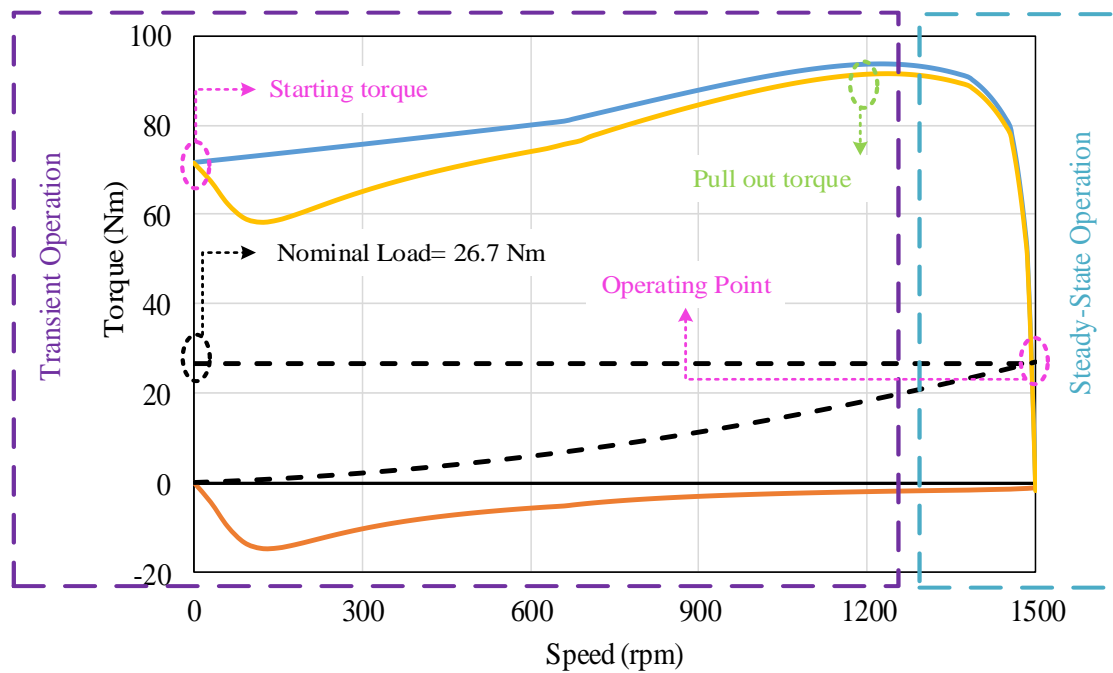
a.   Steady-state torque-speed response.
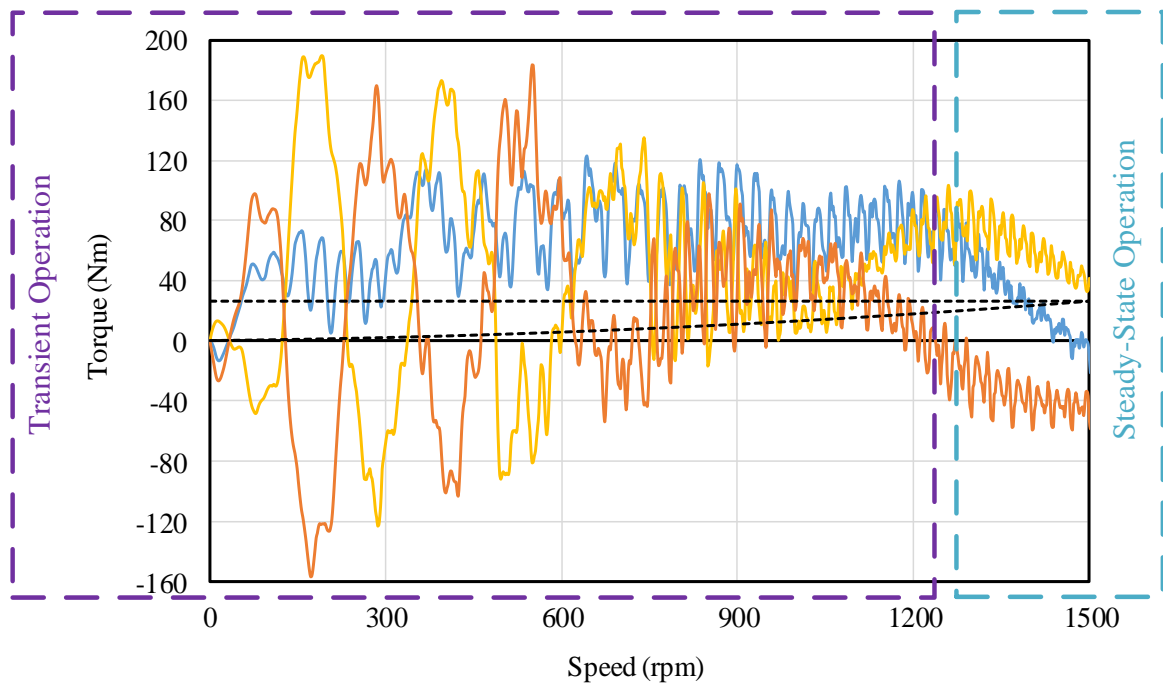
b. Dynamic torque-speed response.

——InductionTorque ——MagnetGeneratedTorque ——LSPMSM Torque - - Constant Load - - Fan Load

Figure 4-1. Steady-state and dynamic torque-speed components of the LSPMSM including cage torque, magnet torque, fan load and constant load.

4.3.2 Proposed Design Methodology

As the transient behaviour of LSPMSMs is like induction motors, it makes sense to improve the transient performance of the LSPMSM by optimising the transient performance of the equivalent IM. To improve the steady-state performance of the LSPMSM, the steady-state performance of the IPM is optimised.

The design procedure based on the sizing equations begins with the motor specification and desired parameters as inputs. There are two essential inputs in designing an electrical motor based on machine sizing: firstly, customer requirements (required mechanical power/torque, desired efficiency and power factor) and, secondly, the key design assumptions (rotor length to inner stator diameter ratio, number of stator and rotor slots, specific electrical loading and specific magnetic loading). In the design process, based on the proposed method, similar input values (customer requirements) are used to design a stator for both the IM and the IPM. The rotor topologies of the IM and the IPM for the same stator are then designed.

4.3.2.1 Stator and winding design

Figure 4-2 shows the process of stator and winding design. The motor dimensions are generally summarized into inner and outer diameters of the cores, motor length, air gap length, winding and the rotor and stator slots. Table 4-1 lists the input parameters required to design the LSPMSM (case study) based on the IM and the IPM.

Table 4-1. Input parameters required to design the motor.

	Parameters	Symbol	Value
Rated parameters	Output Power	*Pout*	4-kW
	Synchronous Speed	N_s	1500 rpm
	Frequency	*f*	50 Hz
	Input Line Voltage (*V_{ph}*)	V	415 V- Delta
	Number of Phase	*m*	3
Desired parameters	Efficiency	*η*	>88%
	Power Factor	*PF*	>0.84
Assumptions or constants	Average flux density	B_{av}	$0.3<B_{avg}<0.9$
	Electrical Loading	*ac*	$10^3<ac<5.5\times10^4$
	Length/Inner Diameter	*ε*	~1.5
	EMF/*V_{ph}*	*e*	$0.7<e<0.95$
	Winding Factor	k_w	0.95
	Lamination Factor	k_i	0.95
	Stator Slots/Pole/Phase	q_s	3
	Number of Rotor Slots	S_r	28
	Shaft Diameter	D_{sh}	38mm
	Current Density	J_s	6 A/mm²
	Stacking factor	k_i	0.95
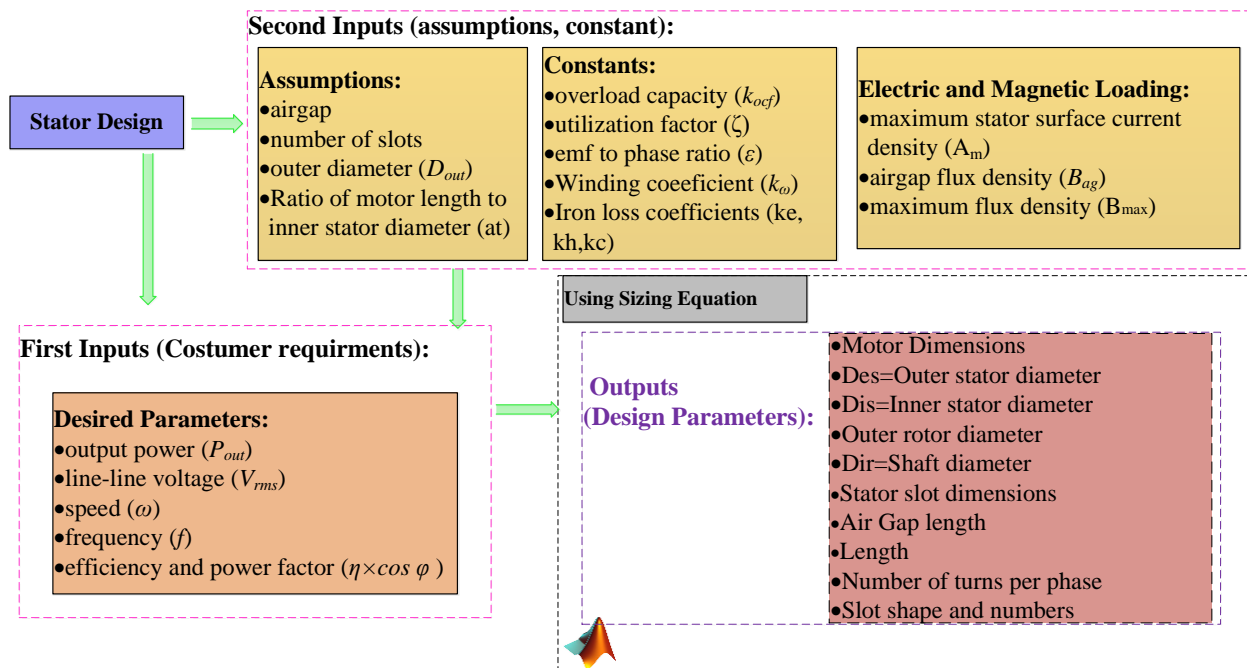
Figure 4-2. Flowchart of the stator design procedure of the proposed method.
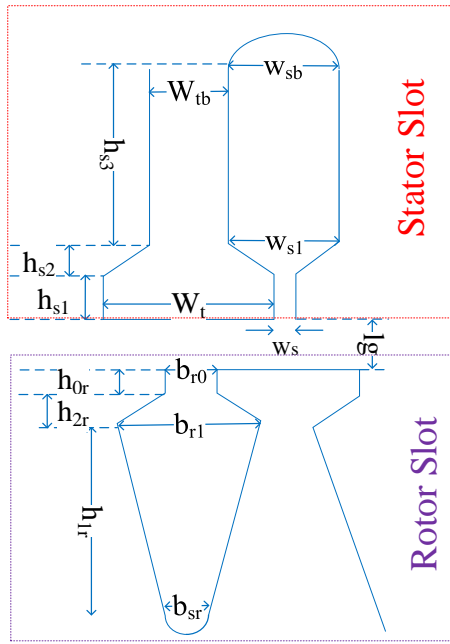
Figure 4-3. Stator and rotor slot shapes.
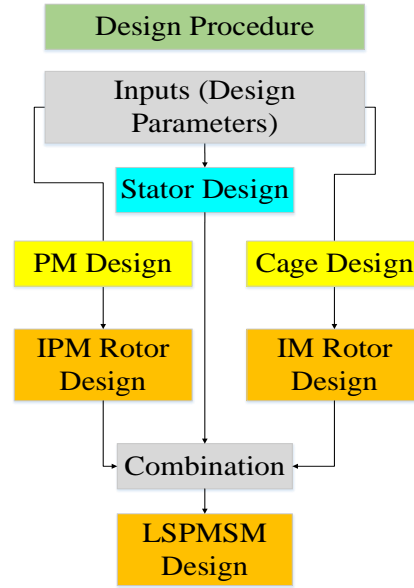
Figure 4-4. LSPMSM design algorithm based on the IM and IPM designs.

Based on the inputs listed in Table **3-1** (for the case study from Chapter 3), the stator inner diameter is calculated by Equation 4.1. Apparent power (S) in kVA, synchronous speed (n_s) in rps and number of poles are calculated according to Equations 4.2 -4.5, respectively. The coefficient $\lambda=1.75$ is assumed based on the desired purpose (high efficiency and low construction cost) of the motor design [27].

$$D_{is} = (\frac{\lambda \times S}{C_o \times n_s})^{1/3}$$ Stator inner diameter (4.1)

$$S = \frac{P_{out}}{\eta \times PF}$$ Apparent power (4.2)

$$C_o = 11 \times k_w \times B_{avg} \times ac \times 10^{-3}$$ Design Coefficient (4.3)

$$n_s = \frac{N_s}{60}$$ Synchronous speed (4.4)

$$P = \frac{120 \times f}{N_s}$$ Number of Poles (4.5)

The motor length is computed based on the stator inner diameter and the defined coefficient (λ). Equation 4.6 presents the motor length formula. The effective length of the rotor is defined by Equation 4.7 where k_i is a coefficient in range 0.9-1.0. The root mean square (rms) of the stator winding phase current is presented in Equation 4.8.

$$L = \frac{\lambda D_{is} \times \pi}{P}$$ Motor length (mm) (4.6)

$$L_i = L \times k_i$$ Effective motor length (mm) (4.7)

$$I_s = S \times 1000/m \times V_{ph}$$ RMS stator phase current (4.8)

78

The step after stator core sizing is the determination of winding factor (k_w), number of turns per phase of coil (N_{ph}) and the required slot area and shape. The average flux density (B_{avg}) and specific electrical loading (ac) for induction motors is chosen from the range of values 0.3-0.6 T and 8000-30000 A/m, respectively [150]. In this research work, the values of B_{avg} and ac are selected as 0.465 T and 26500 A/m. The needed slot size is determined based on the N_{ph}, winding area and fill factor. To calculate wire area, the current density of the winding (J_s) should be selected. Note that the fill factor is considered to be 0.45 in the calculation process. The stator slot dimensions and winding parameters are calculated using Equations 4.9-4.21 based on the inputs and the outcomes from the previous step.

$$t_p = \pi \times D_{is}/P \qquad \text{Pole pitch} \qquad (4.9)$$

$$f_{ip} = B_{avg} \times t_p \times L \qquad \text{Flux per pole} \qquad (4.10)$$

$$S_s = q_s \times P \times 3 \qquad \text{Number of stator slots} \qquad (4.11)$$

$$N_{ph} = ac \times (P/2) \times t_p/(m \times I_s) \qquad \text{Number of coils turns per phase} \qquad (4.12)$$

$$Z_{slot1} = 2 \times m \times N_{ph}/S_s \qquad \text{Number of conductors in a slot} \qquad (4.13)$$

$$t_s = \pi \times D_{is} / S_s \qquad \text{Slot pitch} \qquad (4.14)$$

$$w_{tb} = B_{avg} \times t_s/B_t \qquad \text{See Figure 4-3} \qquad (4.15)$$

$$a_{sc} = I_s/J_s \qquad \text{Area of stator conductor} \qquad (4.16)$$

$$w_s = 1.1 \times \sqrt{(a_{sc} \times 10^{-6} \times 4/\pi} \qquad \text{See Figure 4-3} \qquad (4.17)$$

$$w_t = t_s - w_s \qquad \text{See Figure 4-3} \qquad (4.18)$$

$$h_{bs} = 0.5 \times f_{ip}/(L_i \times B_{ys}) \qquad \text{Stator back iron height} \qquad (4.19)$$

$$w_{sb} = (\pi \times (D_{is} + (2 \times h_s)))/s) - w_{tb} \qquad \text{See Figure 4-3} \qquad (4.20)$$

$$w_{s1} = ((D_{is} + h_{s1} + h_{s2}) \times \pi/s) - w_{tb} \qquad \text{See Figure 4-3} \qquad (4.21)$$

Where B_t, B_{ys}, B_{yr}, h_{s1} and h_{s2} are tooth and yoke magnetic flux density in the stator and rotor, slot dimensions assumptions, respectively. Air gap length, stator slot depth and the stator outer diameter are calculated using Equations 4.22-4.23.

$$l_g = 0.001 \times (0.2 + 2 \times \sqrt{(L \times D_{is})} \qquad \text{Air gap length} \qquad (4.22)$$

$$h_s = 0.5 \times (\frac{B_{avg} \times D_{is}}{B_t} - (D_{is} + 2 \times (h_{s1} + h_{s2})))$$
$$\mp \sqrt{(\frac{B_t \times ((D_{is} + 2 \times (h_{s1} + h_{s2}))}{2 \times B_t})^2 + \frac{B_{avg} \times D_{is}}{\pi \times J_s})} \qquad \text{Stator slot depth} \qquad (4.23)$$

After designing the stator, the stator circuit parameters, like winding resistance (R_s) and stator reactance (X_s), are calculated using Equations 4.24-4.39. Note that, the material used for the winding

is copper with resistivity of ρ_c=1.68×10-8 (ohm.m) at 20°C and increasing factor of end winding (k_{ov}) is considered to be 1.8. k_{sat} is the saturation factor in the d-axis and is considered to be 3, and p is the number of pole pairs. The temperature rise for the winding, ΔT, is assumed to be 65°C, but the temperature rise for the aluminium (cage) and PM materials are considered to be 85°C to avoid demagnetization of the PM due to temperature rise. Accordingly, it is assumed that there is an approximately 10% reduction in the PM remanence for an 85°C temperature rise [28]. Also, the resistivity of the copper and aluminium material should be updated based on the thermal coefficient (α), which for the copper and aluminium is 0.0039 and 0.0043, respectively.

4.3.2.2 Rotor Design

In the design process of the hybrid rotor of the LSPMSM, the IPM rotor is designed first. Braking torque due to the PM should be considered when designing the squirrel cage to supply the required starting torque. The rotor design procedure is described in the following sub-sections. Figure **4-4** shows the procedure of the LSPMSM design based on the IM and IPM.

$D_{os} = D_{is} + (2 \times h_s) + (2 \times h_{bis}) + (2 \times l_g)$	Outer stator diameter	(4.24)
$p_s = \pi \times (D_{is} + (2 \times h_s))/s$	Slot pitch at the end of slot	(4.25)
$y_q = 2 \times (s/P)$	Coil pitch in number of slots	(4.26)
$l_{ew} = ((\pi/2) \times ((p_s + w_t)/2)) + (p_s \times k_{ov} \times (y_q - 1))$	Length of end winding	(4.27)
$l_{av} = 2 \times (L + l_{ew})$	Average length of coil turn	(4.28)
$R_s = (\rho_{co} \times N_{ph} \times l_{av}/a_{sc}) \times (1 + \Delta T \times \alpha)$	Stator Resistance	(4.29)
$h_{s3} = h_s - h_{s1} - h_{s2}$	See Figure **4-3**	(4.30)
$t = w_{sb}/w_{s1}$	factor	(4.31)
$k_t = 3 \times ((4 \times (t^2)) - ((t^4) \times (3 - (4 \times log(t)))) - 1)/(4 \times (((t^2) - 1)^2) \times (t - 1))$	factor	(4.32)
$t_c = t_p$	Coil pitch	(4.33)
$l_s = ((h_{s1} \times k_t/(3 \times w_{s1})) + (2 \times h_{s2}/(w_{s1} + w_s)) + (h_{s1}/w_s)) \times (((3 \times t_c/t_p) + 1)/4)$	Slot leakage permeance	(4.34)
$l_e = (0.47 \times q_s \times (l_{ew}/L)) - (0.3 \times q_s \times (t_p/L))$	End winding leakage permeance	(4.35)
$l_t = (5 \times l_g/w_s)/(5 + (4 \times lg/w_s))$	Tooth-top leakage permeance	(4.36)
$t_d = ((((\pi^2) \times (((10 \times (q_s^2)) + 2))/27)) \times ((sin(\pi/(6 \times q_s)))2)) - 1$	factor	(4.37)
$l_d = m \times q_s \times t_p \times t_d \times (k_w)^2/(\pi^2 \times l_g \times k_{sat})$	Differential leakage permeance	(4.38)

$$X_s = 4 \times \mu_0 \times \pi \times (10^7) \times f \times (N_{ph})^2 \times L_i \times (l_s \\ + ((l_{ew}/L_i) \times l_{ew}) + l_d + l_t)/(p \times q_s)$$

Stator leakage reactance in   (4.39)

a. IM Rotor Design

To design the rotor of an IM, selecting the number of slots (S_r) is important as they restrict the leakage flux. S_r also depends on the number of poles. The flux density in the rotor yoke and tooth are considered similar to those of the stator and, hence, the rotor slot height and width can be determined accordingly. The outer diameter of the rotor is determined, using Equation 4.40, based on the inner diameter of the stator and the air gap length. The back-iron length of the rotor depends on the flux density flowing in the yoke and is calculated from Equation 4.41. The rotor slot dimensions are calculated using Equations 4.42-4.46. The slot shape (stator and rotor) including air gap of the designs are indicated in Figure **4-3**.

$D_{or} = D_{is} - (2 \times l_g)$	Rotor outer diameter	(4.40)
$h_{br} = 0.5 \times f_{ip}/(L_i \times B_{yr})$	Rotor back iron length	(4.41)
$b_{tr} = (B_{avg}/B_t) \times y_{sr}$	See Figure **4-3**	(4.42)
$b_{1r} = (\pi/S_r) \times (D_{is} - (2 \times (l_g + h_{2r}))) - (b_{tr})$	See Figure **4-3**	(4.43)
$b_{sr} = (\pi/S_r) \times (D_{is} - (2 \times (l_g + h_{sr}))) - (b_{tr})$	See Figure **4-3**	(4.44)
$h_{sr} = ((D_{is} - D_{sh})/2) - (h_{bir}) - (l_g)$	See Figure **4-3**	(4.45)
$h_r = h_{sr} + h_{0r} + h_{2r} + (b_{sr}/2)$	Rotor slot depth	(4.46)

b. IPM Rotor Design

There are various rotor topologies for PM motors such as surface mount magnets (SMM), slotted surface mount magnets (SSMM), imbedded radial flux magnets (IRFM) and imbedded circumferential flux magnets (ICFM) [29]. In this study, only the interior radial-flux magnets (IRFM) topology of IPMs is considered. The diameters of the stator and rotor of the IPM are the same as the IM. The air gap flux density range for IPMs is 0.8-1.1 T [31]. Hence, the PM should generate the required air gap flux density (0.85 T), which can be used to calculate the minimum PM volume by Equation 4.47. Table **3-2** (Chapter 3) lists the permanent magnet properties used in this study. Note that the leakage flux in the rotor is assumed to be zero.

$$V_{PM} = 1.4 \times P_{out} \times 1000/(f \times B_r \times H_c \times P)$$

PM volume   (4.47)
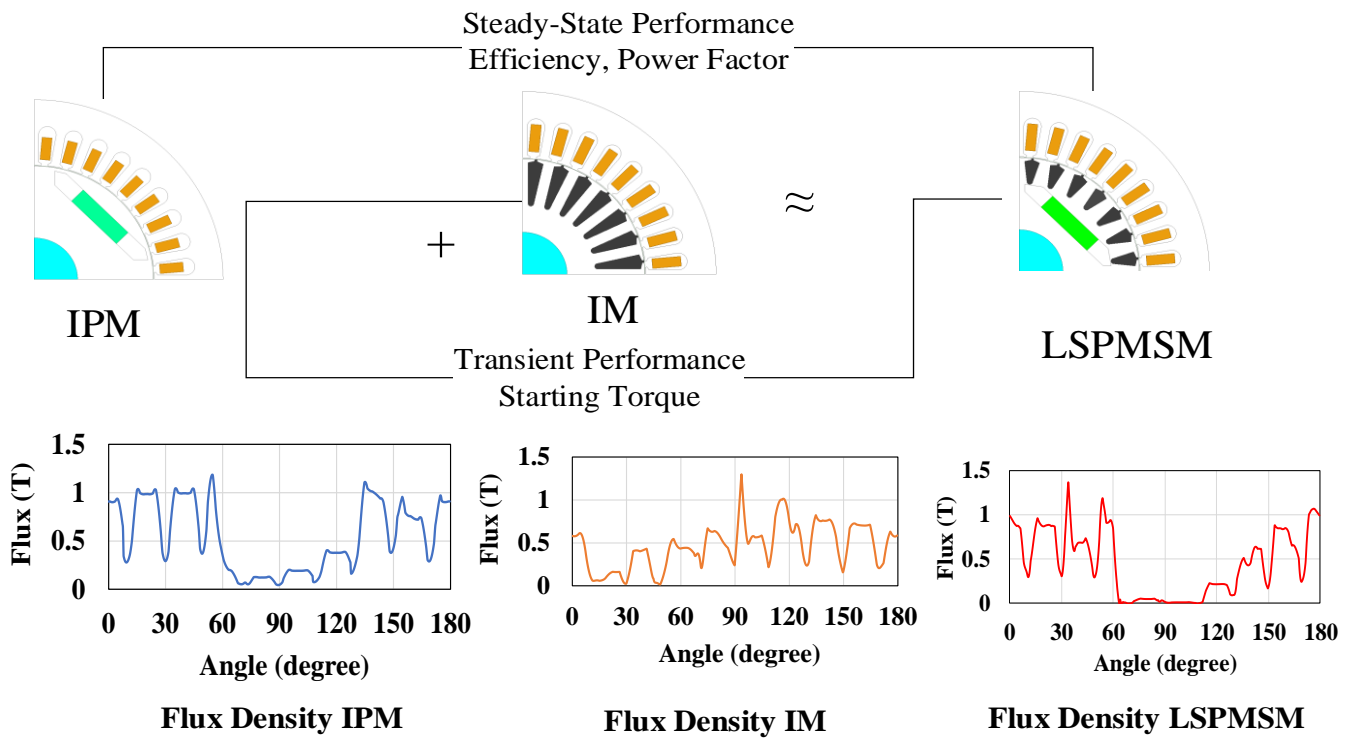
Figure 4-5. 2D cross section views and the air gap flux of IPM0, IM0 and L0.
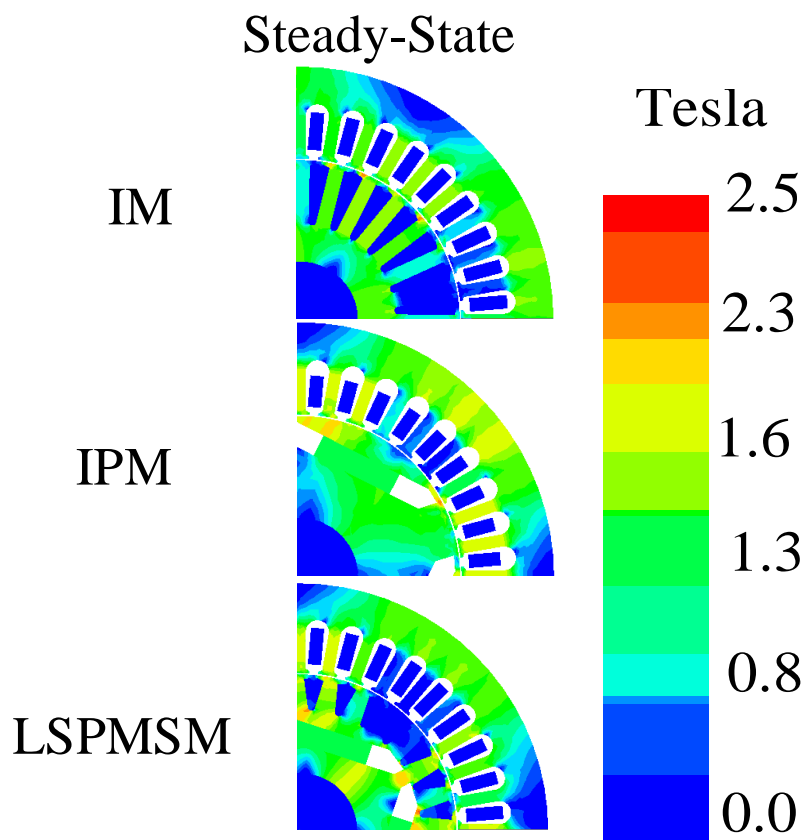
Figure 4-6. Flux density distribution of IM0, IPM0 and L0.

c. Hybrid LSPMSM Rotor Design

The hybrid rotor of the initial LSPMSM (L0) is based on the combination of the initial IM (IM0) and initial IPM (IPM0) rotors. The stator and the rotor cage of the LSPMSM is the same as the IM0 rotor cage and the PM configuration of the LSPMSM is the same as that of IPM0. The space occupied by the PM is designed based on the rotor of IM and if there was an overlap between the PM and the cage bars, the height of the rotor bar is adjusted. There is very minor change in flux path due to this combination as shown in Figure 4-6 and the impact on the combined performance due to this change is assumed negligible. The main dimensions for the case study machine (4-kW 3-phase LSPMSM) designed by the proposed method are presented in Table **4-2**. The stator and rotor magnetic material are chosen as non-oriented steel (M470-50A), which has saturation levels in 1.6-1.9 T, and aluminium is the material for the rotor bars and the end rings.

Table 4-2. Main calculated dimensions of initial LSPMSM (L0) in mm.

Items	Value	Items	Value
D_{os}	165.00	b_{r1}	6.50
D_{is}	105.00	b_{sr}	2.50
D_{or}	104.10	w_s	2.80
D_{ir}	38.00	b_{r0}	1.00
L	145.00	h_{1r}	9.00
h_{s3}	12.65	N_{ph}	336 Turns
W_t	7.70	PM width	28.00
W_{tb}	3.00	PM thickness	7.20
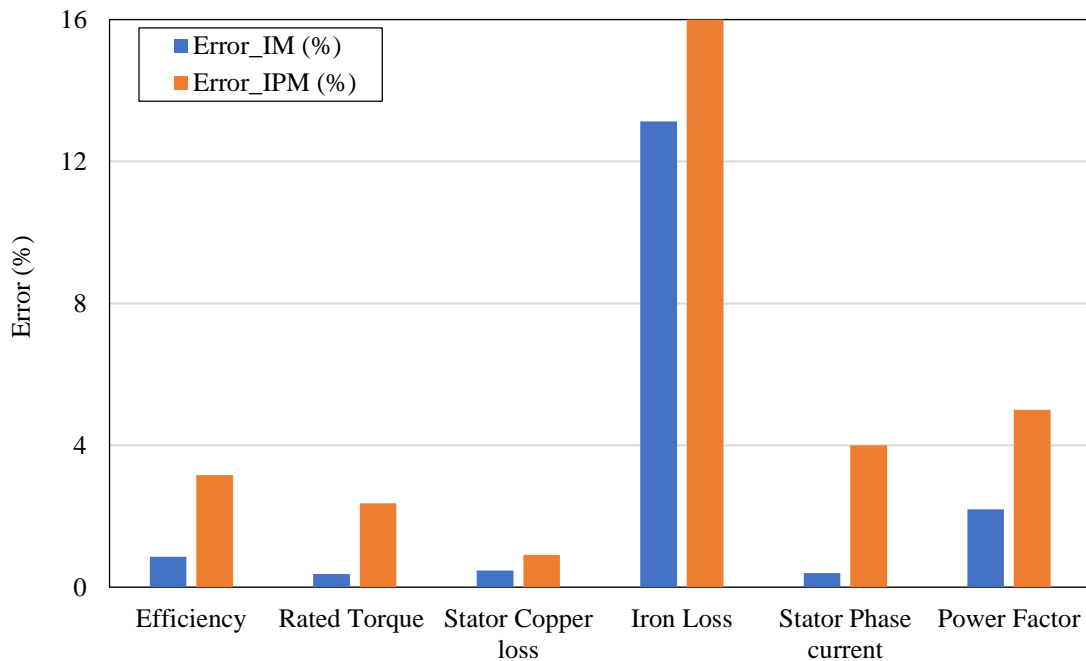
Figure 4-7. Error comparison of the performance parameters calculated by the analytical methods with predicted ones by FEM for IM0 and IPM0 designs.
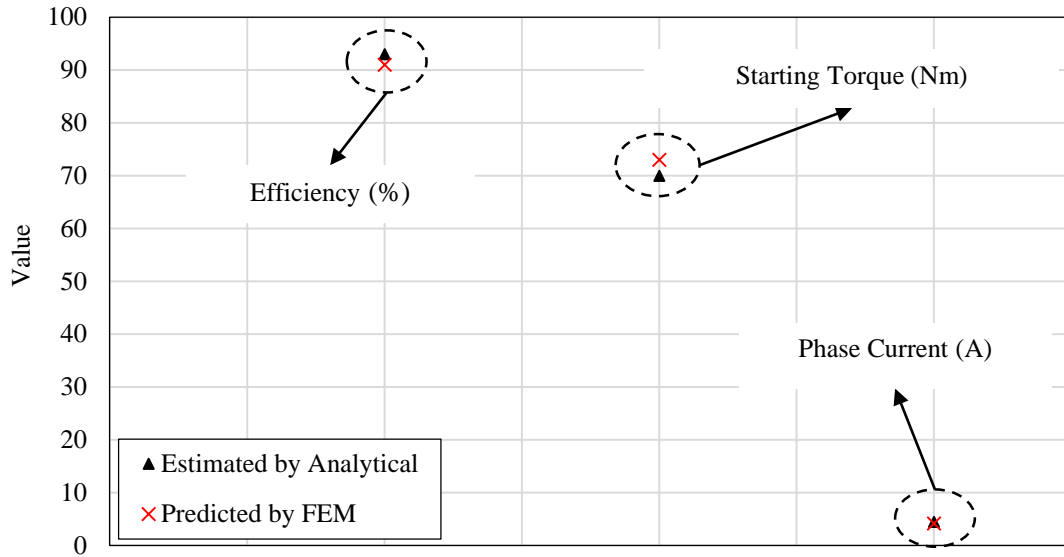
Figure 4-8. Comparison of efficiency, starting torque and phase current values estimated by the proposed method and predicted by FEA for L0.

4.3.3 Verification of the proposed methodology (sizing equations vs. FEM)

In this section, the performance of the proposed mathematical design method is verified using FEM in the Ansys/Maxwell software package. Figure **4-5** and Figure **4-6** show 2D cross section views and the magnetostatic behaviour of the three motors in the steady-state. Magnetostatic in the steady-state is determined when the motor operates with rated speed in the steady-state interval. The air gap flux density (B_g) of the initial LSPMSM (L0) is a combination of those for IM0 and IPM0 (see Figure **4-5**). Flux density distribution illustrated in Figure **4-6** shows the maximum flux density value is approximately 1.9~2.3 T. It is seen that the three motors operate under a constant load at no significant saturation although the LSPMSM has a lower flux density than the IPM.

Figure 4-7 shows the error in the performance prediction determined using the analytical method and FEM for the IM0 and IPM0. It shows that the sizing equation methods can design reliable IMs and IPMs and their performance can be predicted by analytical methods. It is seen that the analytical results are in good agreement with those predicted by FEM. Note that further comparison and verification of the analytical analysis method and FEA of the IM is presented in Appendix A.

Figure 4-8 compares the performance of the proposed method with FEM in terms of predicting the performance parameters of L0. The starting torque of L0 is estimated using the combination of the starting torque of IM0 and braking torque of IPM0. Also, the efficiency of L0 is calculated from the IPM0 considering the cage loss of IM0. It shows the LSPMSM performance predicted by the proposed method is close to that predicted by FEM.

84
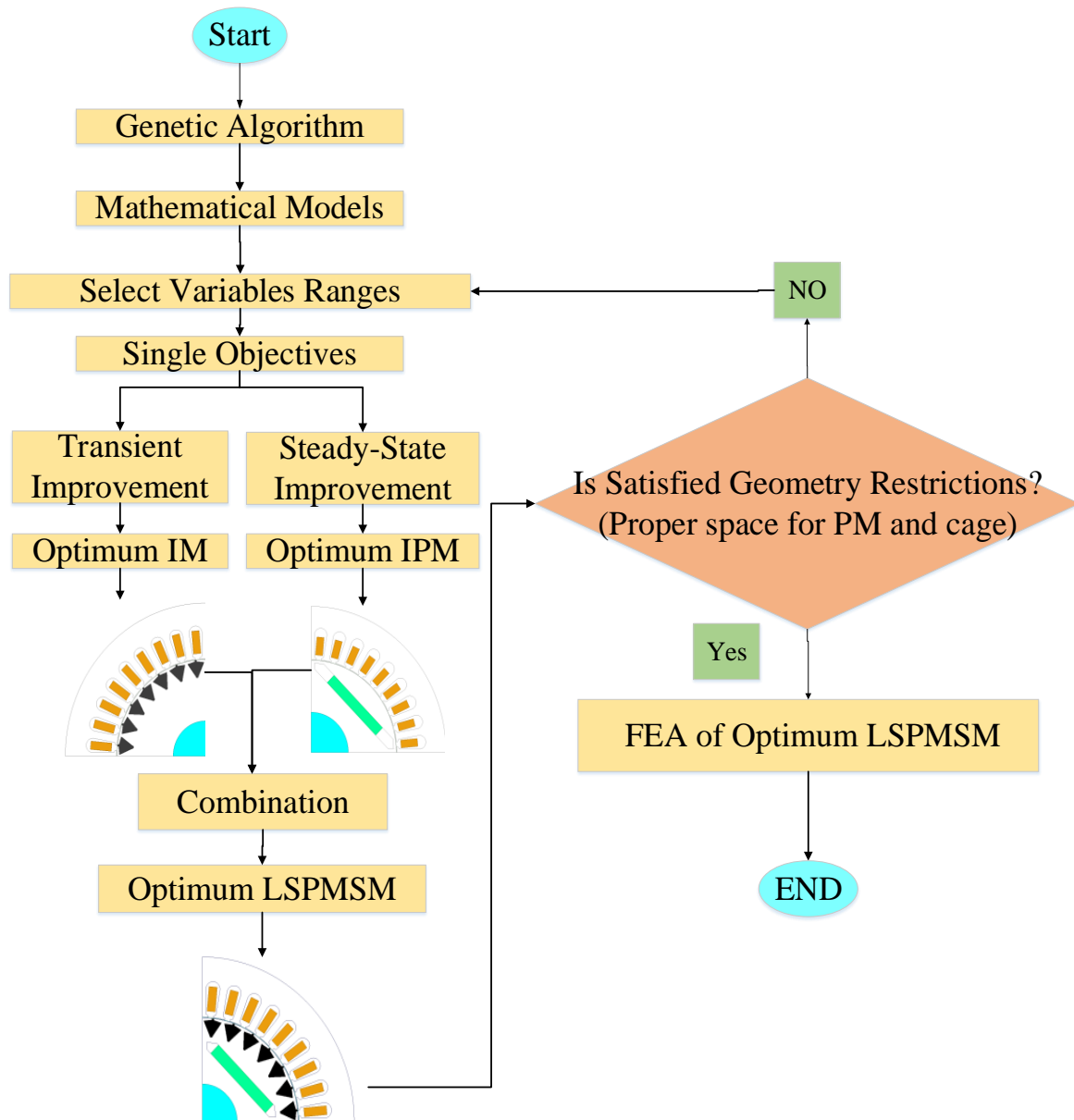
Figure 4-9. Proposed Optimisation Method Flowchart for the optimum LSPMSM.

4.4 Proposed Optimization Methodology

4.4.1   Optimization Implementation

In this study, the initial LSPMSM is designed using the proposed mathematical method and FEM-based optimization is used to verify the optimisation. Table **3-3** (Chapter 3) presented optimization variables, ranges and shapes.

4.4.1.1 Optimization using proposed mathematical method

The genetic algorithm (GA) is used to optimize the IM for transient performance and the IPM for steady-state performance using the sizing equation method. Then, the cage and PM (optimisation variables) of the optimized IM and IPM are used as the basis for the optimum LSPMSM. Figure 4-9 shows the implemented optimization flowchart. The optimization procedure of the LSPMSM using the proposed method is implemented in the scenarios below:

1. Transient improvement: in this case the cage used for the initial LSPMSM is optimised via the induction motor sizing equations to produce the maximum starting torque. The PM used in the optimised LSPMSM in this case is the same as L0. The optimised LSPMSM in this scenario (L1_Ana) is a LSPMSM with higher starting torque than L0 formulated using Equation 4.48 and the rotor cage bar dimensions are the optimization variables. The optimised LSPMSM in this scenario (L1_Ana) is a LSPMSM with higher starting torque than L0.

$$f_1 = Maximizing \left(\frac{(3 \times Vph^2 \times R_r)}{(2 \times \pi \times n_s \times ((R_s + R_r)^2 + (X_s + X_r)^2))}\right) \tag{4.48}$$

where R_r and X_r are the rotor resistance and leakage reactance transferred to the stator side and are calculated using Equations 4.49-4.59. Note that the factor n in Equation 4.61 is the turn ratio and was formulated in [31].

$I_r = (0.85 \times 6 \times N_{ph} \times I_s)/S_r$	Rotor current	(4.49)
$I_{er} = (S_r \times I_r)/(\pi \times P)$	End ring current	(4.50)
$F_{b2} = (b_{0r} \times h_{4r} + ((b_{0r} + b_{r11}) \times h_{2r}/2) + ((b_{r1} + b_{sr}) \times h_{1r}/2) + (0.5 \times (\pi \times (b_{sr}/2)^2))) \times 10^6$	Area of rotor bar	(4.51)
$R_b = \rho_{Al} \times (L/F_{b2}) \times (1 + \Delta T \times \alpha)$	Bar resistance	(4.52)
$P_{rbcl} = I_r^2 \times R_b \times S_r$	Loss in rotor bars	(4.53)
$L_{er} = \pi \times D_{or}$	End ring length	(4.54)
$F_{er} = (F_{b2} \times S_r)/(2 \times P)$	Area of end ring	(4.55)
$R_e = \rho_{Al} \times L_{er}/F_{er} \times (1 + \Delta T \times \alpha)$	End ring resistance at	(4.56)
$R_r = (R_b + R_e) \times n$	Rotor resistance referred to stator	(4.57)
$r_{sp3} = \mu_0 \times ((2 \times (h_{2r} + h_{0r})/(3 \times (b_{sr} + b_{r1}))) + ((2 \times h_{1r})/(3 \times (b_{sr} + b_{r1}))))$	Rotor slot permeance	(4.58)
$X_r = 2 \times \pi \times f \times L \times r_{sp3} \times n$	Rotor slot leakage reactance	(4.59)

2. Steady-state improvement: in this case the IPM is optimised to maximize the efficiency defined in Equation 4.60 by varying the PM dimensions. In this case, the cage used in the optimised LSPMSM and L0 are similar. The optimised LSPMSM (L2_Ana) is expected to operate with higher efficiency than L0.

$f_2 = Maximizing \left(\dfrac{P_{out}}{P_{out} + Losses}\right)$		(4.60)
$Losses = P_{cus} + P_{cage} + P_{Iron}$	Total loss	(4.61)
$P_{cus} = 3 \times R_s \times I_s^2$	Copper loss	(4.62)
$P_{cage} = 3 \times R_r \times I_r^2$	Rotor cage loss	(4.63)

where P_{cus} and P_{cage} are the stator copper loss and rotor cage loss. P_{Iron} is the core loss in the stator and rotor that is defined in [151].

3. Simultaneous transient and steady-state performance improvement: in this case, the optimum cage of L1_Ana and the optimum PM topology of L2_Ana are combined to approximate the optimum rotor. The optimized LSPMSM (L3_Ana) should operate with starting torque and efficiency superior to L0.

In the first scenario, the optimisation tends to increase R_r and decrease X_r through decreasing h_{1r} (leads to rotor bar area reduction) and increasing b_{r1}, respectively. Accordingly, it is predicted that the new cage bar height should be less than the non-optimised cage. In fact, there may be no overlap between the optimum PM and cage in scenario 3. However, the required space of the PM is checked and if there is not enough space for the cage bars it will be optimised using an updated range of variables for the cage bar dimensions.

4.4.1.2 Optimization using FEM

In this section, L0 is directly optimised by FEM to verify the proposed method's performance. Hence, GA called by Maxwell optimizes the 2D model of L0 under the same optimisation variables and conditions applied as in the proposed method. The implementation of the optimisation scenarios in FEM is described as follows:

1. Transient improvement: starting torque maximization as a single-objective function (SOF) is defined for the transient improvement of the initial LSPMSM (L0). The optimized design under this scenario is labelled L1_FEM. The starting torque employed in this optimization is determined as follows.

   When examining the dynamic locked rotor torque in the steady-state, it was found that the average of the first cycle (0-20 ms) of the torque-time graph is a good estimation of the starting torque (objective function) in the optimization implementation. Hence, the average of the dynamic torque in the first cycle is considered to be the objective function. To ensure synchronization, a constraint is established that requires the steady-state speed to be equal to the synchronous speed.

2. Steady-state improvement: efficiency maximization as a SOF is defined to improve the steady-state performance of the initial LSPMSM (L0). The optimised design under this scenario is labelled L2_FEM. The efficiency employed in this optimization is determined from the efficiency averaged in the last cycle of simulation time (380-400 ms), when the motor should be in steady-state.

3. Simultaneous transient and steady-state performance improvement: using a defined multi-objective function (MOF) optimization, L0 is optimised to maximise the starting torque and

the efficiency, simultaneously. The optimised design in this case is L3_FEM. The cost function determination under this scenario is the weighted sum of the two objectives.

Note that FEM-based optimisation implementation procedure was extensively discussed in Chapter 3.

4.4.2 Optimization Result Discussion
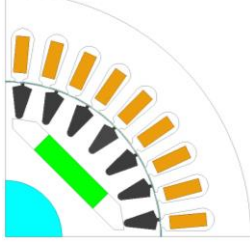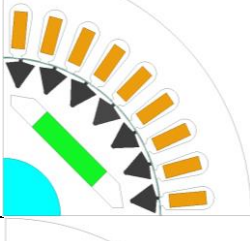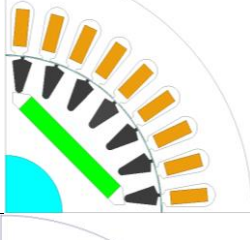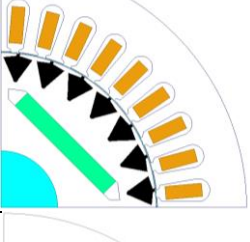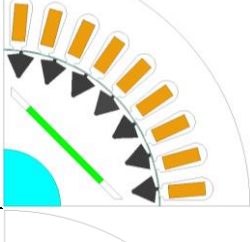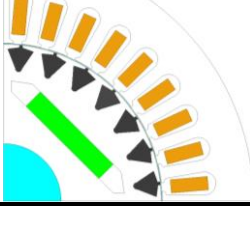
Table **4-3** presents the cross sections of the LSPMSM designs optimized by the proposed method and FEM for the three scenarios and lists the values of the optimized variables. The cross-section variation of the optimized LSPMSM designs is discussed as follows:

➢ Scenario 1: starting torque maximization. The cross-sections of the designs show that the slot depth (h_{r1}) and b_{sr} decreased significantly and b_{r1} increased. The PM volume significantly decreased in the FEM optimization, while in the proposed method, optimisation of the PM size was not considered and only the dimensions of the cage bars were varied.

➢ Scenario 2: steady-state efficiency maximization. In this case, the PM volume increased. In the FEM optimization, the slot widths b_{r1} and b_{sr} sizes increased while the slot height hr1 decreased. In the proposed method optimisation for this scenario, the cage was not considered and only the PM dimensions were varied.

➢ Scenario 3: simultaneous improvement in transient and steady-state performance. In this case, the slot depth (h_{r1}) slightly decreased while the slot width (b_{sr}) and PM volume (width and thickness) increased.

As a result, the cage dimensions are key parameters for the transient improvement and PM dimensions play a key role in the steady-state performance of a LSPMSM.

The locations of the optimized LSPMSM designs in terms of the efficiency and the starting torque are presented in Figure **4-10**. The performance of the proposed method optimisation is compared with FEM optimisation under each scenario. The two optimised designs for the first scenario have nearly identical starting torque values. Likewise, in the efficiency maximization (second scenario), the error between optimised efficiency values of L2_Ana and L2_FEM is only 0.9%. In the third scenario, the errors of efficiency and starting torque values for L3_Ana and L3_FEM are 2% and 3.5%, respectively. Thus, the LSPMSM optimised by the proposed method has comparable performance to the FEM optimised LSPMSM in all scenarios. Both L3_Ana and L3_FEM present optimum designs with better performance in the transient and the steady-state compared with L0.

Table 4-3. Variables and cross-sections of the optimized designs for the IM and LSPMSM.

Motor Type	Cross Sections	Optimised Variables (mm)				
		h_{s1}	b_{r1}	b_{sr}	W	Th
L0		9.00	6.50	2.50	28.00	7.20
L1_Ana		7.02	9.71	1.61	28.00	7.20
L2_Ana		9.00	6.50	2.50	42.00	6.00
L3_Ana		7.02	9.71	1.61	42.00	6.00
L1_FEM		6.4	9.00	1.56	34.7	2.00
L2_FEM		7.68	4.00	2.4	38.10	5.12
L3_FEM		6.10	8.54	2.11	34.00	6.70
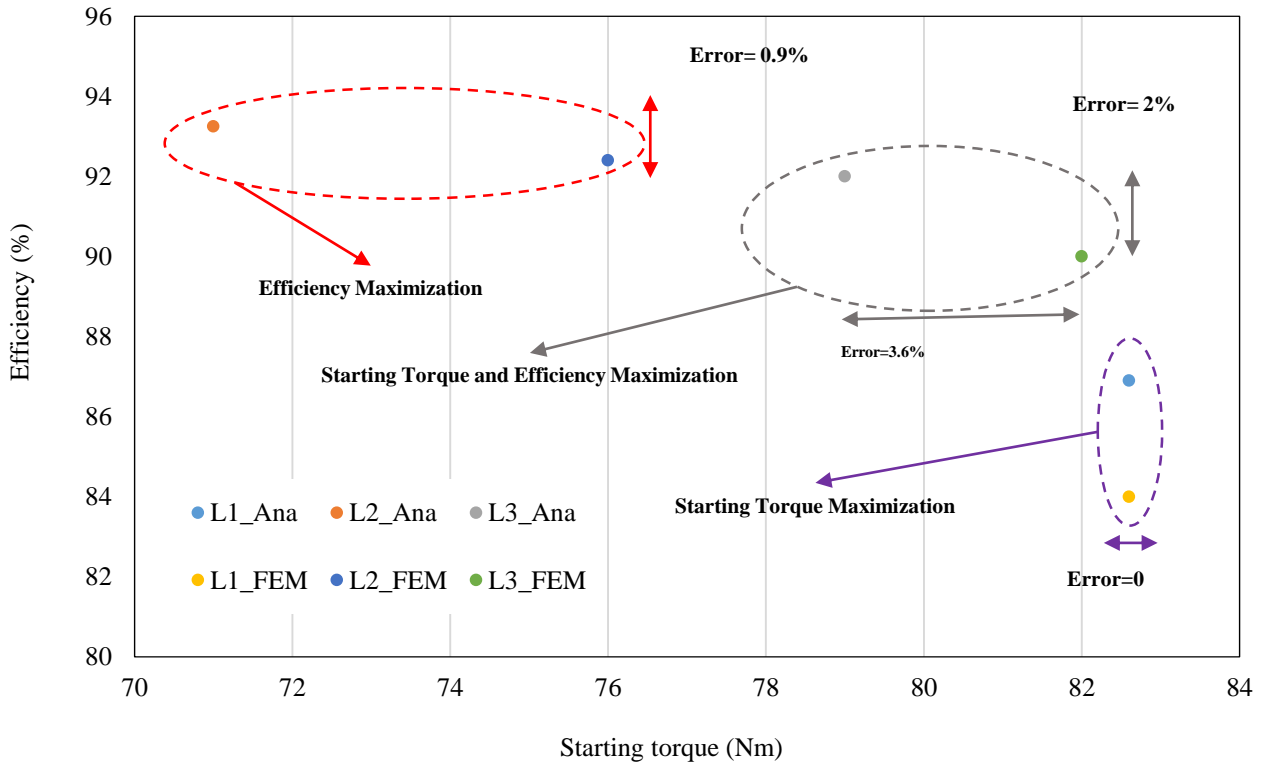
Figure 4-10. Location of the optimized LSPMSM designs by both the proposed method and FEM in efficiency and starting torque plane.
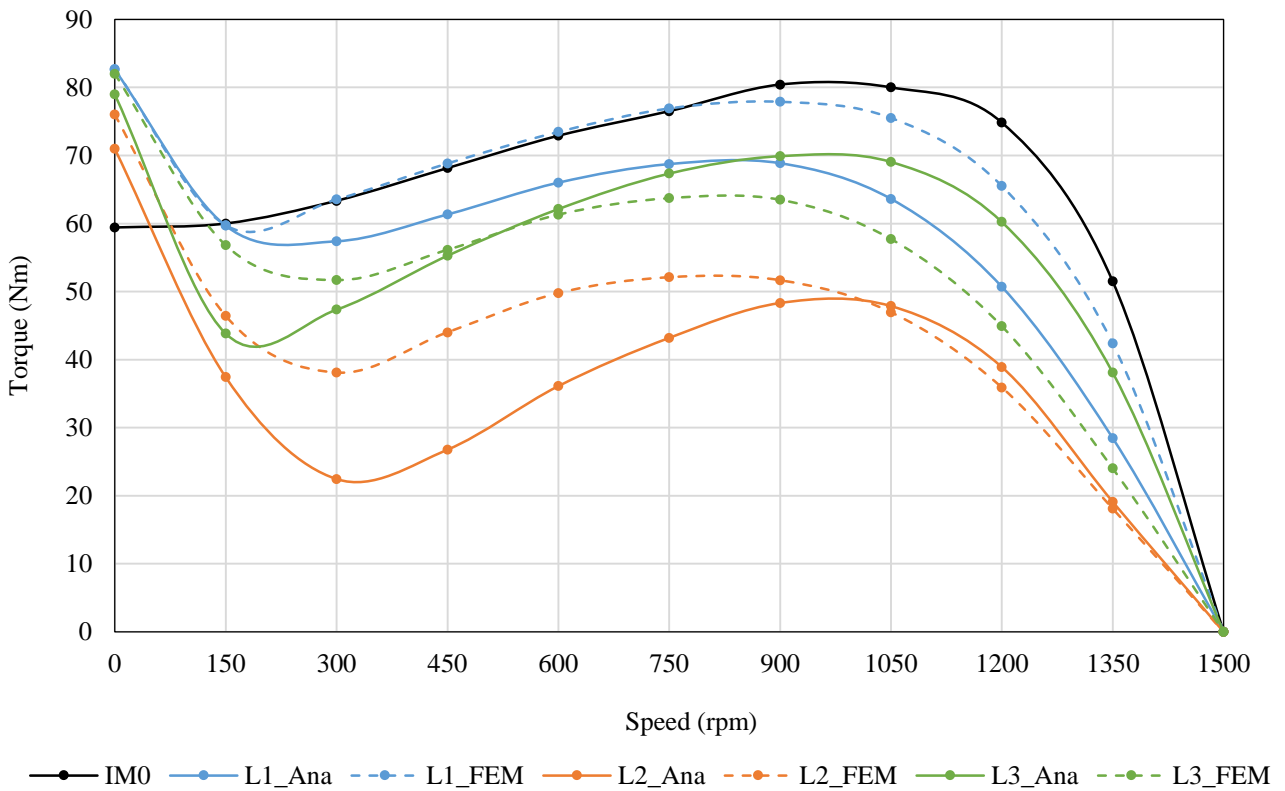
Figure 4-11. Net torque-speed comparison of the LSPMSMs optimised by both the proposed method and FEM.
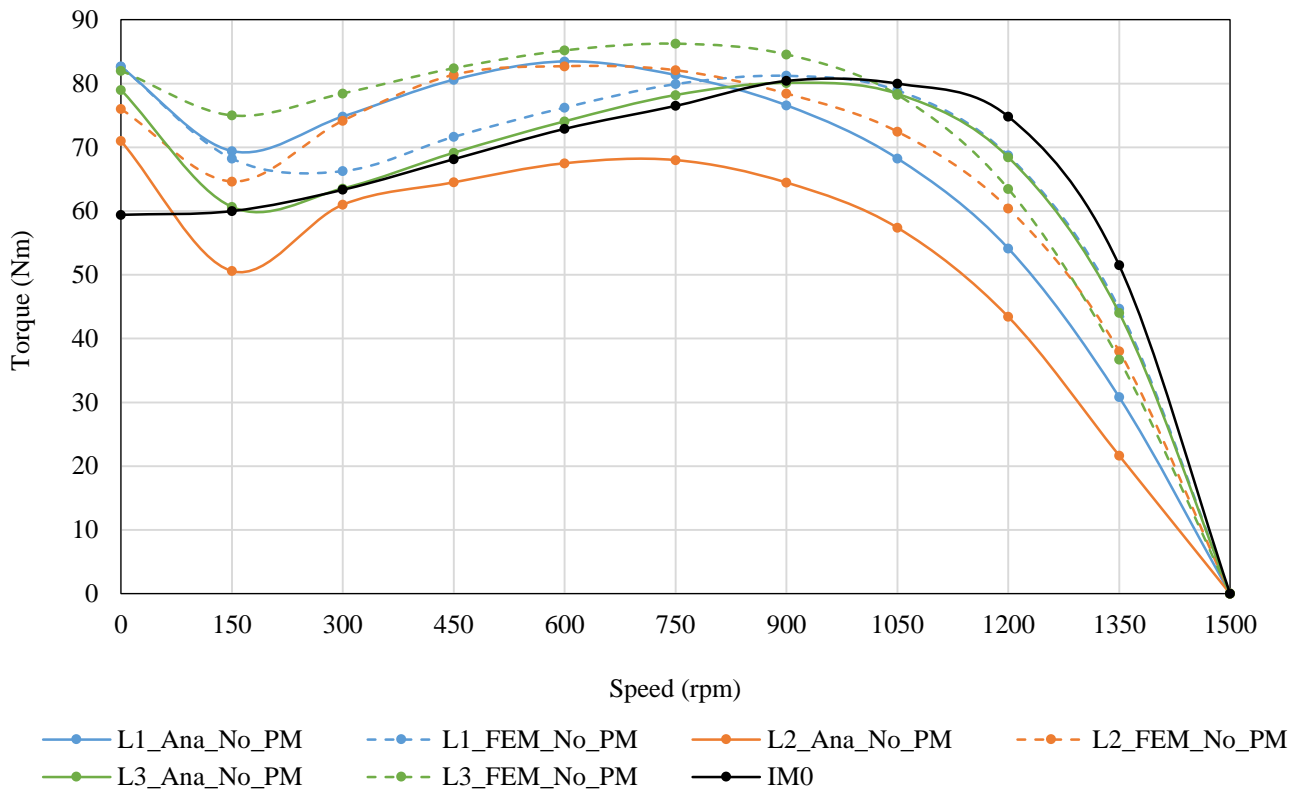
Figure 4-12. Induction torque-speed comparison of the LSPMSMs optimised by both the proposed method and FEM.
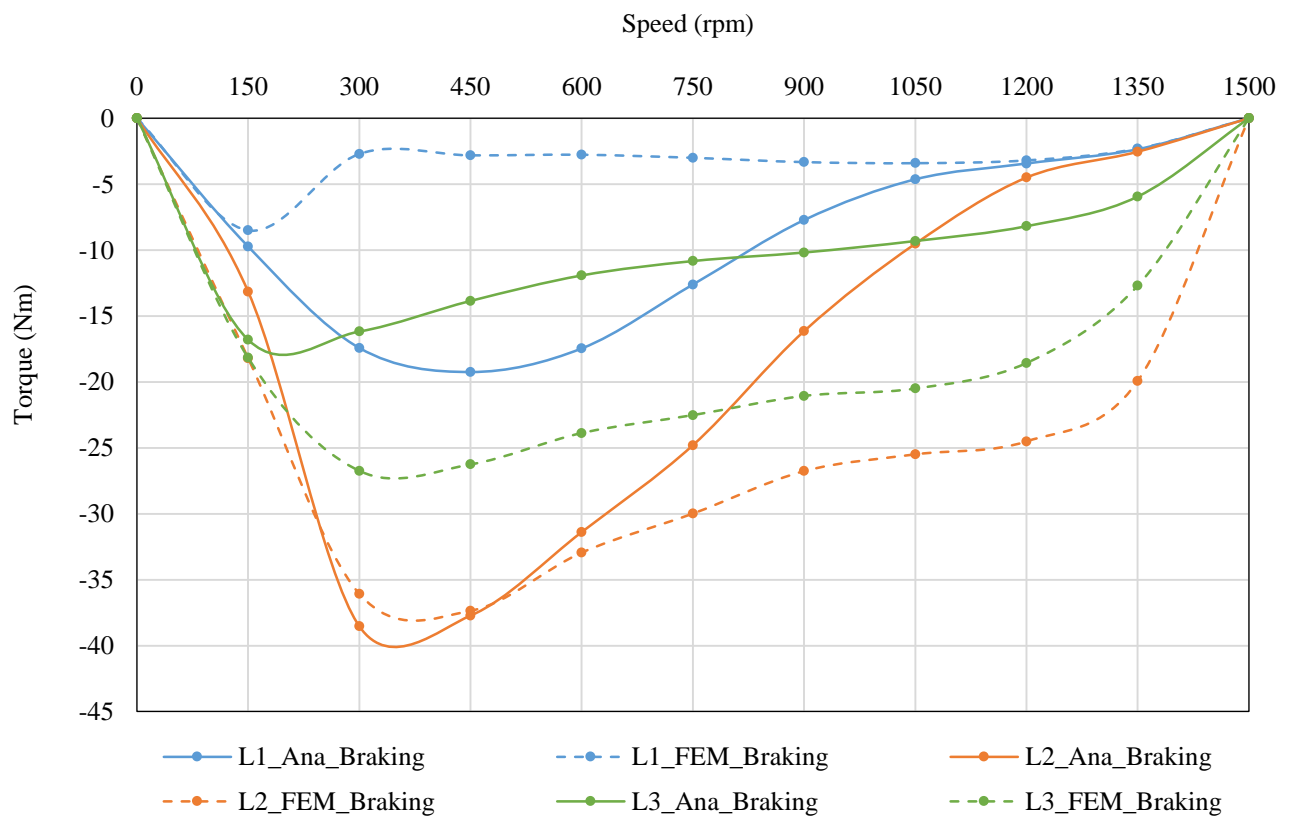
Figure 4-13. Braking torque-speed comparison of the LSPMSMs optimised by both the proposed method and FEM.
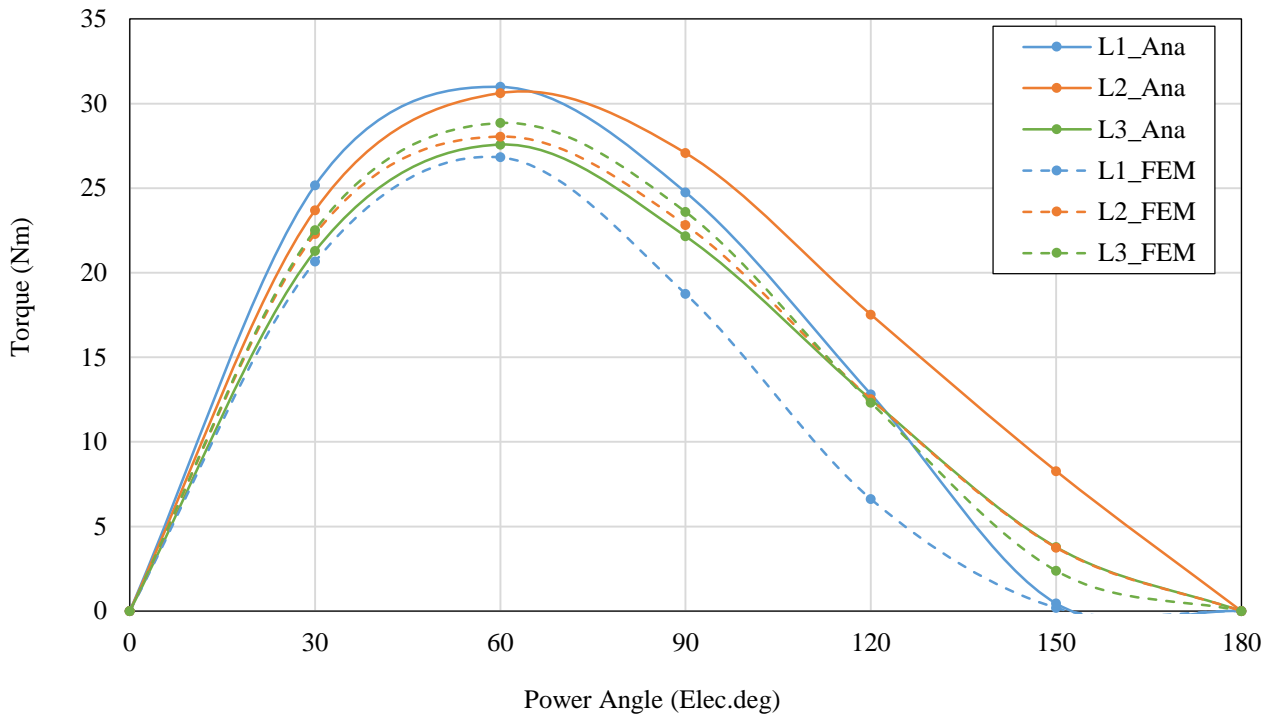
Figure 4-14. Synchronous torque comparison of the LSPMSMs optimised by both the proposed method and FEM versus power angle.
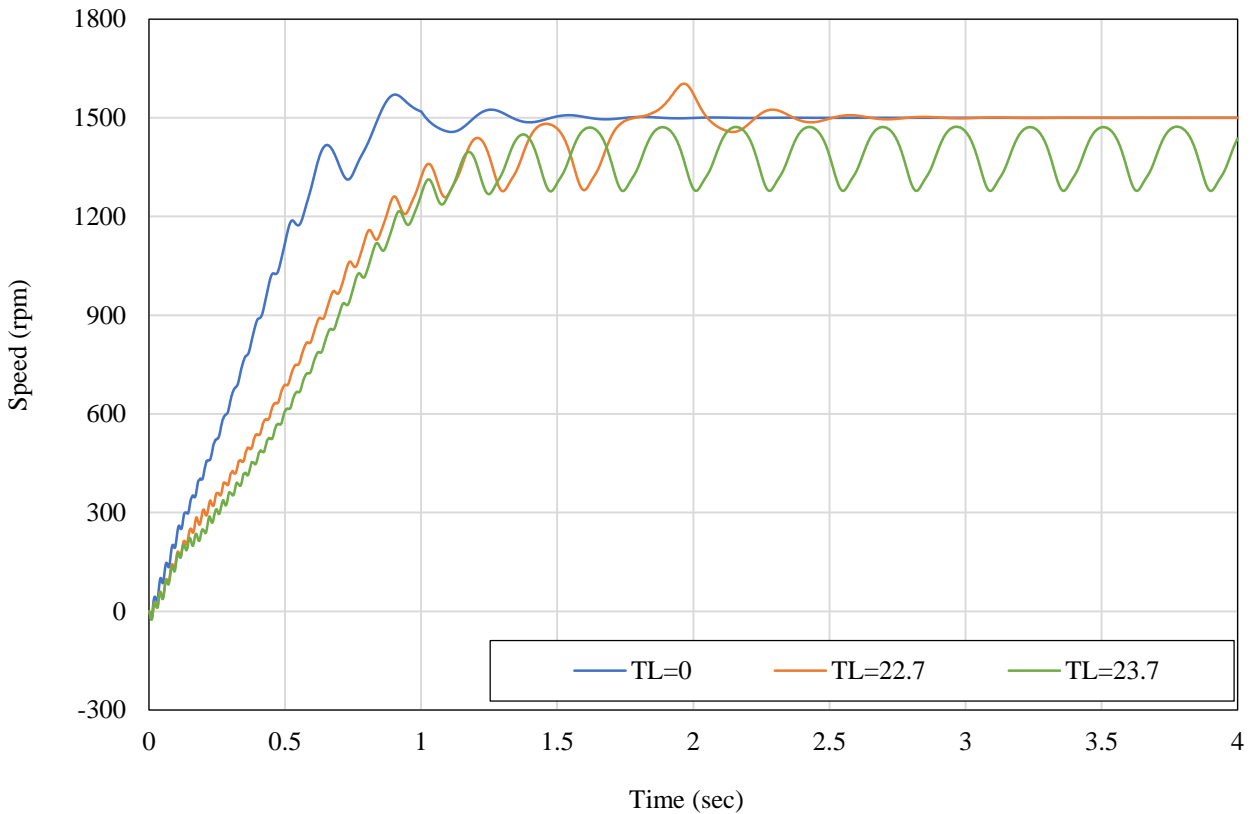
Figure 4-15. Speed-time response of the L3_FEM in an inertia ratio of 14 and three different load torques 0, 22.7 Nm and 23.& Nm.
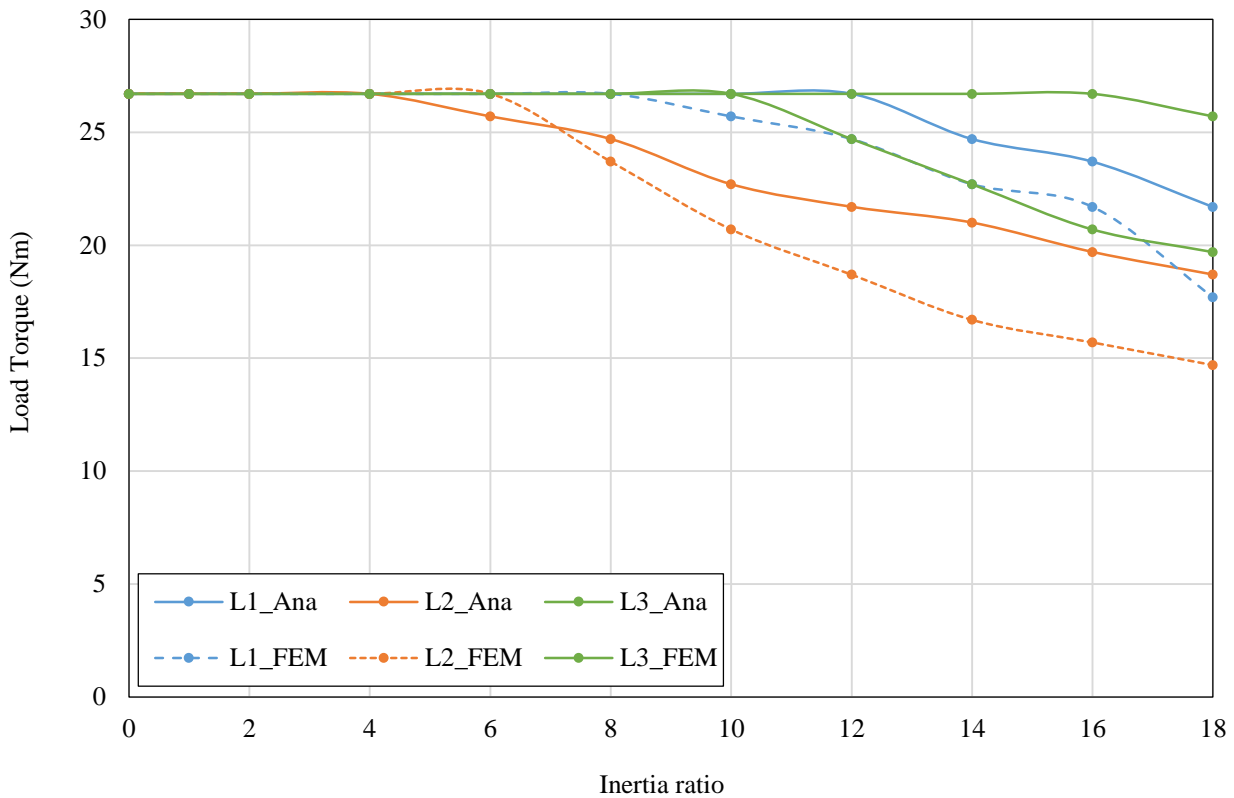
Figure 4-16. Boundaries of successful synchronisation in the plane of load torque versus inertia ratio for the optimised LSPMSMs.

The synchronisation capability of the optimised LSPMSM designs is compared in Figure **4-11** to Figure 4-16. Figure **4-11** to Figure 4-13 show the torque component curves (net torque, induction torque and braking torque) of the optimised LSPMSMs versus speed. To ignore the effect of the PM in Figure 4-12 the remanence of the PM is set to 0. L1_Ana and L1_FEM are less affected by the braking torque because of the smaller amount of PM, while L2_Ana and L2_FEM have greater PM volume and hence a higher braking torque. Accordingly, the optimised designs under the first scenario have improved starting capability compared to those under the second scenario. Figure 4-14 shows the synchronous torque of the optimised LSPMSMs as a function of the power angle. To extract these curves, the motors are excited with a current source and the peak current values used in the excitation are calculated based on the measured rated current of the LSPMSMs.

Figure 4-15 illustrates the speed-time response of L3_FEM with an inertia 14 times the rotor inertia and under different load torques (T_L) to identify the successful synchronisation boundary of the design in this condition. It indicates that L3_FEM has successful synchronisation for load torques less than 21.7 Nm. This test has been done for all the optimised LSPMSMs for different inertia ratios and load torques to detect the successful synchronisation boundaries of these designs. Figure 4-16 shows the boundary of the successful starting and synchronisation of each optimised LSPMSM for different inertia ratios and load torques. The LSPMSM optimised by the proposed method has the best

synchronisation capability and can start successfully under load torque of 25.7 Nm and a load inertia 18 times the rotor inertia.

Table **4-4** presents a comparison between the performance of the proposed optimization method and FEM-based optimization. It is seen that the developed analytical optimization method can present an optimum design comparable with the one optimized by FEM in a significantly shorter time.

Table 4-4. Optimization performance comparison of the developed method and FEM in each scenario.

| Motor Type | Optimum values of objectives | | Error (%) | Optimisation time |
	Starting torque (Nm)	Efficiency (%)		
L1_Ana	82.60	Not included	0.4	4sec
L1_FEM	82.20			6hrs
L2_Ana	Not included	93.25	0.9	5 sec
L2_FEM		92.40		9hrs
L3_Ana	79	92	3.6	9 sec
L3_FEM	82	90	2	12hrs

The proposed design and optimization methodology were demonstrated with a case study of a 4-kW 4-pole LSPMSM. There was a good agreement between the proposed method and finite-element method in terms of the estimated performance parameters and optimisation. In the following section, another case study, a 1-kW 8-pole LSPMSM, is designed according to the proposed method and its performance parameters verified by the FEA as further verification of the proposed analytical design method.

4.5 Further Verification of the Proposed Design Method for a 1-kW 8-pole Case Study

4.5.1 Brief Details of the Case Study 1-kW 8-Pole

The present study considers a 3-phase, 8-pole IM of 1-kW power rating as a benchmark. Typical values for efficiency and power factor of 1-kW, 400-V, 8-pole, 50-Hz three-phase IMs are 77% and 64%, respectively [129].

The initial 1-kW 8-pole LSPMSM is designed based on the proposed design method. Characteristics of the initial LSPMSM design (L0) extracted from the proposed design technique are presented in Table **4-5**. The stator and rotor magnetic materials have been chosen as non-oriented steel (M19-24G). The permanent magnet used in designing the IPM and LSPMSM is NdFe35, the properties of which were presented in Table **3-2**. Note that the effect of the temperature rise is considered in the design process and the material properties are updated for a 55°C temperature rise. Accordingly, it is assumed that there is an approximately 8% reduction in the PM remanence for a 55 °C temperature rise.

Table 4-5. 1-kW 8-pole IM design characteristics.

Component	Value
Stator outer diameter	160 (mm)
Stator inner diameter	110 (mm)
Number of slots of the stator	36
Rotor outer diameter	109.1 (mm)
Rotor inner diameter	30 (mm)
Number of slots of the rotor	24
Fill factor	55 %
Stack length	150 (mm)
Line voltage	400 V Star
Frequency	50 Hz
Number of poles	8
Rated torque	12.5 Nm
Inertia including rotor and load	$0.012 \text{ kg} \cdot \text{m}^2$
Rated slip	0.04
Mass of stator core	7267 kg/m^3
Mass of rotor core	7267 kg/m^3
Mass of PM	7400 kg/m^3
Mass of copper (winding)	8933 kg/m^3
Mass of aluminum (cage)	2700 kg/m^3
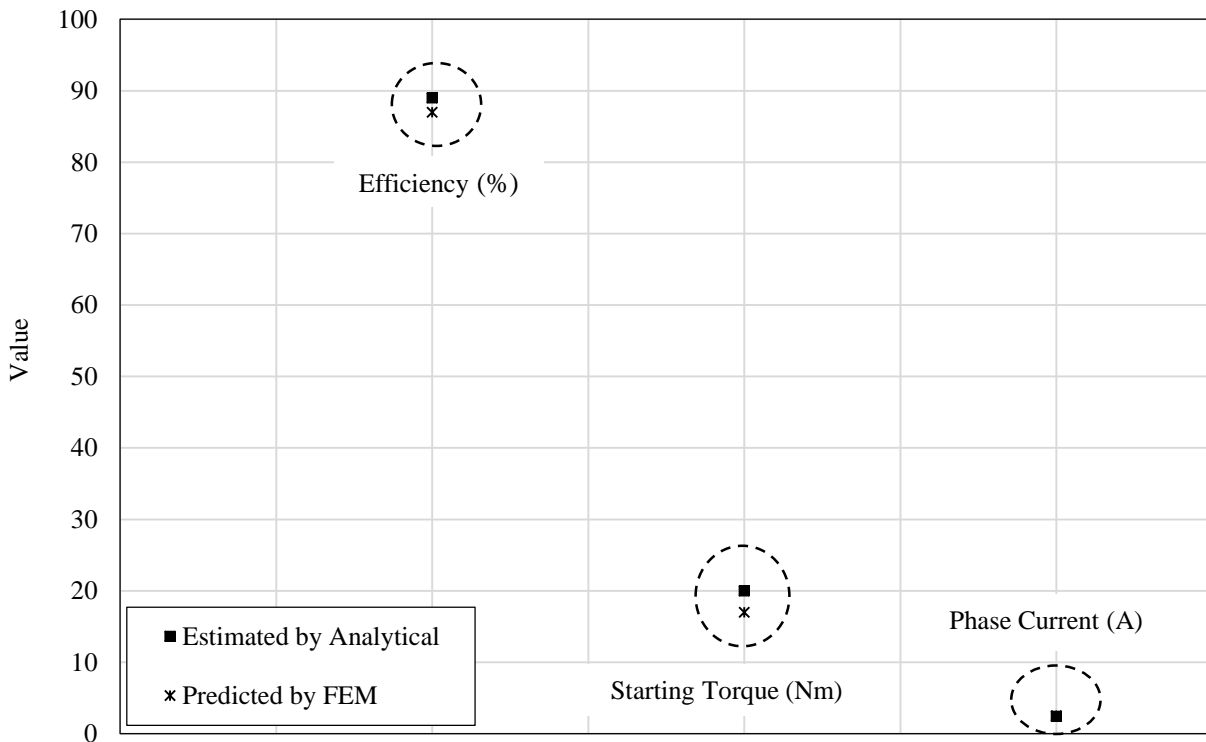
Figure 4-17. Comparison of efficiency, starting torque and phase current values estimated by the proposed method and predicted by FEA for the initial design of the 1-kW 8-pole LSPMSM.

Figure 4-17 compares the performance of the proposed method with FEM in terms of predicting the performance parameters of L0. The starting torque of L0 is estimated using the combination of the starting torque of IM0 and braking torque of IPM0. Also, the efficiency of L0 is calculated from IPM0 considering the cage loss of IM0. It shows the LSPMSM performance predicted by the proposed

95

method is close to that predicted by FEM. This verifies the performance of the proposed analytical design and analysis method. The electromagnetic performance of the designed IM and LSPMSM are extensively analyzed by FEM in the following section.

4.5.2   Electromagnetic (FEA) Performance Analysis

4.5.2.1 Magnetic Analysis

The studies and simulation results are based on operation at a constant rated torque (13 Nm). The performance of the initial LSPMSM and IM in the steady-state and on start-up are analyzed under different loading conditions using FEM. Both motors are simulated over 480 ms with a time step of 0.2 ms using the finite element method. Figure 4-18a and Figure 4-18b illustrate the flux lines and flux density distributions of IM0 and L0. Figure 4-18b shows the maximum flux density value is approximately 1.7~1.9 T. It indicates both motors operate under full constant load safely with the LSPMSM having a slightly lower peak flux density than the IM.

4.5.2.2 Transient Analysis

The transient performance of IM0 and L0 under full-load conditions is studied in this section. The speed-time responses of both motors are compared in Figure 4-19a. Although IM0 has smoother start-up than L0, the speed of L0 reaches synchronous speed. All LSPMSM designs can reach synchronous speed under full load, but not for high load inertia. Figure 4-19b compares the torque-time response of both motors under full load. The overshoot in the torque response curve of the LSPMSM is higher than that of the IM during the start-up.

a.   Flux line distribution

b.   Flux density distribution
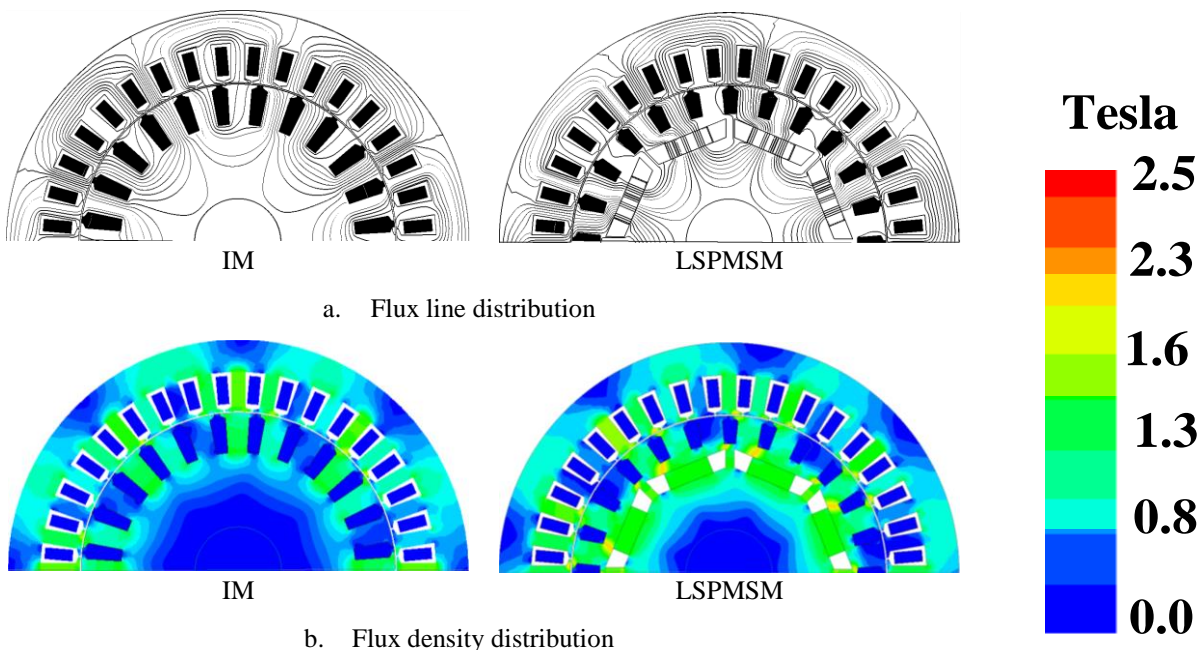
Figure 4-18. Magnetic analysis of IM0 and L0, (a) Flux line and (b) Flux density distribution.
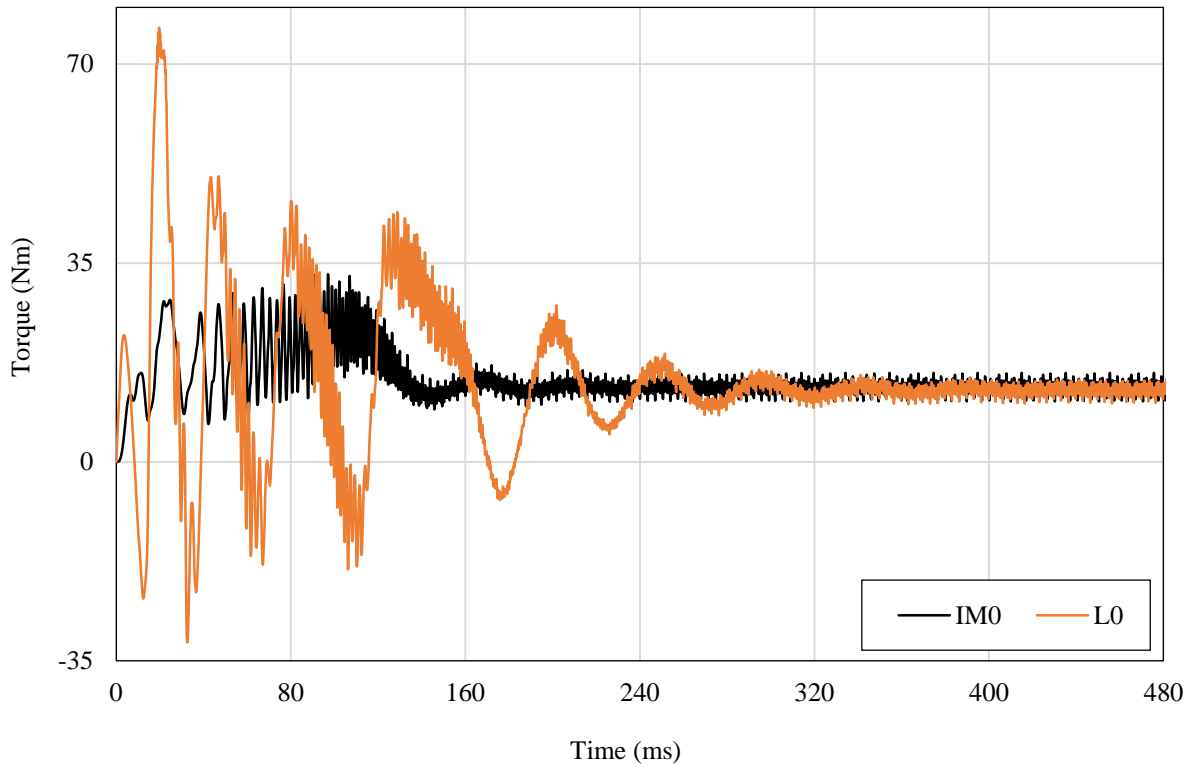
a. Torque-time responses
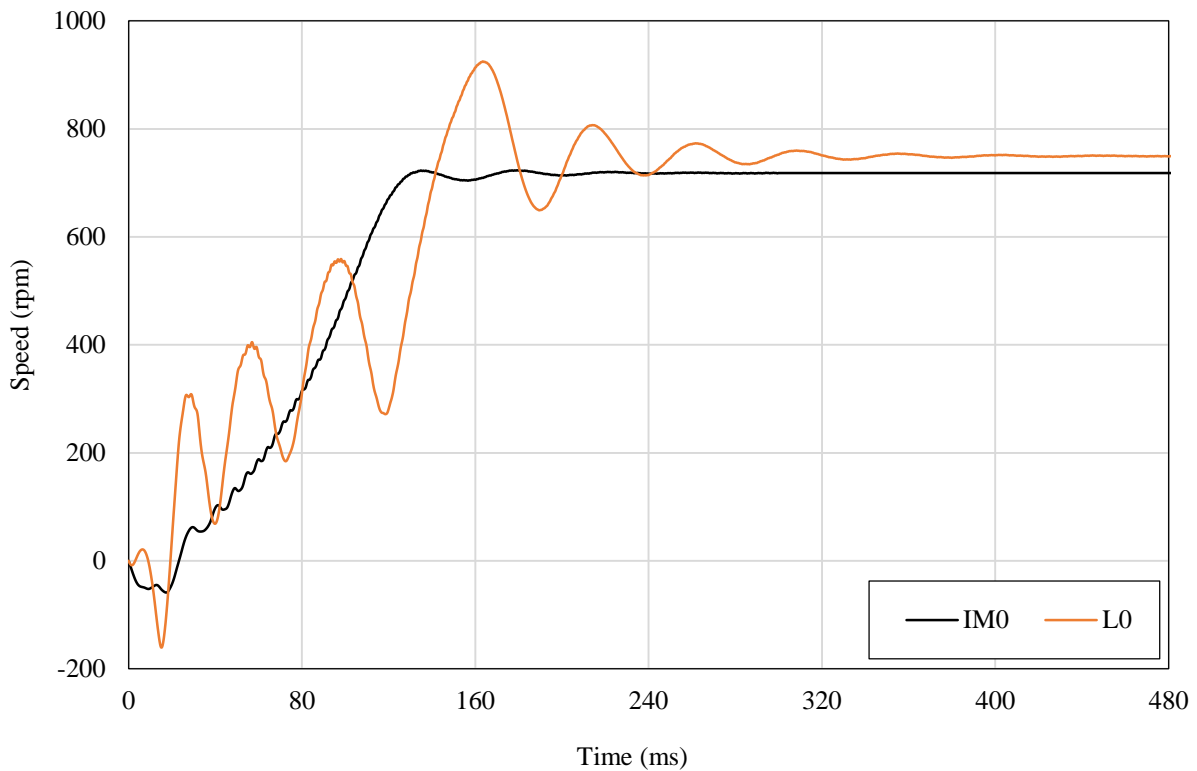
b. Speed-time responses

Figure 4-19. Transient performance comparison of the 1-kW 8-pole IM and LSPMSM under full load.

4.5.2.3 Steady-State Analysis

In this section, the steady-state analysis of IM0 and L0 under full-load conditions is analyzed. Figure 4-20 compares the motor performance parameters under full-load conditions. L0 has better

performance, particularly in the steady state, than IM0. Efficiency improved by around 8% due to the replacement of the rotor of the IM with the hybrid rotor of the LSPMSM. Figure 4-21 shows the loss contributions of the two studied motors (excluding mechanical loss). The loss by L0 is 100 W less than the loss by IM at full-load operation. A significant contributor to this was the rotor cage loss decreasing significantly in the LSPMSM compared with the IM. The rotor cage loss is roughly 20% of the IM0 total loss while for LSPMSM it is 5% of the L0 total loss due to harmonic components of the induced current at synchronous speed. The phase current has dropped because of the significant reduction in magnetization current due to the presence of the PM. Therefore, the stator copper loss in L0 is reduced by 30% in comparison with IM0, which resulted in improvement in the efficiency and power factor. The steady-state performance of IM0 and L0 as a function of the output power are presented in Figure 4-22. Figure 4-22a to Figure 4-22c illustrate the variation of the iron loss and the copper loss and cage loss of IM0 and L0 with output power. Figure 4-22d shows the efficiency variations of IM0 and L0 versus output power. The efficiency of IM0 and L0 is compared with the values of the IE efficiency standards (IE3, IE4) for 1-kW 8-pole motors. The IM efficiency is in the IE3 standard class while the L0 efficiency is in the IE4 category.
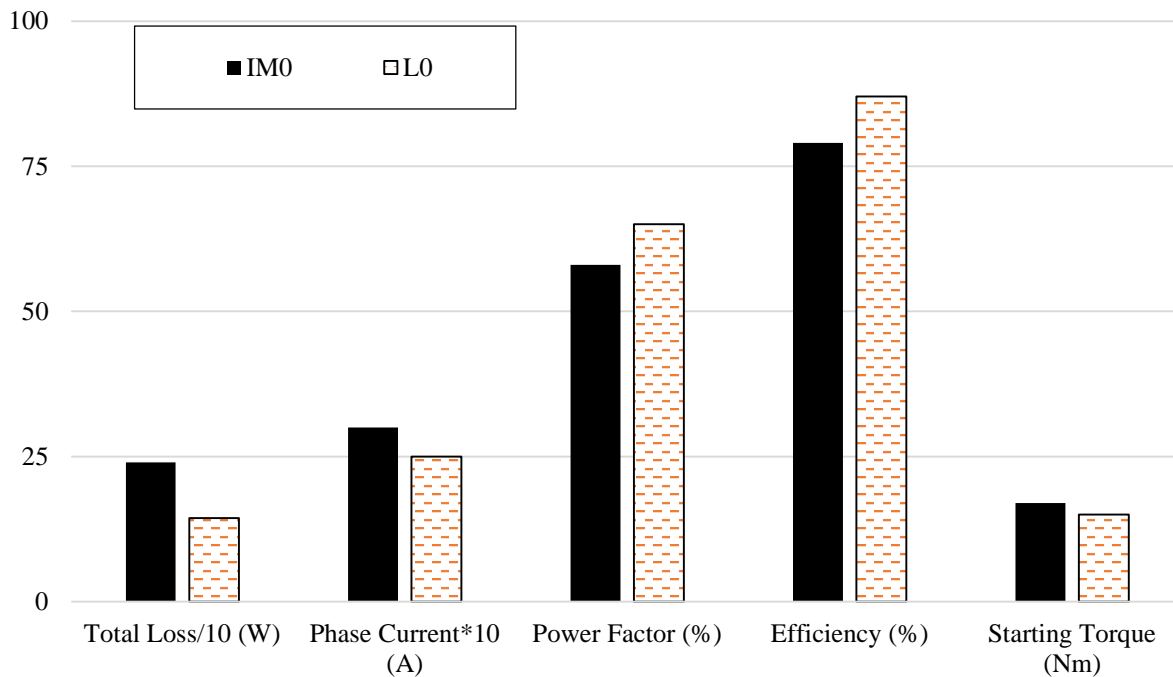
Figure 4-20. FEA predicted performance parameters of the 1-kW 8-pole IM and LSPMSM under full load.
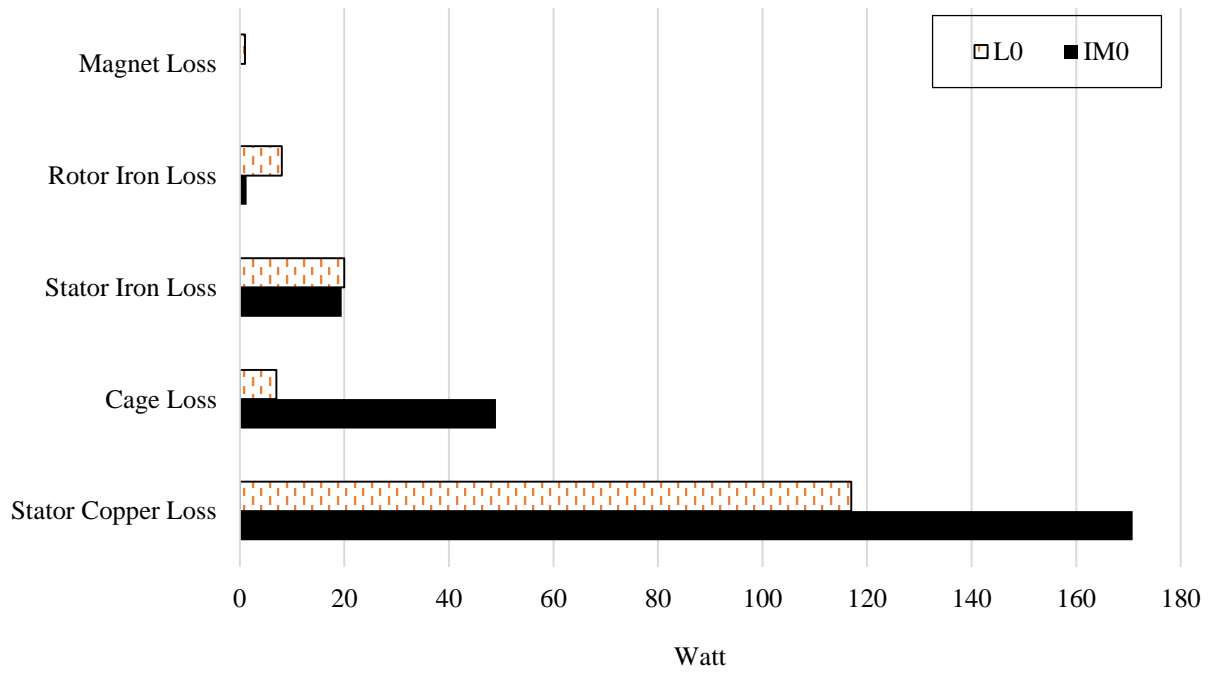
Figure 4-21. Loss component comparison of the 1-kW 8-pole IM and LSPMSM under full load.
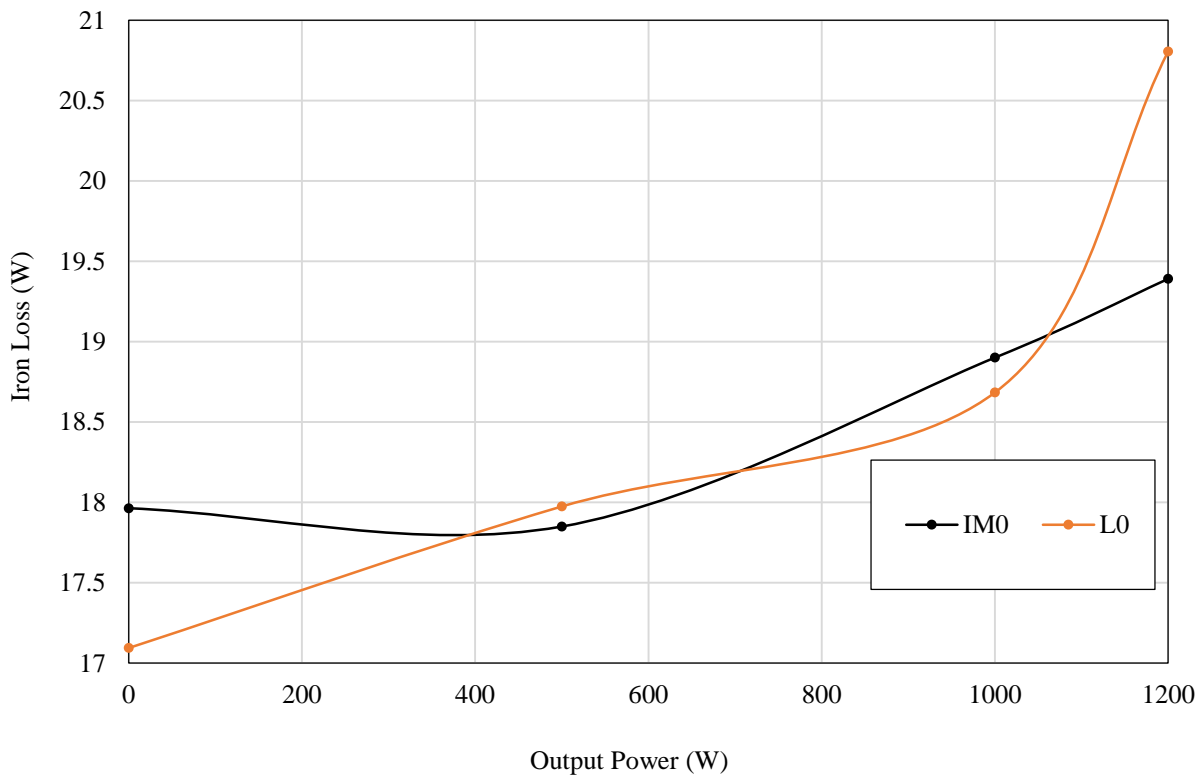
Output Power (W)

a. Iron loss comparison versus output power
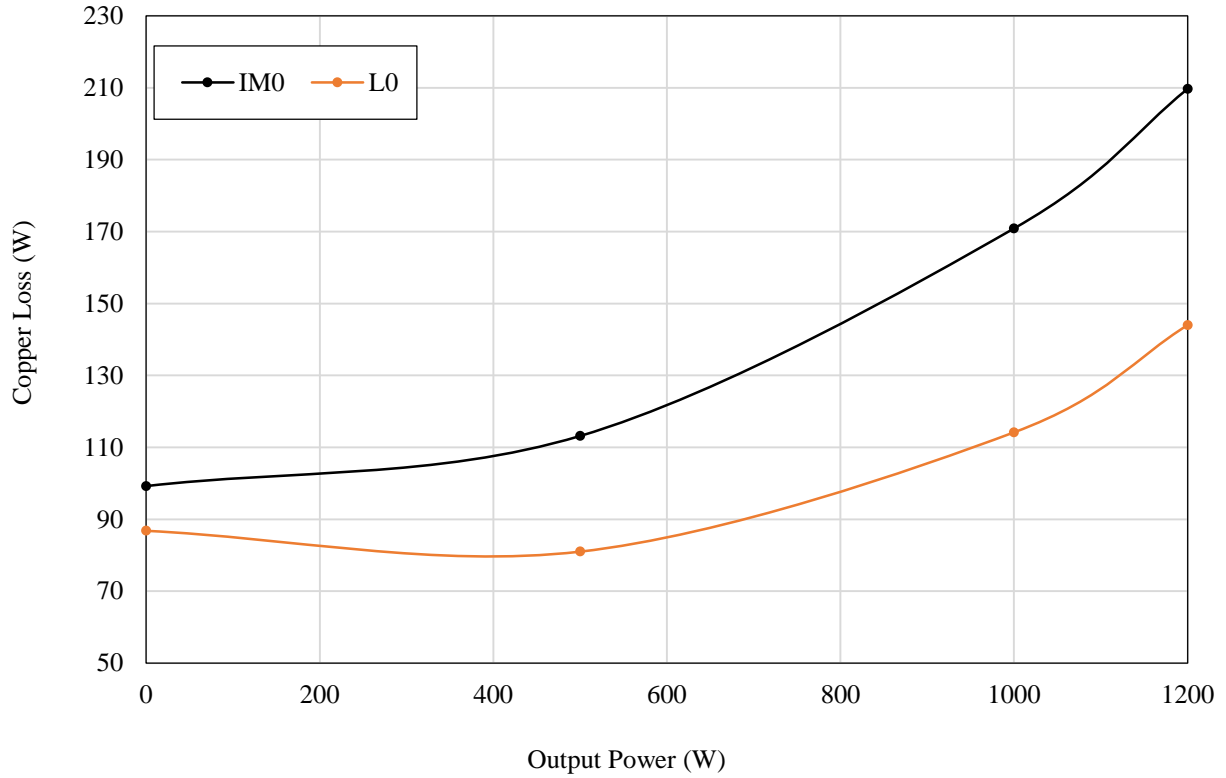
b. Stator copper loss comparison versus output power
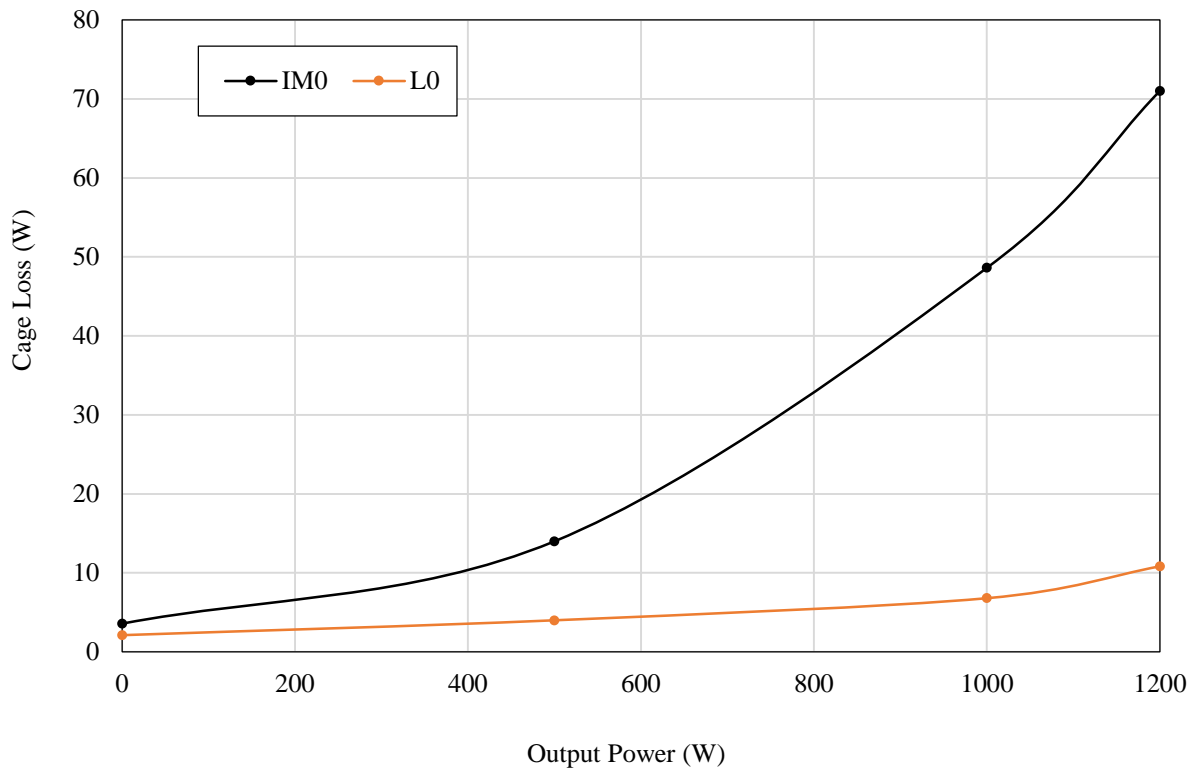
c. Cage loss comparison versus output power
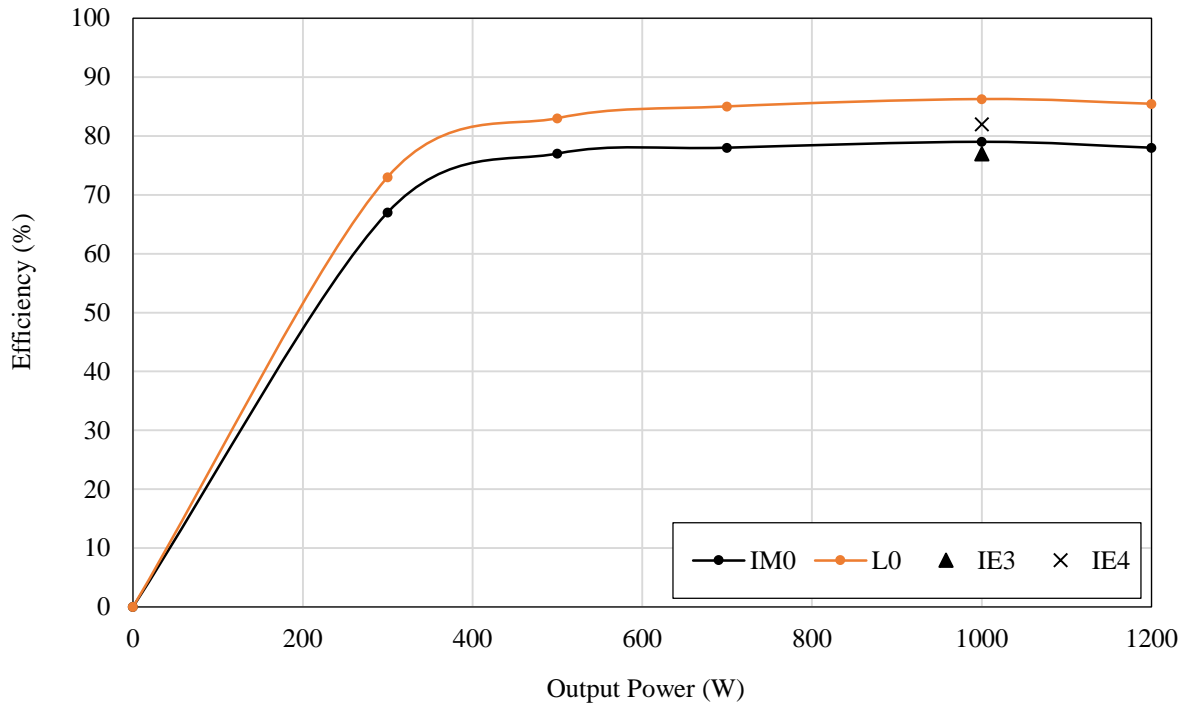
d.   Efficiency comparison versus output power

Figure 4-22. Steady-state performance parameters variations of the 1-kW 8-pole IM and LSPMSM versus output power.

4.5.3   Optimisation challenge and discussion

The initial IM (IM0) and initial LSPMSM (L0) are individually optimised under a third optimization scenario (MOF optimisation) to improve the transient and the steady-state performance. The optimisation is implemented based on FEA and a genetic algorithm (GA) called by Maxwell. Then, an LSPMSM is designed based on the optimised IM as its benchmark to present a comparative study between the performance of the LSPMSM designs.

The transient and the steady-state behaviour of the non-optimised and optimised designs are compared in this section. The cross sections reveal that the optimization for improving the steady-state performance increased the slot depth of the rotor and reduced the slot width. Figure 4-23 shows the cross section of the optimised initial IM (IM1), optimised initial LSPMSM (L1) and the LSPMSM designed based on IM1 (L2). Figure 4-24 compares the performance parameters of the optimised designs with the initial designs. The L1 design has better steady-state performance than the other designs. The results indicate that L2 (designed from IM1) has similar performance to the initial LSPMSM (L0) though the optimised IM (IM1) has better performance than IM0. All designs are compared on axes of efficiency and starting torque in Figure 4-25. It is observed that L1 has higher efficiency and power factor than the other designs. The transient performance of L1 and L2 are compared with L0 in Figure 4-26. The starting torque of L1 improved in comparison with L0, while starting torque of L2 is less than L0. The results reveal that the optimised LSPMSM design (L1) has better performance than the other designs, L0 and L2. The L2 design has performance similar to L0.

Therefore, it is now clear (in this case study) that a LSPMSM designed based on an optimised IM does not necessarily have performance better than the initial LSPMSM designed based on a non-optimised IM with the same magnet volume. Therefore, to get an optimum design of LSPMSM designed based on an IM, an individual optimization study of the LSPMSM should be implemented.

IM1

L1

L2
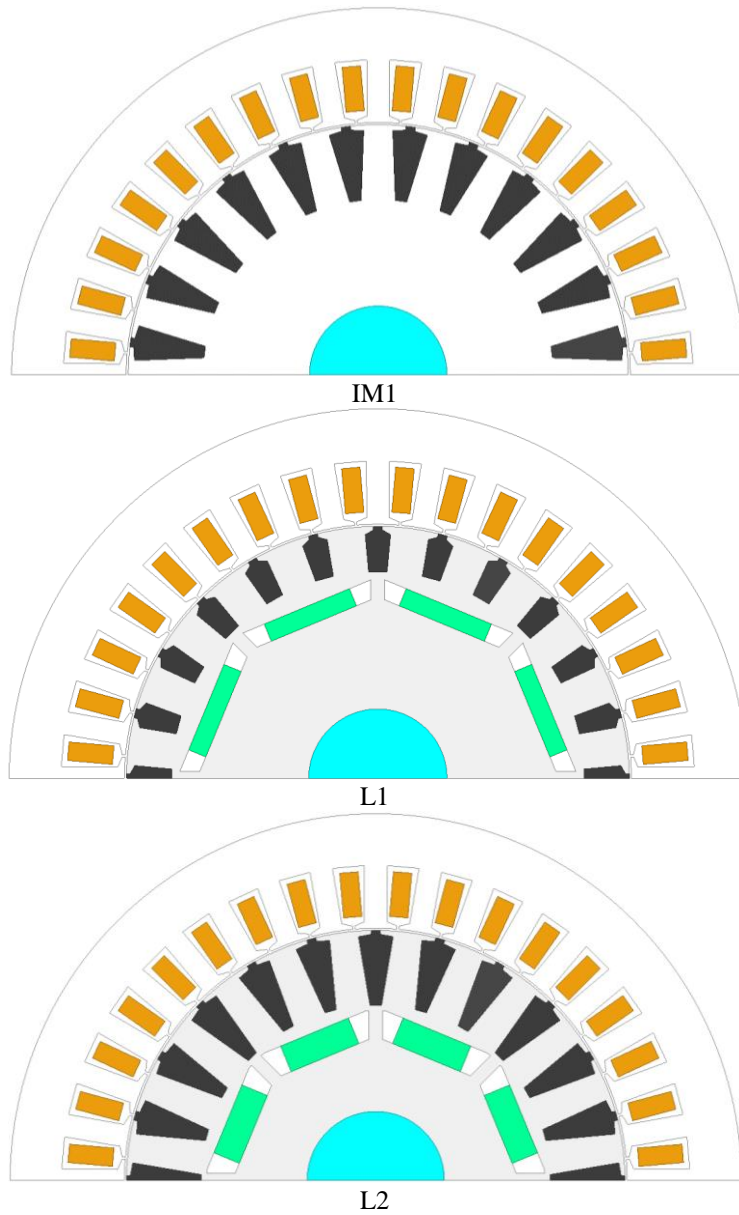
Figure 4-23. The optimised cross-sections of optimised designs.
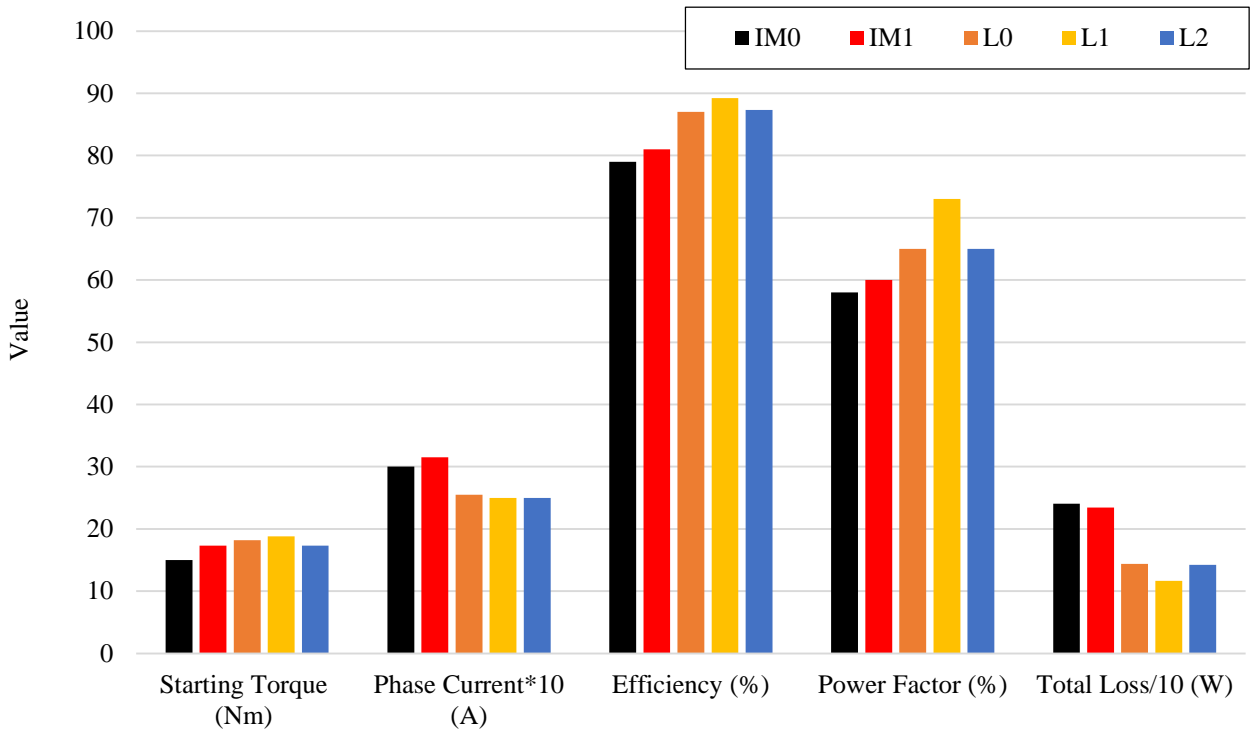
Figure 4-24. Performance parameters of the IM0, IM1, L0, L1 and L2.
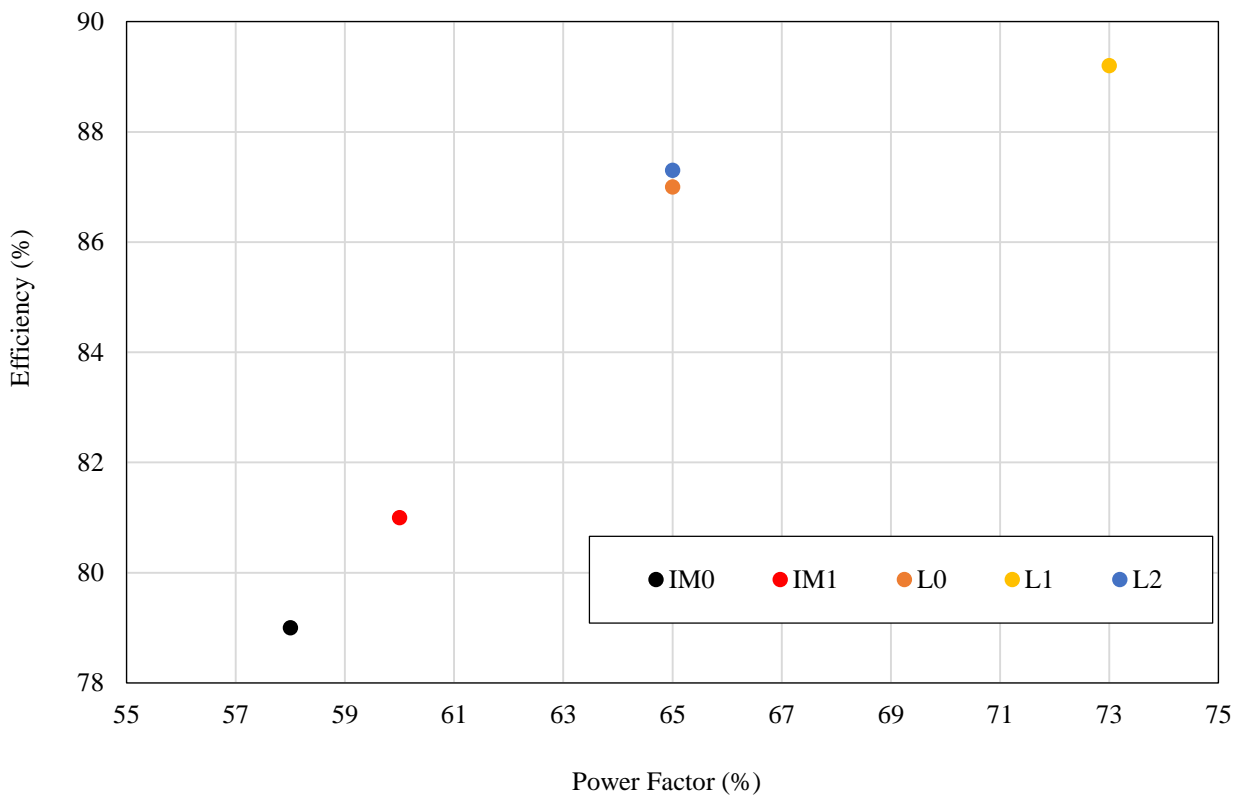
Figure 4-25. Location of the optimised designs in the efficiency and the power factor plane.

a. Speed-time

b. Torque-time
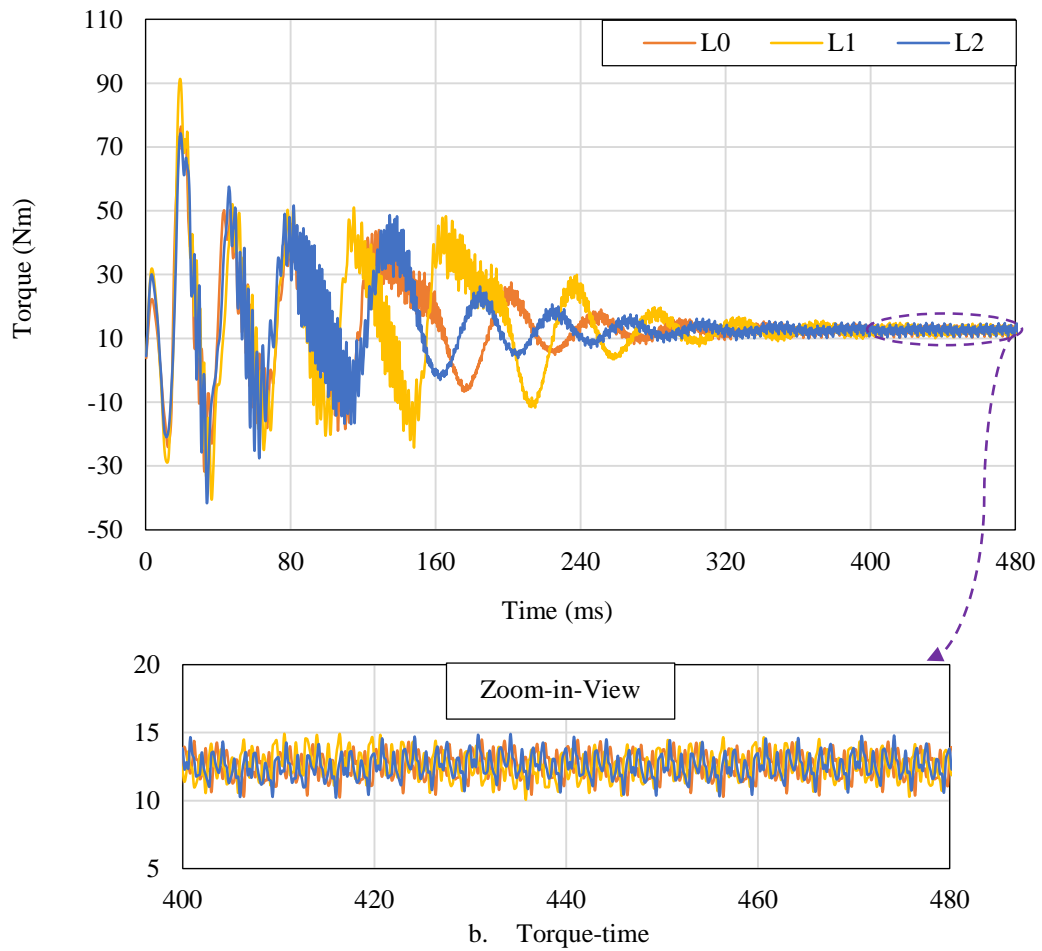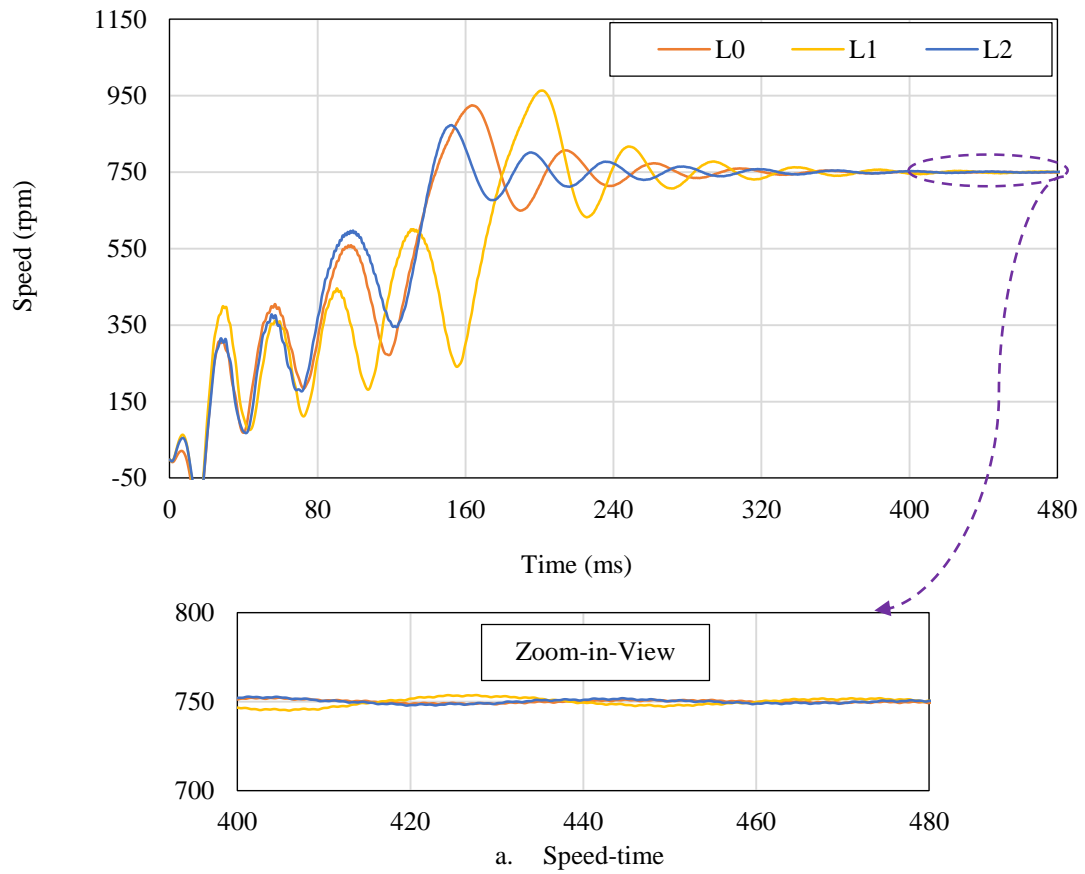
Figure 4-26. Transient performance comparison between the L0 and the L1 and L2 designs.

4.6 Conclusion

This chapter presented an optimum LSPMSM design based on the combination of an IM and an IPM designed by sizing equations. By combining the IM and IPM rotors, the hybrid rotor of the initial LSPMSM (L0) was designed. Two case studies designed a 4-kW 4-pole and a 1-kW 8-pole LSPMSM based on the proposed analytical design method, and the performance parameters of the case studies were estimated by the proposed analytical method. To verify the performance of the proposed design and analysis method, the case studies were analyzed by FEM using Ansys/Maxwell. The performance parameters of the designs estimated by the proposed analytical method and predicted by FEM were compared. Good agreement was observed between the calculated and FEM performance.

An optimisation strategy was proposed based on the proposed analytical design method to provide an optimum LSPMSM. The same optimization study was implemented by FEM to verify the performance of the proposed optimization method. The results of the proposed analytical optimisation method were compared with the FEM optimization. Three scenarios were considered:

- Maximizing starting torque (transient performance improvement).
- Maximizing efficiency (steady-state performance improvement).
- Maximizing starting torque and efficiency, simultaneously (overall performance improvement).

The results of the study showed that the proposed method produced an optimum LSPMSM design with a comparable performance to that by FEM in a much shorter time.

In addition, in this chapter (for the case study 1-kW 8-pole), it was realized that there is no guarantee that performance of an LSPMSM designed based on an optimized IM is superior than an LSPMSM designed based on a non-optimised IM.

In this chapter, an electromagnetic design, analysis, and optimisation platform for the LSPMSM was presented and its performance was verified by FEM. A complete electromagnetic and thermal design and analysis platform is an aim of this thesis. The electromagnetic portion of the platform was successfully presented in this chapter. The next chapter (Chapter 5) proposes a novel analytical thermal design and analysis platform for LSPMSMs. The accuracy of the proposed thermal model is verified by 3D FEM-based thermal analysis and experimental tests.

5. **CHAPTER 5**

5. **DEVELOPING AN ANALYTICAL THERMAL MODEL FOR LINE-START PERMANENT MAGNET SYNCHRONOUS MOTORS**

This chapter studies the thermal analysis of a LSPMSM's main parts. It proposes an analytical thermal method for the analysis of LSPMSMs as a reliable substitute for FEM-based thermal analysis, which is a time-consuming process. The performance of the proposed analytical thermal model is presented in this chapter for two case studies: a 3-kW, three-phase, 4-pole LSPMSM and the commercial IM benchmark. The availability of thermal experimental data of the commercial IM allows us to validate the proposed thermal methodology. This chapter is divided in eight sections. Section 5.1 presents a summary of the chapter. Section 5.2 reviews previous literature in this field (introduction). Design methodology of the machines under study, with a focus on thermal aspects, is presented in Section 5.3. Electromagnetic analysis of machines under study are discussed in Section 5.4. Thermal analysis and results are studied in Sections 5.5 and 5.6, respectively. As further verification of the proposed thermal model, another case study, a 4-kW 4-pole motor (IM and LSPMSM), is studied in Section 5.7. The conclusion for this chapter is presented in the Section 5.8.

5.1 Summary

This chapter proposes a thermal model of a line-start permanent magnet synchronous motor (LSPMSM) based on lumped-parameters to predict/estimate the temperature rise of the main components. The LSPMSM is designed based on a 3-kW commercial induction motor as the benchmark. Hence, the lumped-parameter thermal model of the LSPMSM is proposed based on slight modifications of the lumped-parameter thermal model of the IM by considering the PM in the rotor. In addition, 3D FEM-based thermal models of the case studies are presented to compare the performance of both methods. To validate the performance of the proposed lumped-parameter and FEM thermal models, the commercial IM is tested at three voltage levels (under, rated and over voltage) and two frequencies (50 and 60 Hz) under full-load condition with the temperature of the main components being recorded. There is good agreement between experimental results and the proposed lumped-thermal model and FEM-based model. Overall temperature rise of the LSPMSM is significantly lower than the baseline IM, while the designed LSPMSM uses the same frame size of the commercial IM. So, there is an opportunity to increase the output power of the LSPMSM while the overall temperature rise does not exceed that of the baseline IM.

The advantage of the proposed thermal model is that it can be used to predict the temperature rise of the LSPMSM based on the losses as a heat source. Accordingly, the model is used to study the

temperature rise in the LSPMSM for maximum achievable output power, and it removes the need for computationally intensive FEM analysis and experimental tests to conduct a thermal analysis of the LSPMSM. Electromagnetic and thermal results show that the 3-kW LSPMSM has higher efficiency than the baseline IM and it operates in the steady-state with a temperature approximately half that of the benchmark IM. Also, the LSPMSM can provide 4.2-kW with higher efficiency than the 3-kW IM in the same frame size. The overall temperature of the LSPMSM providing 4.2-kW is roughly the same as the 3-kW IM.

5.2 Introduction

Temperature rise is an important characteristic in the design of electrical machines as the material properties change based on temperature variations [152]. The operating temperature of motors increase due to losses. Thermal studies of induction motors [153]-[167] and permanent magnet motors have been presented extensively in the literature [168]-[171].

Estimation of rotor temperature has been studied using several methods: parameter temperature estimation method [153]-[154], intelligent and LSM algorithms [155]-[156], different solution (H-H and H-g method) [157]-[158], hybrid methods [159]-[160], and IM thermal model (lumped-thermal network) [161]-[162]. Thermal behaviour of total enclosed fan cooled (TEFC) induction motors of different sizes (4-kW to 55-kW) was studied in [163]-[165]. Temperature variations of the motor components as a function of frequency was investigated to give a guideline on the motor de-rating calculation when inverter driven [153]. Calculation of the convection heat transfer and flow were predicted using formulations based on empirical dimensionless analysis in [165]. The natural convection thermal resistance between the frame and ambient of motors as a function of output power was predicted. The air velocity in the air gap of the motors was determined based on the shaft speed. Electromagnetic and thermal analysis/design of an induction motor for electric vehicle applications was studied, and it was concluded that temperature difference between the rotor core and the rotor bar is small, and the highest temperature appears in the stator windings [166]. The temperature dependence of losses in permanent magnet motors and induction motors was studied in [167] and it was concluded that joule losses in winding and cage bars increase with temperature rise while iron losses decrease.

Steady-state thermal analysis of a 60-kW permanent magnet (PM) motor was studied in [168]. The temperature behaviour of the PM motor was analyzed based on the lumped parameter thermal model and compared with the experimental results. A 3-kW 150,000 rpm PM motor was designed and its temperature distribution analyzed in [169]. A comparative thermal analysis of an interior permanent magnet synchronous motor with integral-slot distributed-winding (ISDW) and fractional-slot concentrated-winding (FSCW) was conducted for electric vehicle application. It was concluded that

ISDW has better thermal behaviour in comparison with FSCW, particularly at high speed [170]. Temperature prediction of a surface-mounted PM motor was analyzed using a lumped-parameter thermal network (LPTN) in [171] seeking to develop a fast and accurate analysis approach.

All thermal analysis research mentioned above were studied on induction motors and permanent magnet motors. There has been very limited study on thermal analysis for LSPMSMs. Recently published work on the thermal analysis of a LSPMSM was presented in [172]. Losses and permanent magnet dependency on operating temperature were studied, and losses variations versus temperature were predicted using a proposed analytical method. The iron loss and the PM remanence dependency on the temperature rise were considered. It was interesting to see that the calculated efficiency increased with temperature rise, which is unusual. Although the iron loss decreases as temperature rises, the increase in stator and rotor conductive losses normally offset this.

There are several thermal analysis studies based on numerical methods in the context of electrical machines [173]-[176]. 3D FEM thermal analysis of a water-cooled 30-kW induction motor for a hybrid electric vehicle was studied in [173] to determine the temperature rise at the full-load condition. A water-cooling system in a double-stator switched reluctance motor was analyzed using a FEM-based thermal method [174]. Thermal analysis for the LSPMSMs using numerical methods has not been extensively studied in the literature. In addition, it is desirable to understand better the electromagnetic and thermal performance improvement that a line-start PM motor designed based on a commercial induction motor (as a benchmark) can provide. The thermal analysis in the above mentioned works based on FEM methods are computationally intensive in comparison with an analytical method (like lumped-parameter method).

5.3 Design Methodologies

Four-pole commercial super premium (IE4) LSPMSMs are designed to be replaceable with conventional, commercial IMs (IE2). The presence of permanent magnets in the LSPMSMs produces a higher power density than the squirrel cage IMs, although PMs increase the material cost of the motor.

In the design process of an electric machine, the operating temperature is an important factor. The temperature rise of different components of 4-pole induction motors (4-kW-55-kW) was presented in [163]-[165]. Accordingly, in the design process of the 4-kW IM and the LSPMSM, the temperature rise was assumed to be 85°C. This affects the properties of the permanent magnets and the stator and rotor winding resistances, calculated as:

$$R = R_{ref} \times (1 + \alpha \times (T - T_{ref})) \tag{5.1}$$

which R_{ref}, T_{ref} and α are the resistance at the reference temperature, reference temperature and temperature coefficient of resistivity of the conductor, respectively [167].

5.3.1 Commercial Induction Motor Design

The present study considers a 4-pole, 3-phase commercial IM as it is widely used in the industrial sector. A 2D model of the commercial IM is developed based on the dimensions of the main components. The stator and rotor magnetic material are non-oriented steel (W600-50A). Considering iron losses, the thickness of lamination material is chosen to be 0.5 mm and the rotor cage material is aluminium as well as copper for the winding. The same materials are selected in 2D design to obtain more realistic results.

5.3.2 LSPMSM Design

In the design process of the LSPMSM, the rotor bar height is reduced to have a balance between successful start-up and good steady-state performance. Stator and winding for both motors are the same input source: 415V-Y, 50 Hz.

The magnetic properties of the permanent magnet (NdFe35) used in this study were presented in Table **3-2**. The PM remanence (B_r) is reduced when the temperature rises. The range of remanence reduction because of temperature rise was determined to be 0.1%-0.15% per °C [167]-[172]. Accordingly, in this study, it is assumed that there is approximately a 10% reduction in B_r of the PM used in the LSPMSM for an 85°C temperature rise.

5.4 Electromagnetic Results Discussion (FEA)

The electromagnetic analysis of the LSPMSM providing 3-kW and 4.2-kW is compared with a 3-kW IM. This section predicts how the LSPMSM performs in the transient and the steady-state when it provides 4.2-kW in the same frame size as that of the 3-kW IM. The steady-state performance, particularly loss variation analysis of the motor components in this section, will give a useful insight into predicting thermal behaviour of the components.

5.4.1 Magnetic Performance

The IM and LSPMSM are compared in terms of generated flux density in the air gap as shown in Figure **5-1**. The flux density distribution at stator teeth and yoke is different while saturation is observed at some points in the rotor of the LSPMSM around the PM edges.

5.4.2 Starting Performance

In this section the starting capability of the IM and the LSPMSM are compared and the aim is to show the performance of the LSPMSM in comparison with the 3-kW IM.

The start-up transients of the motors are presented in Figure **5-2**. As expected, the start-up of the IM is smoother than the LSPMSM due to the lack of PM braking torque, and the IM reaches the steady-state faster than the LSPMSM. The LSPMSM can successfully start the 4.2-kW load, but has a longer start-up time.
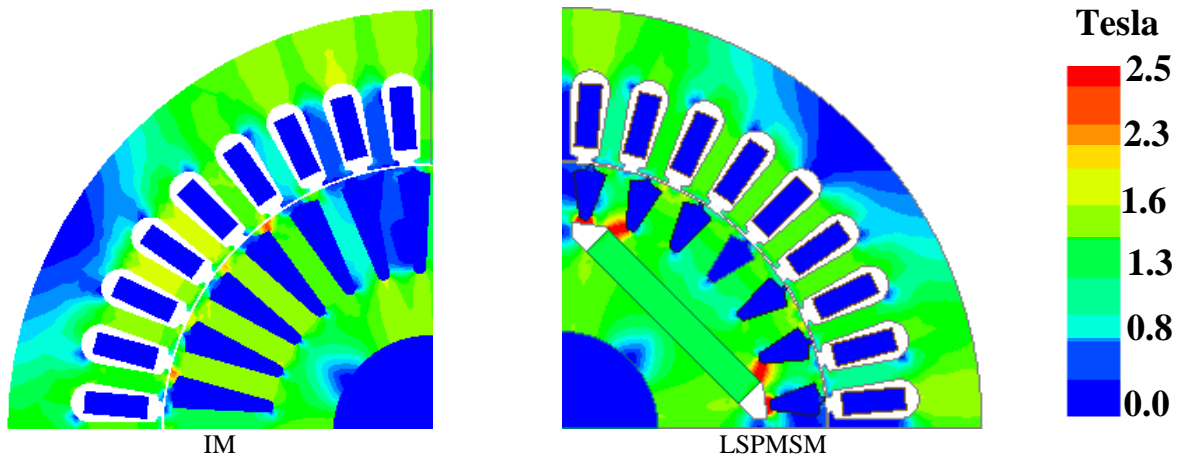
Figure 5-1. Flux density distribution of the 3-kW IM and LSPMSM.
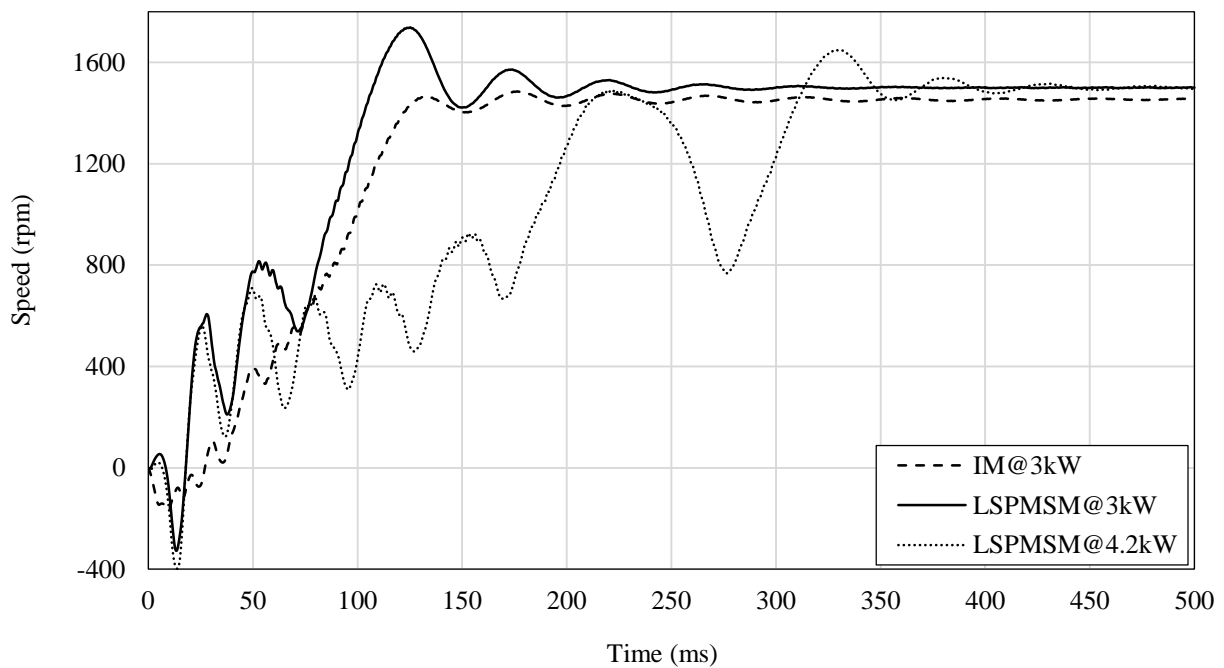
Figure 5-2. Speed-time response of the 3-kW IM and LSPMSM@ 3-kW and 4.2-kW.
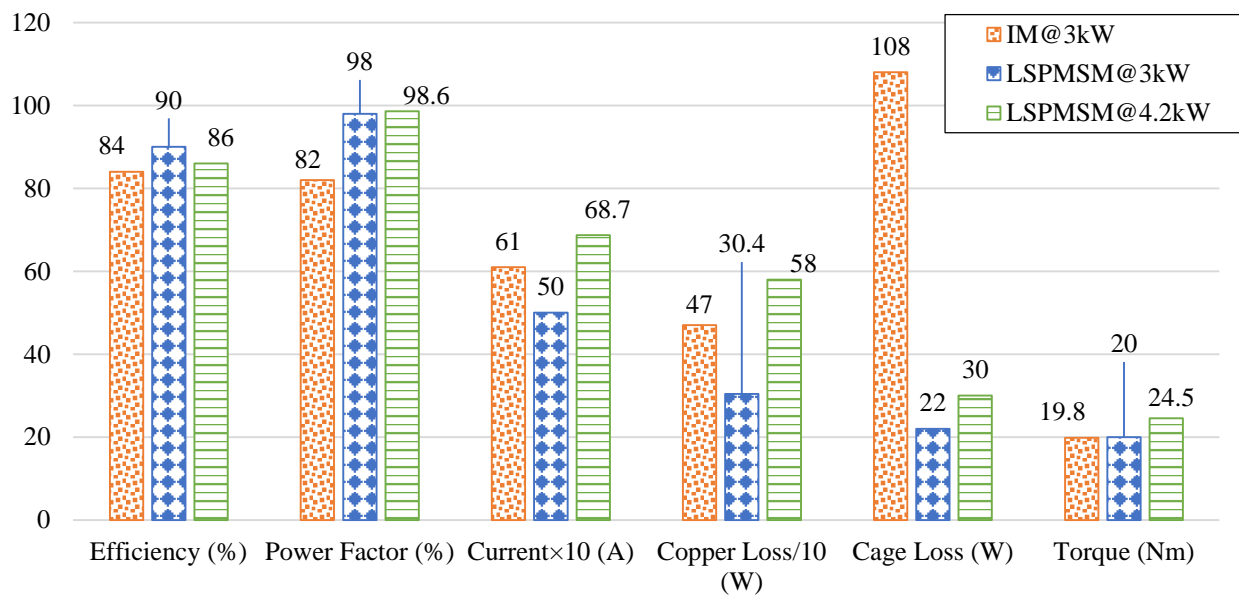
Figure 5-3. Steady-state performance parameters of the 3-kW IM and LSPMSM@ 3-kW and 4.2-kW.

5.4.3 Steady-State Synchronous Performance

The LSPMSM has better steady-state performance than the baseline IM. Figure 5-3 compares the performance parameters of the IM at 3-kW and the LSPMSM at the rated load (3-kW) and at overload (4.2-kW). The efficiency of the IM at 3-kW is 84% while the LSPMSM efficiency at 3-kW is 90% and at 4.2-kW is 86%, still higher than the IM. For the same output power, the stator winding current in the LSPMSM is less than the baseline IM due to the lack of magnetising current. It results in lower copper loss and hence higher efficiency for the LSPMSM. The copper loss of the LSPMSM providing 4.2-kW is higher than the baseline IM and it is expected that the temperature of the end winding of the LSPMSM in this case is higher than the IM.

5.5 Thermal Analysis

The temperature distribution of an electric motor gives valuable information. Means for reducing high temperatures include decreasing losses, changing the effective cooling type, adjusting the fins and frame, proposing a new cooling type, or optimizing the motor. There are two techniques to implement thermal analysis for an electrical machine: 1) the lumped parameter thermal network, and 2) the finite element/volume method such as computational fluid dynamics (CFD) and steady-state thermal analysis [177]. Finite element-based thermal analysis is implemented to analyse the thermal behaviour of the IM and LSPMSM designs in this study. Ansys is employed to perform the steady-state thermal analysis and then the component losses are determined by mapping the electromagnetic FEA to the 3D geometry of the components to identify heat sources. The boundary conditions and type of heat transfers in the case study should be defined carefully.

There are three ways that heat is transferred: conduction, convection, and radiation. Conduction is the primary heat transfer mechanism from the inside of the stator and rotor to their outer surfaces. Heat transfer between the stator and rotor and from the stator and rotor to the frame/ambient occurs through convection. Generally, radiation is not taken into consideration in electric motors as its effect is relatively small [175].

With regards to convection, there are two types:1) natural convection and 2) forced convection. Forced convection is due to the motor's speed and it influences the parts of the motor that are in contact with the air flow (air gap, end winding, end ring, end rotor and stator faces). The air flow can be classified as laminar or turbulent based on the Reynolds number [177]-[179]. The Reynolds and critical Reynolds numbers in the air gap are calculated as follows [178]:

$$Re = 2\pi \times r_{or} \times n_r \times \frac{lg}{60 \times \mu} \tag{5.2}$$

$$Re_{cr} = 41.3 \times \sqrt{r_{or}/lg} \tag{5.3}$$

where r_{or}, n_r, lg and μ are rotor outer radius (m), rotor speed (rpm), air gap length (m) and the kinematic viscosity of the fluid (m/s^2). The calculated Reynolds number for the IM and the LSPMSM at rated speed are 225 and 235, respectively. The critical Reynolds number is calculated at 445, and because the Reynolds numbers are less than the critical Reynolds number, the flow type in the air gap of the motors is determined to be laminar.

In this chapter thermal analysis of the case studies (IM and LSPMSM) is studied by three methods: 1) thermal analysis based on a proposed lumped-parameter; 2) FEM-based thermal analysis; and, 3) experimental tests. Note that, firstly, the thermal analysis of the IM is studied to validate the proposed thermal circuit model and FEM model with the experimental data and then the proposed thermal circuit model and FEM model are used to predict the temperature of the main parts of the LSPMSM. As the LSPMSM was designed based the baseline IM, the proposed thermal circuit model of the IM was modified by adding a PM in the rotor with rotor bar size modification. Ansys was employed to perform the steady-state thermal analysis and then the component losses were determined by electromagnetic FEA mapped to the 3D geometry of the components to identify the heat sources. The thermal modelling (boundary conditions definition) of the motors' components is described in the following sub-sections.

5.5.1 *Proposed Thermal Circuit Model of the IM and LSPMSM Based on Lumped-Parameter Network*

The thermal circuit model of the IM and the permanent magnet synchronous motor are well-known from studies and various thermal circuit models have been proposed in [180]-[183]. The lumped-parameter thermal network model of an IM proposed in [180] is developed in this study. It includes 11 nodes (see Figure 5-4a and Figure 5-4b without node 12). In the proposed thermal circuit model, the convective heat transfers between stator end faces with inner air, and the rotor cage are modelled. It needs minor modifications to tune the thermal circuit model of the LSPMSM by including the PM as node 12 in the rotor core as shown in Figure 5-4a and Figure 5-4b (highlighted in red), and each node is linked with its immediate nodes. The losses are injected into corresponding nodes as heat generation sources (Figure 5-4b).
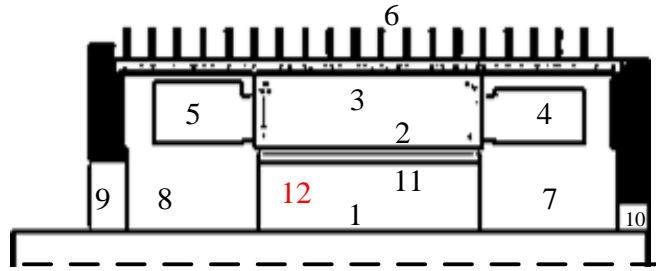
1: Rotor Core
2: Slot Winding
3: Stator Core
4: End Winding (right)
5: End Winding (left)
6: Frame

7: Inner air (right)
8: Inner air (left)
9: End Cap (right)
10: End Cap (left)
11: Cage bar
12: PM

a.   Schematic axial view of an induction motor (without node 12) and LSPMSM.
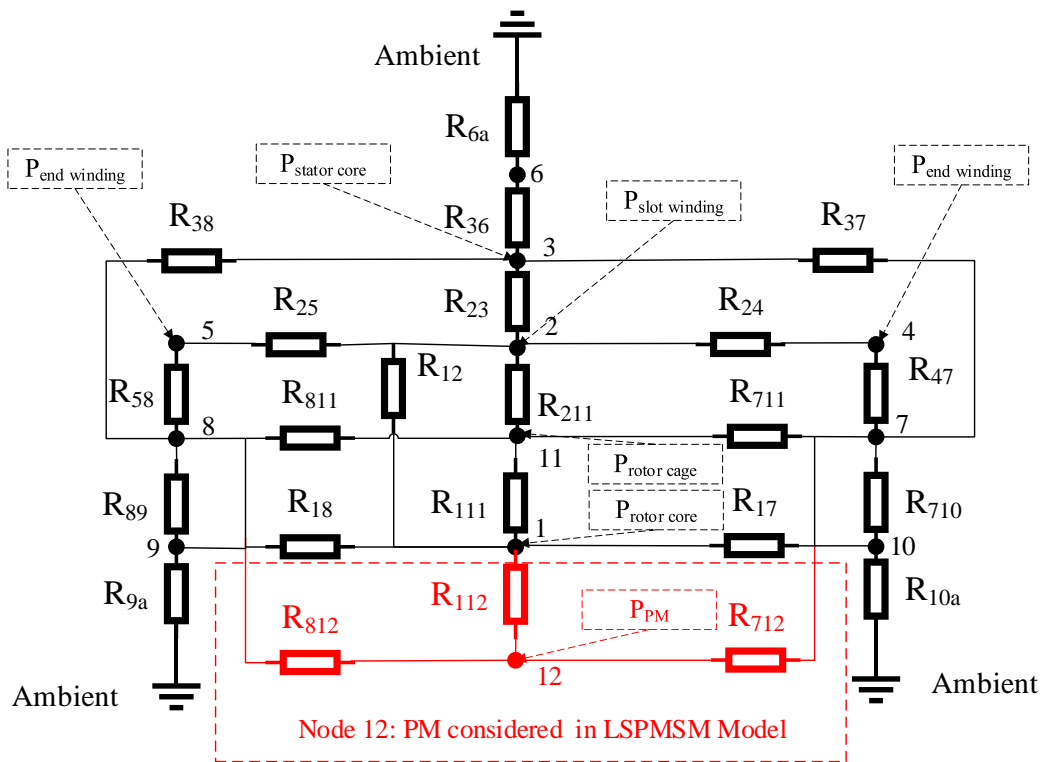
b.   Proposed thermal circuit model based on lumped-parameter method for the IM an LSPMSM.
Thermal model of induction motor.
Figure 5-4. Thermal model of induction motor.

5.5.1.1 Thermal conductance

The steady-state temperature rise of each node of the lumped parameter thermal model is calculated as follows:

$$\Delta T = G^{-1} \times P \tag{5.4}$$

$$G = \begin{bmatrix} \displaystyle\sum_{j=2}^{n} G(1,j) & \cdots & -G(1,n) \\ \vdots & \ddots & \vdots \\ -G(n,1) & \cdots & \displaystyle\sum_{i=1}^{n-1} G(i,n) \end{bmatrix}_{n \times n}$$

(5.5)

where P is the loss vector including the loss at each node, ΔT is the temperature rise vector in each node and n is the number of nodes. G is the thermal conductance matrix where the diagonal elements consist of a summation of the conductances linked to the target node, and $G(i,j)$ is the thermal conductance connecting the ith node to the jth node [182]-[183]. To determine the conductance of each node, we need to calculate the resistance of each node. The procedure of determining thermal resistances of the main components have been studied in the literature [164]-[165], [182]-[185]. The most important thermal resistances are determined as follows:

- Convection Resistances

a) Frame to ambient resistance

Natural convection thermal resistance between the frame and ambient is calculated as follows [164]:

$$R_{fa\_natural} = \frac{\Delta T}{Loss}$$

(5.6)

where ΔT and *Loss* are the temperature rise (°C) of the frame measured experimentally and total dc supply losses (W), respectively.

The calculated resistance is matched with frame to ambient resistance variation versus motor rating (frame size) presented in [164]-[165]. Therefore, the natural heat transfer coefficient of the air is determined according the well-known formula of the convection thermal resistance as follows:

$$R_{th\_c} = \frac{1}{h \times A}$$

(5.7)

where h and A are the convection heat transfer coefficient (W/m^2.°C) and surface area (m^2), respectively.

Forced convection includes different methods such as liquid coolant [163]-[165], and total enclosed fan-cooled (TEFC) with open fin channels. The case study is provided with TEFC and the forced convection thermal resistance between frame and ambient are calculated as follows:

$$R_{fa\_forced} = \frac{1}{h_{forced} \times A_f}$$

(5.8)

where h_{forced} and A_f are convection heat transfer coefficient (W/m^2.°C) caused by air flow in fins and surface area of frame (m^2), respectively. The procedure for calculating h_{forced} based on air velocity, the Nusselt and Reynolds number, was studied in the literature [165], [185].

b) Air gap resistance

There are three methods to build a thermal model of the air gap: 1) heat transfer coefficient (HTC), 2) coupled field method (CFM), and 3) equivalent thermal conductivity (ETC) [177]. Because the air gap length in electrical motors is narrow, calculation of the heat transfer coefficient in the air gap uses a complex convection method. The heat transferred from the rotor side to the stator side in the air gap is independent of the rotational speed in the laminar state [177]. The effective conductivity of a fictitious stationary fluid transfers the same amount of heat as the actual moving fluid in a concentric cylinder like air gap [179]. Hence, in this study, the HTC method is employed to model the thermal analysis of the air gap. The convection coefficient and resistance of the air gap is determined as follows [181]:

$$Re = \frac{v_r \times lg}{\mu} \tag{5.9}$$

$$T_a = \frac{Re^2 \times lg}{r_{or}} \tag{5.10}$$

$$h_g = \frac{Nu \times \lambda_{air}}{lg} \tag{5.11}$$

$$R_g = h_g \times 2\pi \times r_{or} \times L \tag{5.12}$$

where Re, v_r and μ are Reynolds number, rotor surface velocity (m/s) and kinematic viscosity of air (m²/s). The symbols T_a, r_{or}, λ_{air} and h_g stand for Tylor number, outer rotor radius, air thermal conductivity and convection coefficient (W/m².°C). The Nusselt (Nu) calculation procedure corresponding to Tylor number can be found in [181]. R_g and L are the air gap thermal resistance and the stack length of the motors. The determination of the convection heat transfer coefficient for the other parts like the end-winding, end faces of stator, rotor and end ring are presented in section (5.5.2), and then, using Equation 5.7, the resistance of each of the parts is calculated.

- Conduction Resistances

The conduction heat transfer happens from the inner side of a component to the outside surface in a radial direction, and in axial direction from right to left or vice versa. Conduction thermal resistance of the main components are determined in the following sections.

a) Hollow cylinder parts

Based on the geometry of the main component of an induction motor, it is well-known that the main components of the machine are considered to be hollow cylinder [182]. Generally, a hollow cylinder consists of two types of thermal resistances: 1) radial thermal resistance, and 2) axial thermal resistance, which are calculated as follows [186]:

$$R_{th\_radial} = \frac{\ln(\frac{r_o}{r_i})}{2\pi \times \lambda \times L} \tag{5.13}$$

$$R_{th\_axial} = \frac{L}{2\pi \times (r_o - r_i)^2 \times \lambda} \tag{5.14}$$

where r_o, r_i, L and λ are the outer radius, inner radius, axial length of the hollow cylinder and thermal conductivity of the material. Note that the axial and radial thermal conductivity in lamination stack are different and there is no accurate information produced by the manufacturer [163]. Aspects like the clamping pressure, lamination thickness, stacking factor, lamination surface finish, and the interlamination insulation material affect the axial thermal conductivity [187]. In fact, the axial thermal conductivity of laminated structures is much lower in the radial direction due to dielectric coating layers [182]. Thermal conductivity of the main components is listed in Table 5-1.

Table 5-1. Thermal Conductivity of Main Components.

Material	Value (W/m$\cdot$°C)
Lamination Iron (600W50A)	36
Copper	387
Aluminium	230
PM	8
Air	0.026

b) Resistance between winding and stator lamination

The composite thermal conductivity method [188] is considered to determine the heat transfer within a winding. It is important to determine the proper equivalent thermal conductivity of air and insulation material in the slots (k_{eq}). We use Equation 5.15 [163] to calculate k_{eq} as follows:

$$k_{eq} = 0.1076 \times k_f + 0.029967 \tag{5.15}$$

where k_f is the fill factor of a stator slot. The thermal resistance between the winding and the stator lamination is calculated as follows [163]:

$$R_{eq} = \frac{th_{eq}}{k_{eq} \times A_s} \tag{5.16}$$

where th_{eq} and A_s are the equivalent thickness of the air and the insulation material in the stator slots, and interior slot area, respectively. These are defined as follows [163]:

$$th_{eq} = \frac{S_{slot} - S_{cu}}{S_p} \tag{5.17}$$

$$A_s = S_p \times L \tag{5.18}$$

where S_{slot}, S_{cu}, and S_p are stator slot surface (m^2), copper surface in the stator slot (m^2), and stator slot perimeter (m), respectively.

5.5.2 FEM-Based Thermal Model of the IM and LSPMSM

Analysing thermal behaviour of the machines by FEM, including transient and steady-state thermal analysis, is a well-known method [189]. In this study, a 3D thermal analysis based on a FEM model using steady-state thermal analysis software is studied. Hence, an electromagnetic analysis is first studied and it is then coupled with the steady-state thermal analysis to map the losses onto the 3D model to identify heat generation sources. The conductive heat transfer coefficient between components is determined based on the geometry and material properties of each component. The convective heat transfer is defined as boundary conditions on parts of the geometry that are in contact with flow. Table 5-2 shows the boundary conditions for convections applied to the LSPMSM in the FEM thermal analysis and similar boundary conditions apply for the IM with the exception that there is no PM in the rotor part.

The value of convection heat transfer coefficients are determined based on defined formula for the main components. Equations 5.6-5.12 shows how to calculate the convection heat transfer coefficients for the frame and the air gap.

The fluid in the air gap removes a certain amount of the heat generated from the stator, end winding and rotor to the outside. Forces occurring from the rotating rotor force the fluid to tangential movement and, therefore, toroidal vortices are induced [173]. Hence, the heat transfer coefficients of the motor's end faces are calculated in the following sections.

5.5.2.1 Stator core end face

The heat transfer coefficient of the stator core end face is defined as [178]:

$$h_{sc} = 15 + 6.5 \times v_r^{0.7} \tag{5.19}$$

where v_r is the rotor surface velocity (m/s).

5.5.2.2 Stator end winding

The stator end winding heat transfer coefficient is calculated as [178]:

$$h_{ew} = \frac{Nu_{ew}\lambda_{air}}{r_{eq\_ew}} \tag{5.20}$$

$$Nu_{ew} = 0.456 \times R_{e\_ew}^{0.6} \tag{5.21}$$

$$R_{ey\_ew} = \frac{2\pi \times r_{or} \times n_r \times r_{eq\_ew}}{60\mu} \tag{5.22}$$

$$r_{eq\_ew} = \frac{r_{os} + r_{is}}{2} \tag{5.23}$$

where Nu_{ew} is the Nusselt number of the end winding, R_{ey_ew} is the air Reynolds number of the end winding, r_{eq_ew} is the mean radius of the end winding, and r_{os} and r_{is} are the outer and inner radius of the stator, respectively.

5.5.2.3 Rotor end face

The rotor end face heat transfer coefficient is described as follows [178]:

$$h_{rc} = \frac{Nu_{rc}\lambda_{air}}{r_{or}} \tag{5.24}$$

$$Nu_{rc} = 1.67 \times R_{ey\_r}^{0.385} \tag{5.25}$$

$$R_{e\_ew} = \frac{2\pi \times r_{or}^2 \times n_r}{60\mu} \tag{5.26}$$

where Nu_{rc} is the Nusselt number of the rotor end face, R_{ey_r} is the air Reynolds number of the end core rotor.

5.5.2.4 End ring face

The heat transfer coefficient of the end ring is calculated as follows [178]:

$$h_{er} = \frac{Nu_{er}\lambda_{air}}{h_{er}} \tag{5.27}$$

$$Nu_{er} = 0.456 \times R_{ey\_er}^{0.6} \tag{5.28}$$

$$R_{e\_er} = \frac{2\pi \times r_{or} \times n_r \times h_{er}}{60\mu} \tag{5.29}$$

where Nu_{er} is the Nusselt number of the end ring, R_{ey_er} is the air Reynolds number of the end ring and h_{er} is the end ring height (m). Table 5-3 shows the boundary conditions applied to the LSPMSM in the FEM thermal analysis and similar boundary conditions exist for the IM with the exception that no PM is present in the rotor part.

5.5.3 Experimental Test Procedure

The IM is tested at three voltage levels (under, rated and over voltage) and two frequencies (50 and 60 Hz). Figure 5-5 shows the tested motor and the temperature sensors used to measure the temperature of the frame parts. The motor was on full load (19.5 Nm) at start up, and temperature measurements were captured from the beginning of the test. However, the motor was still warm from the previous test. This test ran for 1hr 26 mins, and the previous test ran for 3hrs. We run the motors until the temperature rise achieved a defined steady state of 2 °C/hr rise. The error of the tests only needed to be ±2°C. So, all this meant that the sensor time constant was not considered, and instrument/sensor accuracy only needed to be mid-range. Winding temperature was measured by two methods, an embedded PT100 sensor in the head winding, and the resistance method (RT Resistance) on cool down. RT photo is data from photos taken of the instrument measuring the winding resistance during the cool down phase at a period of 30 secs (see Figure 5-6a). The rotor temperature was measured by a probe being inserted through a hole in the end-shield after power off and the rotor forced to a stop as quickly as possible (See Figure 5-6b).

Table 5-2. Applied boundary conditions.
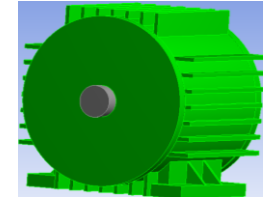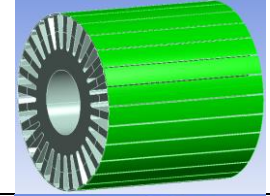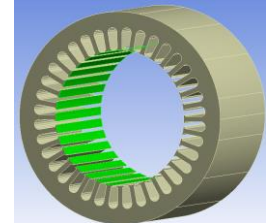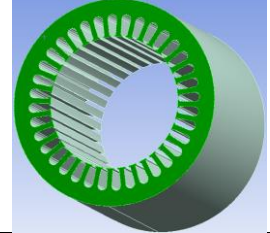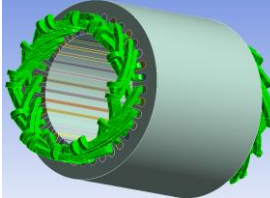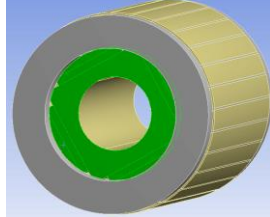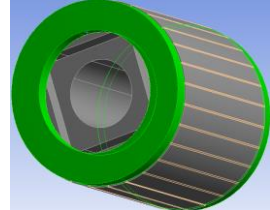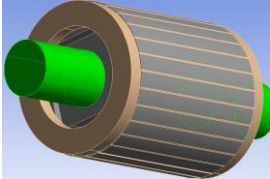
Parts	Heat transfer type	Boundary
Frame	Convection to the outside air	
Outer Rotor Surface	Convection to the air gap	
Inner stator slots Surface	Convection to the air gap	
Stator End Faces	Convection to the inside air	
End Windings	Convection to the inside air	
Rotor End Faces	Convection to the inside air	
Cage End Faces	Convection to the inside air	
Shaft	Convection to the outside air	

Table 5-3. Thermal convection coefficient calculated for each part of the 3-kW IM and LSPMSM.

Parts	Convection heat transfer coefficient (h)		Unit
	IM	LSPMSM	
Frame	133.0	133.2	W/m^2.°C
Air gap	116.0	116.0	W/m^2.°C
End face stator	53.0	54.0	W/m^2.°C
End winding	92.0	94.0	W/m^2.°C
End face rotor	42.0	42.5	W/m^2.°C
End ring	160.0	164.0	W/m^2.°C

Winding is in direct contact with a heat sink so will cool down from the point in time that power is turned off. The rotor probe is on the shorting ring (end ring) so there is some lag for the heat in the centre of the rotor to reach the shorting rings. There is also minimum conduction mechanism of heat dissipation due to air gap. There is a lag in the temperature probe stabilising to the same temperature as the point on the rotor. This will manifest as a rising temperature trace until the probe and rotor are at the same temperature. Afterwards, a downward trend will result indicating cooling down.

As experimental temperature is recorded on cool down, there are drops in temperature during this time, particularly in the rotor where the probe takes around 250 s to stabilise. In fact, the reported rotor temperature is the rotor temperature after 250 s of power off and so there is a drop in temperature estimated between 0–10 °C. Likewise, the first winding temperature is reported 30 s after power off and the temperature drop in this case is estimated to be between 0–4 °C.
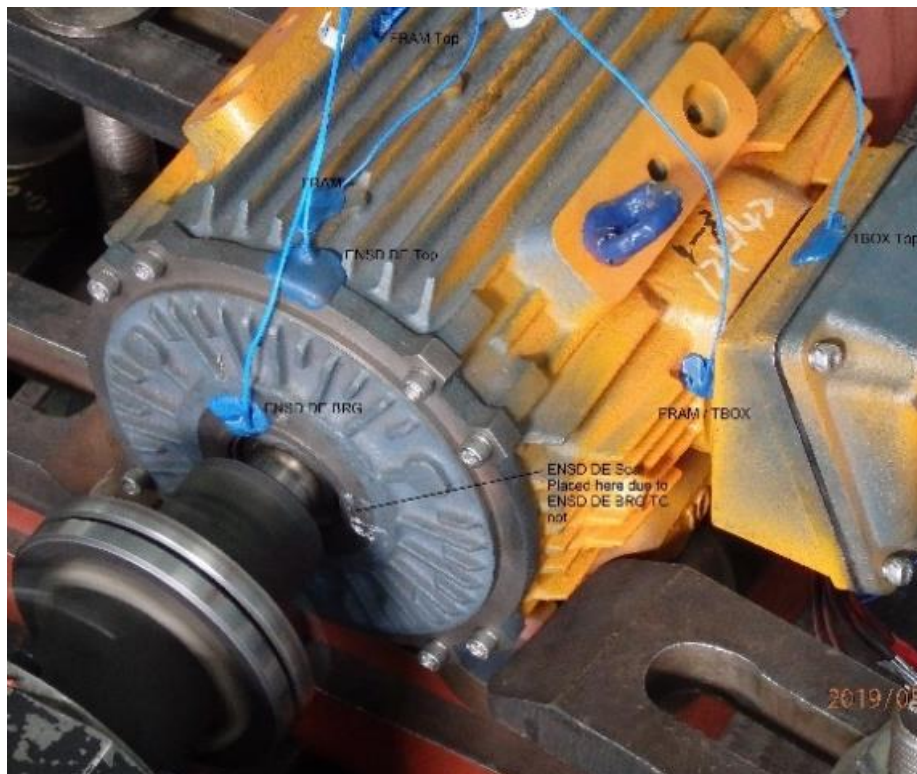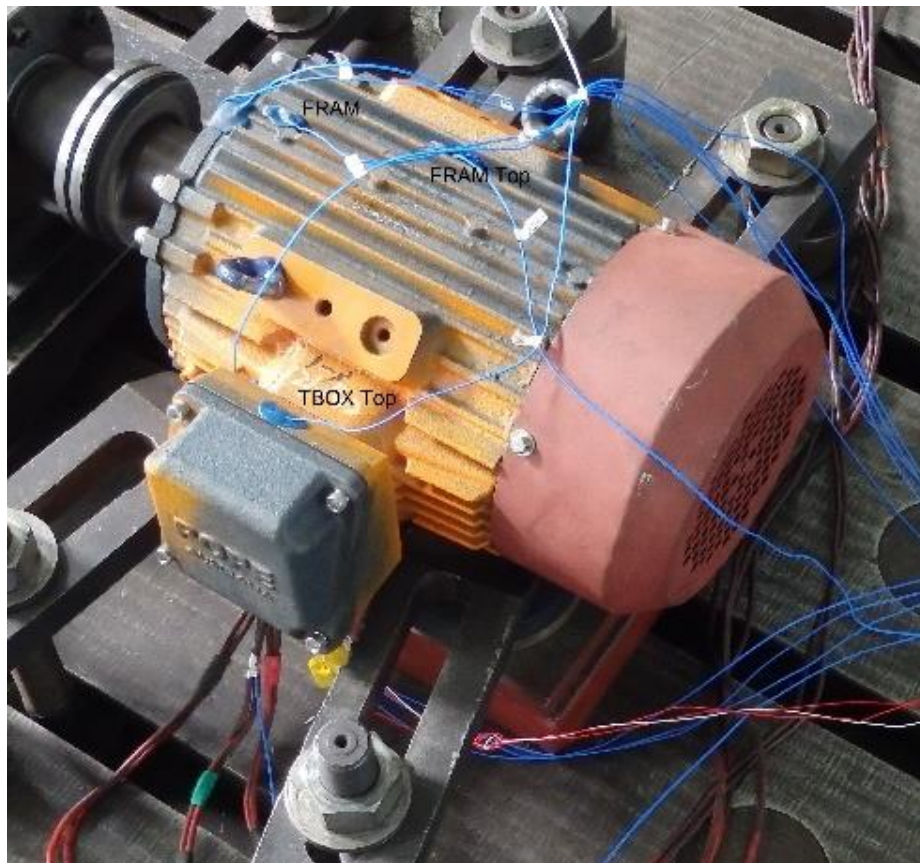
Figure 5-5. 3kW IM under test and temperature sensors mounted on frame parts.

$y = 62.437e\text{-}6E\text{-}04x$
$R^2 = 0.938$

$y = 62.566e\text{-}7E\text{-}04x$
$R^2 = 0.965$
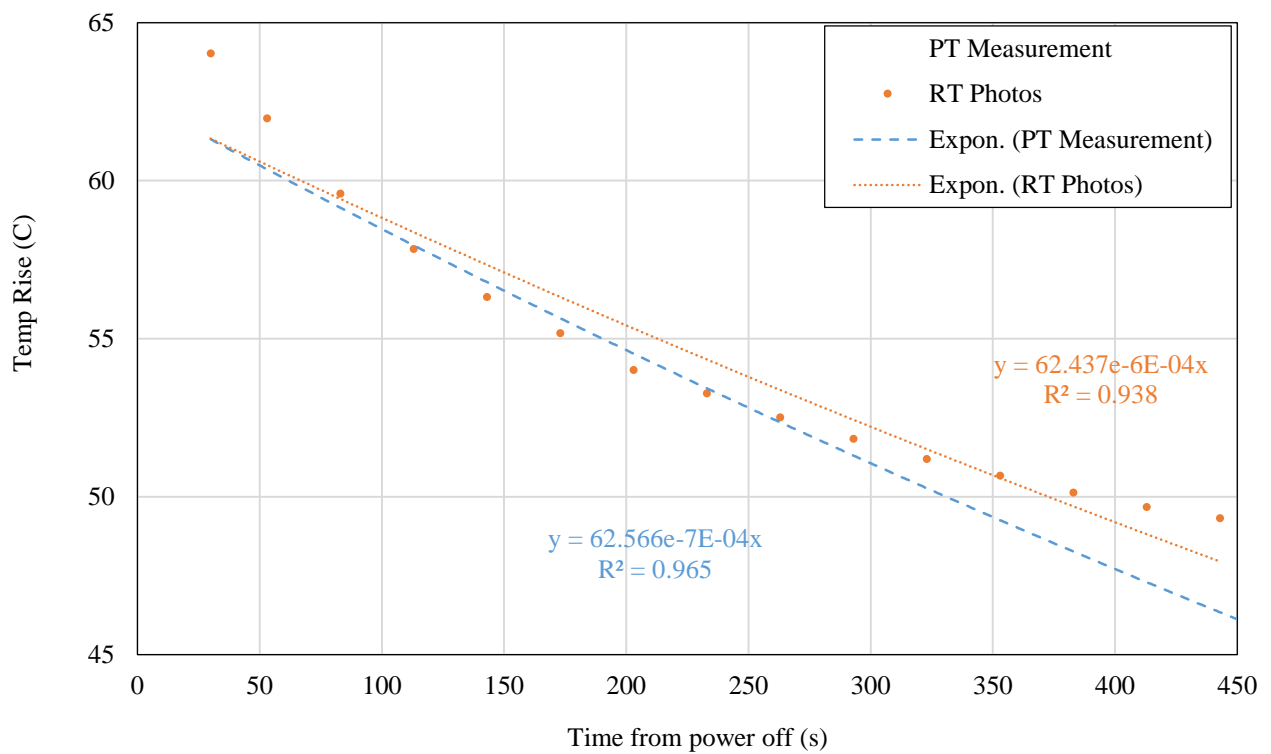
a. Stator winding temperature
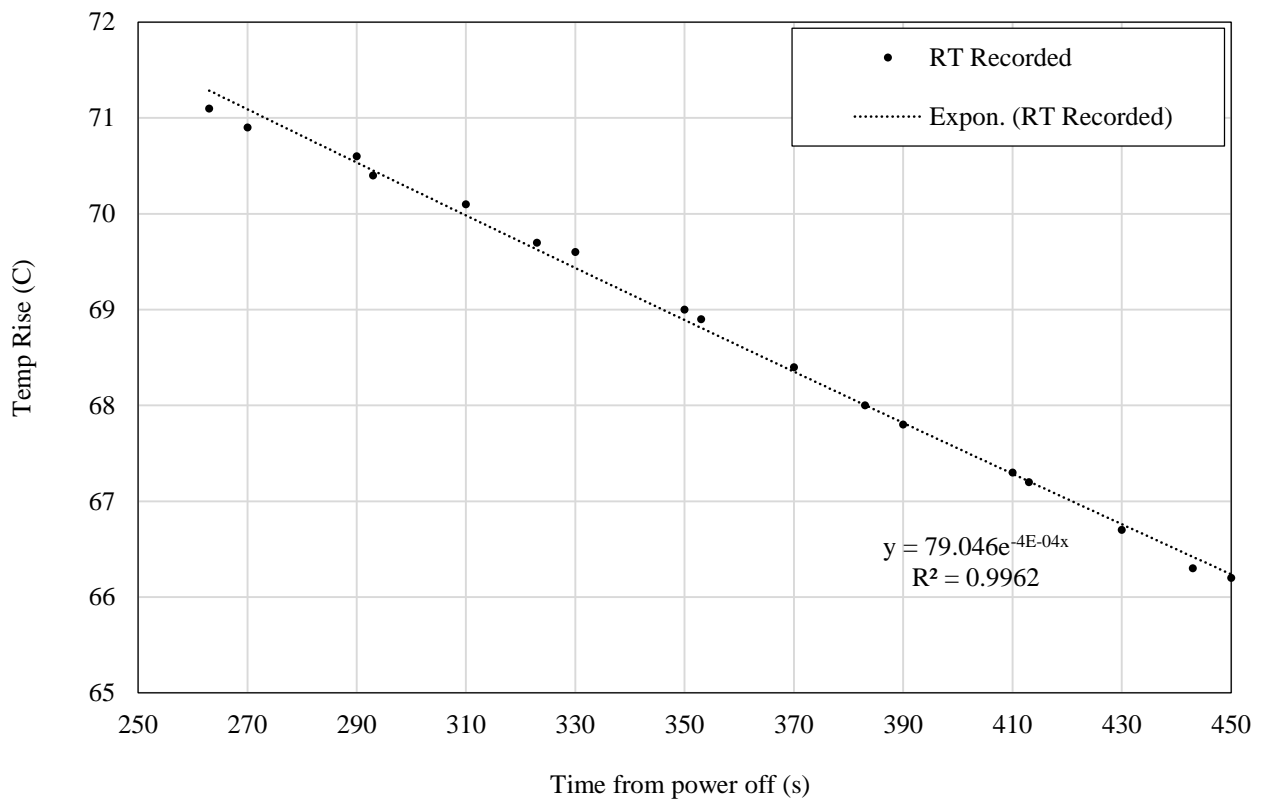
b. Rotor end ring temperature

Figure 5-6. Experimental winding and end ring temperature of the IM @ 415 V, 50 Hz.

Power off is the calculated time at which the power was isolated from the motor and the cool down phase started. It is also the point in time that we must exploit. From their cool down curves, the rotor and stator temperature rise back in order to find the stable temperature rise (as per explosive atmosphere standard IEC 60079-7).

5.6 Thermal Analysis and Result Discussion

In this section, the performance of the proposed lumped-parameter model is compared with the FEM-based model and experimental data to validate the proposed model. As the lumped-parameter model of LSPMSM is quite similar to the IM, we can predict temperature rise of each node of the LSPMSM motor, using the proposed thermal circuit model, with high accuracy. This lumped model will take less time than a thermal analysis of the LSPMSM based on FEM and cost less than expensive experimental tests. Prior to discussing temperature distributions, we would like to discuss the temperature dependency of the main components in the following section to understand how temperature affects the performance parameters of an electric motor.

5.6.1 Temperature Dependency Analysis of Main Components

The properties of materials used in an electric motor are dependent on temperature and their properties such as conductivity change as temperature changes. Hence, motor performance is dependent on operating temperature and temperature rise causes total loss to grow although core loss

reduces [167], [172]. The core loss reduction due to temperature rise in PM motors is higher than IMs [167], and it is important to consider this phenomenon in the post processing calculation of core loss to get accurate results. Hence, a FEA is implemented to show temperature dependency of the main components for the IM at 415 V, 50 Hz using 2D FEA simulations and the similarly for the LSPMSM. For this purpose, in FEA simulation, the conductivity of the aluminium and steel core were defined dependent on the temperature rise and the stator resistance is dependent on temperature as well. Then, a parametric analysis is studied based on the variable variation that is the winding temperature. Figure 5-7 shows the temperature dependency of the main performance parameters such as the stator winding loss, the rotor cage loss, core loss and efficiency of the IM. It shows motor performance (Efficiency) affected by the total loss growth. As expected, the efficiency of the IM dropped with temperature growth and, hence, it is important to consider the operating temperature in the design process to get a precise design.

Winding temperature (C)
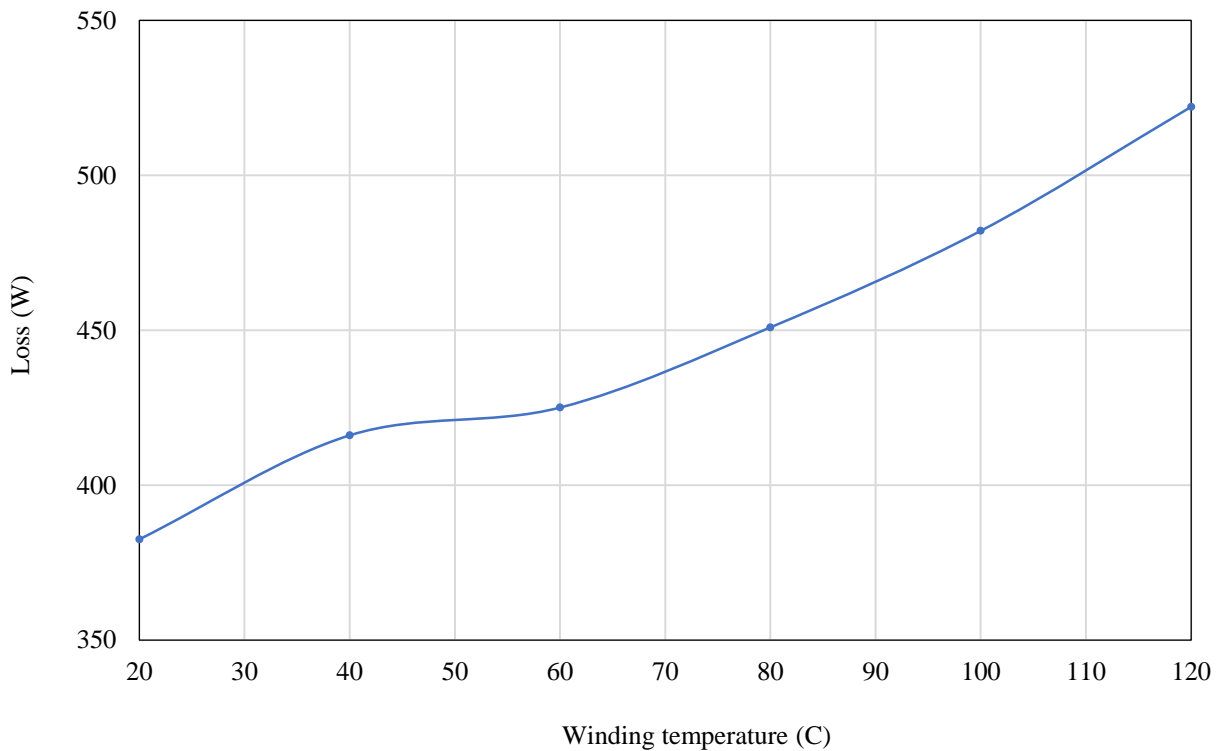
a.   Copper loss
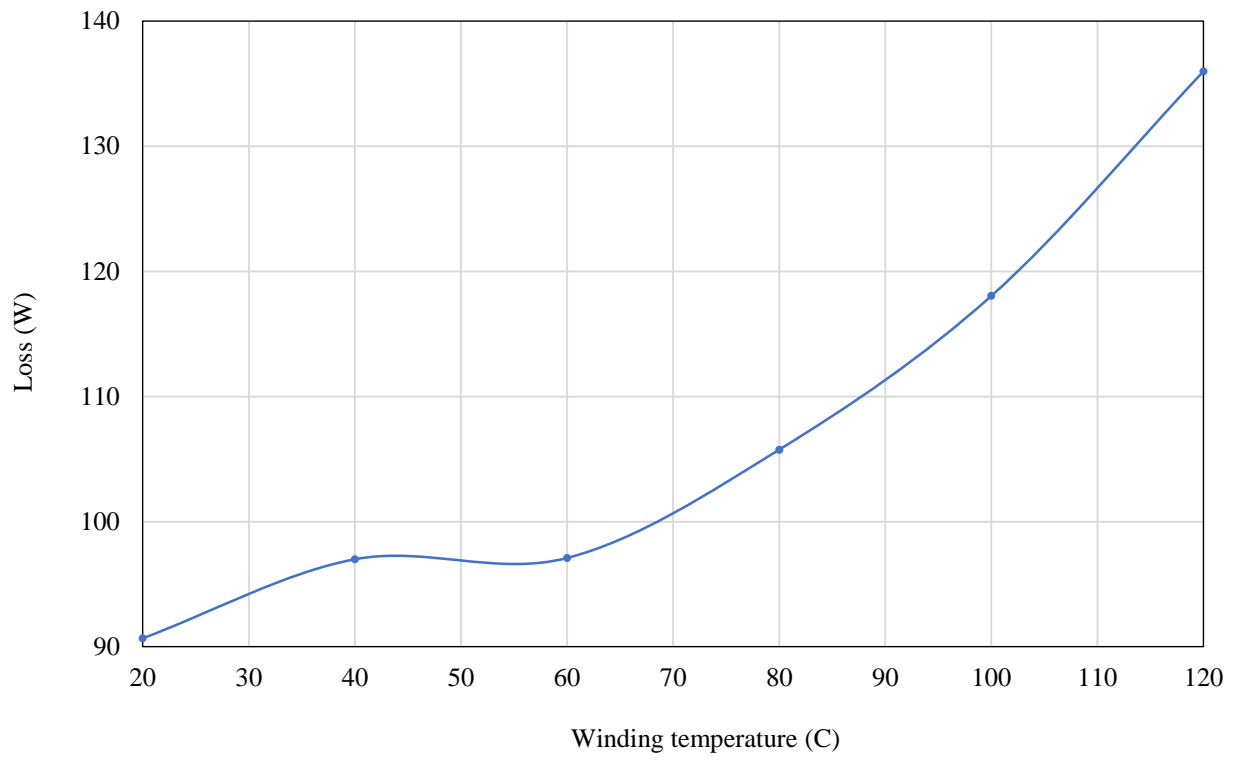
b. Cage loss
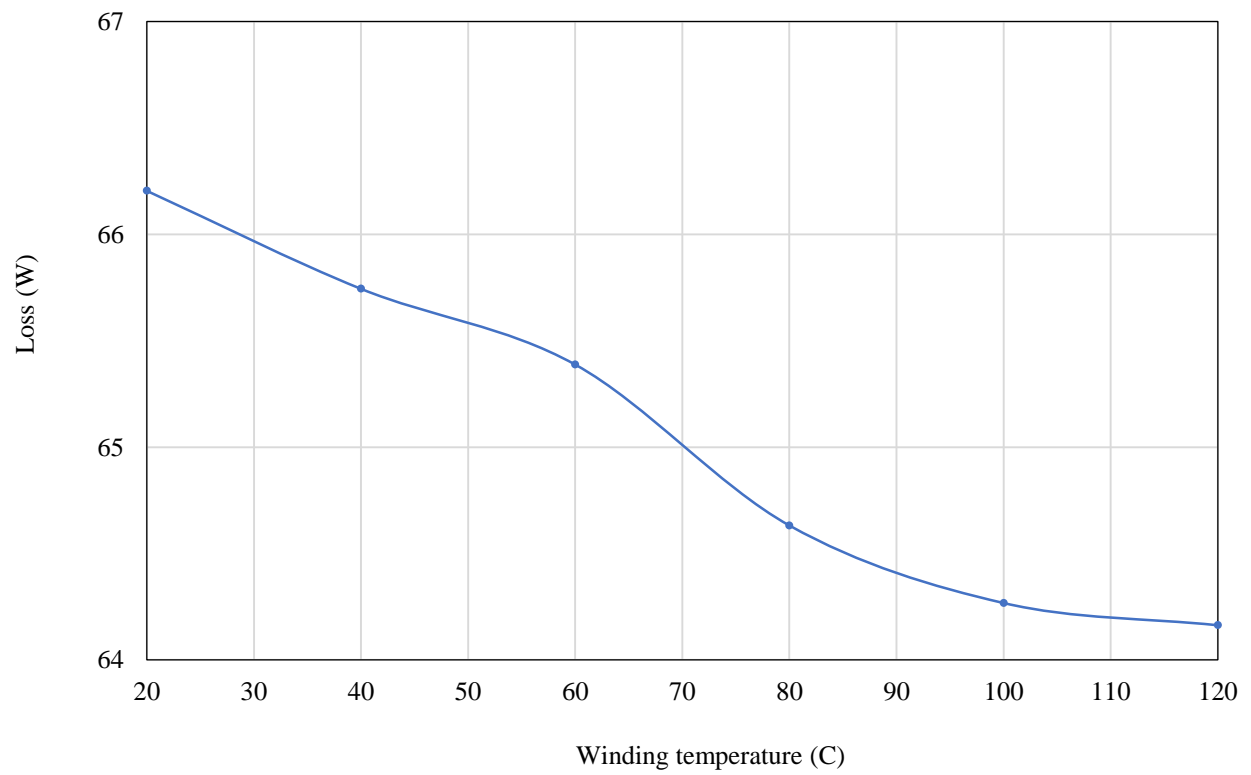
c. Iron loss
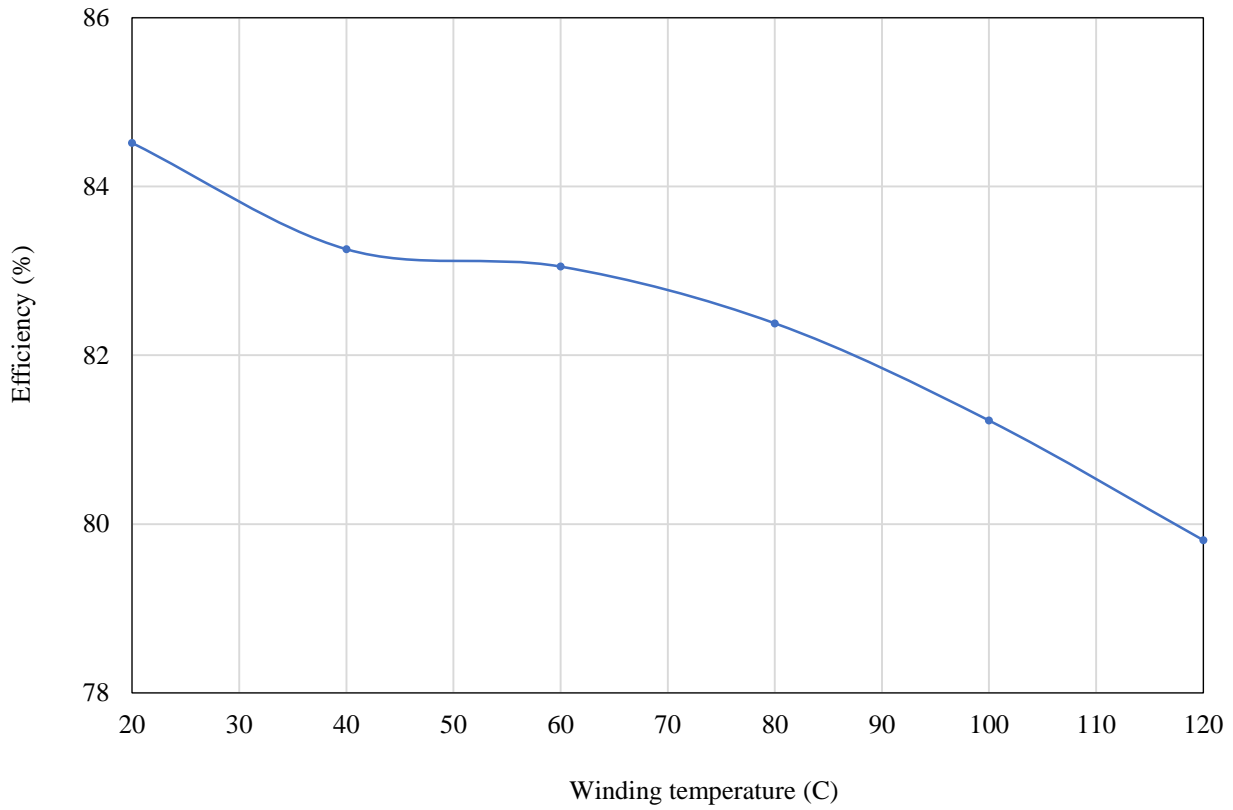
d. Efficiency

Figure 5-7. Performance parameters variations versus temperature of the 3-kW IM @ 415 V, 50 Hz.

5.6.2 Temperature Rise Distribution of Case Studies

Using experimental data of frame-top temperature rise of the 3-kW IM tested at 374 V, 50 Hz, the thermal time constant (τ) is calculated from the well-known formula as follows:

$$T(t) = T_0 + (1 - e^{(\frac{t}{\tau})}) \times \Delta T \qquad (5.30)$$

where T_0 is the ambient temperature and ΔT is the steady-state temperature rise of the frame-top, which was 51 °C. It is well-known that temperature rise in t=τ equals 63.2% of the steady-state temperature rise and using this information and experimental data the thermal time constant is calculated as 29 minutes. To predict the temperature rise of each node over time using Equation 5.30, we need to know ΔT of each node. Table 5-4 to Table 5-6 list the temperature rise of the main components estimated by the proposed lumped-parameter model, FEM model and experimentally measured values at under-voltage (374 V), rated-voltage (415 V) and over-voltage (460 V) at frequency 50 Hz. Note that the losses injected in each node were extracted from FEA simulation validated with reported experimental values (see Figure 5-8 as sample). Copper losses for end-winding is measured with considering the impact of end-winding resistance in excitation.

Table 5-4. Temperature rise of main components of 3-kW IM under 374 V, 50 Hz.

Component	Proposed lumped-parameter Model	FEM	Experimental (average)
Frame	50.24	47.14	58.7
Winding	83.41	83.00	81.5
End Winding	89.00	86.00	
Rotor Iron	96.82	99.16	98
Rotor End Ring	102.24	103.00	

Table 5-5. Temperature rise of main components of 3-kW IM under 415 V, 50 Hz.

Component	Proposed lumped-parameter Model	FEM	Experimental (average)
Frame	45.55	40.00	47.5
Winding	66.60	60.50	62.5
End Winding	71.43	64.01	
Rotor Iron	77.80	84.12	79
Rotor End Ring	81.7	87.46	

Table 5-6. Temperature rise of main components of 3-kW IM under 460 V, 50 Hz.

Component	Proposed lumped-parameter Model	FEM	Experimental (average)
Frame	47.38	39.00	47
Winding	63.11	63.01	61.5
End Winding	68.44	66.43	
Rotor Iron	73.50	72.45	73.5
Rotor End Ring	76.17	75.34	
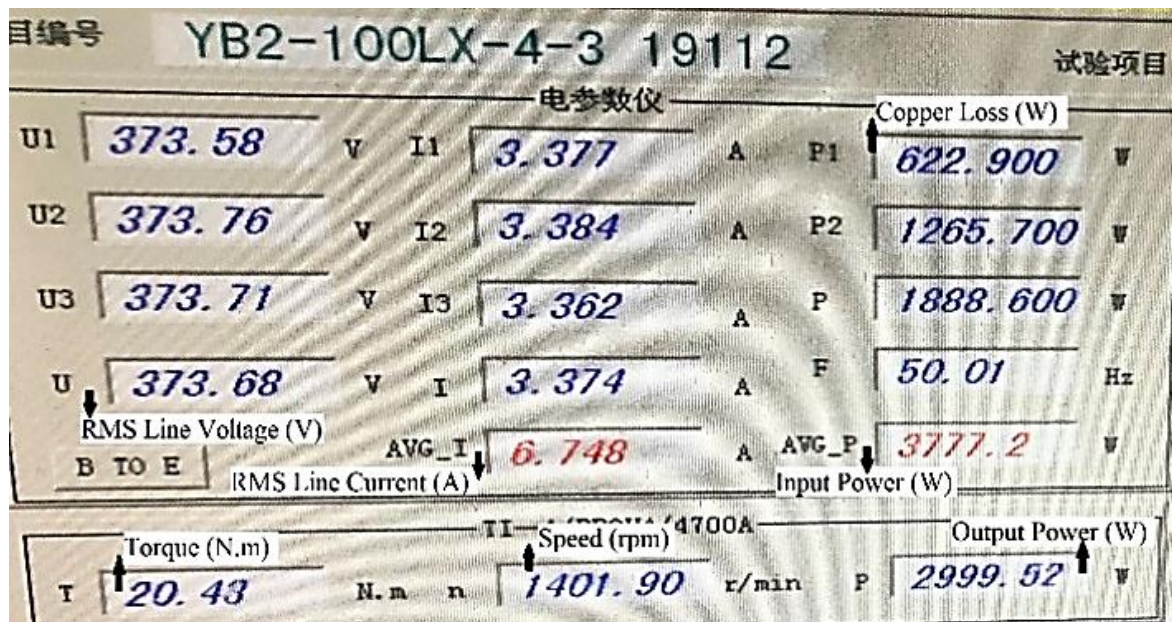
a. Experimental recorded data
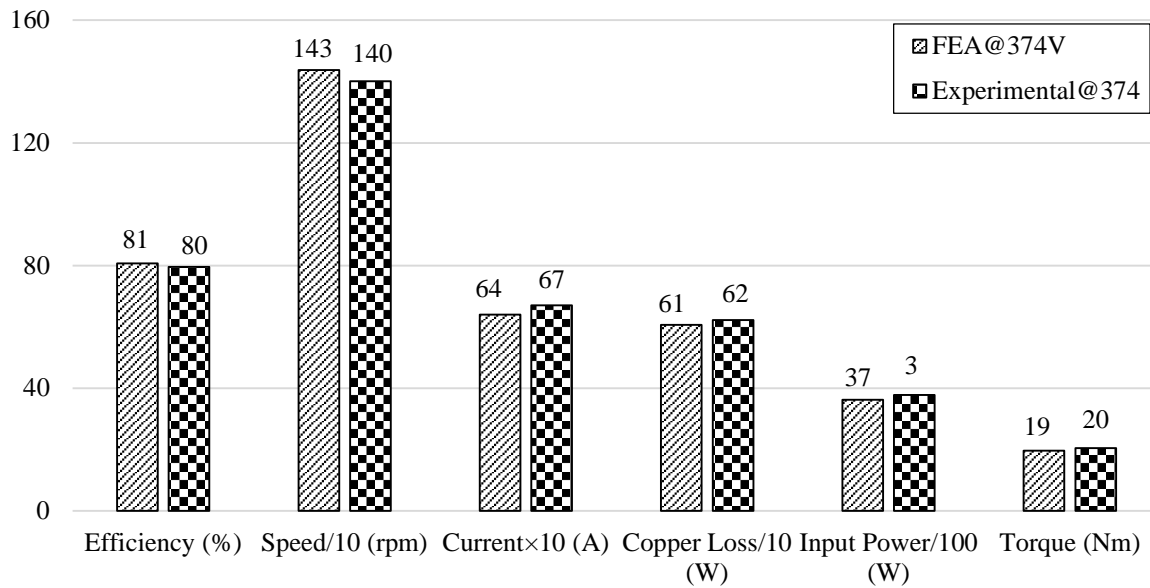
b. Experimental versus FEA simulations

Figure 5-8. Experimental data of the 3-kW IM tested at 374V, 50 Hz in comparison with FEA.

Figure 5-9a shows the frame-top (see Figure 5-5) absolute temperature variations versus time for the IM tested under 374 V, 50 Hz. This temperature is used to calculate the thermal time constant using Equation 5.30. This figure indicates the precision of the calculated thermal time constant using Equation 5.30 in comparison with experimental temperature variations versus time. Then, using the calculated thermal time constant, the steady-state temperature rise and Equation 5.30, the absolute temperature variations versus time of the main components are estimated by the proposed lumped-parameter model for the IM under 374 V, 50 Hz (see Figure 5-9b). The experimental data of the temperature rise of the frame (see Figure 5-5) was higher than temperature rise of the frame-top and we can see that the predicted temperature of the frame by the proposed lumped-parameter is also higher than the experimentally measured frame-top temperature over time, and this shows the accuracy of the proposed thermal model.

Figure 5-10 and Figure 5-11 illustrate absolute temperature variations of the main parts versus time of the 3-kW IM at 415 V and 460 V, respectively. The main components temperature rise of the IM at under-voltage (374 V) was higher than rated-voltage (415 V) and this was higher than over-voltage (460 V) (see Tables V-5 and V-6). For example, the temperature rise of frame at 374 V and 415 V are 58.7 and 47.5 °C, respectively. From experimental data, the temperature rise of the frame at 415 V (47.5 °C) is slightly lower than the temperature of the frame-top at 374 V (51 °C). In Figure 5-10, it is clearly seen that the frame temperature predicted by the proposed lumped-parameter model is slightly lower than the measured frame-top temperature of the IM at 374 V.
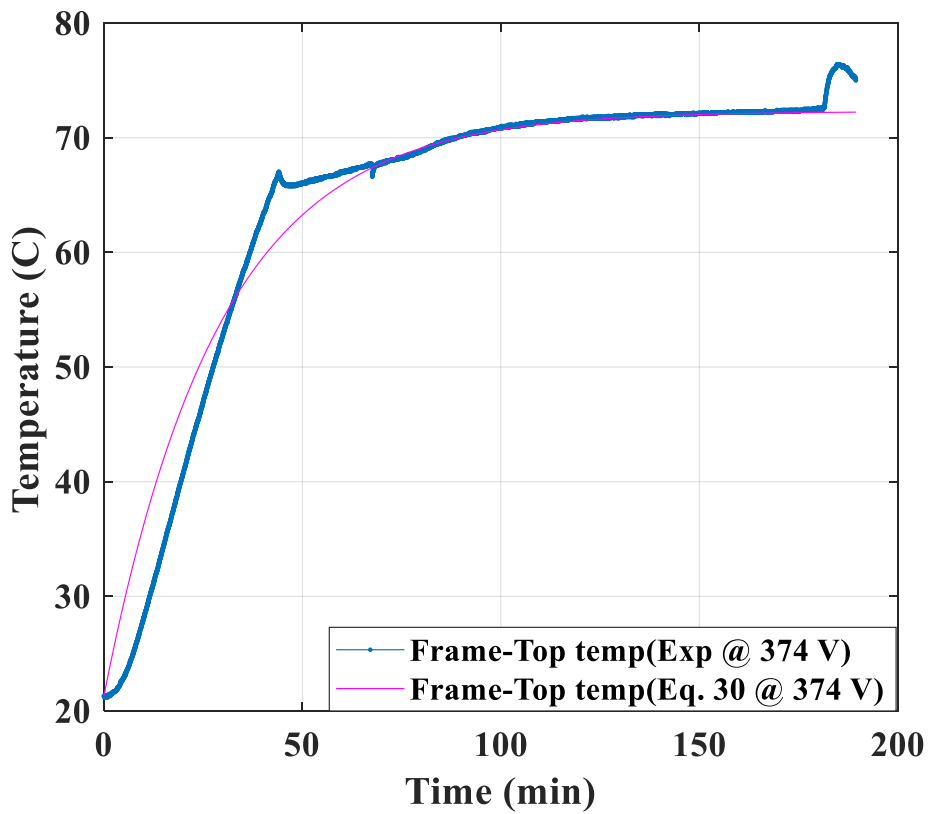
a. Absolute temperature variation versus time measured experimentally and analytically using eq. 5.30 for the frame-top.
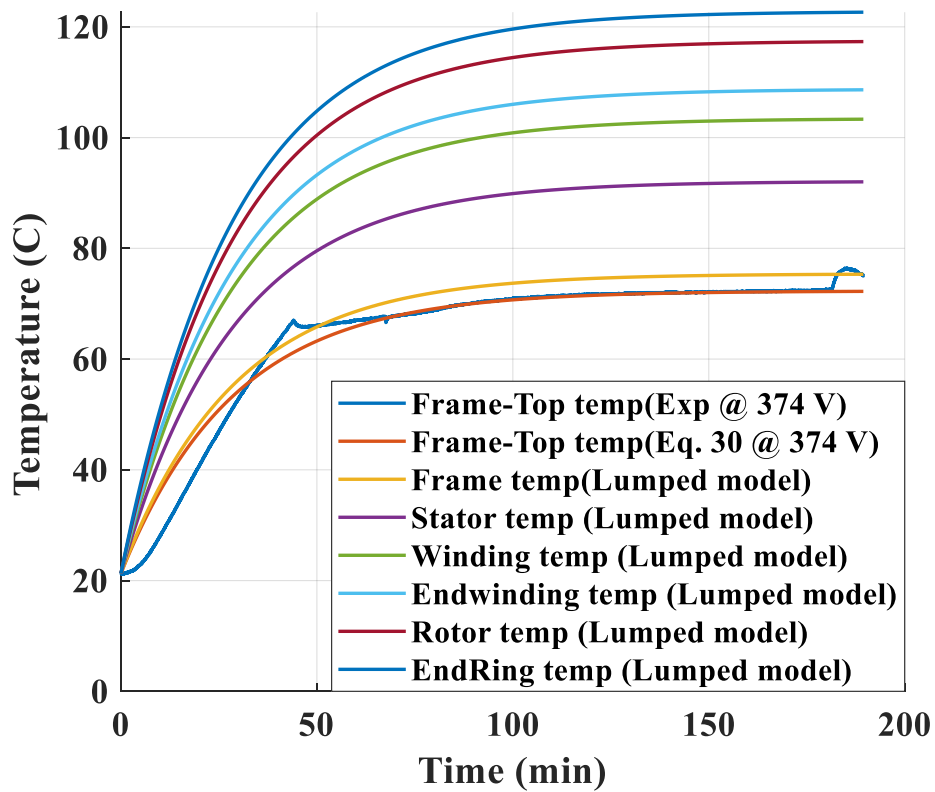
b. Main components temperature variation versus time.

Figure 5-9. Absolute temperature of the main parts estimated by the proposed lumped thermal model of the 3-kW IM at 374 V.

128
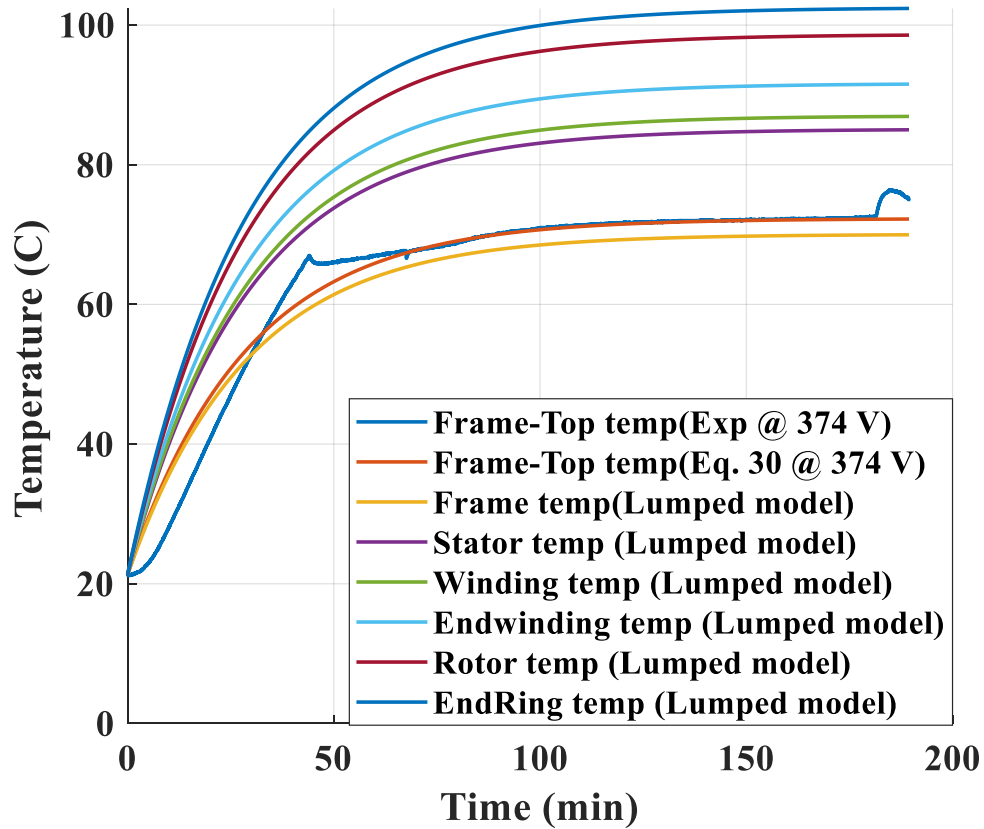
Figure 5-10. Absolute temperature of the main parts estimated by the proposed lumped thermal model of the 3-kW IM at 415 V.
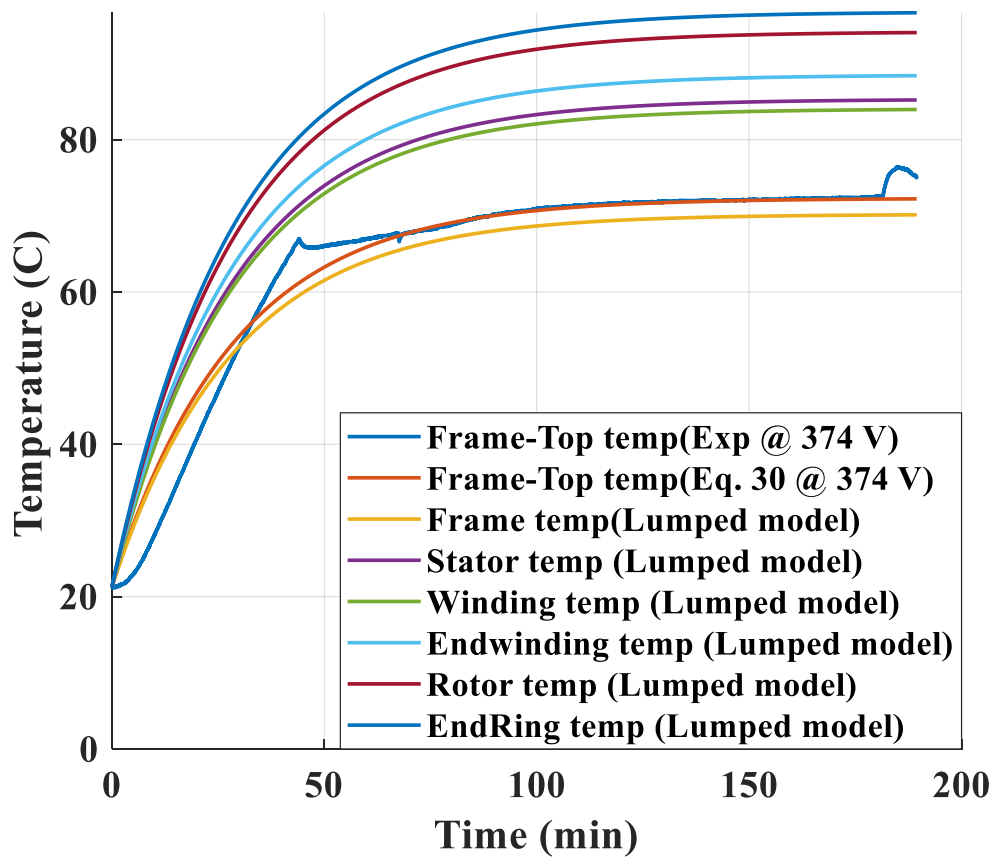
Figure 5-11. Absolute temperature of the main parts estimated by the proposed lumped thermal model of the 3-kW IM at 460 V.

129

The winding and rotor temperature rise of the IM predicted by the proposed method and the FEM model are compared with experimental test data at two frequency levels (50 and 60 Hz) and three voltage levels (under, rated and over voltage). This analysis confirmed the reliability and accuracy of the proposed method and is considered to be a calibration for the proposed lumped-parameter model. Figure 5-12a and Figure 5-12b illustrates variations of the winding temperature rise of the IM versus voltage changes at frequencies 50 Hz and 60 Hz, respectively. Similar analysis is studied for the rotor end ring shown in Figure 5-12c and Figure 5-12d. The predicted temperature by the proposed lumped-parameter model is in good agreement with FEM model and experimental data. So, the proposed thermal model of the LSPMSM is studied to predict the temperature rise of the main components of the LSPMSM when it provides 3-kW and 4.2-kW. Based on the results of both case studies, it is clear that the rotor end ring and end winding are hotter than other components of the motor.
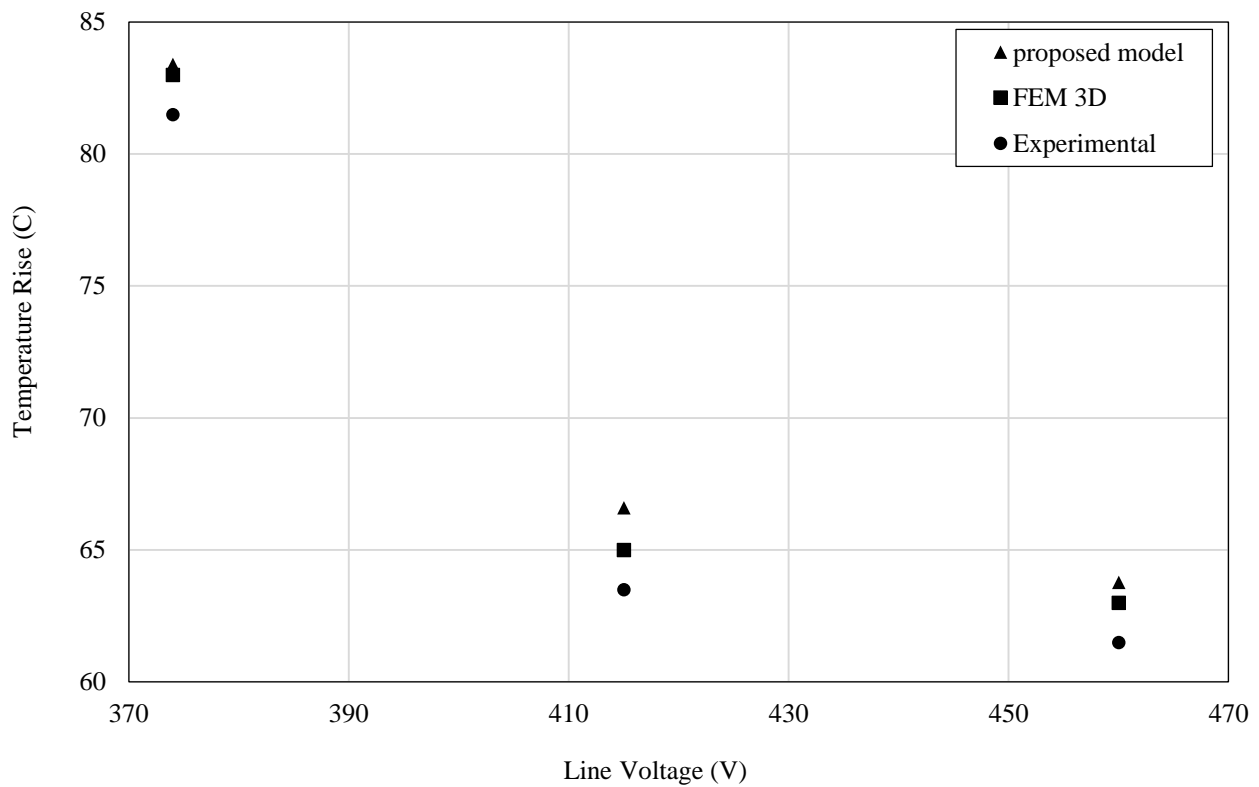
a.   Winding temperature rise at 50 Hz
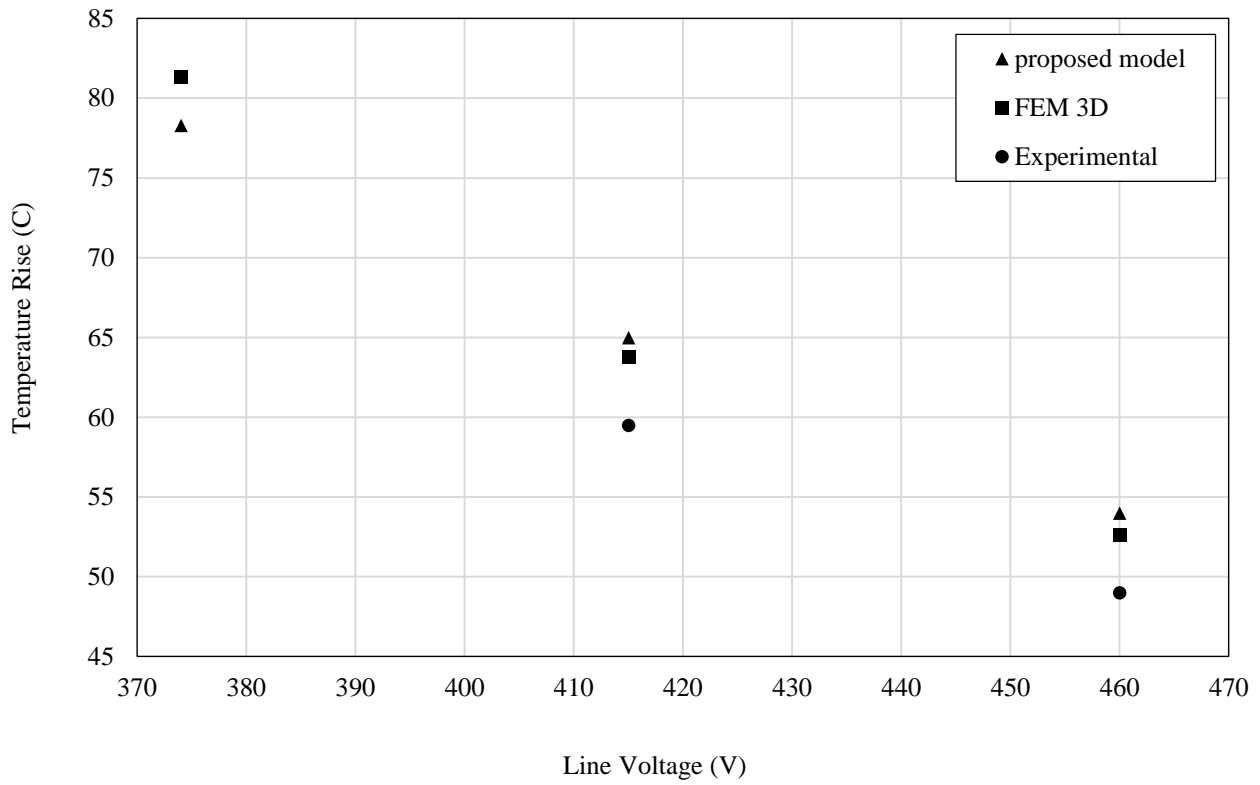
b.   Winding temperature rise at 60 Hz*
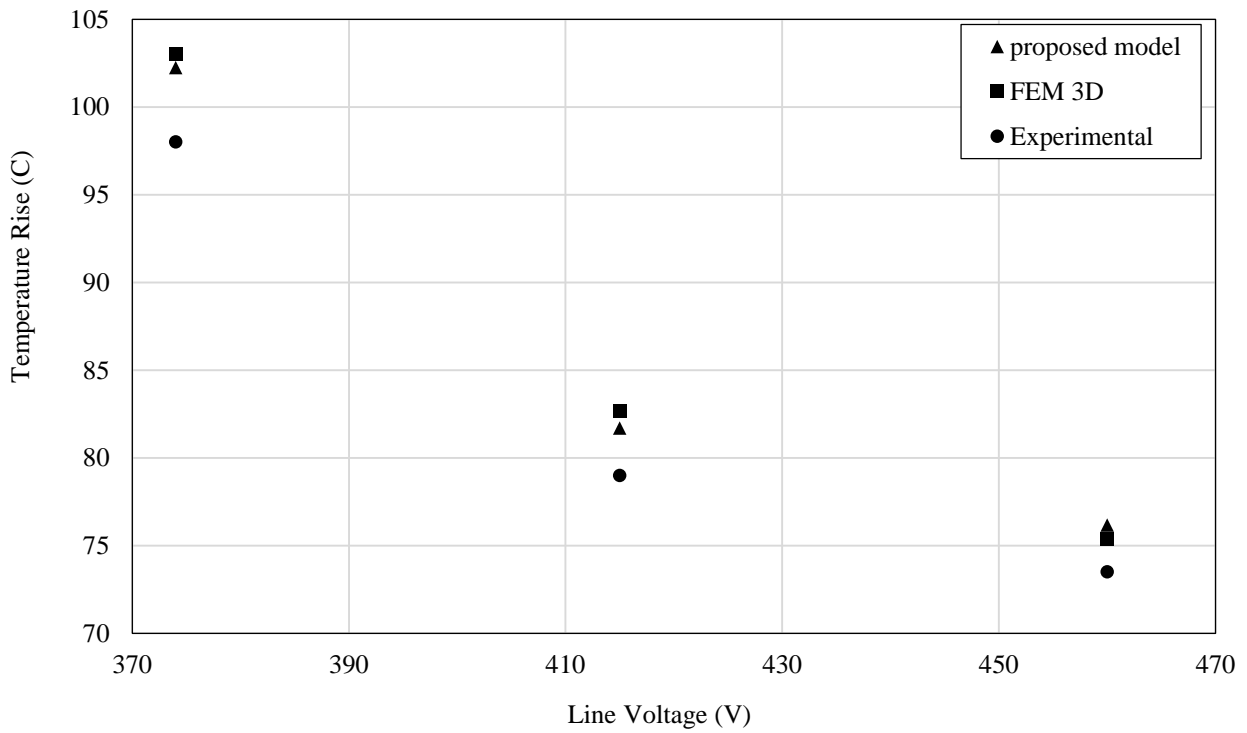
c.   End ring temperature rise at 50 Hz

131
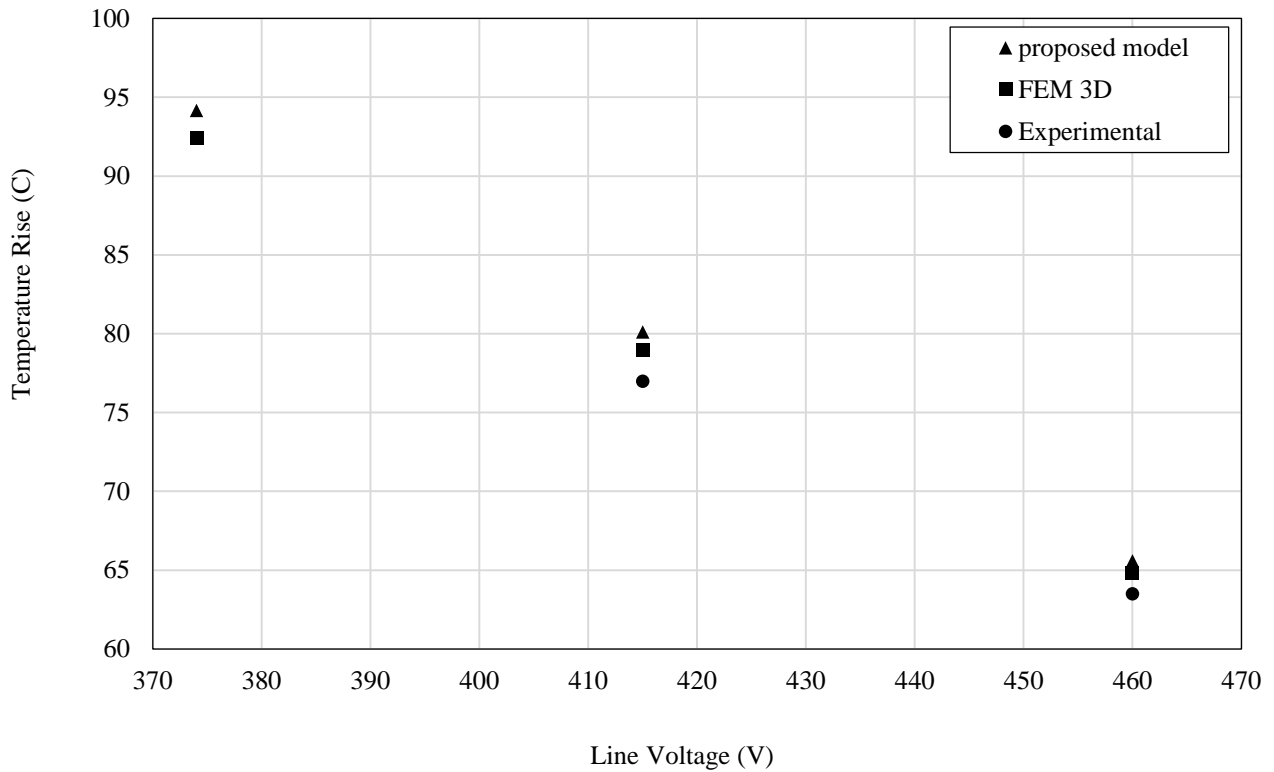
d. End ring temperature rise at 60 Hz*

* The motor was not tested at voltage 374 for frequency 60 Hz.

Figure 5-12. Winding and end ring temperature rise comparison at different voltage and frequency levels.

Figure 5-13a and Figure 5-13b show the absolute temperature distribution of the LSPMSM at 3-kW and 4.2-kW under 415V, 50 Hz. There is considerable temperature reduction in the LSPMSM providing 3-kW compared with the baseline 3-kW IM due to loss reduction, particularly in the rotor. It is seen that the temperature of the main components in the LSPMSM are considerably lower than those in the baseline IM. In fact, replacing the rotor of the IM with the hybrid rotor including a PM leads to not only efficiency improvement (IE4) but the operating temperature of the LSPMSM is also much lower than the IM. The FEM-based thermal analysis of the LSPMSM has been studied to verify the performance of the proposed lumped-parameter model.
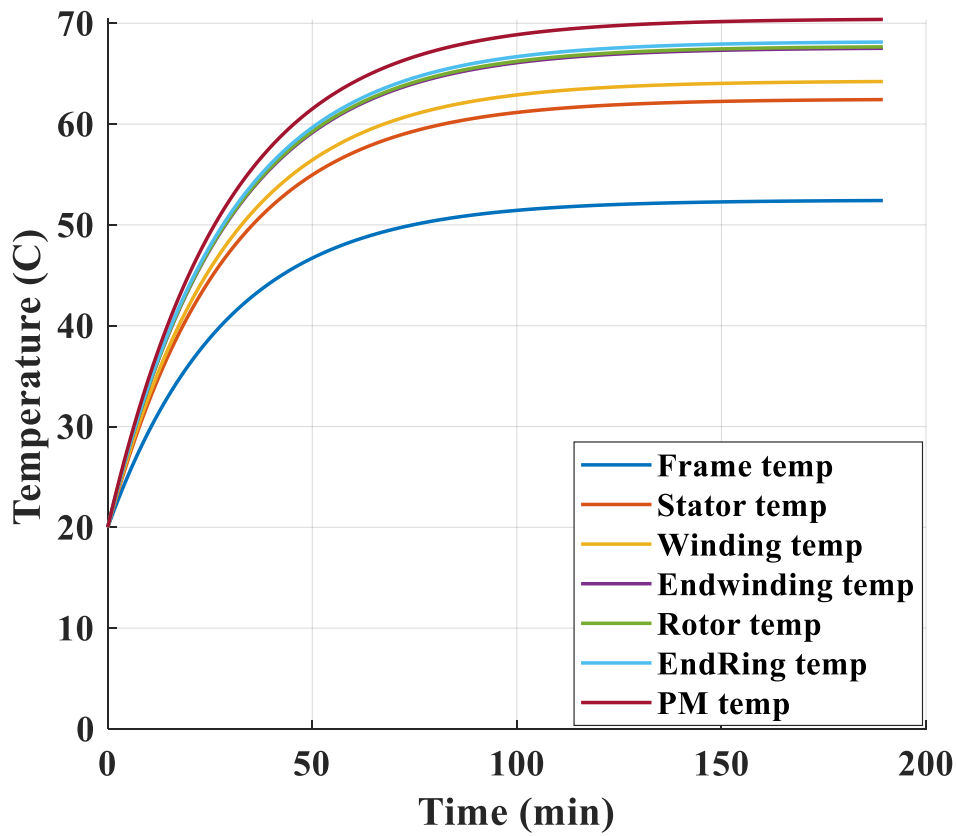
a. LSPMSM @ 3-kW
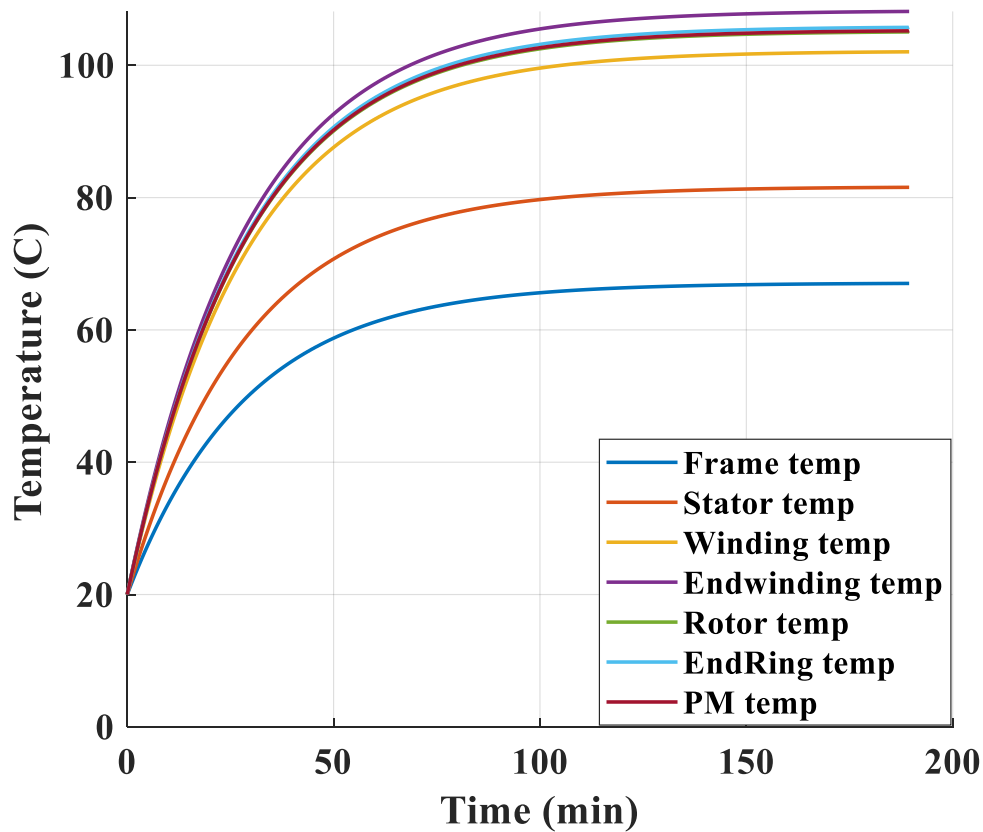
b. LSPMSM @ 4.2-kW

Figure 5-13. Absolute temperature estimated by the proposed lumped thermal model of the LSPMSM at 3- and 4.2-kW under rated condition 415 V, 50 Hz.

Figure 5-14 illustrates temperature distribution of the 3-kW IM and LSPMSM at 3-kW and 4.2-kW under 415 V, 50 Hz based on FEM thermal analysis using commercial software package Ansys/ steady-state thermal analysis. Thermal analysis of the LSPMSM operating at 4.2-kW indicates that the overall temperature of the LSPMSM is comparable with the baseline IM providing 3-kW. The winding temperature of the LSPMSM at 4.2-kW is higher than the 3-kW IM and the LSPMSM at 3-kW, as was predicted by the proposed lumped thermal model. This experiment verifies the reliability and performance of the proposed lumped-parameter thermal model for estimating the temperature rise of the LSPMSMs' parts by knowing the value of the losses.

In this part of chapter, the methodology of the proposed thermal model has been discussed for a case study, 3-kW motors, both IM and LSPMSM. The experimental test data has been employed to support the performance of the proposed method. In the next part (Section 5.7), the thermal analysis of another case study, a 4-kW motor (the case study from Chapter 4), is studied based on the proposed model as further verification. In this case, the performance of the proposed thermal method is verified by 3D FEM-based thermal analysis due to lack of experimental data for this case study.
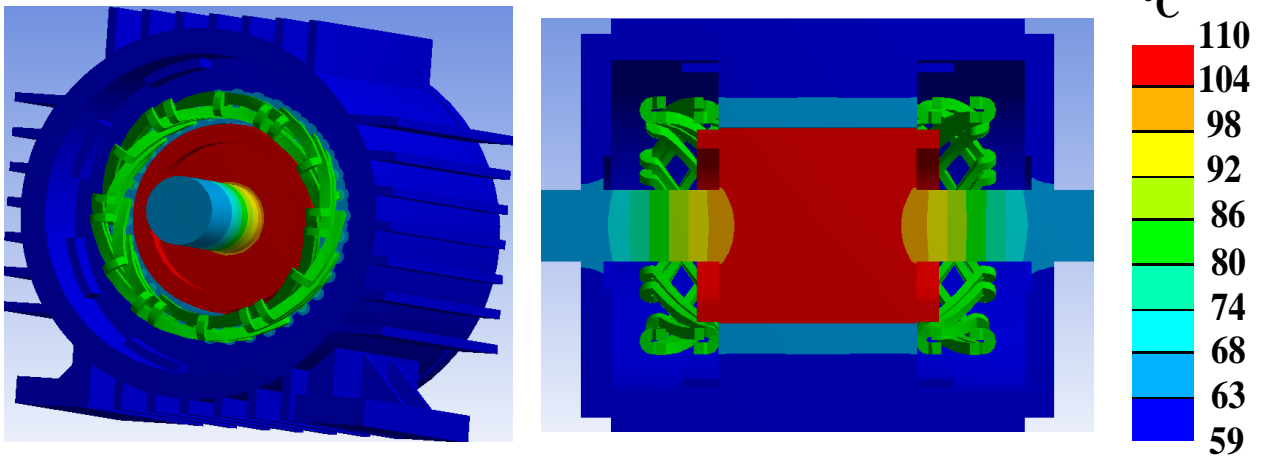
a.   3-kW IM
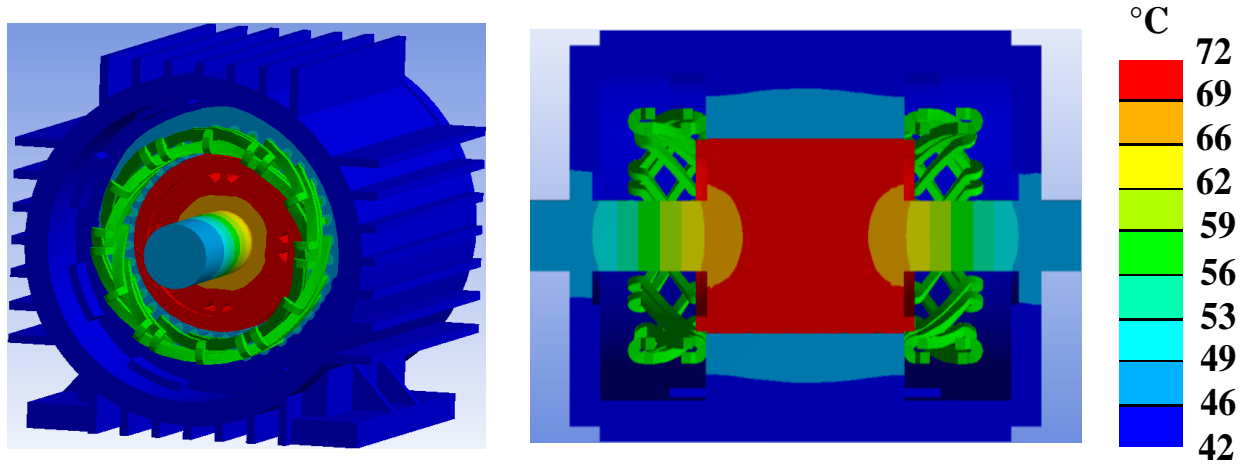
b.   LSPMSM @ 3-kW
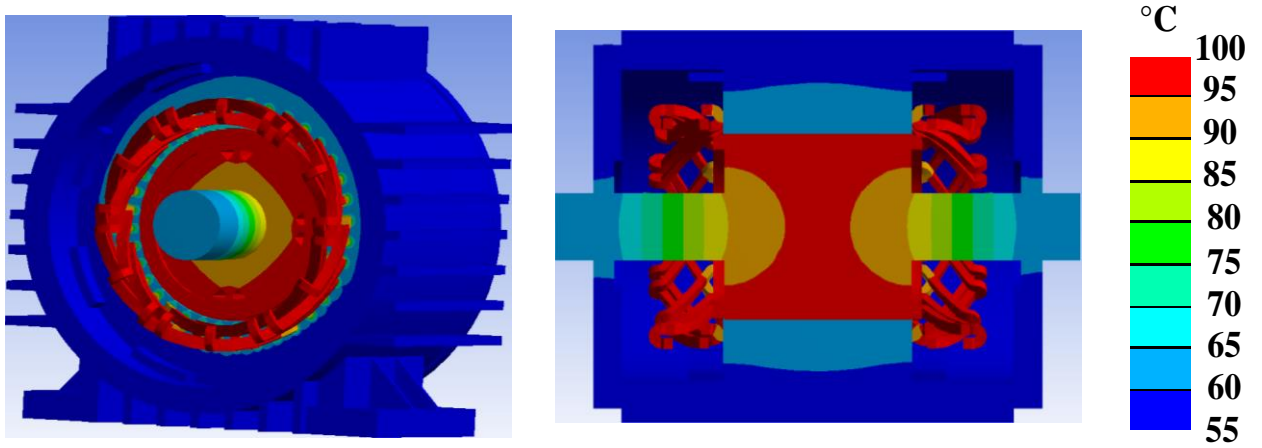
c.   LSPMSM @ 4.2-kW

Figure 5-14. 3D temperature distribution of the 3-kW IM and the LSPMSM at 3- and 4.2-kW at under 415V, 50 Hz.

5.7 Thermal Analysis of 4-kW IM and LSPMSM (further verification)

5.7.1 Analysis Strategy

In this part, the 4-kW LSPMSM and the 4-kW commercial IM (discussed in Chapter 4) are studied in terms of thermal behaviour using the proposed lumped thermal model. Temperature affects machine performance and, hence, studying the temperature dependency of the performance parameters has been a subject of research [190]-[191]. The designed 4-kW LSPMSM is studied to provide the maximum achievable output power in the same frame size as the 4-kW IM under rated condition 415 V, 50 Hz. The finite-element analysis (FEA) is used to study the motors' performance. Thermal analysis of the motors is studied using the proposed method and FEM-based thermal model to verify the accuracy of the proposed method.

5.7.2 Electromagnetic Results Discussion (FEA)

The electromagnetic analysis of the LSPMSM providing 4-kW and 6.5-kW is compared with the 4-kW IM. This section predicts how the LSPMSM performs in the transient and the steady-state when it provides 6.5-kW in the same frame size as the 4-kW IM. The steady-state performance, particularly loss variation analysis of the motor components, in this section will give a useful insight into predicting thermal behaviour of the components.

5.7.2.1 Starting performance

In this section the starting capability of the IM and the LSPMSM are compared with the aim being to show the performance of the LSPMSM providing 6.5-kW in comparison with the 4-kW IM. The start-up transients of the motors are presented in Figure 5-15. The zoomed-in view of the curve indicates that the IM reaches steady-state faster than the LSPMSM. The LSPMSM can successfully start the 6.5-kW load but has a longer start-up time in comparison with 4-kW IM and the LSPMSM providing 4-kW.

5.7.2.2 Steady-state synchronous performance

Figure 5-16 shows the FE calculated LSPMSM torque versus current angle characteristics at currents of 5A and 9A, which correspond to output powers of 4-kW and 6.5-kW. For the 5A/4-kW case, the machine was simulated both with magnets to find the net torque and without magnets to find the reluctance torque. The magnet torque was found by the difference between these results. The maximum value of the electromagnetic torque occurs at a current angle of about 60 electrical degrees. Figure 5-17 compares the performance parameters of the IM at 4-kW and the LSPMSM at the rated load (4-kW) and overload (6.5-kW). The efficiency of the IM at 4-kW is 86.6% while the LSPMSM efficiency at 4-kW is 92 % and at 6.5-kW is still 89%.
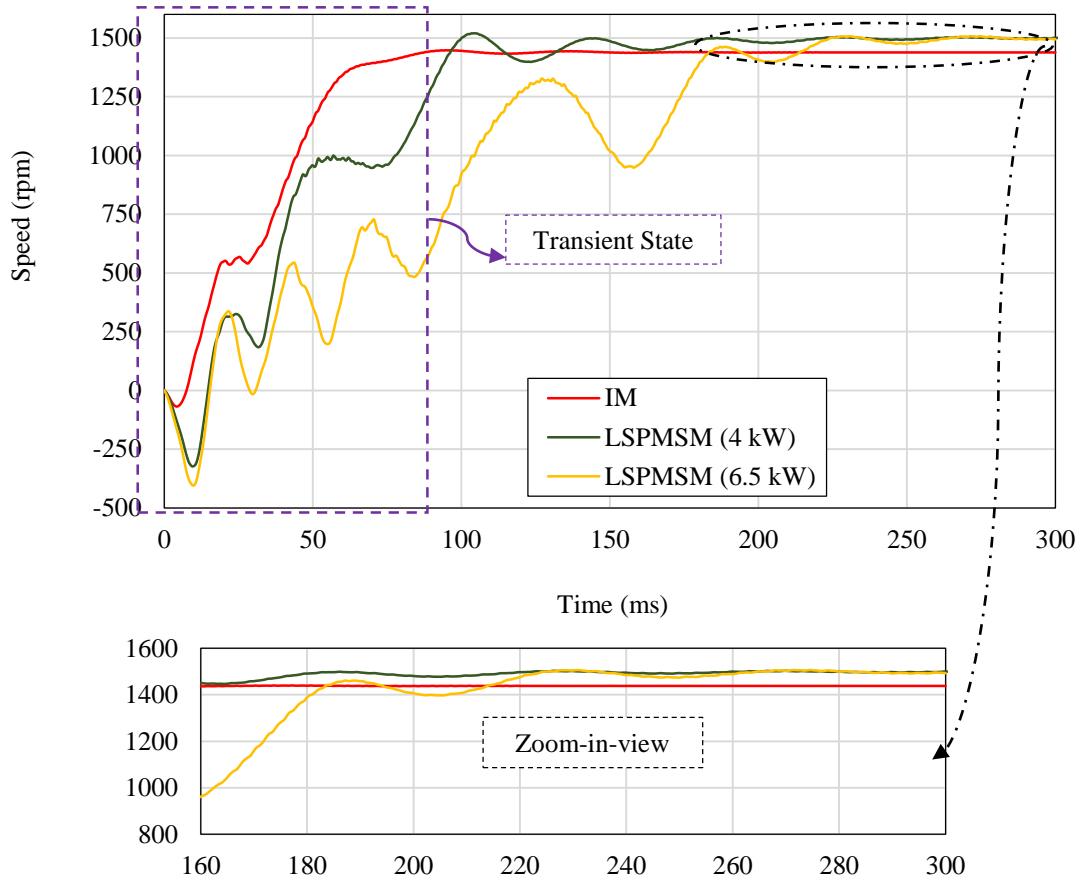
Figure 5-15. Speed-time responses of the IM with a 4-kW load and the LSPMSM with 4- and 6.5-kW loads.

Current Angle (el.deg)
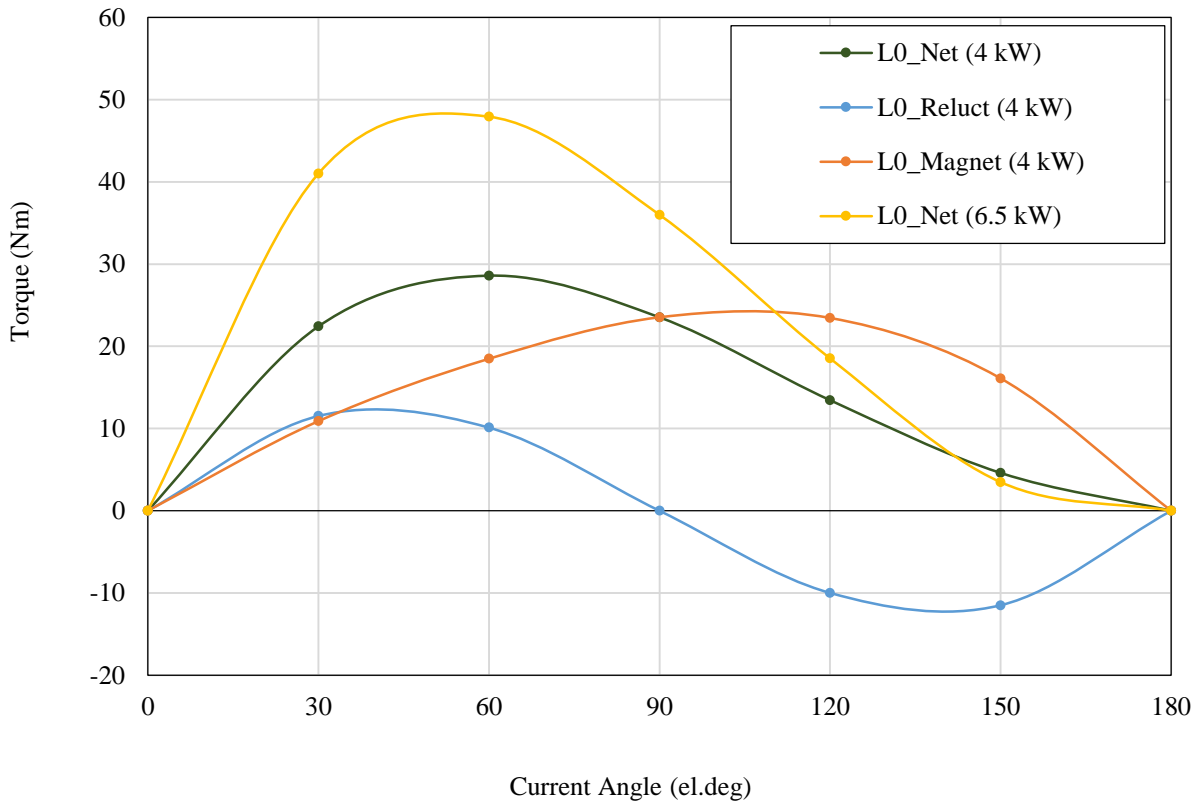
Figure 5-16. Synchronous torque versus current angle of the 4-kW IM and the 4-kW LSPMSM.
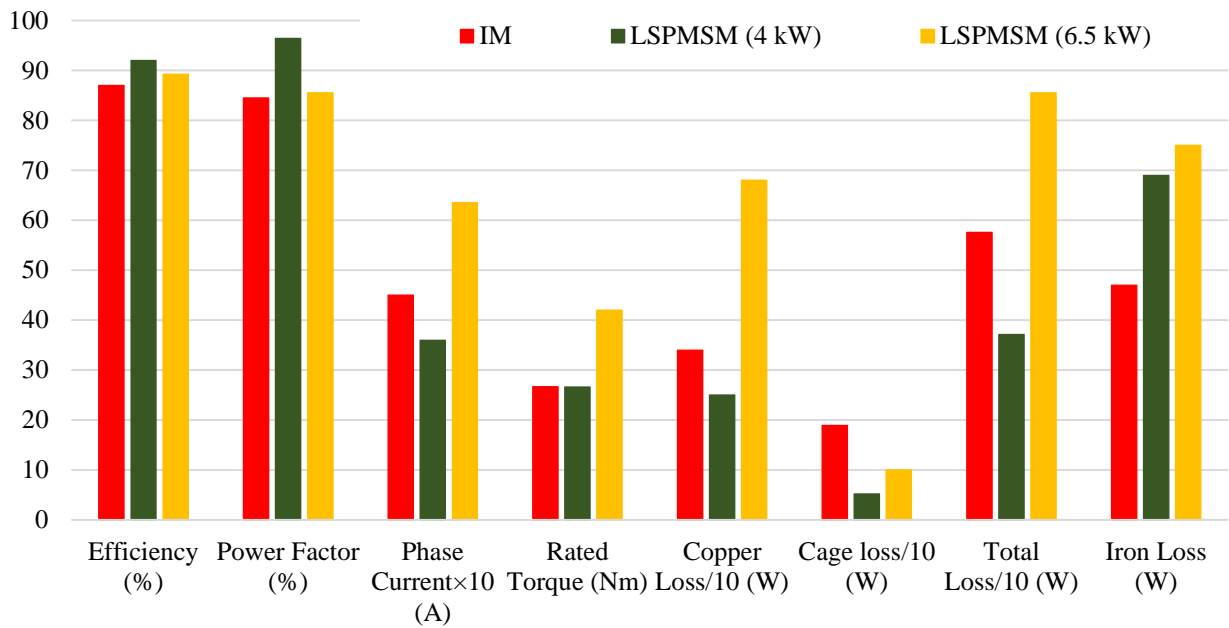
Figure 5-17. Performance parameter comparison of the IM and the LSPMSM when providing 4-kW and 6.5-kW.

Figure 5-18 shows the variations of the cage loss, stator copper loss and iron loss of the IM and the LSPMSM versus output power. Figure 5-18a compares the cage loss variations and it is seen that the cage loss of the IM is significantly higher than the LSPMSM, particularly at high output powers due to slip in the IM. This loss is small in the LSPMSM because the rotor of the LSPMSM rotates with synchronous speed. Figure 5-18b and Figure 5-18c show the winding copper loss and the iron loss of the case study as function of output power. For the same output power, the stator winding current in the LSPMSM is less than the IM due to the lack of magnetising current. It results in a lower copper loss and, hence, higher efficiency for the LSPMSM. The copper loss of the LSPMSM providing 6.5-kW is significantly higher than copper loss of the 4-kW. Therefore, it is expected the winding temperature of the LSPMSM at 6.5-kW should be higher than that of the 4-kW (this will be discussed in the next section).
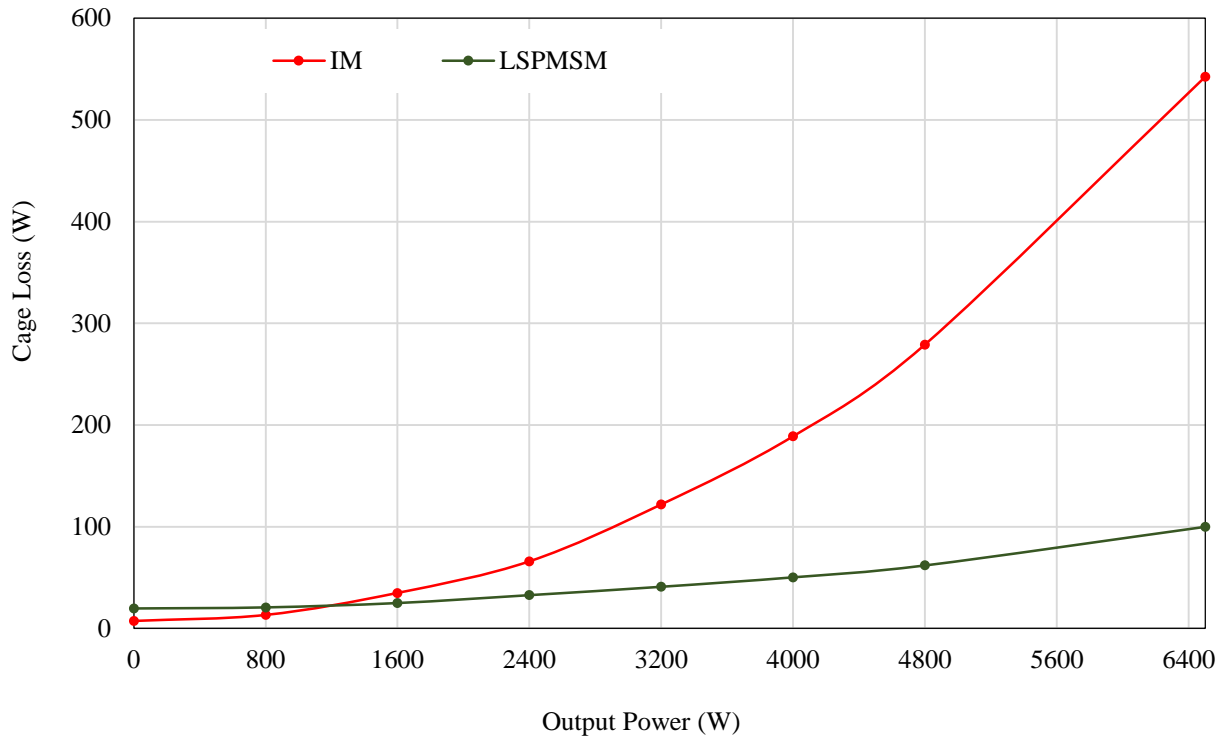
a.   Cage Loss
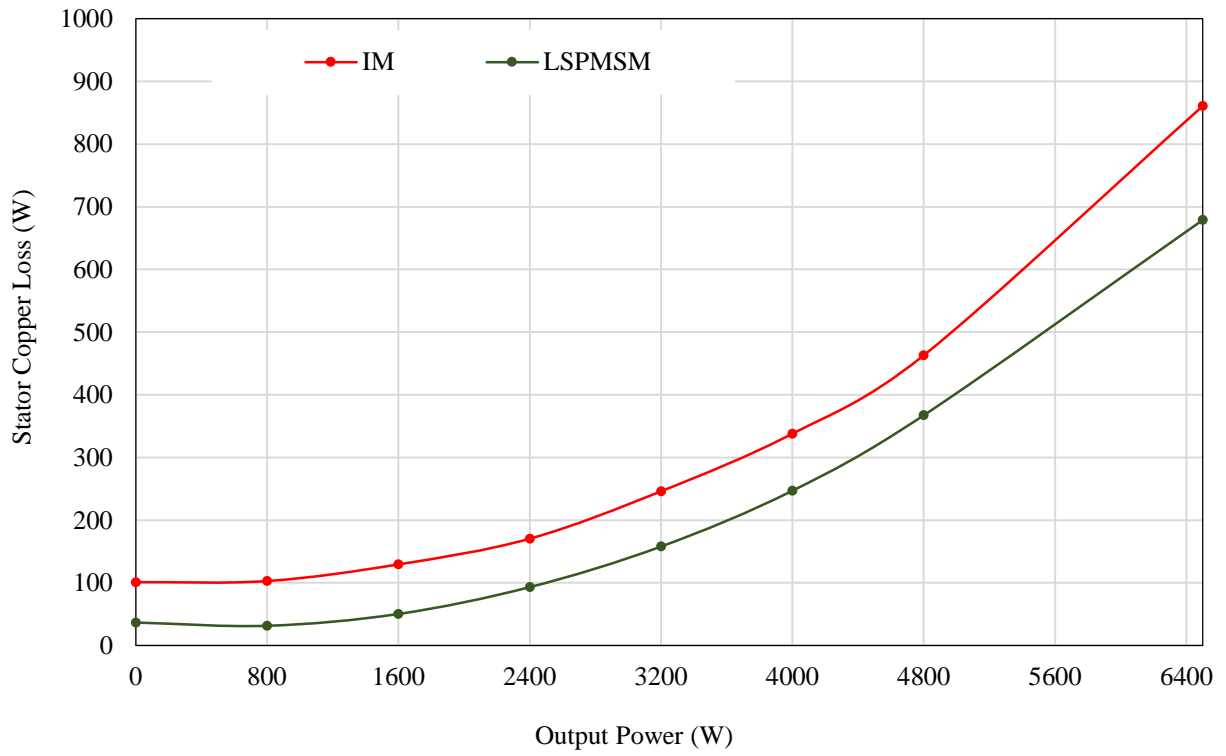
b.   Copper Loss
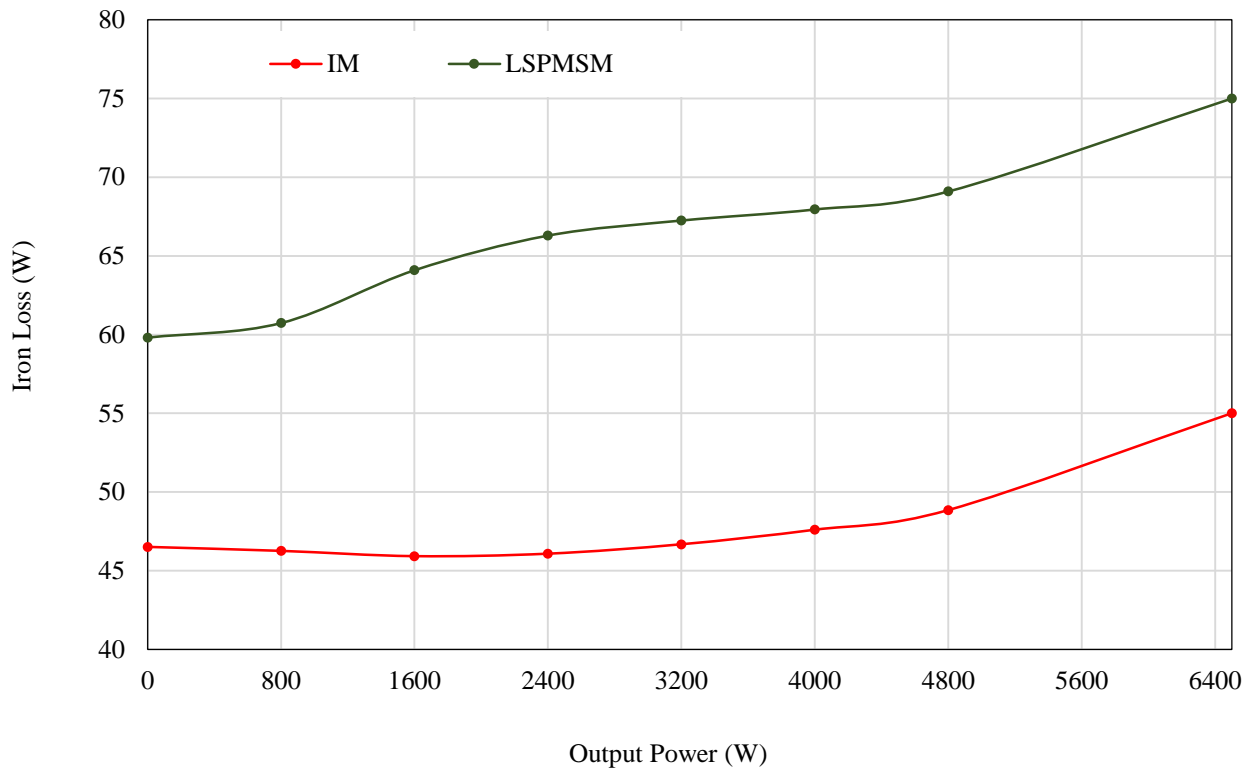
c.   Iron Loss

Figure 5-18. Loss variation versus output power for the IM and the LSPMSM.

5.7.3   Thermal Result Discussion

5.7.3.1 Thermal analysis of 4-kW case study by the proposed lumped-parameter model

The frame size and air gap length of the commercial 4-pole, 4-kW IM is the same as for the 4-pole, 3-kW IM studied in first part of this chapter. Hence, the value of the convection heat transfer coefficients of the main parts of the 4-kW IM and the LSPMEM are the same as those calculated for the 3-kW motors (same boundary conditions). Figure 5-19a to Figure 5-19c show the estimated absolute temperature variations versus time of the main parts of the 4-kW IM and the LSPMSM at 4-kW and 6.5-kW, respectively. It is seen that the winding temperature of the LSPMSM providing 6.5-kW is higher than both the 4-kW IM and the LSPMSM at 4-kW, as expected due to higher copper losses in the LSPMSM at 6.5-kW. The rotor temperature of the LSPMSM at 6.5-kW is comparable with the IM at 4-kW.
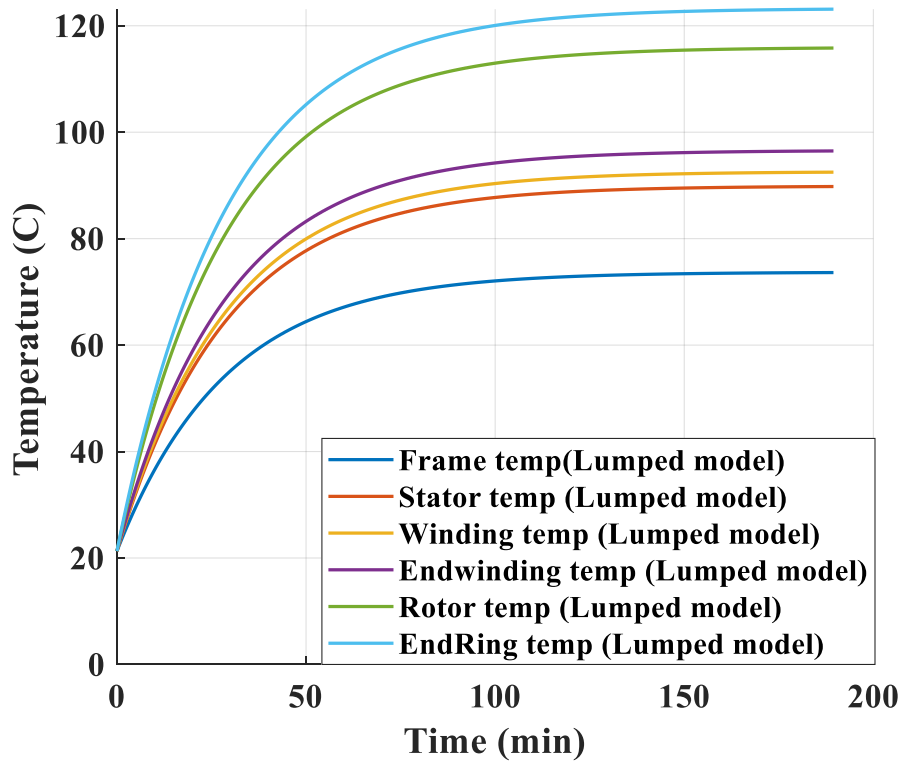
a. IM @ 4-kW

b. LSPMSM @ 4-kW

141
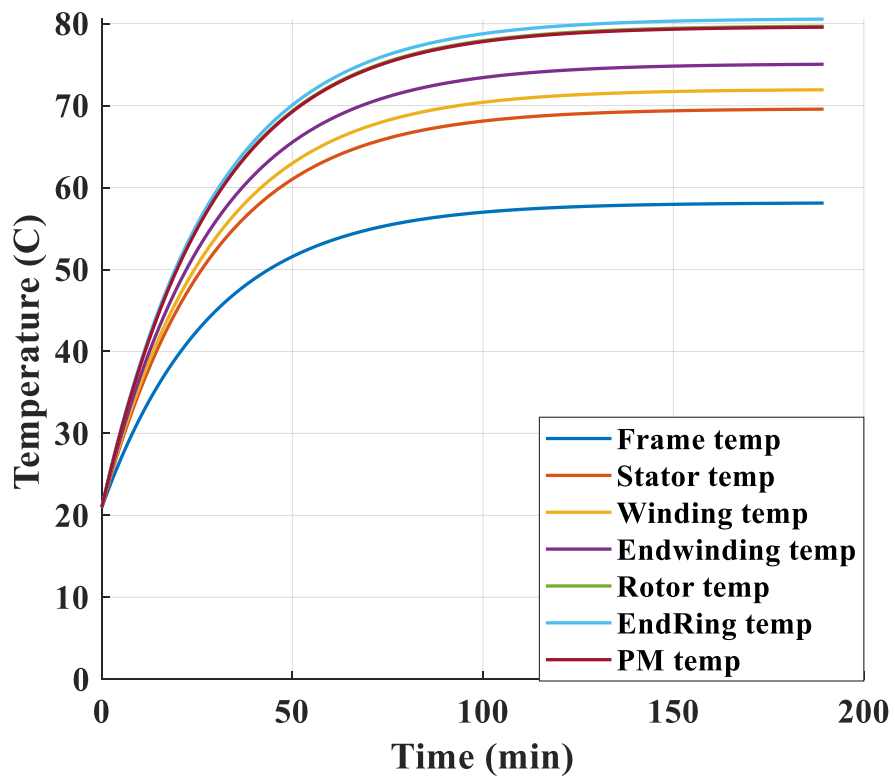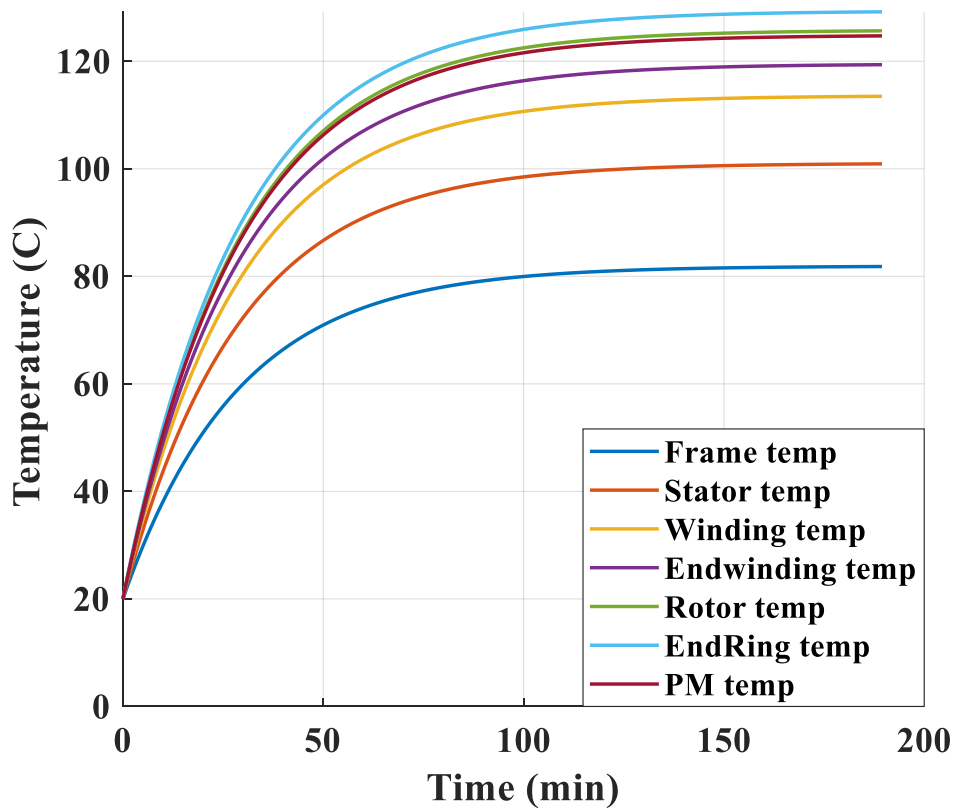
c. LSPMSM @ 6.5-kW

Figure 5-19. Absolute temperature estimated by the proposed lumped thermal model of the LSPMSM at 4- and 6.5-kW under rated condition 415 V, 50 Hz.

5.7.3.2 Thermal analysis of 4-kW case study by 3D FEM-based model

Figure 5-20 shows the temperature variations of the winding, the stator and the rotor as a function of output power for the IM and the LSPMSM as determined by 3D FEM-based thermal analysis. For the IM providing 6.5-kW, the large rotor losses cause the rotor to be significantly hotter than the stator winding. However, for the LSPMSM, the low rotor losses mean the rotor is comparable in temperature to the stator winding. The rotor temperature of the LSPMSM at 6.5-kW output power is comparable to that of the IM at 4-kW output power.

The 3D temperature distribution of the 4-kW IM and the LSPMSM in both rated load (4-kW) and maximum achievable output power (6.5-kW) conditions are presented in Table 5-7. The temperature differences between the rotor core and the rotor cage as well as the PM are very small, and the highest temperature appears in the end of the rotor bars. The overall operating temperature of the LSPMSM at 4-kW is significantly lower than the 4-kW baseline IM in the same frame size. The maximum temperature within the LSPMSM at 6.5-kW belonged to the rotor and end winding while the maximum temperature of the 4-kW IM is the rotor part.

The average temperature in all components of the IM and the LSPMSM are compared with the 4-kW IM (as the baseline). There is a 17 °C drop in the stator winding temperature of the LSPMSM at 4-kW, while the stator winding temperature of the LSPMSM at 6.5-kW increased 35 °C. The

142

temperature of the rotor, including cage and core, of the LSPMSM at 4-kW dropped by 45 °C while there was a slight increase of 4 °C for the rotor of the LSPMSM at 6.5-kW compared to the 4-kW IM. Therefore, the LSPMSM provides 6.5-kW with increased stator winding temperatures but comparable rotor temperatures compared with the 4-kW IM in the same frame size.
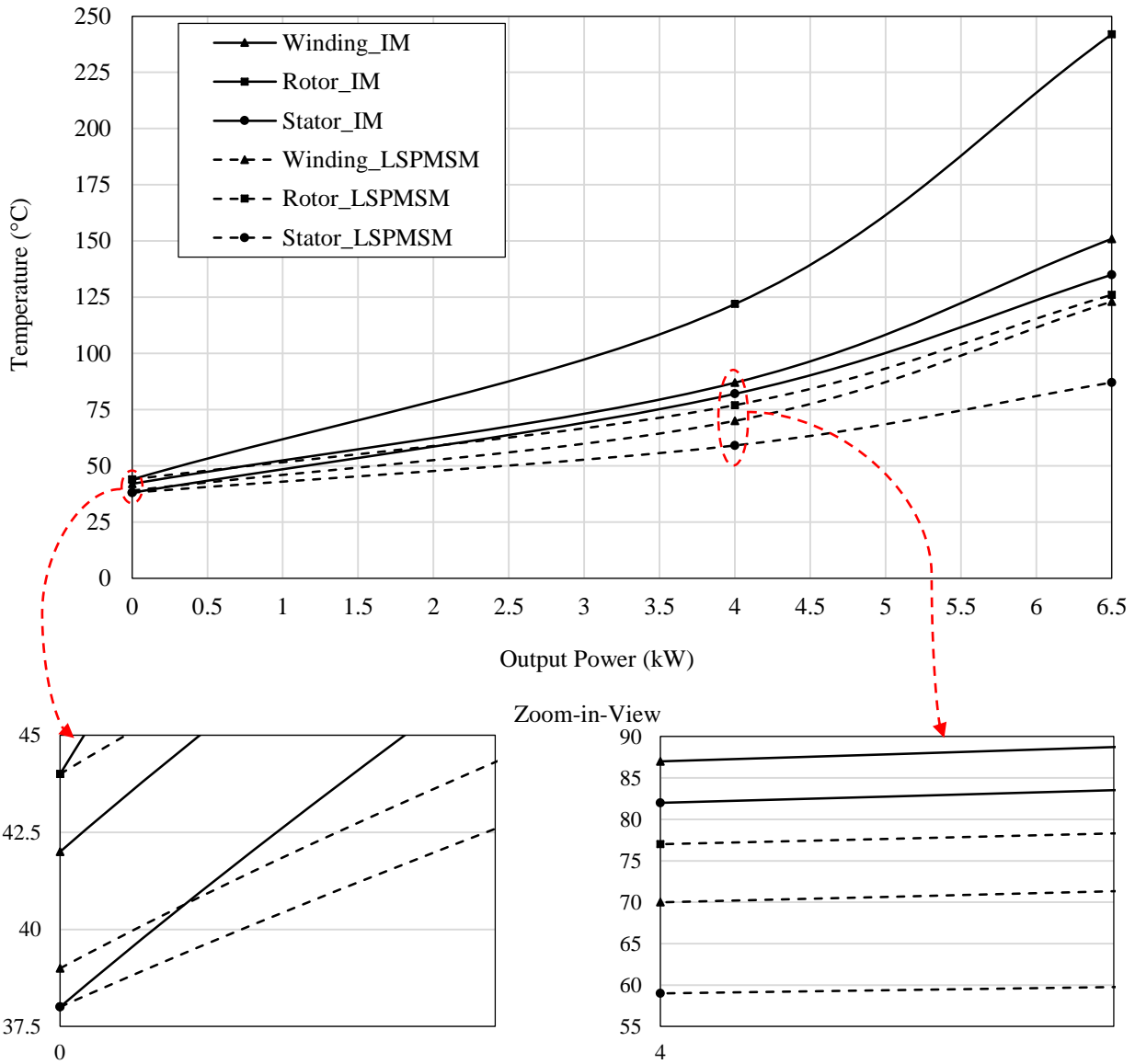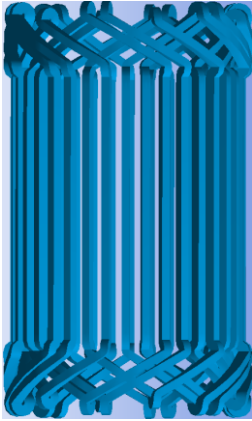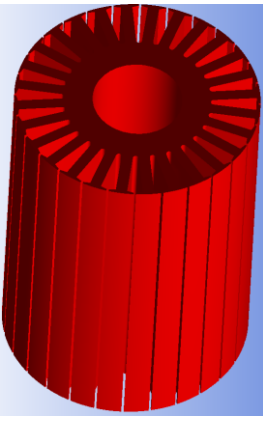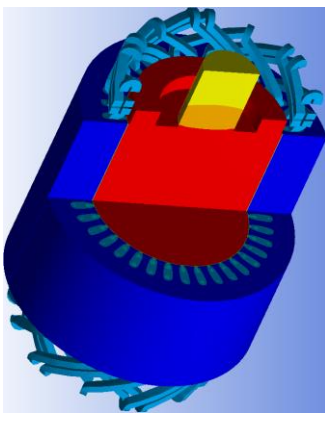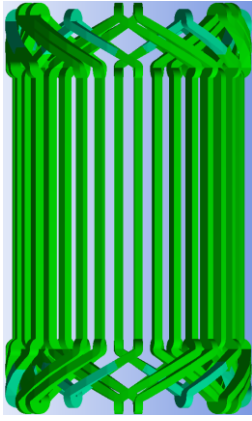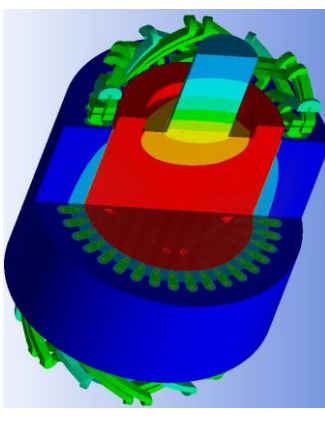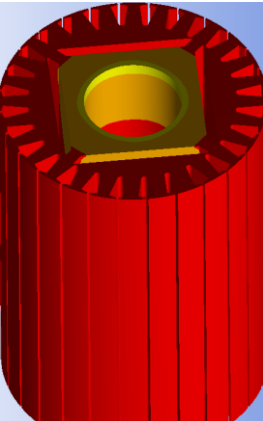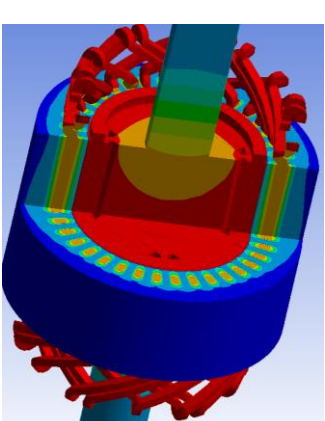
Figure 5-20. Temperature variations of the winding, the rotor, and the stator versus output power for the IM and LSPMSM.

Table 5-7. Temperature distribution of the 4-kW IM and LSPMSM@ 4- and 6.5-kW with same frame size.

Components / Motors type	Winding	Rotor	Overall	Color Bar
IM @ 4-kW				°C 125 120 115 110 105 100 95 89 84 78
LSPMSM @ 4-kW				°C 78 76 74 72 71 70 67 64 61 58
LSPMSM @ 6.5-kW				°C 128 123 118 113 108 103 98 93 88 83

The temperature rise of the main parts as estimated by the proposed method and predicted by 3D FEM-based model is compared in Table 5-8 to Table 5-10. There is good agreement between the estimated temperature of the design components with 3D FEM-based thermal analysis results. It verifies the accuracy of the proposed thermal method in estimating the temperature of the LSPMSMs.

The electromagnetic and thermal simulation results show that the 4-kW LSPMSM operates with higher efficiency and lower temperature than the IM at rated condition. Also, the designed LSPMSM provides 6.5-kW in the same frame size of the 4-kW IM with higher efficiency and lower maximum temperature.

Table 5-8. Temperature rise of main components of 4-kW IM under 415 V, 50 Hz.

Components	Proposed lumped-parameter model	3D FEM-based model
Frame	53	48
Winding	72	67
End winding	76	70
Rotor core	96	98
End ring	103	104

Table 5-9. Temperature rise of main components of 4-kW LSPMSM under 415 V, 50 Hz.

Components	Proposed lumped-parameter model	3D FEM-based model
Frame	38	37
Winding	51	50
End winding	54	52
Rotor core	59	56
End ring	60	58

Table 5-10. Temperature rise of main components of 6.5-kW LSPMSM under 415 V, 50 Hz.

Components	Proposed lumped-parameter model	3D FEM-based model
Frame	60	57
Winding	95	98
End winding	101	103
Rotor core	107	104
End ring	110	108

5.8 Conclusion

In this chapter, an analytical thermal model has been proposed for line-start permanent magnet synchronous motors (LSPMSM) based on the lumped-parameter method. Hence, a thermal circuit model was proposed for the IM and, as there is not a considerable difference between the LSPMSM and the IM, the thermal circuit model was tuned to a LSPMSM. To verify the performance of the proposed thermal model, a 3D FEM-based thermal analysis was conducted for case studies. The LSPMSMs were designed based on commercial IMs (3- and 4-kW) using some modifications in the rotor with same stator, winding and frame size. Electromagnetic performance of both motors was studied using FEA, and the LSPMSMs were studied to figure out the maximum achievable output power in the same frame size. Also, their operating temperature were compared with the baseline IMs.

In the first part of the chapter, an extensive discussion of the proposed methodology was presented for a 3-kW case study (IM and LSPMSM). The 3-kW IM was experimentally tested at three voltage levels (under, rated and over) and two frequencies (50 and 60 Hz) to validate the simulation results estimated by the proposed thermal model and FEM-based model. The results indicate that the performance of the proposed lumped thermal model is in good agreement with the FEM-based model and experimental tests. The temperature of the LSPMSM at 3- and 4.2-kW (maximum achievable output power for the LSPMSM) was estimated by the proposed thermal model for the LSPMSMs and verified by 3D FEM-based thermal analysis. It showed that the designed LSPMSM is able to provide 4.2-kW in the same frame size of the baseline 3-kW IM with higher efficiency and a comparable overall temperature.

In addition, the thermal analysis of a 4-kW case study (IM and LSPMSM) was investigated by the proposed thermal model as a further verification in the dedicated section. The 3D FEM-based steady-state thermal model of the designs was studied to verify the performance of the proposed thermal model. Likewise, there was good agreement between the proposed analytical thermal method with the 3D FEM-based thermal model for the case study 4-kW IM and LSPMSM. In addition, it revealed that the designed LSPMSM is able to provide 6.5-kW in the same frame size of the baseline 4-kW IM with successful synchronisation, higher efficiency, and comparable overall temperature.

6. CHAPTER 6

6. CONCLUSIONS AND RECOMMENDATIONS FOR FUTURE STUDIES

6.1 Conclusion

This thesis was an industry-framed project to design a LSPMSM based on a commercial IM to improve the efficiency of the motor (studied in Chapter 3). As it aimed to use the same housing, there were manufacturing constraints such as using the same stator and winding for the LSPMSM. The LSPMSM was designed based on modifications to the rotor of the IM. It was targeted to meet the IEC super premium efficiency (IE4) standard with good starting performance. Knowing that a focus only on steady-state performance causes degradation in starting performance, an aim was to implement an optimization with a focus on both transient and steady-state. Hence, a multi-objective optimization based on FEM was studied to optimize the initial LSPMSM to improve the efficiency and starting torque as representatives of steady-state and transient performance, respectively. The optimization was conducted by two different optimization approaches to present a comprehensive optimization study. This part of the project was successfully completed, and the optimum LSPMSM not only met IE4, but its starting torque was comparable with the benchmark IM. The only disadvantage recognised in this part was time of optimization by FEM. Optimization implementation using FEM is time-consuming and, hence, a follow on aim was to propose a faster method that was comparable with FEM in terms of accuracy.

The next step of this thesis proposed an analytical electromagnetic and thermal design, analysis, and optimization process of LSPMSMs. Hence, this research was divided into two parts: (a) electromagnetic analysis (studied in Chapter 4), and (b) thermal analysis (studied in Chapter 5). The electromagnetic part was divided into two phases: (a) design and analysis, (b) optimization. In the design and analysis phase, an analytical design and analysis method based on machine sizing techniques of IMs and PM motors was developed. Hence, an IM and an IPM were designed based on the developed sizing equation methods and the performance of them was extensively analyzed using FEA. Next, the LSPMSM was designed using a combination of the rotors of the IM and the IPM. The LSPMSM used the same stator of the IM and the hybrid rotor of the LSPMSM was designed by combining the rotors of the IM and the IPM. The combination process included inserting the interior permanent magnet in the rotor core and modifying the induction cage of the IM to provide a successful start-up. The configuration of the permanent magnet locations and volume and rotor cage bar shape were calculated based on sizing equations to reach a balance between starting and synchronization performance. Then, the performance parameters of the LSPMSM were estimated analytically by the developed method. Using the dimensions of the designed LSPMSM extracted from the proposed design, a 2D FEA was studied to verify the performance of the developed method. There was good

agreement between the results estimated by the analytical method and FEA for the two different motor ratings studied, i.e., 4-kW 4-pole and 1-kW 8-pole.

In the optimization phase, an analytical optimization approach was proposed to design an optimum LSPMSM based on the developed design method. The optimization strategy was based on a combination of the optimized IM and PM motor. The improvement focused on the transient and the steady-state performance of the LSPMSM. Since LSPMSM performance when starting is like an IM motor and, in the steady-state, its performance is like a PM motor, the optimization strategy was to optimize the IM and PM motor individually, and then combine them to obtain an optimum LSPMSM. The IM aimed to improve the starting performance via maximizing starting torque and the cage bar dimensions were selected as optimization variables. The PM motor was optimized to maximize efficiency and the PM dimensions were the optimization variables. There were constraints in each optimization to keep a balance between starting and synchronization performance. To verify the performance of the proposed optimization method, the initial LSPMSM design was optimized by FEM-based optimization under the same optimization conditions. The performance of the optimum design extracted from the proposed method was analyzed by 2D FEA and then compared with the optimized design by FEM for an accurate verification. The results of this study showed that the proposed optimization method can generate an optimum LSPMSM comparable with FEM optimisation in a much shorter time than FEM optimization techniques. In fact, the proposed analytical design and optimization method is a fast and reliable technique to design an LSPMSM and it can be used as a substitute in performance analysis and optimization implementation for FEM, which is time-consuming and computationally intensive.

The thesis then shifted to present an analytical thermal model based on the lumped-parameter thermal network to analyse the thermal behaviour of the LSPMSMs. Hence, a lumped-parameter thermal circuit was proposed for the LSPMSM based on a developed thermal circuit of the IM. The contribution to knowledge from this part was the development of a thermal model of the IM and then modifying the model to be a fine-tuned model for the LSPMSM. The model included a novel thermal circuit model of the LSPMSM and a method to calculate the temperature of the main parts based on the thermal resistance, calculated based on the lumped-parameter network, and losses (as heat generation source), calculated in the electromagnetic part of the platform. Also, a 3D FEM-based thermal analysis was studied to present a comparison between the two methods.

The performance of the developed lumped-parameter thermal model of the IM was verified with a 3D FEM-based model and all simulations were validated with experimental tests for a case study (3-kW, 4-pole IM). Then, the analytical thermal model of a LSPMSM was proposed based on slight modifications in the IM thermal model. The modification includes adding PM, adjusting the rotor bars and considering different rotor speeds in computations. The inputs for the proposed lumped

thermal model are the dimensions of the design parts in order to calculate the thermal resistance of each part and the main loss values as heat generation in each node. The proposed analytical thermal method was verified by a 3D FEM-based thermal model for two case studies: 3-kW and 4-kW motors (IM and LSPMSM). The results indicated that the proposed thermal model could estimate the temperature of the main parts of the designs with a high accuracy and comparable with the 3D FEM-based model and experimental tests (for the 3-kW IM) in a time much shorter than FEM and experimental tests. The advantage of the proposed analytical thermal model is that it can be used in optimization studies where temperature of the design can be an objective for optimization. This removes the requirement to execute time-consuming methods like FEM and CFD analysis for this purpose.

The two parts of this thesis, 1) an analytical electromagnetic design, analysis and optimization method, and 2) an analytical thermal design and analysis method for LSPMSMs, when combined provide a novel electromagnetic and thermal design and analysis platform for LSPMSMs. The advantage of the proposed platform is that it can generate an optimum LSPMSM with complete electromagnetic and thermal performance analysis in a short time with accuracy comparable with FEM.

6.2 Recommendations for Future Studies

Improving the performance of line-start permanent magnet motors is a hot topic with extensive research in terms of electromagnetic performance improvement focussing on transient and synchronisation operation. However, there are research gaps in LSPMSM performance improvement research that can be taken as suggestions for future work. The potential studies in this field are presented in the following subsections.

6.2.1 Electromagnetic performance analysis

Although there are extensive optimization studies in LSPMSM electromagnetic performance improvement, there are places in this area that can be studied in future work.

6.2.1.1 Optimization study considering the stator and winding parameters as optimization variables

In the literature review (Chapter 2), the optimization strategies studied in LSPMSM performance improvement were discussed. It was recognized that most of the research has focused on rotor factors such as rotor bar and PM dimensions to improve LSPMSM performance, with very limited research considering stator factors such as the number of turns per slot and stator slot dimensions in the optimization of LSPMSMs, particularly using MOF optimization.

6.2.1.2 Multi-objective optimization study considering cogging torque

Cogging torque is a serious challenge in PM motors and is of great significance to consider cogging torque minimization in LSPMSMs. There were design methods to reduce the cogging torque in the LSPMSMs, but there is very limited work studying cogging torque reduction in a multi-objective optimization as one of the objectives.

6.2.2   Thermal performance analysis

There has been limited work studying the thermal behaviour of LSPMSMs whereas there has been extensive thermal analysis of IMs and PM motors in the literature. Hence, this is an area of research that has space to be considered in future works. Some suggestions in this area are discussed as follows:

6.2.2.1 Analytical transient thermal model of LSPMSM based on the lumped-parameter thermal model proposed in this thesis

Transient thermal analysis of the LSPMSM gives useful information that can be considered in implementing an optimization with a focus on reducing the risk of overheating in the transient state. The steady-state thermal analysis was studied in this thesis and transient thermal analysis can be modelled using the proposed thermal circuit model of the LSPMSM in this thesis considering thermal capacitance of the main parts.

6.2.2.2 Optimization study considering temperature dependency of the material as an optimization variable

The material used in an electric machine depends on temperature and their properties changes with increasing temperature. Hence, an area for research is the temperature dependency of the material in an optimization problem as an optimization factor to improve the accuracy of the optimization study in terms of temperature effect.

6.2.2.3 Multi-objective optimization study considering thermal performance of the design as a key optimization objective,

Based on the LSPMSM performance improvement literature, it was recognised a main focus has been on electromagnetic performance improvement. There is a lack of studies considering performance improvement of an LSPMSM in both electromagnetic and thermal performance. The proposed platform in this thesis can be used to improve LSPMSM performance with a focus on electromagnetic and thermal performance.

7. APPENDIX A

7. FURTHER RESULT DISCUSSION OF 4-kW IM

The proposed analytical design procedure based on the developed sizing equation techniques was extensively discussed in Chapter 3 and its performance was verified by FEM for two case studies (4-pole, 4-kW and 8-pole, 1-kW). In this section, an extended comparison between the developed analytical design method and FEM is studied in analysing the steady-state performance parameters of an IM. Hence, the 4-kW IM is selected as the case study in this section. Next, further dynamic results studied by FEA of the 4-kW IM are discussed.

7.1 Analytical Method vs. FEM for the 4-kW IM

Determining performance parameters of the motors based on the extracted equivalent circuit is a well-known strategy studied in [192]-[197]. It is feasible to approximate the parameters of the equivalent motor circuit from the manufacturer's data sheet [199]-[200]. To analyse steady-state performance parameters of the 4-kW IM, equivalent circuits (*EC*) of the motor are extracted by the analytical design method (sizing equation) and FEM. Resistance and inductance of the stator, rotor and magnetizing branch are the main EC parameters that need to be determined. In the following sections, the EC of the 4-kW IM is extracted based on both methods.

7.1.1 EC Extracted from FEM Tests

To extract a FEM-based equivalent circuit of a motor, it is tested based on the routine tests' procedure including no-load (TL=0) and locked-rotor (N_r=0) [201]. Then, the EC parameters are calculated based on the proposed method. The calculation process of the equivalent circuit parameters for the commercial 4-kW IM based on no-load and locked-rotor tests using FEA is as follows.

7.1.1.1 No-load test:

The no-load test is conducted by exciting stator winding with a 3-phase balanced voltage (rated voltage) at the frequency of 50 Hz. The slight input power delivered to the IM is due to friction loss, no-load copper loss, and core loss. This test is performed to calculate magnetizing branch parameters (R_c and X_m). These parameters are because of the stator and rotor iron losses containing hysteresis, eddy current and additional losses. Thanks to Ansys Maxwell we can directly extract iron losses, which depend on the stator and rotor material properties such as the specific iron loss, mass density, maximum flux density and iron losses coefficients [201]. The value of the iron coefficients like hysteresis, eddy current and additional coefficients are calculated based on the value of the mass, conductivity, maximum flux density and corresponding specific loss of iron at a specific frequency (50 or 60 Hz), which is normally reported by the manufacturer. Table **7-1** shows properties of the iron

151

steel (M470-50A) used in the 4-kW IM. Figure 7-1a and Figure 7-1b show BH curve of the steel and specific iron loss variations versus corresponding maximum flux density, respectively.

Table 7-1. M470-50A properties.

B_m (T)	Specific Iron Loss (W/kg)	ac (A/m)
0.1	0.03	65.6
0.2	0.12	83.8
0.3	0.25	94.1
0.4	0.42	103
0.5	0.61	110
0.6	0.82	118
0.7	1.05	127
0.8	1.3	136
0.9	1.57	147
1	1.87	159
1.1	2.21	177
1.2	2.59	205
1.3	3.01	255
1.4	3.53	370
1.5	4.13	718
1.6	4.78	1840
1.7	5.39	4370
1.8	5.82	8330

a.   BH curve

y = 1.759x² + 0.0586x + 0.0779
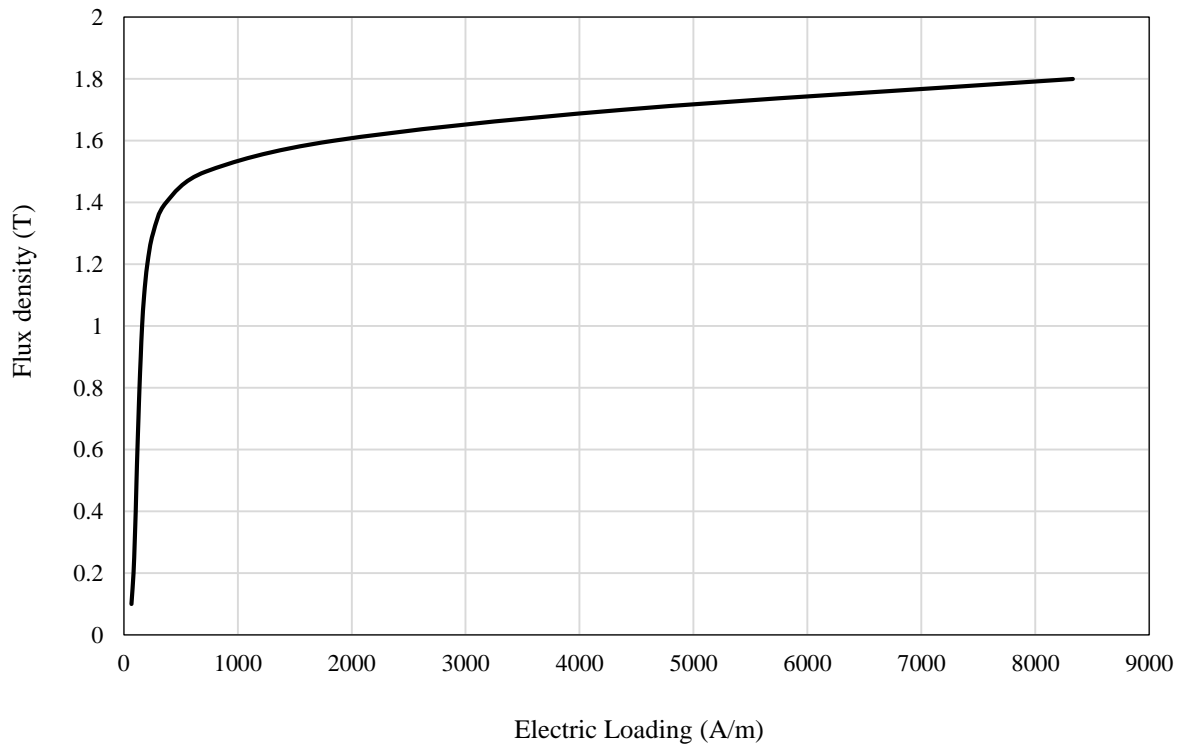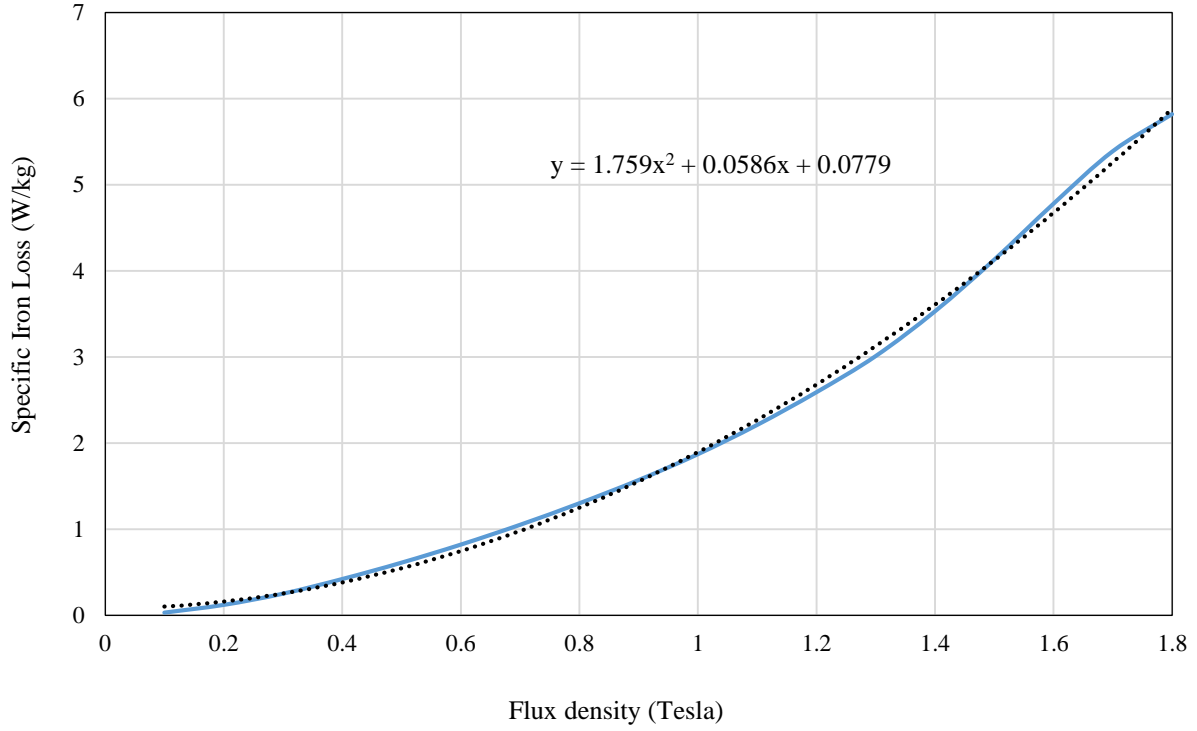
b.   Specific graph of the M470-50A vs flux density.

Figure 7-1. BH curve and specific iron loss variations vs flux density.

The iron loss of the motor was determined by FEA and the values of R_c and X_m are defined in Equations 7.1- 7.4.

$$\cos(\emptyset_{NL}) = P_{NL}/ (3 \times V_{ph} \times I_{NL}) \tag{7.1}$$

$$I_m = I_{NL} \times \sin(\emptyset_{NL}) \tag{7.2}$$

$$I_{mc} = I_{NL} \times \cos(\emptyset_{NL}) \tag{7.3}$$

$$R_c = V_{ph}/I_c \tag{7.4}$$

$$X_m = V_{ph}/I_m \tag{7.5}$$

The calculation process of the stator phase resistance including end winding effect was described extensively in Chapter 3. In the following section, the stator reactance and rotor resistance and reactance are calculated based on the locked-rotor test conducted using FEA.

7.1.1.2 Locked-rotor test:

The values of the leakage reactance and rotor resistance are determined by the locked-rotor test. The rotor is forced at a zero speed and the stator windings are excited with a small voltage to provide similar value of the rated current. The measured phase voltage and power are used to calculate EC parameters as follows:

$$\cos (\emptyset_{LR}) = P_{LR}/(3 \times Vph \times P_{LR}) \tag{7.6}$$

$$\sin (\emptyset_{LR}) = \sqrt{1 - \cos (\emptyset)^2} \tag{7.7}$$

$$Z_{LR} = V_{ph\_LR}/I_{LR} \qquad\qquad\qquad\qquad\qquad\text{(VII.8)}$$

$$R_r = Z_{LR} \times cos\,(\emptyset) - R_s \qquad\qquad\qquad\qquad\text{(VII.9)}$$

$$X_{LR} = Z_{LR} \times sin\,(\emptyset) \qquad\qquad\qquad\qquad\quad\text{(VII.10)}$$

$$X_r = 0.6 \times X_{LR} \qquad\qquad\qquad\qquad\qquad\quad\text{(VII.11)}$$

$$X_s = 0.4 \times X_{LR} \qquad\qquad\qquad\qquad\qquad\quad\text{(VII.12)}$$

The FEM-based EC of the 4-kW machine provided based on the no-load and locked-rotor tests in FEA is illustrated in Figure 7-2.

7.1.2   EC Extracted from Analytical Method

The calculation procedure for the EC parameters of the motor based on the analytical design method was discussed in Chapter 3. According to the analytical sizing equations and 4-kW IM characteristics, the EC of the 4-kW IM extracted from analytical sizing equations is presented in Figure 7-3. As expected, both ECs have similar values for their EC parameters. The steady-state performance parameters of the 4-kW IM are studied in the following section to compare the performance of the developed analytical design method with 2D FEM simulation.
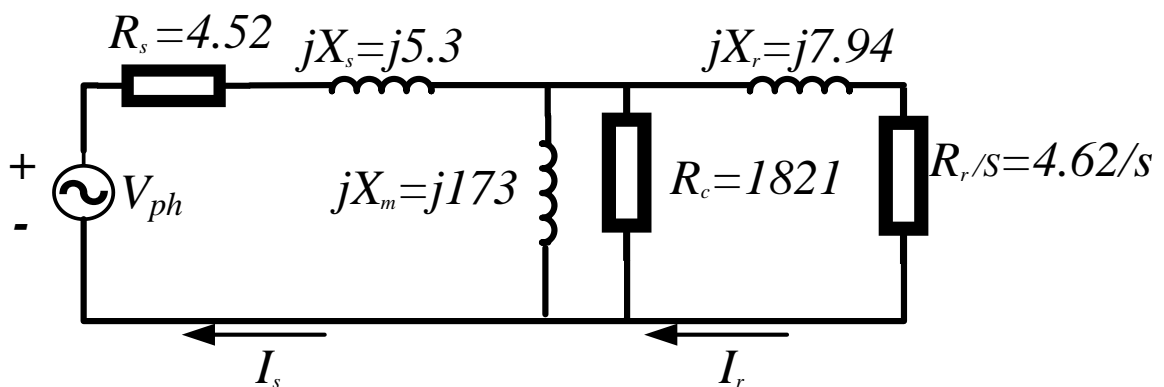
Figure 7-2. Equivalent circuit of 4-kW IM extracted from FEM tests.
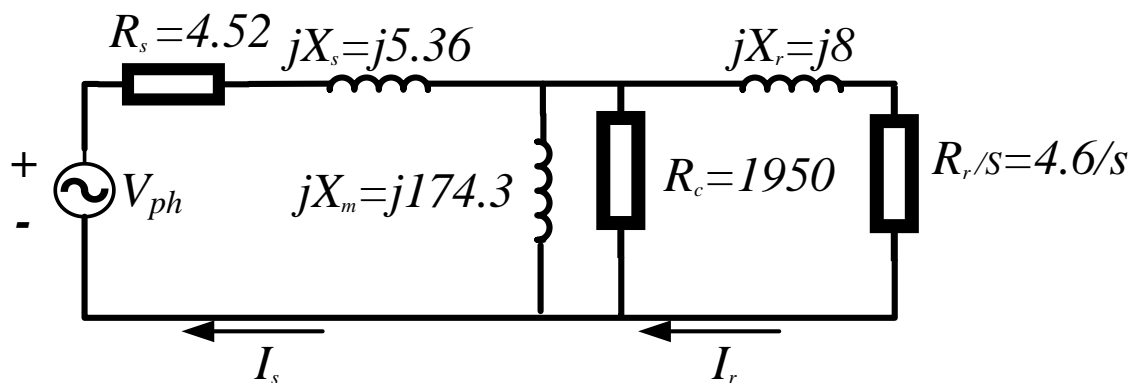
Figure 7-3. Equivalent circuit of 4-kW IM extracted from analytical sizing equations.

7.1.3 Comparison of Performance Parameters of the IM by Three Methods

Steady-state performance parameters of the 4-kW IM calculated by FEA, EC from FEM tests and EC extracted from the analytical method are studied in Figure **7-4**. Figure **7-4**a shows the torque vs speed of the motor for the three methods. Note that in the analytical method the torque is calculated as follows:

$$T_{em} = \frac{(3 \times Vph^2 \times R_r/s)}{(2 \times \pi \times n_s \times ((R_s + R_r/s)^2 + (X_s + X_r)^2))} \tag{VII.13}$$
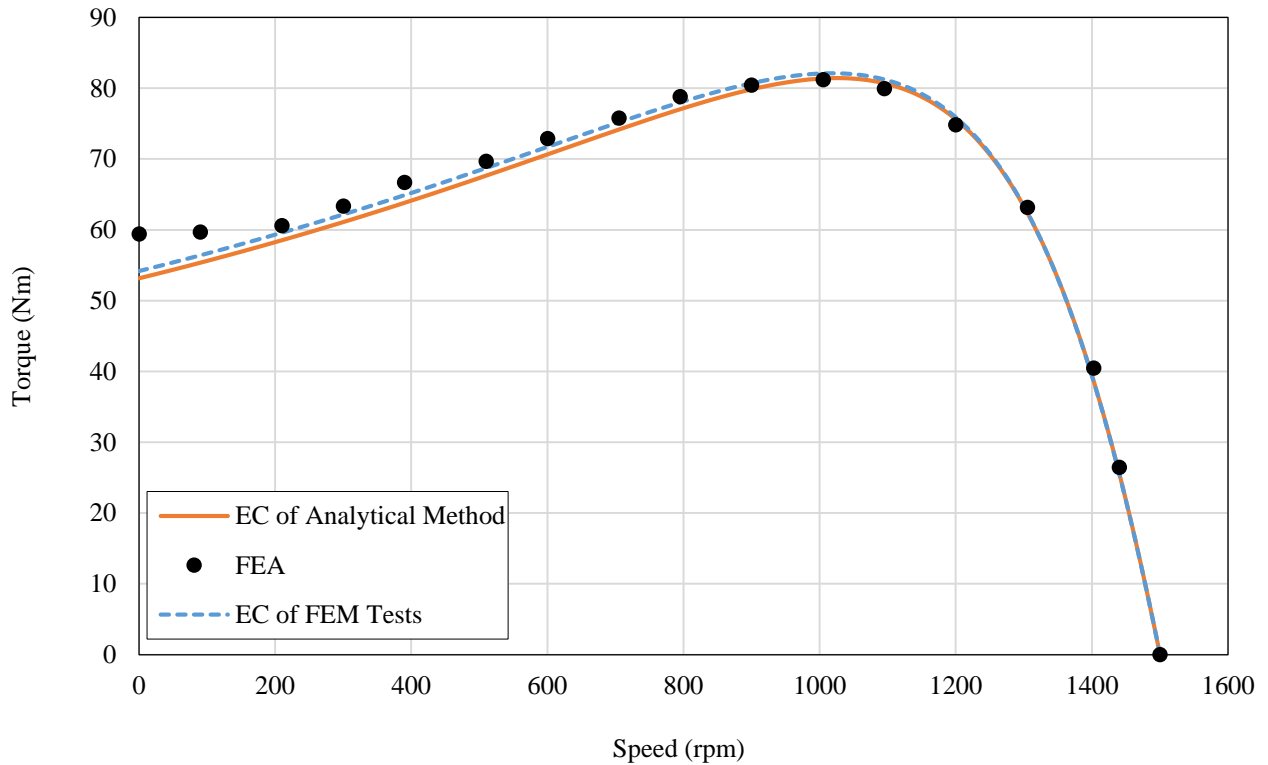
c.   Torque vs speed
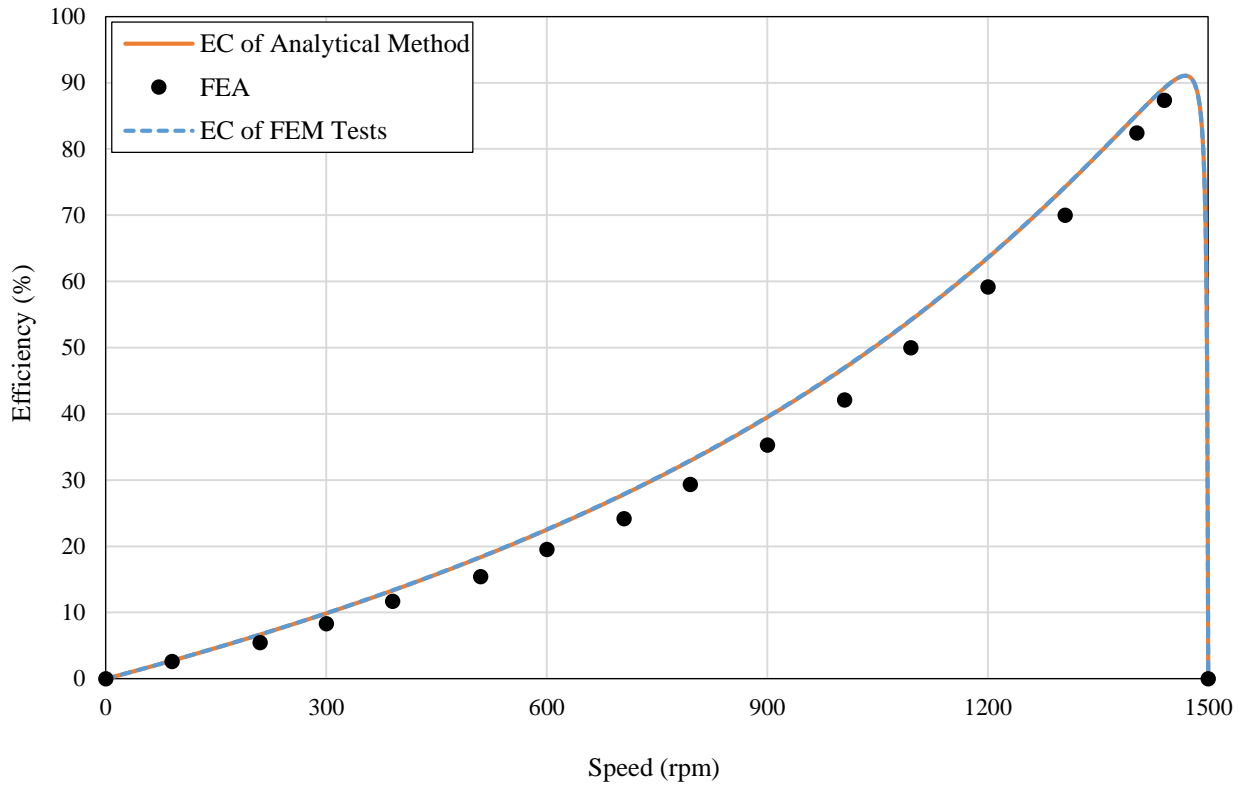
d.   Efficiency vs speed
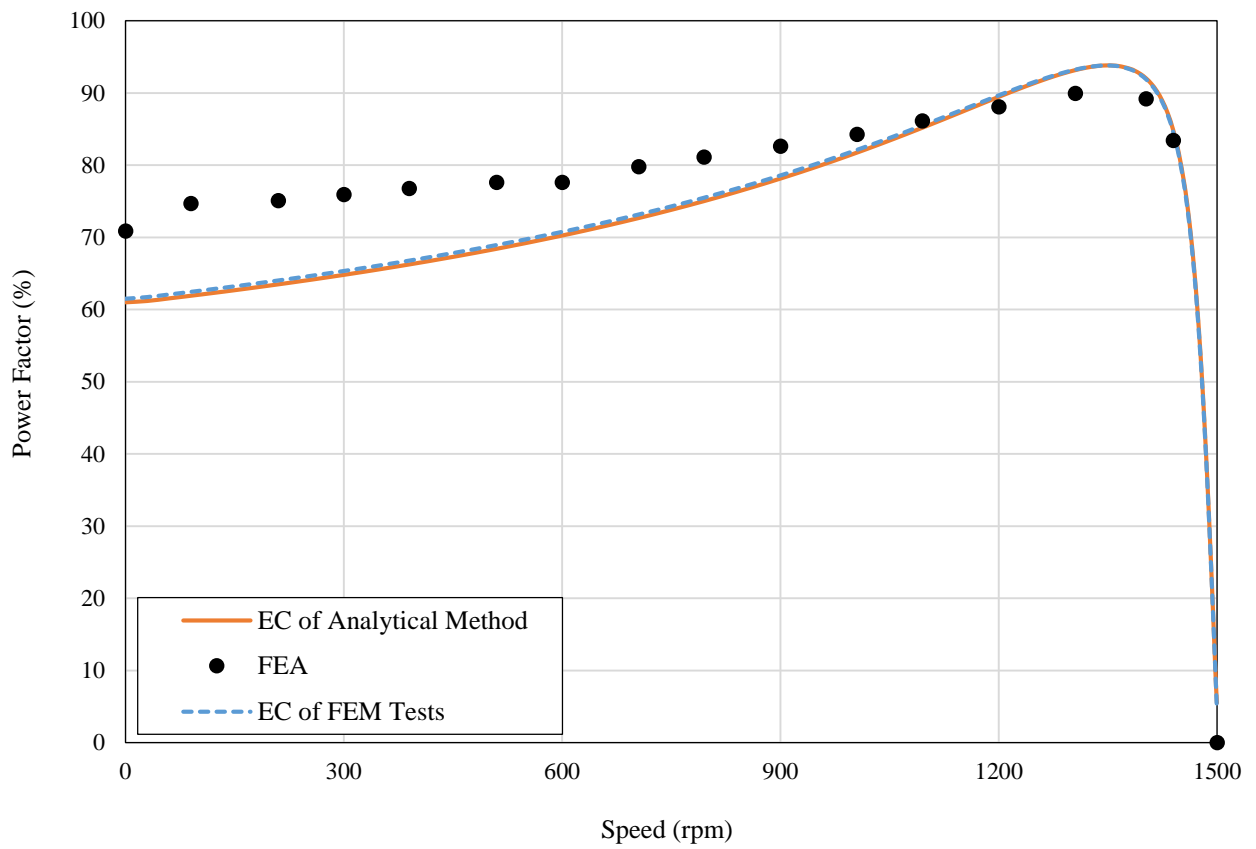
e.   Power factor vs speed
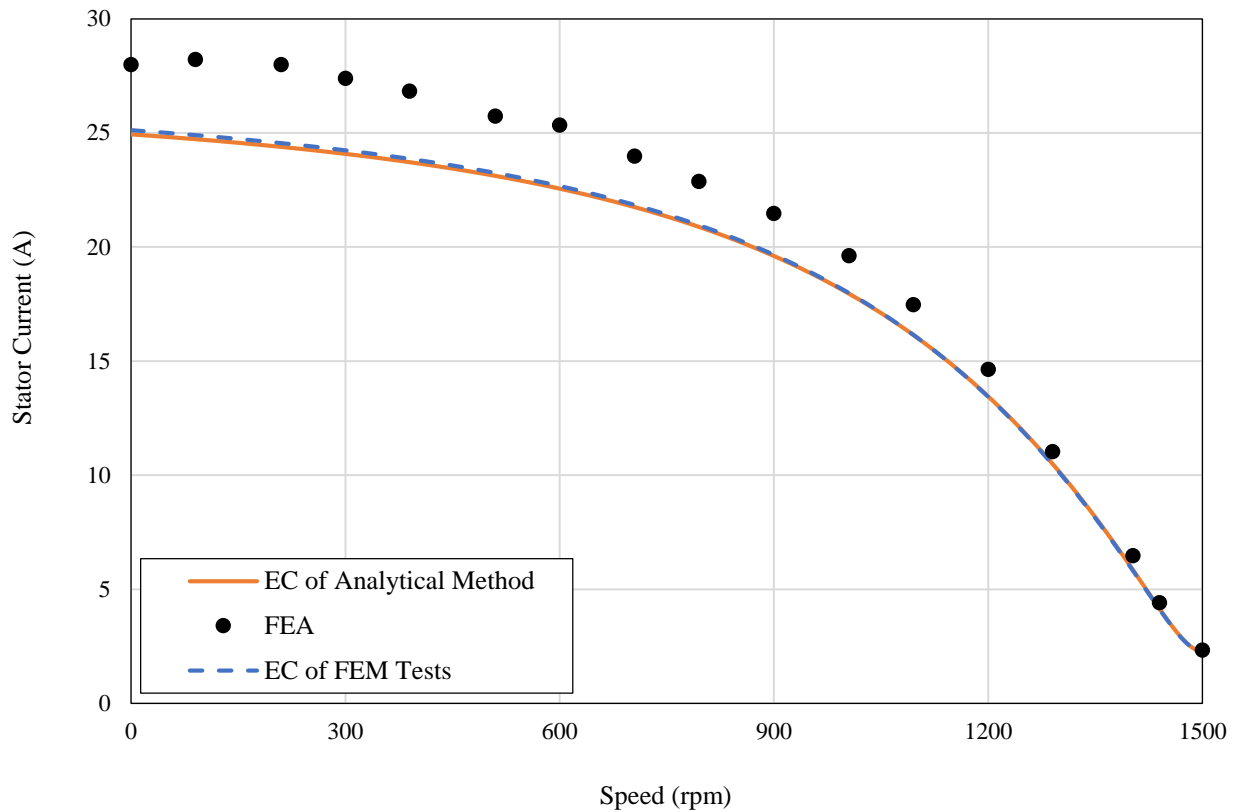
f.   Stator current vs speed

Figure 7-4. Comparison of steady-state performance parameters calculated by three methods as function of shaft speed.

Efficiency, power factor and current variations versus speed of the motor as determined by the three methods are compared in Figure **7-4**b to Figure **7-4**d. It is seen that there is good agreement between the developed analytical method and 2D FEA.

In Figure 7-5 the variation of the steady-state performance parameters as a function of output power (load) are studied. These parameters are computed using FEA, ECs extracted from FEM tests and analytical methods. It verifies the accuracy of the analytical method to analyse steady-state performance of an IM in a time much shorter than a 2D FEA simulation. Figure 7-5a illustrates the efficiency variations versus output power. FEA indicates the efficiency drops in overload (120% of the rated load) and it has highest value at 75% of the rated load. It is seen that the developed analytical design predicted similar performance to the 4-kW IM.

Variations of the power factor, rotor speed, copper loss and rotor cage loss are studied in Figure 7-5b to Figure 7-5e, and they illustrate the capability of the developed method in analysing steady-state performance of an IM under different load conditions.
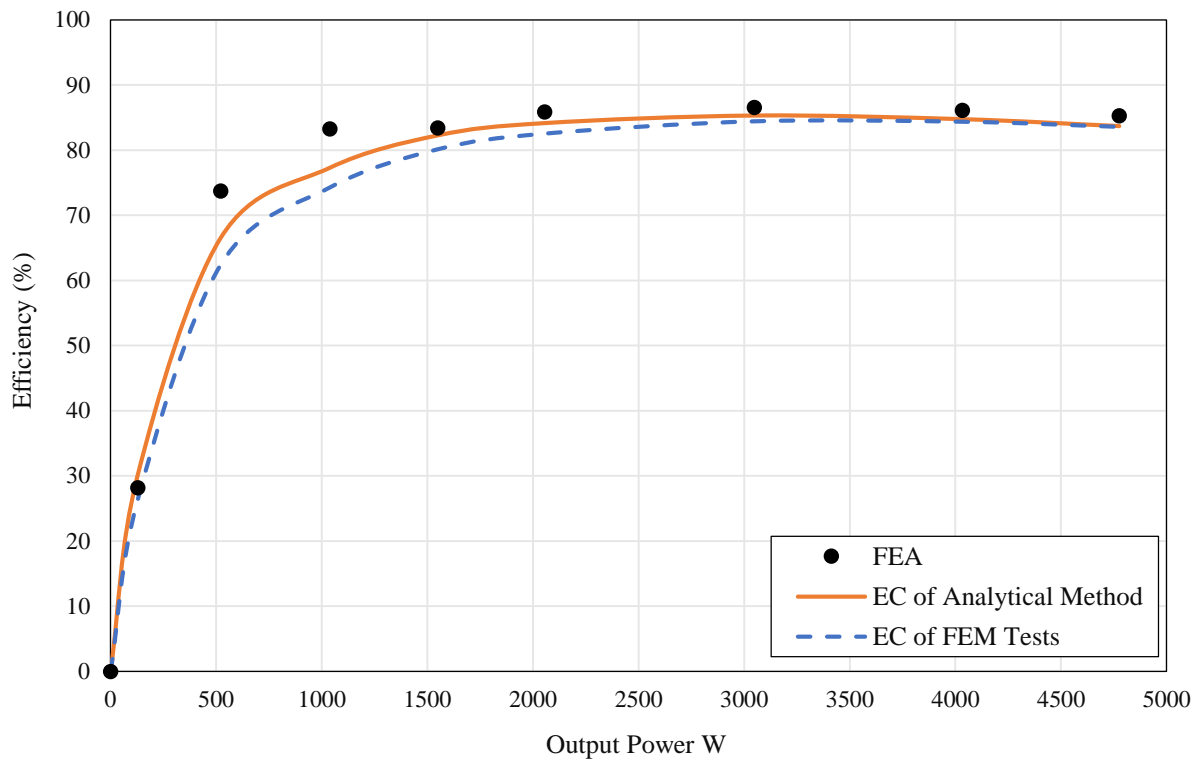
a. Efficiency vs output power
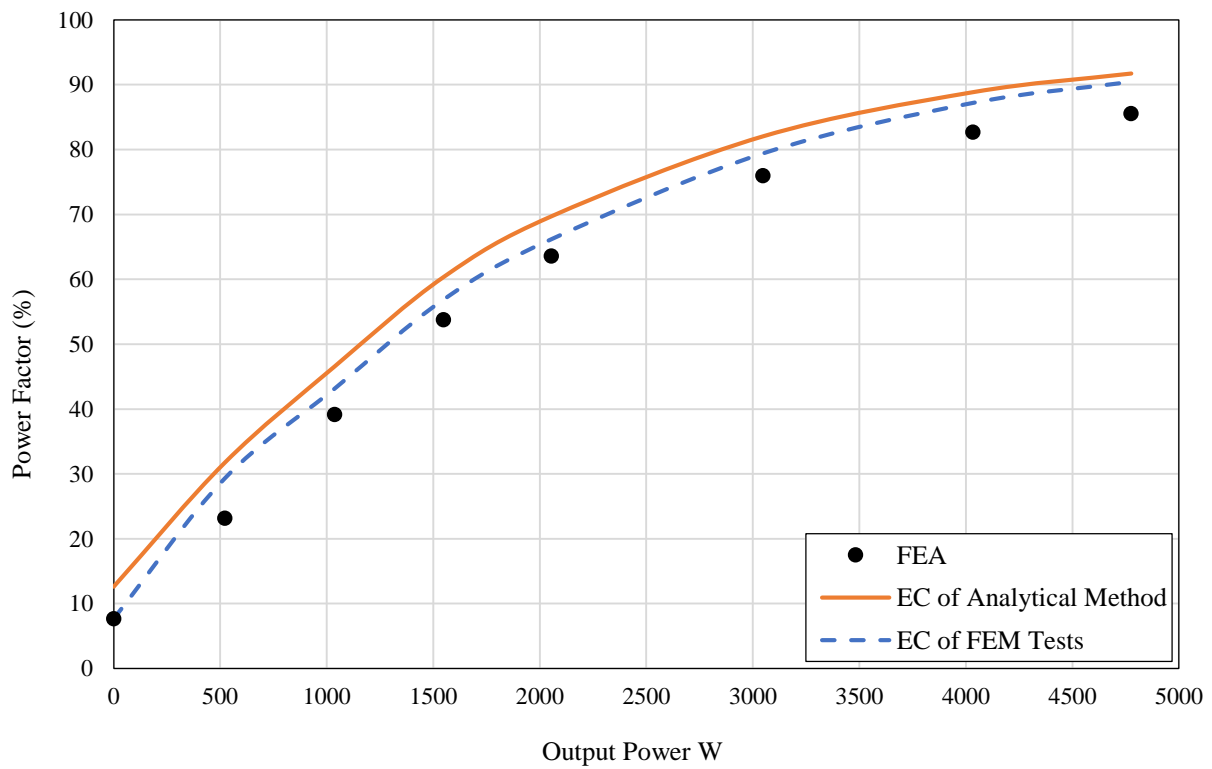
b. Power factor vs output power
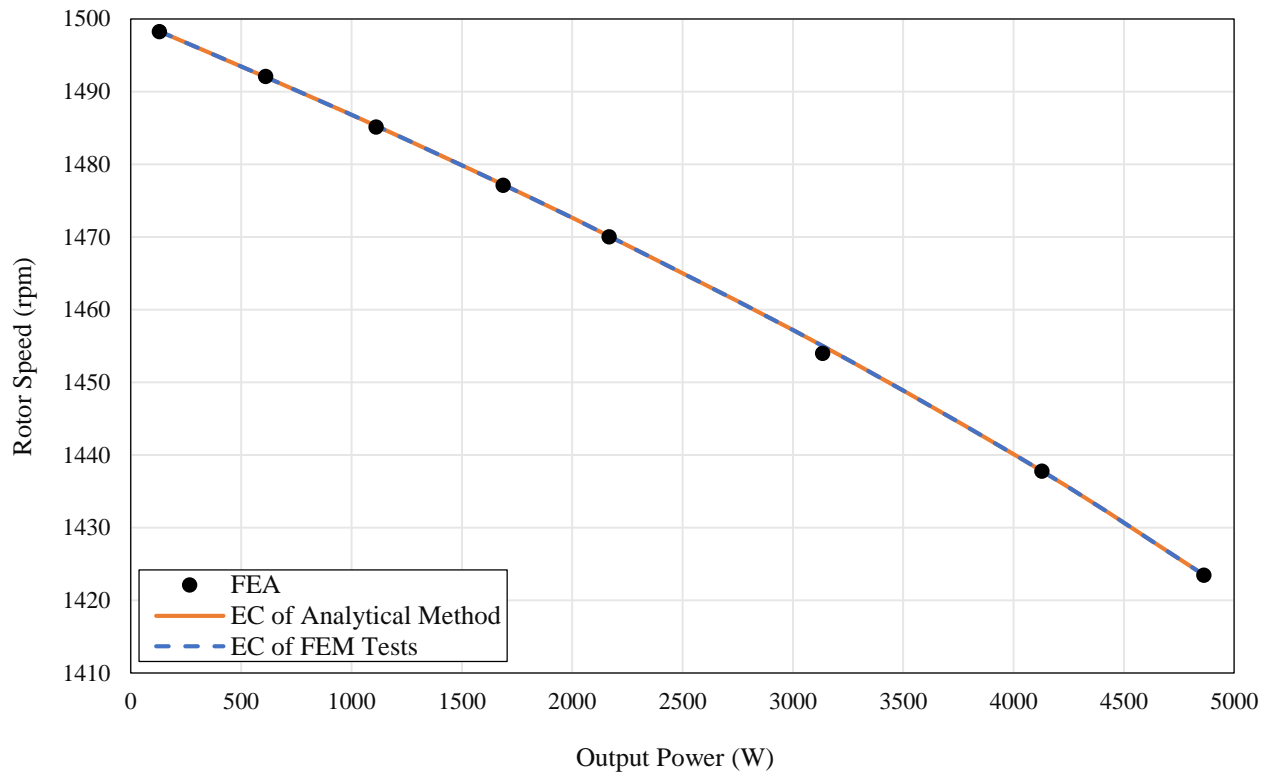
c. Rotor speed vs output power
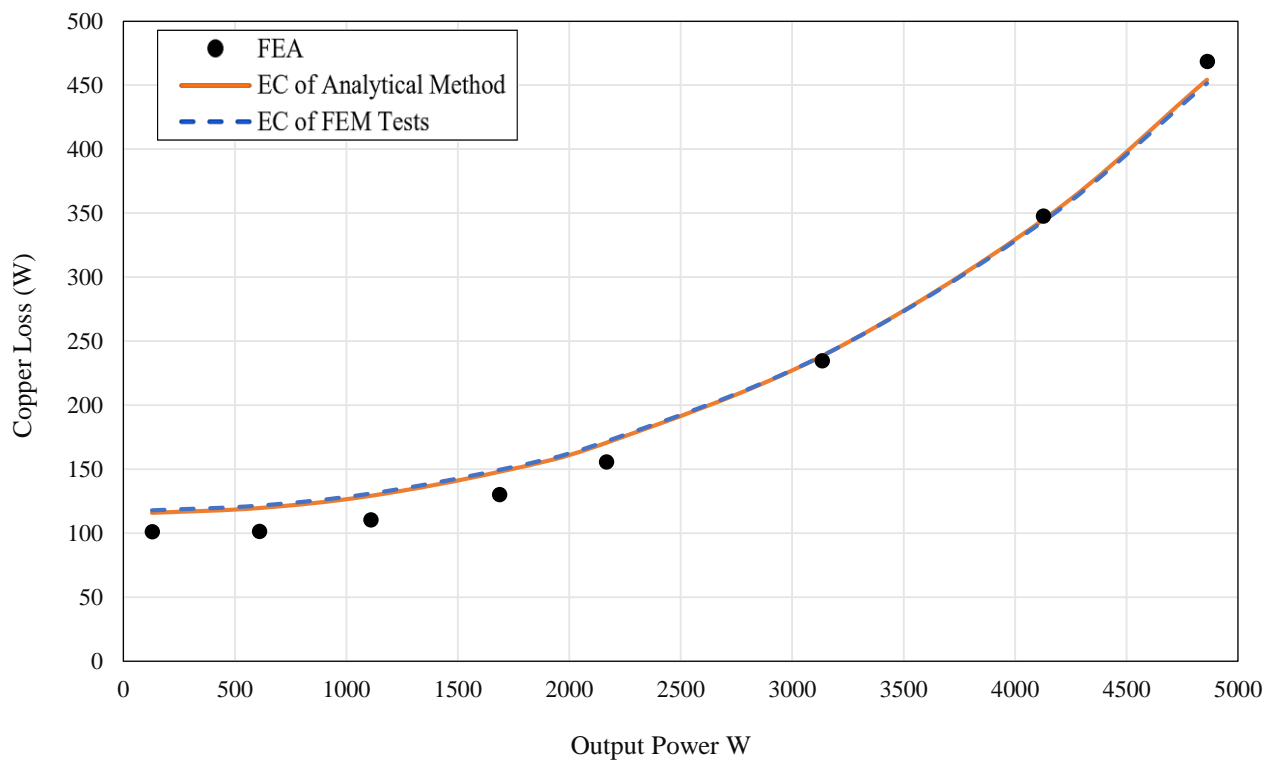
d. Copper loss vs output power
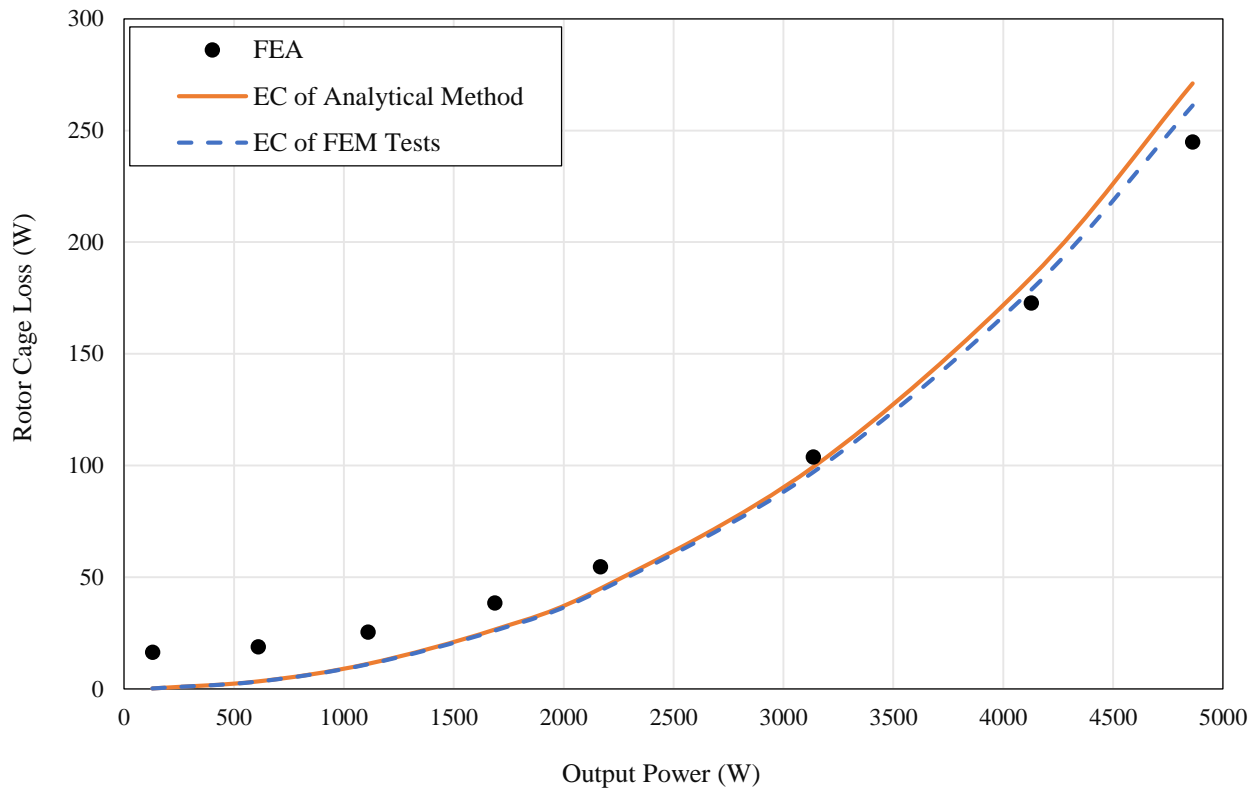
e.   Cage loss vs output power

Figure 7-5. Comparison of steady-state performance parameters calculated by three methods as function of output power.

7.2 Further Electromagnetic Analysis of the 4-kW IM

The motor's electromagnetic performance (transient and steady-state) is extensively studied by 2D FEA. To study transient performance, an initial shaft speed of 0 rpm is defined at the transient solution and the motor is simulated for 400 ms using a time-step of 0.2 ms.

7.2.1   *Mesh Independency Analysis*

To find the best meshing giving the fixed results, the design was tested under five levels of the mesh quantities types. Table **7-2** and Table **7-3** show the meshing characteristics including length and surface mesh applied in bar and cores (stator and rotor) in this analysis. Comparison of the performance parameter under each mesh is presented in Table **7-4**. It is seen that the results of the performance parameters for meshes 3-5 are independent of the mesh type. Therefore, mesh 3 was applied in the design to start the motor performance evaluation. Note that the time step in this analysis was 1 ms for half geometry fractions. Schematic view of meshing for default mesh, mesh 3 and mesh 6 is depicted in Figure **7-6a** to Figure **7-6c**, respectively. It shows the level of mesh resolution for these three mesh types.

Table 7-2. Surface Mesh characteristics defined in each mesh type.

Mesh Type	Surface Mesh in Bar		Surface Mesh in Cores	
	Surface deviation (mm)	Normal deviation (deg)	Surface deviation (mm)	Normal deviation (deg)
Default	0.05205	15	0.0825	15
Mesh 1	0.05205	15	0.0425	15
Mesh 2	0.02705	10	0.04125	10
Mesh 3	0.02	20	0.0265	20
Mesh 4	0.02	5	0.0265	5
Mesh 5	0.02	10	0.03	10

Table 7-3. Length mesh characteristics defined in each mesh type.

Mesh Type	Length Mesh in Bar		Length Mesh in Cores	
	Max length (mm)	Max elements number	Max length (mm)	Max elements number
Default	Non	Non	Non	Non
Mesh 1	2	1000	10.82	1000
Mesh 2	1.6	1000	8	1000
Mesh 3	1.6	1000	8	1000
Mesh 4	1.6	1000	8	1000
Mesh 5	1.6	1000	8	1000

Table 7-4. Main performance parameters dependency to mesh type.

Parameters	Torque (Nm)	Mechanical power (W)	Cage loss (W)	Copper loss (W)	Core loss (W)
Default	27.13	4088.62	145	341.4	36.9
Mesh 1	27.1	4083.81	144.8	340.5	36.9
Mesh 2	27.1	4084.08	145.3	341.3	37
Mesh 3	26.64	4018.32	137.7	329.3	37.6
Mesh 4	26.64	4018.32	137.7	329.3	37.6
Mesh 5	26.64	4018.3	137.6	329.7	37.4
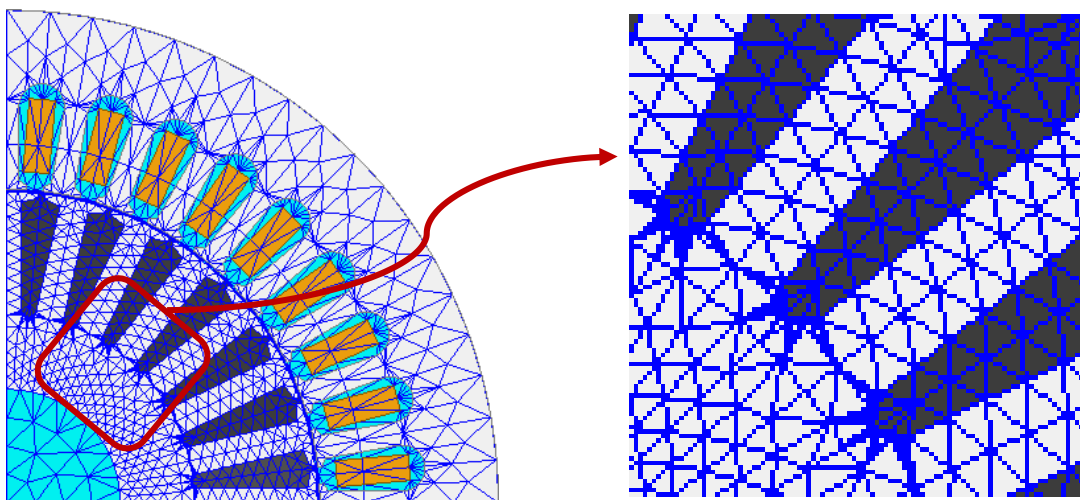
a.   Default Mesh
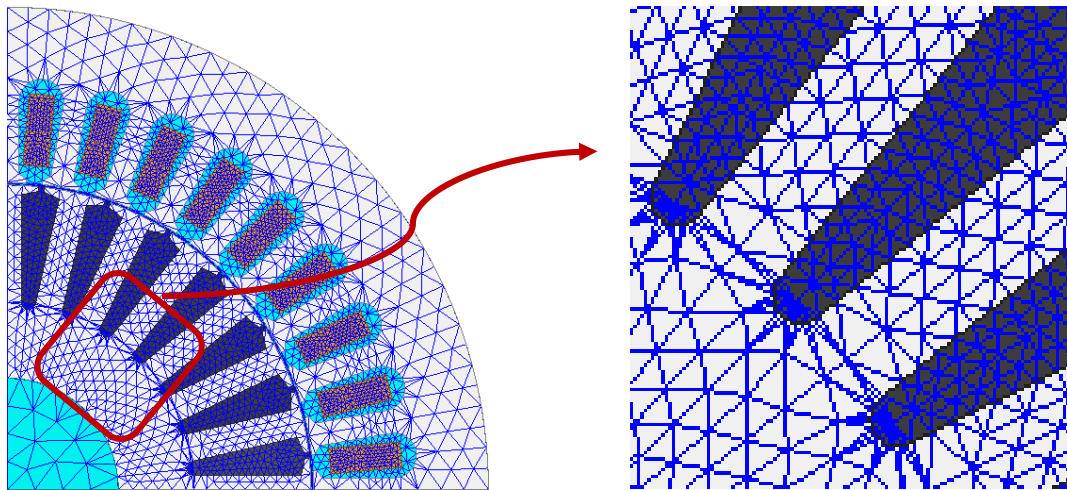
b.   Mesh 3
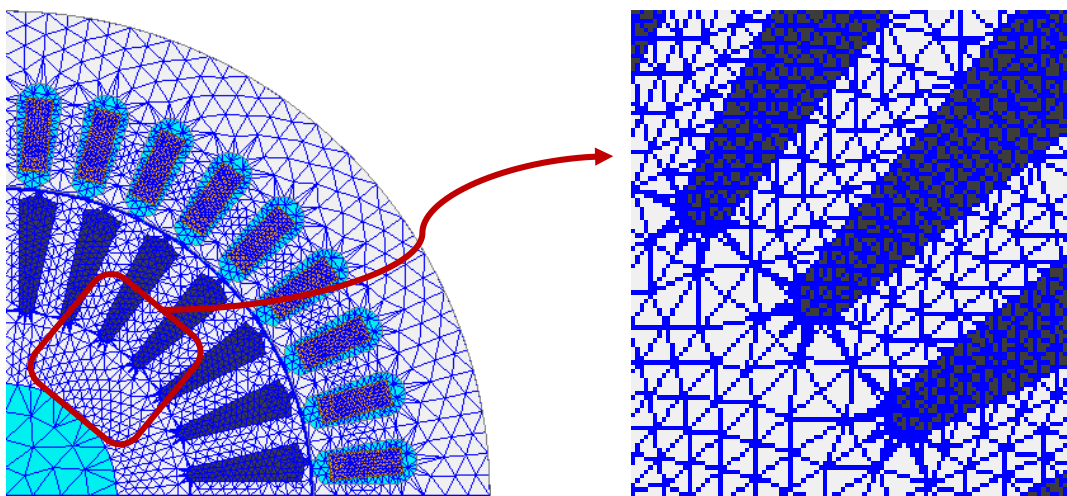
c.   Mesh 5

Figure 7-6. Comparison of applied mesh for cases default, mesh 3 and mesh 6.

7.2.2   *Magnetic Analysis*

Magnetic analysis of the motor includes flux density and flux lines variations on the motor surface, and flux density in the air gap. These plots give a useful understanding of the motor performance in terms of the magnetic behaviour.

7.2.2.1 Flux density

Figure 7-7 depicts the saturation state of the cores (stator and rotor) in no-load and full-load conditions through plotting the flux density field on the surface of the stator and rotor. Locations of the cores highlighted in red express that saturation occurred in those areas that corresponded to core losses growth. The value of the flux density in saturation locations is 2 T.

7.2.2.2 Flux Lines

Magnetic vector potential (A) is measured along the motor's surface and the result is called magnetic flux line (Wb/m). Figure 7-8 illustrates flux lines distribution on the surface of the motor in

no-load and full-load conditions. Flux moves in clockwise (blue lines) and anti-clockwise (red lines) directions. The clockwise direction provides negative potential and anti-clockwise generates positive potential.
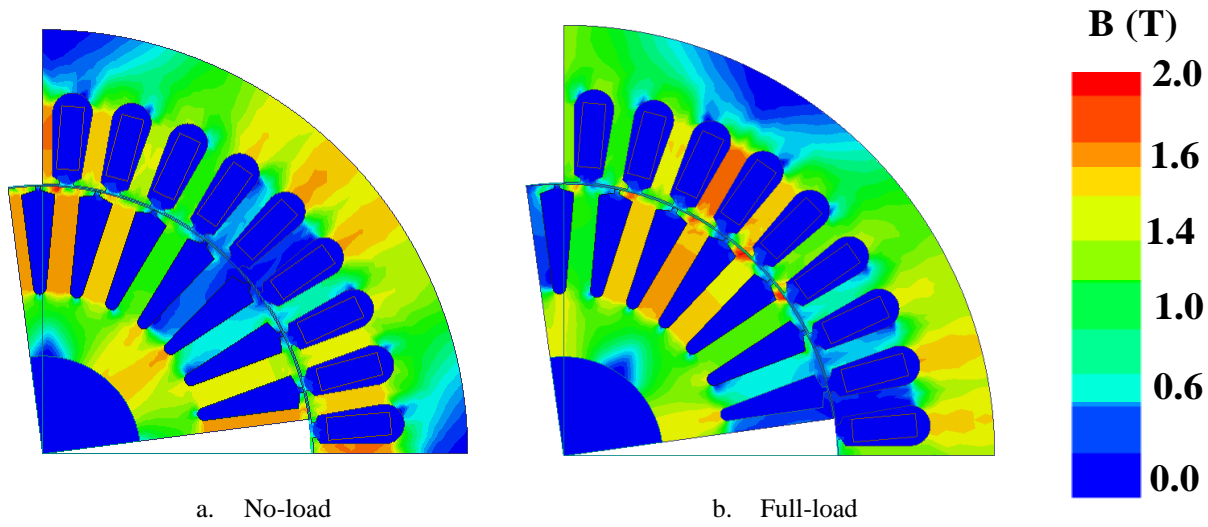
a. No-load   b. Full-load
Figure 7-7. Magnetic flux density (B) geometry overlay plots.
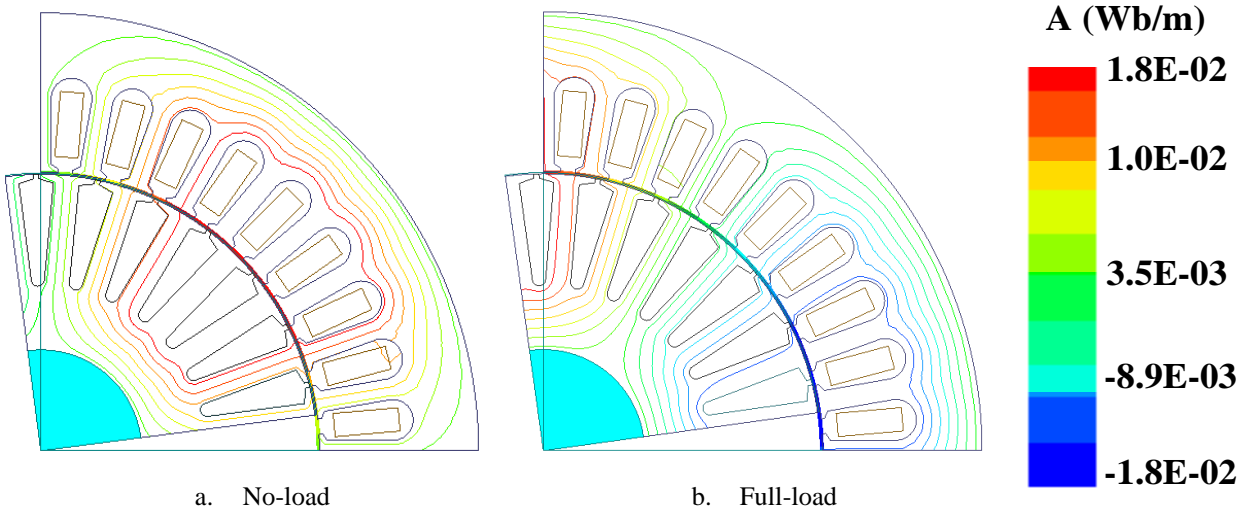
a. No-load   b. Full-load
Figure 7-8. Magnetic flux field lines.
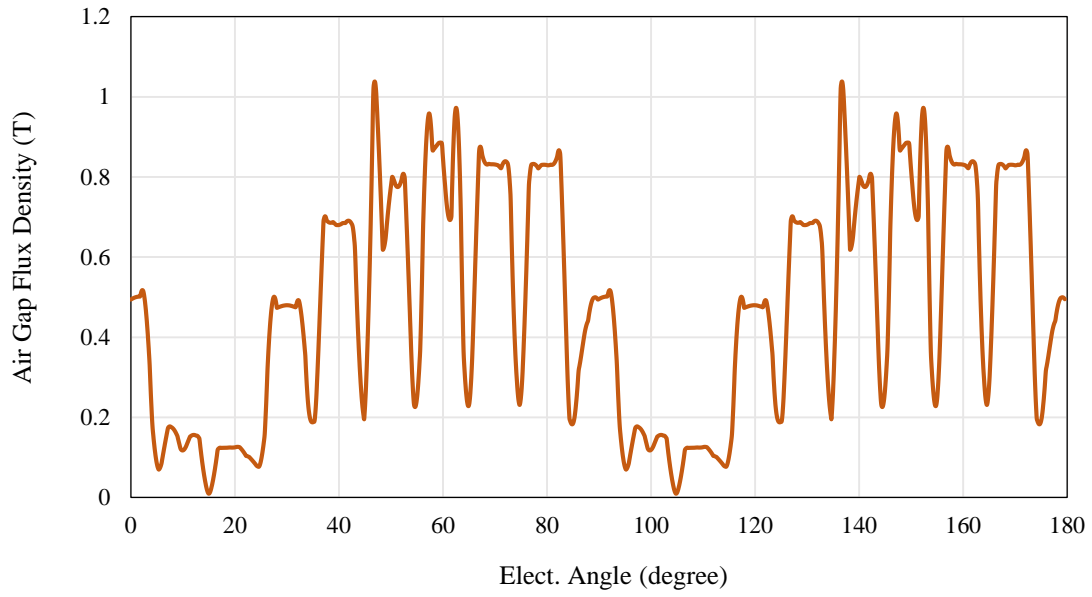
a. No-load
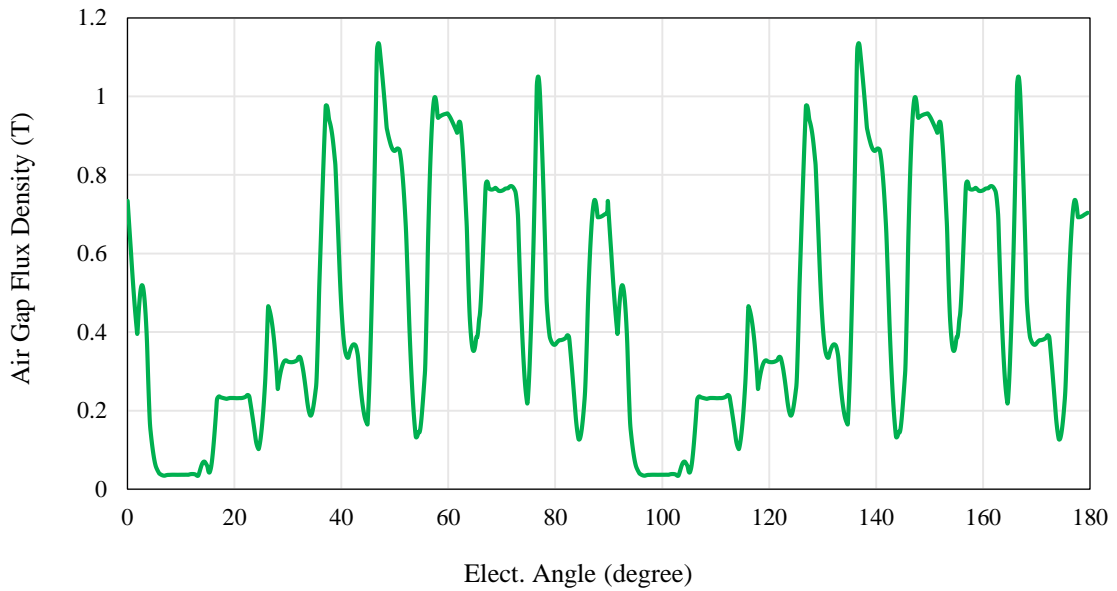
b. Full-load
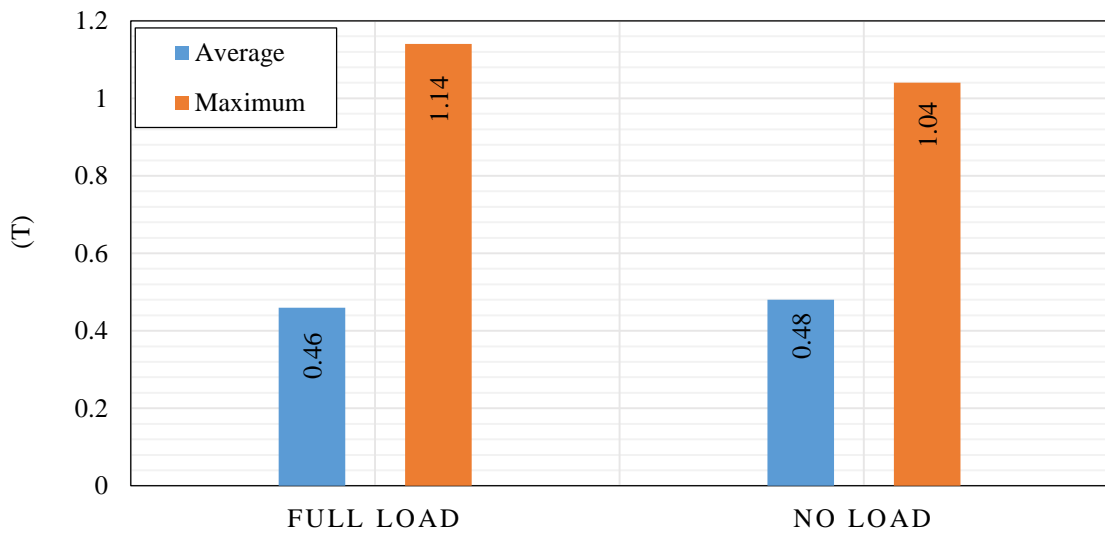
c. Full-load and no-load air gap flux density comparison

Figure 7-9. Flux density distribution in the air gap measured at time of 400 (ms).

7.2.2.3 Air gap flux density distribution

An arc line is drawn in the air gap section for one pole corresponding to 180 electrical degrees (or 90 mechanical degree) to plot the flux density distribution in the air gap. Figure 7-9a and Figure 7-9b present no-load and full-load stands for the air gap flux density measured at time of 400 ms. Maximum and average values of the air gap flux density in no-load and full-load are compared in Figure 7-9c.

7.2.3 *Harmonics Analysis*

Phase current and induced voltage of the motor is analysed in terms of harmonic components in this section. Figure 7-10 and Figure 7-11 show no-load and full-load phase current and induced voltage signals including their harmonics components. The values of fundamental and 3rd harmonic component of the signals are presented. The effect of saturation on the phase current in no-load and full-load is seen in Figure 7-10a and Figure 7-10b, which illustrates phase current signal containing critical harmonics components. The well-known method to eliminate harmonic impact on the phase current is skewing rotor bars. Figure 7-11 indicates the effect of skewing on the phase current and induced voltage signals extracted from no-load and full-load conditions. It is seen that skewing of 6.5 degrees in the rotor bars leads to harmonic reduction in phase current and makes a sinusoidal signal, which is desired to improve the quality of electricity system.
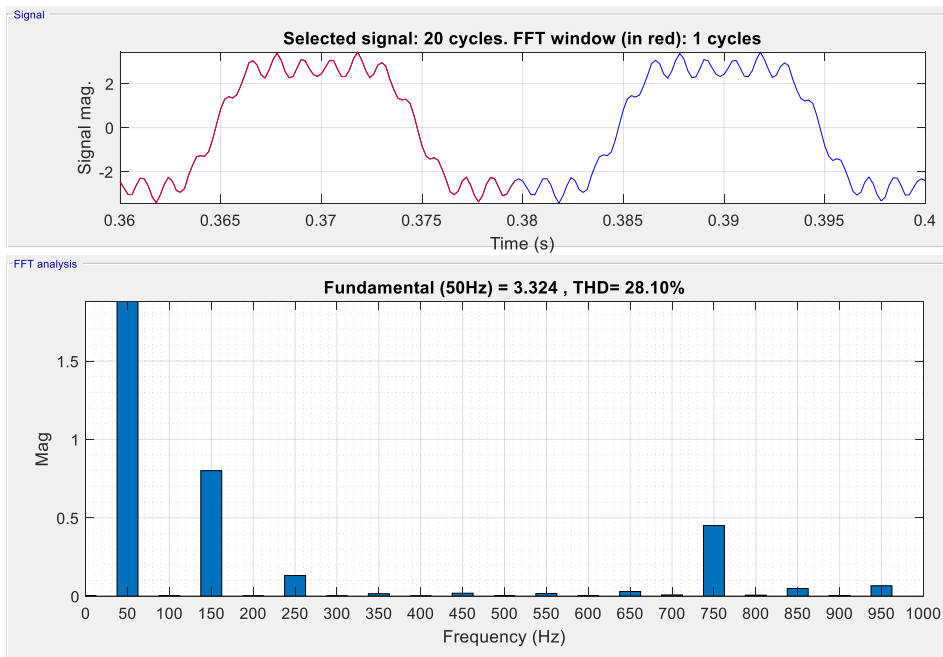
RMS phase current (A)

Fundamental	2.35
3rd harmonic	0.41

a.   No-load phase current signal and its harmonic components
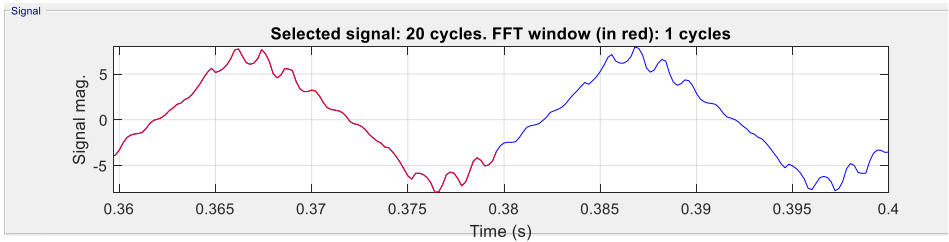
RMS phase current (A)	
Fundamental	4.47
3rd harmonic	0.44
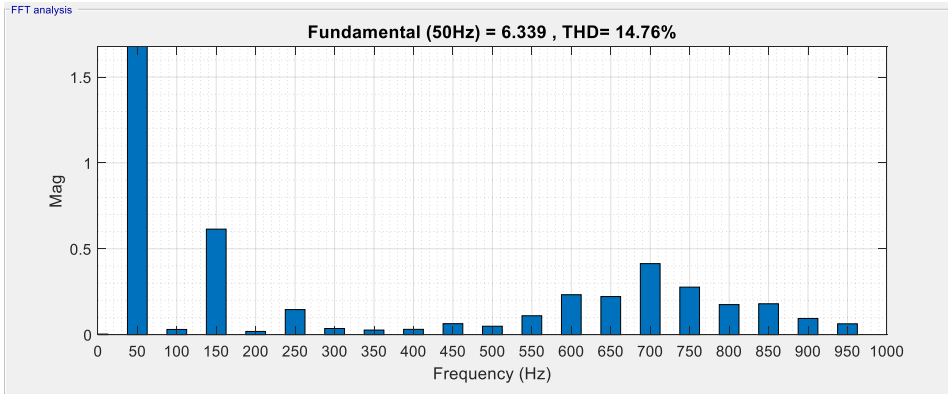
b.   Full-load phase current signal and its harmonic components
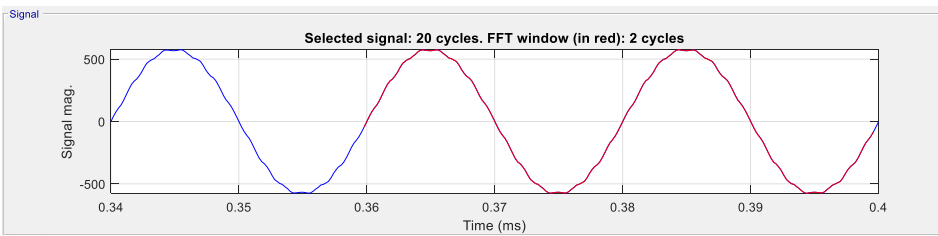
RMS induced voltage (V)	
Fundamental	410.5
3rd harmonic	4.1

c.   No-load phase current signal and its harmonic components

166

Selected signal: 20 cycles. FFT window (in red): 1 cycles

Fundamental (50Hz) = 551.9 , THD= 2.96%
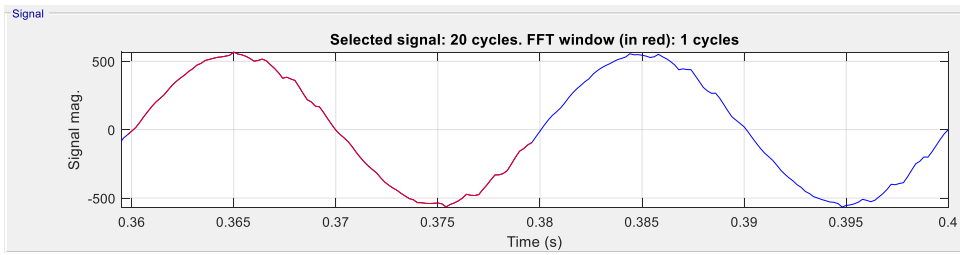
RMS induced voltage (V)

Fundamental	390.2
3rd harmonic	3.3
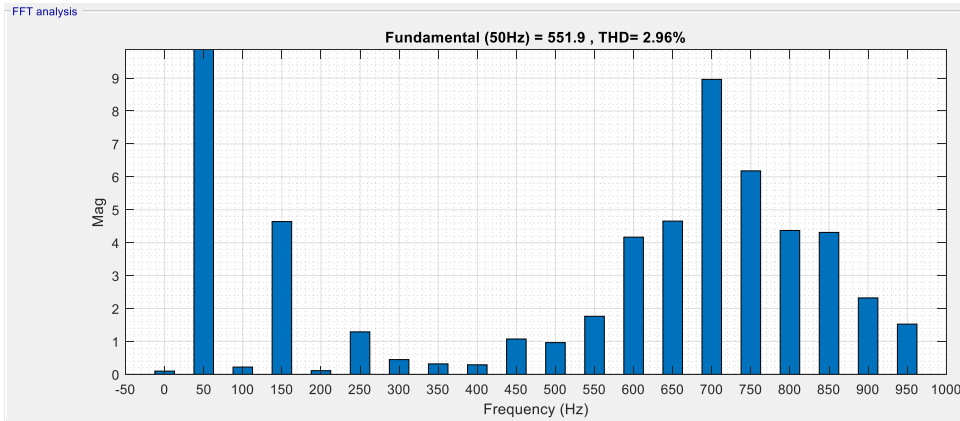
d. Full-load phase current signal and its harmonic components

Figure 7-10. No-load and full-load phase current and induced voltage signals including harminc components of the 4-kW.
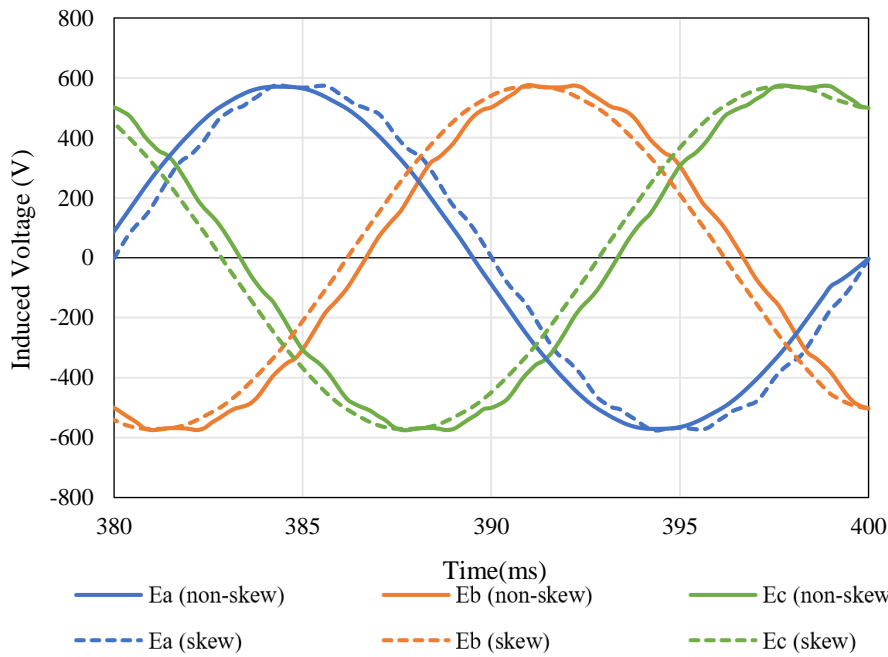
RMS induced voltage (V)

Non-skew	411
Skew (6.8 degree)	409

a. No-load induced voltage
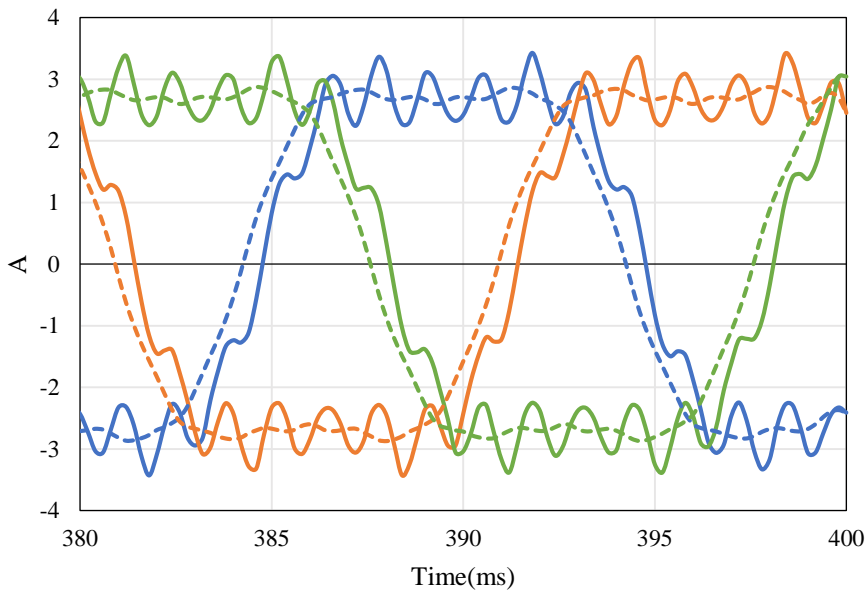
RMS phase current (A)

Non-skew	2.45
Skew (6.8 degree)	2.39
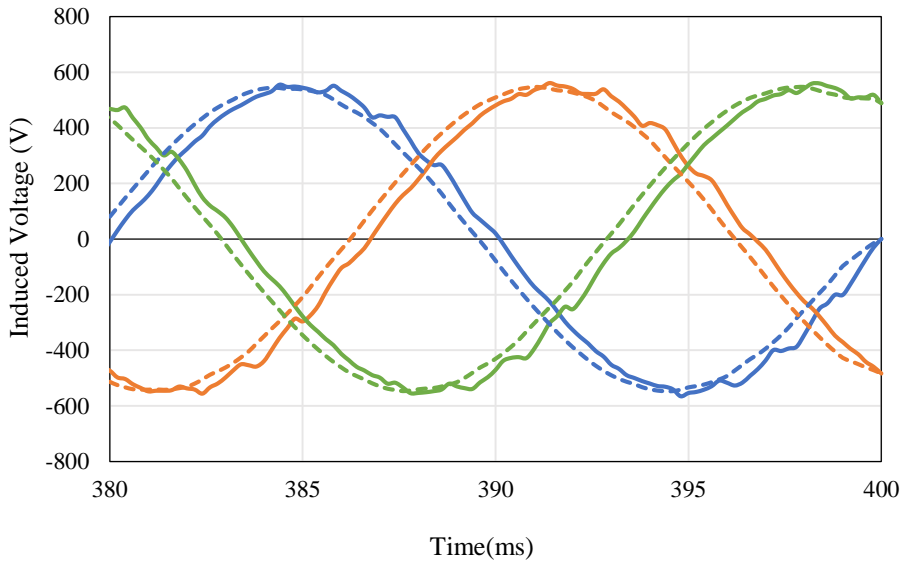
b.   No-load phase current

RMS induced voltage (V)

Non-skew	390
Skew (6.8 degree)	388

c.   Full-load induced voltage
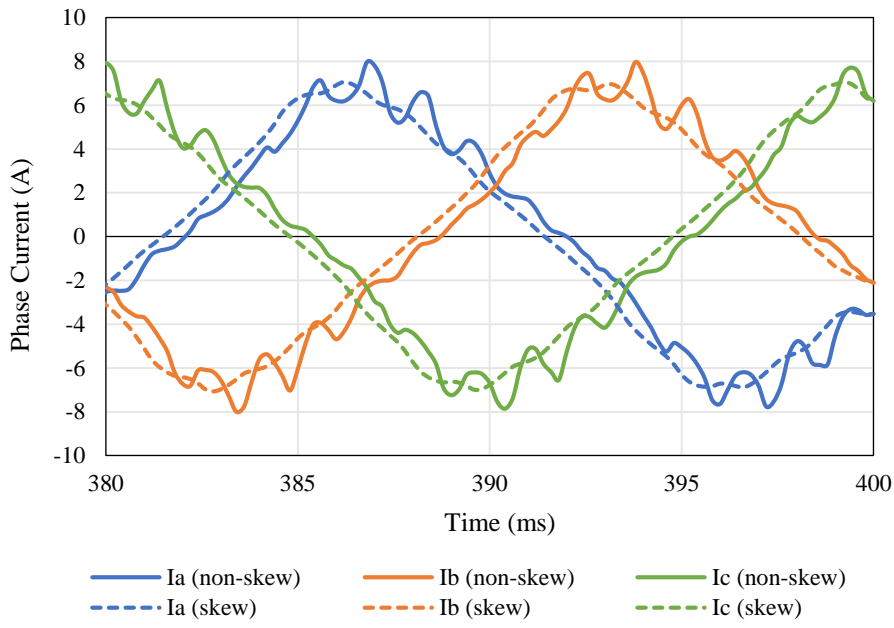
RMS phase current (A)	
Non-skew	4.53
Skew (6.8 degree)	4.49

d. Full-load phase current

Figure 7-11. Effect of rotor bar skewing on the phase current and induced voltage of the 4-kW at no-load and full-load.

8. **APPENDIX B**

8. **ABBREVIATIONS LIST**

Abbreviations	Description
AC	Alternative current
AFLSPMSM	Axial-flux line-start permanent magnet synchronous motors
CFD	Computational fluid dynamics
CFM	Coupled field method
DC	Direct current
DEAs	Differential evolution algorithms
EC	Equivalent circuit
EMF	Electromotive force
EAs	Evolutionary algorithms
ETC	Equivalent thermal conductivity
FEM	Finite-element method
FEA	Finite-element analysis
FSCW	Fractional-slot concentrated-winding
GA	Genetic algorithm
GBA	Gradient-based algorithm
GFA	Gradient-free algorithm
HTC	Heat transfer coefficient
IEC	International electro-technical commission
IRFM	Imbedded radial flux magnets
ICFM	Imbedded circumferential flux magnets
ISDW	Integral-slot distributed-winding
IE	International efficiency
IE1	Standard Efficiency
IE2	High Efficiency
IE3	Premium Efficiency

Abbreviations	Description
IE4	Super Premium Efficiency
IE5	Ultra-Premium Efficiency
IM	Induction motor
IPM	Interior permanent magnet
LSPMSMs	Line-start permanent magnet synchronous motors
LPTN	Lumped-parameter thermal network
MOF	Multi-objective function
PM	Permanent magnet
PSO	Particle swarm optimization
PF	Power factor
rms	Root mean square
RFLSPMSM	Radial-flux line-start permanent magnet synchronous motors
RS	Response Surfaces
SMM	Surface mount magnets
SSMM	Slotted surface mount magnets
SNLP	Sequential nonlinear programming
TEFC	Total enclosed fan cooled

9. APPENDIX C

9. LATIN SYMBOLS LIST

Symbols	Description	Unit
A	Vector magnetic potential	[Wb/m]
A_g	Cross section area of air gap	[m²]
A_{pm}	Cross section area of permanent magnet	[m²]
A_f	Air flow in fins and surface area of frame	[m²/s]
A_s	Interior slot area	[m²]
ac	Electric loading	[A/m]
a_{sc}	Stator conductor area	[m²]
B_{av}	Average flux density	[T]
B_g	Air gap flux density	[T]
B_{g1}	Fundamental of the air gap flux density	[T]
B_{pm}	Permanent magnet flux density	[T]
B_r	Residual Flux Density	[T]
B_{sat}	Saturation level of flux density	[T]
B_t	Teeth magnetic flux density	[T]
B_{ys}	Stator yoke magnetic flux density	[T]
B_{yr}	Rotor yoke magnetic flux density	[T]
C_0	Design Coefficient	-
D_{is}	Inner stator diameter	[m]
D_{os}	Outer stator diameter	[m]
D_{ir}	Outer rotor diameter	[m]
D_{sh}	Shaft diameter	[m]
E	Back-EMF	[V]
E_0	No load phase back-EMF	[V]
e	EMF to input phase voltage ratio	-
F_{b2}	Area of rotor bar	[m²]
f	frequency	[Hz]

Symbols	Description	Unit
f_{ip}	Flux per pole	[Wb]
$\mathbf{G}$	Thermal conductance matrix	-
H_c	Coercive force	[A/m]
h_s	Stator slot depth	[m]
h_r	Rotor slot depth	[m]
h_{bs}	Stator back iron height	[m]
h_{br}	Rotor back iron height	[m]
h_{sc}	Stator end face heat transfer coefficient	[W/m^2.°C]
h_{ew}	End winding end face heat transfer coefficient	[W/m^2.°C]
h_{rc}	Rotor end face heat transfer coefficient	[W/m^2.°C]
h_{er}	End ring end face heat transfer coefficient	[W/m^2.°C]
h_g	Air gap heat transfer coefficient	[W/m^2.°C]
I_s	RMS stator phase current	[A]
I_r	Rotor current	[A]
I_{er}	End ring current	[A]
I_{sd}	Stator d-axis current	[A]
I_{sq}	Stator q-axis current	[A]
I_{rd}	Rotor d-axis current	[A]
I_{rq}	Rotor q-axis current	[A]
J_s	Stator winding current density	[A/m^2]
J_c	Moment of load inertia	[Kg. m^2]
J_{cr}	Critical inertia	[Kg. m^2]
k_{eq}	Equivalent thermal conductivity of air and insulation material in the slots	[W/m^2.°C]
k_c	Carter's factor	-
k_{fill}	Fill factor coeficient	-
k_{ov}	End winding increasing factor	-
k_{sat}	Saturation factor	-
k_w	Winding factor	-
k_i	Lamination Factor	-

Symbols	Description	Unit
L	Motor stack length	[m]
L_i	Effective motor length	[m]
L_{sd}	d-axis stator inductances	[H]
L_{sq}	q-axis stator inductances	[H]
L_{rd}	d-axis rotor inductances	[H]
L_{rq}	q-axis rotor inductances	[H]
L_{md}	d-axis mutual inductances	[H]
L_{mq}	q-axis mutual inductances	[H]
L_{er}	End ring length	[m]
l_g (lg)	Air gap length	[m]
l_{ew}	Length of end winding	[m]
l_{av}	Average length of coil turn	[H]
l_s	Slot leakage permeance	[H]
l_e	End winding leakage permeance	[H]
l_t	Tooth-top leakage permeance	[H]
l_d	Differential leakage permeance	[H]
m	Number of phase	-
N_s	Synchronous speed	[rpm]
N_r (or n_r)	Rotor speed	[rpm]
N_{ph}	Number of coils turns per phase	-
Nu	Nusselt number	-
Nu_{ew}	Nusselt number of the end winding	-
Nu_{rc}	Nusselt number of the rotor end face	-
Nu_{er}	Nusselt number of the end ring end face	-
n	Number of nodes	-
$\boldsymbol{P}$	Loss vector matrix	-
P	Number of poles	-
P_{cus}	Stator copper loss	[W]

174

Symbols	Description	Unit
P_{cage}	Rotor cage loass	[W]
P_{Iron}	Iron loss	[W]
P_{in}	Rated input power	[W]
P_{out}	Rated output power	[W]
P_{NL}	Measured no-load loss	[W]
P_{LR}	Locked-rotor Power	[W]
PF	Power factor	-
P_s	Slot pitch at the end of slot	[m]
q_s	Stator slots per pole per phase factor	-
R_s	Stator resistance	[ohm]
R_r	Rotor resitance	[ohm]
R_b	Bar resistance	[ohm]
R_e	End ring resistance	[ohm]
R_c	Core losses resistance	[ohm]
R_{ref}	Resistance at the reference temperature	[ohm]
R_{rd}	Rotor d-axis resitance	[ohm]
R_{rq}	Rotor q-axis resitance	[ohm]
R_{th_c}	Convection thermal resistance	[K/W]
$R_{fa\_natural}$	Natural convection thermal resistance between frame to ambient	[K/W]
R_{fa_forced}	Forced convection thermal resistance	[K/W]
R_{th_radial}	Radial condution thermal resistance	[K/W]
R_{th_axial}	Axial condution thermal resistance	[K/W]
R_{eq}	Thermal resistance between winding and stator lamination	[K/W]
R_g	Air gap thermal resistance	[K/W]
Re	Reynolds number	-
Re_{cr}	Critical Reynolds number	-
Re_{y_ew}	Air Reynolds number of the end winding	-
Re_{y_r}	Air Reynolds number of the end face rotor	-
Re_{y_er}	Air Reynolds number of the end ring	-

Symbols	Description	Unit
r_{sp3}	Rotor slot permeance	[H]
r_{eq_ew}	Mean radius of the end winding	[m]
r_{or}	Rotor outer radius	[m]
r_{ir}	Rotor inner radius	[m]
r_{os}	Stator outer radius	[m]
r_{is}	Stator inner radius	[m]
S	Apparent power	[kVA]
S_{pm}	Cross-sections of the PM	[m^2]
S_{min}	Maximum cross-sections of the PM	[m^2]
S_{maz}	Minimum cross-sections of the PM	[m^2]
S_s	Stator slot number	-
S_r	Rotor slot number	-
S_{slo}	Stator slot area	[m^2]
S_{cu}	Copper area in the stator slot	[m^2]
S_p	Stator slot perimeter	[m]
T_{cage}	Asynchronous torque	[Nm]
T_{mag}	Magnet-generated torque (braking torque)	[Nm]
T_{tot}	Total resultant torque of LSPMSM	[Nm]
T_{st}	Starting torque	[Nm]
T_{end}	Torque near synchronous speed	[Nm]
T_{80}	Torque generated at 80% of synchronous speed	[Nm]
T_{ripple}	Torque ripple	[Nm]
T_{avg}	Average electromanetic torque	[Nm]
T_L	Load torques	[Nm]
T_{ref}	Reference temperature	[^{o}C]
T_a	Tylor number	-
Th	PM Thickness	[m]
T_0	Ambient temperature	[^{o}C]
th_{eq}	Equivalent thickness of the air and the insulation material in the stator slots	[m]

Symbols	Description	Unit
t_p	Pole pitch	[m]
t_s	Slotpitch	[m]
V	Input line voltage	[V]
V_{ph}	Input phase voltage	[V]
V_{PM}	PM volume	[m^3]
v_{sd}	Stator d-axis voltage	[V]
v_{sq}	Stator q-axis voltage	[V]
v_{rd}	Rotor d-axis voltage	[V]
v_{rq}	Rottor q-axis voltage	[V]
v_r	Rotor surface velocity	[m/s]
W	PM widh	[m]
X_s	Stator reactance	[ohm]
X_r	Rotor reactance	[ohm]
X_m	Magnetising reactance	[ohm]
X_{LR}	Locked-rotor reactance	[ohm]
X_d	d-axis synchronous reactance	[ohm]
X_q	q-axis synchronous reactance	[ohm]
x_{cr}	Maximum allowed load inertia coefficient	-
Y_q	Coil pitch in number of slots	[m]
Z_{slot}	Number of conductor in stator slot	-
Z_{LR}	Locked-rotor impedance	[ohm]

10.APPENDIX D

10. GREEK SYMBOLS LIST

Symbols	Description	Unit
α	Temperature coefficient of the conductor resistivity	-
Ψ_{sq}	Stator q-axis flux linkage	[Wb]
Ψ_{sd}	Stator d-axis flux linkage	[Wb]
Ψ_{rq}	Rotor q-axis flux linkage	[Wb]
Ψ_{rd}	Rotor d-axis flux linkage	[Wb]
Ψ_m	Permanent magnet flux-linkage	[Wb]
ω_r	Angular speed of the rotor	[rad/s]
μ	Kinematic viscosity of the fluid	[m^2/s]
η	steady-state efficiency	[%]
ε	Stack length to stator inner diameter	-
λ	Stack length to pole pitch ratio	-
λ	Thermal conductivity of the material	[W/m^2.°C]
λ_{air}	Air thermal conductivity	[W/m^2.°C]
ρ	resistivity	[ohm.m]
ΔT	Temperature rise	[°C]
$\Delta \boldsymbol{T}$	Temperature rise vector matrix	-
τ	Thermal time constant	minute

LIST OF REFERENCES

[1] http://www.eamagnetics.com/info_samarium_cobalt_charts01.asp.

[2] P-W. Hung, S-H. Mao, and M C Tsai, "Investigation of line start permanent magnet synchronous motors with interior-magnet rotors and surface-magnet rotors," Electrical Machines and Systems, pp. 2888 - 2893, October 2008.

[3] R. T. Ugale, "Inset-Consequent and Inset Rotors for Line Start Permanent Magnet Synchronous Motor", ICEM, 2012.

[4] T. Ruan, H. Pan, Y. Xia, "Design and Analysis of Two Different Line-Start PM Synchronous Motors", Artificial Intelligence, Management Science and Electronic Commerce (AIMSEC), 2011.

[5] P-W. Huang, M-C. Tsai, "Investigation of V-Shaped Line Start Permanent Magnet Motors Based on Reactance Effect", IEEE Transactions on Magnetics, Vol.49, No.5, pp.2311-2314, May 2013.

[6] Elistratova, "Optimal design of line-start permanent magnet synchronous motors of high efficiency" Electric power. Ecole Centrale de Lille, 2015.

[7] I. Boldea, L. Tutelea, "Electric Machines: Steady State, Transients, and Design with MATLAB" 1st Edition, CRC Press Tylor & Francis, 2009.

[8] K. G. Upadhyay, "Design of electrical machines", 1st Edition, New Age International Publisher, 2000.

[9] F. Tao, L. Jian, W. Xuhui, L. Xiaofeng, "A new sizing equation and it's application in electrical machine design," 2011 International Conference on Electric Information and Control Engineering, Wuhan, 2011.

[10]   H. J. Lee, S. H. Im, D. Y. Um, G. S. Park, "A Design of Rotor Bar Improving Starting Torque by Analyzing Rotor Resistance and Reactance in Squirrel Cage Induction Motor", IEEE Transactions on Magnetics, Vol. 54, No. 3, March 2018.

[11]   C. G. Heo, H. M. Kim, G. S. Park, "A Design of Rotor Bar Inclination in Squirrel Cage Induction Motor", IEEE Transactions on Magnetics, Vol. 53, No. 11, November 2017.

[12]   A. Hassanpour Isfahani, S.Vaez-Zadeh, "Line start permanent magnet synchronous motors: Challenges and opportunities", Energy, Vol. 34, No. 11, pp. 1755-1763 November 2009.

[13]   America's Climate Choices. Washington, D.C.: The National Academies Press. 2011. p. 15. ISBN 978-0-309-14585-5.

[14]   AM. Knight, CI. McClay, "The design of high-efficiency line-start motors", IEEE Trans Ind Appl, Vol. 36, No. 15, pp. 55-62, 2000.

[15]   Int. Eletrotechnical Commission (IEC), Standard for Efficiency classe of line operated AC motors (IE code), No. 60034-30-1:2014, 2014.

[16]   P. L. Alger and R. E. Arnold, "The history of induction motors in America," in Proceedings of the IEEE, vol. 64, no. 9, pp. 1380-1383, Sept. 1976, doi: 10.1109/PROC.1976.10329.

[17]   W. Fei, P. C. K. Luk, J. Ma, J. X. Shen and G. Yang, "A High-Performance Line-Start Permanent Magnet Synchronous Motor Amended From a Small Industrial Three-Phase Induction Motor", IEEE Transactions on Magnetics, Vol. 45, No. 10, pp. 4724–4727, September 2009.

[18]   AT de. Almeida, F. Ferreira, and A. Duarte, "Technical and Economic Considerations on Super High-Efficiency Three-Phase Motors", IEEE Trans. Ind. Appl., Vol. 50, No. 2, pp. 1274–1285, 2014.

[19]   V. Elistratova, M. Hecquet, P. Brochet, D. Vizireanu, M. Dessoudev, "Optimal Design of a Line-Start Permanent Magnet Synchronous Motor", ISEF 2013 – XVI International Symposium on Electromagnetic Fields in Mechatronics, Electrical and Electronic Engineering, August 2013.

[20]   M. Barcaro, N. Bianchi and F. Magnussen, "Faulty Operations of a PM Fractional-Slot Machine With a Dual Three-Phase Winding", IEEE Trans. on Ind. Elect., Vol. 58, No. 9, pp. 3825-3832, 2011.

[21]   B.A. Welchko, T.M. Jahns, W. L. Soong, et al., "IPM synchronous machine drive response to symmetrical and asymmetrical short circuit faults", IEEE Tran. on Energy Conversion, Vol. 18, pp. 291–298, 2003.

[22]   S. Taravat, A. H. Niasar and A. Rabiee, "Sensorless Vector Control of Single-Phase Line Start Permanent Magnet Motors (LSPMs)", Int. J. Sci. & Adv. Tech., Vol. 2, pp. 126-131, 2012.

[23]   T. Marˇciˇc, B. Štumberger, G. Štumberger, "Comparison of Induction Motor and Line-Start IPM Synchronous Motor Performance in a Variable-Speed Drive", IEEE Transactions on Industry Applications, Vol. 48, No. 6, pp. 2341–2352, December 2012.

[24]   A. Abbas, H.A. Yousef, O.A Sebakhy, "FE Parameters Sensitivity Analysis of an Industrial LS Interior PM Synchronous Motor". Power and Energy Society General Meeting–Conversionand Delivery of Electrical Energy in the 21st Century (2008), pp.1-6.

[25]   M. Hosseinzadeh Soreshjani, A. Sadoughi, "Conceptual comparison of Line-Start Permanent Magnet Synchronous and Induction Machines for Line-fed of different conditions", JWEET, Vol. 3, No. 1, pp. 26-36, 2014.

[26]   A. Sadoughi, M. Zare, M. Azizi, "Comparison Between Line Start PM Synchronous Motor and Induction Motor with Same Nominal Power and Same Pole Pairs When Fed by VF Control Drive", International Journal of Electronics Communication and Computer Engineering, Vol. 6, No. 2, pp. 2278–4209, 2015.

[27]   Hamzeh Khezri, Homayoun meshgin kelk, "Design and Performance Analysis of a Line Start Permanent Magnet Synchronous Motor", Tafresh University, 2015.

[28]   M.F. Palangar, A. Mahmoudi, S. Kahourzade, W. L. Soong, "Electromagnetic and Thermal Analysis of a Line-Start Permanent-Magnet Synchronous Motor", IEEE Energy Conversion Congress and Exposition (ECCE), September 2020, Detroit, Michigan, United States.

[29]   A. J. Sorgdrager, R. J. Wang and A.J. Grobler, "Design procedure of a line-start permanent magnet synchronous machine", Proceedings of the 22nd South African Universities Power Engineering Conference 2014, Durban.

[30]   M.F. Palangar, A. Mahmoudi, S. Kahourzade, W.L. Soong, "Optimum Design of Line-Start Permanent-Magnet Synchronous Motor Using Mathematical Method", IEEE Energy Conversion Congress and Exposition (ECCE), September 2020, Detroit, Michigan, United States.

[31]   J. Pyrhonen, "Design of rotating electrical machines", 1st ed. West Sussex, United Kingdom: John Wiley & Sons, Ltd, 2008.

[32]   I. Boldea, "Electric machines", 1st ed. USA: CRC Press, 2010.

[33]   M. Eker, M. Akar, C. Emeksiz, Z.Dogan, "Rotor design for line start AF-PMSM", IET Electric Power Applications, Vol. 13 No. 9, pp. 1273-1279, 2019.

[34]   M. Eker, M. Akar, C. Emeksiz, et al., "Design of self-starting hybrid axial flux permanent magnet synchronous motor connected directly to line", J. Electr. Eng. Technol., Vol. 13, No. 5, pp. 1921–1930, 2018.

[35]   M.A Rahman and T.M. Osheiba, "Performance of a large line start permanent magnet synchronous motor", IEEE Trans. Energy Conversion, Vol. 5, pp.211-217, Mar.1990.

[36]   F. Libert, J. Soulard, J. Engstro¨m, "Design of a 4-pole line start permanent magnet synchronous motor", in Proceedings of international conference on electrical machines. ICEM; Aug 2002. pp. 1166–71.

[37]   K. Kiurihara, MA. Rahman, "High-efficiency line-start interior permanent magnet synchronous motors", IEEE Trans Ind Appl, Vol. 40, No. 7, pp.89–96, 2004.

[38]   X. Lu, K. L. Varaha Iyer and N. C. Kar, "Mathematical modeling and comprehensive analysis of induction assisted permanent magnet synchronous AC motor," 2011 1st International Electric Drives Production Conference, Nuremberg, 2011, pp. 147-152, doi: 10.1109/EDPC.2011.6085532..

[39]   Yang BY, Kwon BI, Lee CK, Woo KI, Kim BT, "Comparison of dynamic characteristics of the line start permanent magnet motor and the induction motor", KIEE International Transactions on Electrical Machinery and Energy Conversion, Vol. 2B, No. 3, pp. 90–94, 2002.

[40]   T. J. E. Miller, "Synchronization of Line-Start Permanent-Magnet AC Motors," in IEEE Power Engineering Review, vol. PER-4, no. 7, pp. 57-58, July 1984, doi: 10.1109/MPER.1984.5525902.

[41]   The effect of repair/rewinding on motor efficiency. St. Louis, MO: Electrical Apparatus Service Association/Association of Electrical and Mechanical Trades; 2003.

[42]   T. Marcic, B. Stumberge, G. Stumberger, M. Hadziseli, P. Virtic, D. Dolinar, "Line-Starting Three- and Single-Phase Interior Permanent Magnet Synchronous Motors—Direct Comparison to Induction Motors", IEEE Transactions on Magnetics, Vol. 44, No. 11, pp. 4413-4416, 2008.

[43]   Reducing power factor cost. Fact Sheet, Motor challenge program. U.S. Department of Energy.

[44]   J. Li, J. Song, Y. Cho, "High Performance Line Start Permanent Magnet Synchronous Motor for Pumping System", IEEE International Symposium on Industrial Electronics, pp. 4-7, July 2010, Bari, Italy.

[45]   M. Tian, X. Wang, D. Wang, W. Zhao, Ch. Li, "A Novel Line-Start Permanent Magnet Synchronous Motor With 6/8 Pole Changing Stator Winding", IEEE Transactions on Energy Conversion, Vol. 33, No. 3, September 2018.

[46]   A. Damaki Aliabad, M. Mirsalim, N. Farrokhzad Ershad, "Line-Start Permanent-Magnet Motors: Significant Improvements in Starting Torque, Synchronization, and Steady-State Performance", IEEE Transactions on Magnetics, Vol. 46, No. 12, December 2010.

[47]   B. Yan, X. Wang, Y. Yang, "Starting Performance Improvement of Line-Start Permanent-Magnet Synchronous Motor Using Composite Solid Rotor", IEEE Transactions on Magnetics, Vol. 54, No. 3, March 2018.

[48]   M. Niaz Azari, M. Mirsalim, "Line-start permanent-magnet motor synchronisation capability improvement using slotted solid rotor", IET Electric Power Applications., Vol.: 7, No. 6, pp. 462–469, July 2013.

[49]   M. Niaz Azari, M. Mirsalim, "Performance Analysis of a Line-start Permanent Magnet Motor with Slots on Solid Rotor Using Finite-element Method", Electric Power Components and Systems, Vol. 41, No. 12, pp. 1159-1172, 2013.

[50]   B. T. Kim and B. I. Kwon, "Influence of space harmonics on starting performance of a single-phase line start permanent magnet motor," IEEE Trans. Magn., Vol. 44, No. 12, pp. 4668–4672, Dec. 2008.

[51]   B. Kim, D. Kim, B. Kwon, and T. A. Lipo, "Optimal skew angle for improving of start-up performance of a single-phase line-start permanent magnet motor," in Proc. IEEE IAS Conf., pp. 1–6, Oct. 5–9, 2008, Edmonton, Canada.

[52]   A. Hassanpour Isfahani, S. Vaez-Zadeh, "Effects of Magnetizing Inductance on Start-Up and Synchronization of Line-Start Permanent-Magnet Synchronous Motors", IEEE Transactions on Magnetics, Vol. 47, No. 4, April 2011.

[53]   A. Takahashi, S. Kikuchi, K. Miyata, A. Binder, "Asynchronous Torque of Line-Starting Permanent-Magnet Synchronous Motors", IEEE Transactions on Energy Conversion, Vol. 30, No. 2, June 2015.

[54]   L. Jing, J. Gong, Y. Lin, "Analysis and Reduction of Cogging Torque of Line-Start Permanent Magnet Motors", Progress in Electromagnetics Research M, Vol. 78, pp.115–124, 2019.

[55]   Z. Bing-yi, C. Gang, W. Sen, F. Gui-hong, "Study of Cogging Torque in Line-Start PMSM with Proper Fractional Slot Winding", International Conference on E-Product E-Service and E-Entertainment, pp. 7-9, Nov. 2010.

[56]   H. Behbahanifard, A. Sadoughi, "Line Start Permanent Magnet Synchronous Motor Performance and Design; a Review", Journal of World's Electrical Engineering and Technology, Vol. 4, No.2, pp. 58–66, 2015.

[57]   G. Lei, J. Zhu, Y. Guo, Ch. Liu and B. Ma, "A Review of Design Optimization Methods for Electrical Machines," Energies, Vol. 10, No. 12, 2017.

[58]   Francesco Cupertino, Gianmario Pellegrino, Chris Gerada, "Design of synchronous reluctance machines with multi-objective optimization algorithms," IEEE Energy Conversion Congress and Exposition, pp. 15-19, Sept. 2013.

[59]   S. Kahourzade, A. Mahmoudi, W. Ping Hew, M. Nasir Uddin, "Design and Performance Improvement of a Line-Start PMSM", 2013 IEEE Energy Conversion Congress and Exposition, pp. 15-19 Sept. 2013, Denver, CO, USA.

[60]   M. Niaz Azari, M. Mirsalim, S. M. Abedi Pahnehkolaei, S. Mohammadi, "Optimum Design of a Line-Start Permanent Magnet Motor with Slotted Solid-Rotor Using Neural Network and Imperialist Competitive Algorithm", IET Electric Power Applications, Vol. 11, No. 1, pp. 1-8, 2017.

[61]   C. Jȩdryczka, Ł. Knypiʹnski, A. Demenko, J. K. Sykulski, "Methodology for Cage Shape Optimization of a Permanent Magnet Synchronous Motor Under Line Start Conditions", IEEE Transactions on Magnetics, Vol. 54, No. 3, pp. 1-4, March 2018.

[62]   C. Jedryczka, R. Marek Wojciechowski A. Demenko. "Influence of squirrel cage geometry on the synchronisation of the line start permanent magnet synchronous motor", IET Science, Measurement and Technology, Vol. 9, No. 2, pp. 197–203, April 2015.

[63]   S. Baek, B. Kim, B. Kwo, "Practical Optimum Design Based on Magnetic Balance and Copper Loss Minimization for a Single-Phase Line Start PM Motor", IEEE Transactions on Magnetics, Vol. 47, No. 10, October 2011.

[64]   Y. Xie, J. Li, Zh. Yang, Ch. Qu, "Optimization Design of Line-start Permanent Magnet Synchronous Motor Based on Ant Colony Algorithm", 17th International Conference on Electrical Machines and Systems (ICEMS), Oct. 22-25, 2014, Hangzhou, China.

[65]   Ł. KnypiĚski, "Application of Bat Algorithm in the Optimal Design of Line-Start Permanent Magnet Synchronous Motor", 18th International Symposium on Electromagnetic Fields in Mechatronics, Electrical and Electronic Engineering (ISEF) Book of Abstracts, 14-16 Sept. 2017, Lodz, Poland.

[66]   S. Saha, G. Choi, Y. Cho, "Optimal Rotor Shape Design of LSPM With Efficiency and Power Factor Improvement Using Response Surface Methodology", IEEE Transactions on Magnetics, Vol. 51, No. 11, November 2015.

[67]   B. Minh Dinh, "Optimal Rotor Design of Line Start Permanent Magnet Synchronous Motor by Genetic Algorithm", Advances in Science, Technology and Engineering Systems Journal, Vol. 2, No. 3, pp. 1181-1187, 2017.

[68]   S. Shamlou, M. Mirsalim, "Design, optimisation, analysis and experimental verification of a new line-start permanent magnet synchronous shaded-pole motor", IET Electric Power Applications, VOL. 7, NO. 1, pp. 16-26, January 2013.

[69]   A. M. Knight, C. I. McClay, "The Design of High-Efficiency Line-Start Motors". IEEE Transactions on Industry Applications, Vol. 36, No. 6, December 2000.

[70]   M. Faramarzi Palangar, A. Mahmoudi, W. L. Soong, S. Kahourzade, "Design Optimisation of an 8-pole Line-Start Permanent-Magnet Synchronous Motor", International Conference on Electrical, Control and Instrumentation Engineering (ICECIE2020), November 28, Kuala Lumpur, Malaysia.

[71]   D. Mingardi, N. Bianchi, "Line-Start PM-Assisted Synchronous Motor Design, Optimization, and Tests", IEEE Transactions on Industry Electronics, Vol. 64, No. 12, December 2017.

[72]   A. Johan Sorgdrager, R. J. Wang, A. J. Grobler, "Multiobjective Design of a Line-Start PM Motor Using the Taguchi Method". IEEE Transactions on Industry Applications, Vol. 54, No. 5, September 2018.

[73]   E. Sarani, S. Vaez-Zadeh, "Design Procedure and Optimal Guidelines for Overall Enhancement of Steady State and Transient Performance of Line Start Permanent Magnet Motors", IEEE Transactions on Energy Conversion, Vol. 32, No. 3, pp. 885 - 894, 2017.

[74]   Stoia D., Ilea D., Cernat M., Dezsi Al. B., Jimoh A.: Stability of the line-start permanent magnet synchronous motor sensorless drive. In Proc. AFRICON, Windhoek, South Africa (2007).

[75]   S. Taravat, A. H. Niasar, A. Rabiee, "Sensorless Vector Control of Single Phase Line Start Permanent Magnet Motors (LSPMs)", Int. J. Sci. & Adv. Tech., Vol. (2), pp. 126-131, 2012.

[76]   T. Marcic, B. Stumberger, G. Stumberger, M. Hadziselimovic, P. Virtic, D. Dolinar, "Line-Starting Three- and Single-Phase Interior Permanent Magnet Synchronous Motors-Direct Comparison to Induction Motors". IEEE Transactions on Magnetics, Vol. 44, No. 11, pp. 4413-4416, 2008.

[77]   G. Lei, C. Liu, Y. Guo and J. Zhu, "Robust Multidisciplinary Design Optimization of PM Machines With Soft Magnetic Composite Cores for Batch Production," IEEE Transactions on Magnetics, Vol. 52, No. 3, pp. 1-4, March 2016.

[78]   S. Lee, K. Kim, S. Cho, J. Jang, T. Lee, J. Hong, "Optimal design of interior permanent magnet synchronous motor considering the manufacturing tolerances using Taguchi robust design", IET Electr. Power Appl. Vol. 8, pp. 23–28, 2014.

[79]   X. Ge and Z. Q. Zhu, "Influence of Manufacturing Tolerances on Cogging Torque in Interior Permanent Magnet Machines with Eccentric and Sinusoidal Rotor Contours," IEEE Transactions on Industry Applications, Vol. 53, No. 4, pp. 3568-3578, July-Aug. 2017.

[80]   M. Degano, E. Carraro and N. Bianchi, "Selection Criteria and Robust Optimization of a Traction PM-Assisted Synchronous Reluctance Motor," IEEE Transactions on Industry Applications, Vol. 51, No. 6, pp. 4383-4391, Dec. 2015.

[81]   Koch, P.N, Yang, R.J, Gu, L, "Design for six sigma through robust optimization", Struct. Multidiscip. Optim, Vol. 26, pp. 235–248, 2004.

[82]   X. Meng et al., "Robust Multilevel Optimization of PMSM Using Design for Six Sigma," IEEE Transactions on Magnetics, Vol. 47, No. 10, pp. 3248-3251, Oct. 2011.

[83]   G. Lei, J. G. Zhu, Y. G. Guo, J. F. Hu, W. Xu and K. R. Shao, "Robust Design Optimization of PM-SMC Motors for Six Sigma Quality Manufacturing," IEEE Transactions on Magnetics, Vol. 49, No. 7, pp. 3953-3956, July 2013.

[84]   G. Lei, Y. G. Guo, J. G. Zhu, T. S. Wang, X. M. Chen and K. R. Shao, "System Level Six Sigma Robust Optimization of a Drive System With PM Transverse Flux Machine," IEEE Transactions on Magnetics, Vol. 48, No. 2, pp. 923-926, Feb. 2012.

[85]   G. Lei, T. Wang, J. Zhu, Y. Guo and S. Wang, "System-Level Design Optimization Method for Electrical Drive Systems—Robust Approach," IEEE Transactions on Industrial Electronics, Vol. 62, No. 8, pp. 4702-4713, Aug. 2015.

[86]   G. Lei, J.G. Zhu, C. Liu, B. Ma, "Robust design optimization of electrical machines and drive systems for high quality mass production", In Proceedings of the 6th International Electric Drives Production Conference and Exhibition, Nuremberg, Germany, December 2016.

[87]   B. Ma, G. Lei, C. Liu, J. Zhu and Y. Guo, "Robust Tolerance Design Optimization of a PM Claw Pole Motor With Soft Magnetic Composite Cores," IEEE Transactions on Magnetics, Vol. 54, No. 3, pp. 1-4, March 2018.

[88]   B. Ma, G. Lei, J. Zhu, Y. Guo and C. Liu, "Application-Oriented Robust Design Optimization Method for Batch Production of Permanent-Magnet Motors," IEEE Transactions on Industrial Electronics, Vol. 65, No. 2, pp. 1728-1739, Feb. 2018.

[89]   G. Lei, J.G. Zhu, Y.G. Guo, "Multidisciplinary Design Optimization Methods for Electrical Machines and Drive Systems", Springer-Verlag: Berlin/Heidelberg, Germany, 2016.

[90]   D. Yao, D.M. Ionel, "A review of recent developments in electrical machine design optimization methods with a permanent magnet synchronous motor benchmark study", IEEE Trans. Ind. Appl., Vol. 49, pp. 1268–1275. 2013.

[91] G. Papa, B. Korousic-Seljak, B. Benedicic and T. Kmecl, "Universal motor efficiency improvement using evolutionary optimization," IEEE Transactions on Industrial Electronics, Vol. 50, No. 3, pp. 602-611, June 2003.

[92] K. Yamazaki and H. Ishigami, "Rotor-Shape Optimization of Interior-Permanent-Magnet Motors to Reduce Harmonic Iron Losses," IEEE Transactions on Industrial Electronics, Vol. 57, No. 1, pp. 61-69, Jan. 2010.

[93] K. I. Laskaris and A. G. Kladas, "Permanent-Magnet Shape Optimization Effects on Synchronous Motor Performance," IEEE Transactions on Industrial Electronics, Vol. 58, No. 9, pp. 3776-3783, Sept. 2011.

[94] J. A. Tapia, J. Pyrhonen, J. Puranen, P. Lindh and S. Nyman, "Optimal Design of Large Permanent Magnet Synchronous Generators," IEEE Transactions on Magnetics, Vol. 49, No. 1, pp. 642-650, Jan. 2013.

[95] D. Lim, D. Woo, I. Kim, J. Ro and H. Jung, "Cogging Torque Minimization of a Dual-Type Axial-Flux Permanent Magnet Motor Using a Novel Optimization Algorithm," IEEE Transactions on Magnetics, Vol. 49, No. 9, pp. 5106-5111, Sept. 2013.

[96] M. H. Ravanji and Z. Nasiri-Gheidari, "Design Optimization of a Ladder Secondary Single-Sided Linear Induction Motor for Improved Performance," IEEE Transactions on Energy Conversion, Vol. 30, No. 4, pp. 1595-1603, Dec. 2015.

[97] S. Noguchi and S. Matsutomo, "Rational Design Optimization Method for Reducing Cost and Improving Performance of Commonalized IPM Motors," IEEE Transactions on Magnetics, Vol. 51, No. 3, pp. 1-4, March 2015.

[98] Y. Yang, G. Shih, "Optimal Design of an Axial-Flux Permanent-Magnet Motor for an Electric Vehicle Based on Driving Scenarios", Energies, Vol. 9, No. 285, 2016.

[99] J. Song, F. Dong, J. Zhao, S. Lu, L. Li, Z. Pan, "A New Design Optimization Method for Permanent Magnet Synchronous Linear Motors", Energies, Vol. 9, No. 992, 2016.

[100] F. Chai, P. Liang, Y. Pei and S. Cheng, "Magnet Shape Optimization of Surface-Mounted Permanent-Magnet Motors to Reduce Harmonic Iron Losses," IEEE Transactions on Magnetics, Vol. 52, No. 7, pp. 1-4, July 2016.

[101] W. Kong, R. Qu, M. Kang, J. Huang and L. Jing, "Air-Gap and Yoke Flux Density Optimization for Multiphase Induction Motor Based on Novel Harmonic Current Injection Method," IEEE Transactions on Industry Applications, Vol. 53, No. 3, pp. 2140-2148, May-June 2017.

[102] Y. Wang, G. Bacco and N. Bianchi, "Geometry Analysis and Optimization of PM-Assisted Reluctance Motors," IEEE Transactions on Industry Applications, Vol. 53, No. 5, pp. 4338-4347, Sept.-Oct. 2017.

[103] M. Demirtas, E. Ilten, H. Calgan, "Pareto-Based Multi-objective Optimization for Fractional Order PIλ Speed Control of Induction Motor by Using Elman Neural Network", Arab J Sci Eng, Vol. 44, pp. 2165–2175, 2019.

[104] M. Mamdouh, M.A. Abido, Z. Hamouz, "Weighting Factor Selection Techniques for Predictive Torque Control of Induction Motor Drives: A Comparison Study, Arab J Sci Eng, Vol. 43, pp. 433–445, 2018.

[105] M. Mutluer, M.A. Şahman, M. Çunkaş, "Heuristic Optimization Based on Penalty Approach for Surface Permanent Magnet Synchronous Machines", Arab J Sci Eng, Vol. 45, pp. 6751–6767, 2020.

[106] L. Maraaba, Z. Al-Hamouz, A. Milhem, M. Abido, "Modelling of interior-mount LSPMSM under asymmetrical stator winding", IET Electric Power Applications Vol. 12, No. 5, pp. 693–700, 2018.

[107] H. M. Hasanien, "Torque ripple minimization of permanent magnet synchronous motor using digital observer controller", Energy Conversion and Management, Vol. 51, No. 1, pp. 98-104, 2010.

[108] M. A. Khan, I. Husain, M. R. Islam and J. T. Klass, "Design of Experiments to Address Manufacturing Tolerances and Process Variations Influencing Cogging Torque and Back EMF in the Mass Production of the Permanent-Magnet Synchronous Motors," IEEE Transactions on Industry Applications, Vol. 50, No. 1, pp. 346-355, Jan.-Feb.

[109] I. Coenen, M. van der Giet and K. Hameyer, "Manufacturing Tolerances: Estimation and Prediction of Cogging Torque Influenced by Magnetization Faults," IEEE Transactions on Magnetics, Vol. 48, No. 5, pp. 1932-1936, May 2012.

[110] L. Gasparin, R. Fiser, "Impact of manufacturing imperfections on cogging torque level in PMSM", In Proceedings of the 2011 IEEE Ninth International Conference on Power Electronics and Drive Systems (PEDS), Singapore, 5–8 December 2011.

[111] X. Ge and Z. Q. Zhu, "Influence of Manufacturing Tolerances on Cogging Torque in Interior Permanent Magnet Machines with Eccentric and Sinusoidal Rotor Contours," in IEEE Transactions on Industry Applications, Vol. 53, No. 4, pp. 3568-3578, July-Aug. 2017.

[112] J. Lee, J. Chang, D. Kang, S. Kim and J. Hong, "Tooth Shape Optimization for Cogging Torque Reduction of Transverse Flux Rotary Motor Using Design of Experiment and Response Surface Methodology," IEEE Transactions on Magnetics, Vol. 43, No. 4, pp. 1817-1820, April 2007.

[113] K. Deb, A. Pratap, S. Agarwal and T. Meyarivan, "A fast and elitist multiobjective genetic algorithm: NSGA-II," IEEE Transactions on Evolutionary Computation, Vol. 6, No. 2, pp. 182-197, April 2002.

[114] M. Reyes-Sierra, C.A.C. Coello, "Multi-objective particle swarm optimizers: A survey of the state-of-the-art", Int. J. Comput. Intell. Res., Vol. 2, pp. 287–308, 2006.

[115] M. E. Beniakar, P. E. Kakosimos and A. G. Kladas, "Strength Pareto Evolutionary Optimization of an In-Wheel PM Motor With Unequal Teeth for Electric Traction," IEEE Transactions on Magnetics, Vol. 51, No. 3, pp. 1-4, March 2015.

[116] C. Ma and L. Qu, "Multiobjective Optimization of Switched Reluctance Motors Based on Design of Experiments and Particle Swarm Optimization," IEEE Transactions on Energy Conversion, Vol. 30, No. 3, pp. 1144-1153, Sept. 2015.

[117] C. Lin and C. Hwang, "Multiobjective Optimization Design for a Six-Phase Copper Rotor Induction Motor Mounted With a Scroll Compressor," IEEE Transactions on Magnetics, Vol. 52, No. 7, pp. 1-4, July 2016.

[118] C. T. Krasopoulos, I. P. Armouti and A. G. Kladas, "Hybrid Multiobjective Optimization Algorithm for PM Motor Design," IEEE Transactions on Magnetics, Vol. 53, No. 6, pp. 1-4, June 2017.

[119] H. Duan and L. Gan, "Orthogonal Multiobjective Chemical Reaction Optimization Approach for the Brushless DC Motor Design," IEEE Transactions on Magnetics, Vol. 51, No. 1, pp. 1-7, Jan. 2015.

[120] G. Lei, J. Zhu, Y. Guo, K. Shao and W. Xu, "Multiobjective Sequential Design Optimization of PM-SMC Motors for Six Sigma Quality Manufacturing," IEEE Transactions on Magnetics, Vol. 50, No. 2, pp. 717-720, Feb. 2014.

[121] S. Stipetic, W. Miebach, D. Zarko, "Optimization in design of electric machines: Methodology and workflow", In Proceedings of the 2015 International Aegean Conference on Electrical Machines & Power Electronics (ACEMP), 2015 International Conference on Optimization of Electrical & Electronic Equipment (OPTIM) & 2015 International Symposium on Advanced Electromechanical Motion Systems (ELECTROMOTION), Antalya ˙Ili, Turkey, 2–4 September 2015.

[122] H.M. Hasanien, "Particle swarm design optimization of transverse flux linear motor for weight reduction and improvement of thrust force", IEEE Trans. Ind. Electron. Vol. 58, No. 9, pp. 4048 – 4056, Sept. 2011.

[123] M. Sreejeth, M. Singh and P. Kumar, "Particle swarm optimisation in efficiency improvement of vector controlled surface mounted permanent magnet synchronous motor drive", IET Power Electronics, Vol. 8, No. 5, pp. 760-769, April 2015.

[124] C. Zhang, Z. Chen, Q. Mei and J. Duan, "Application of Particle Swarm Optimization Combined With Response Surface Methodology to Transverse Flux Permanent Magnet Motor Optimization", IEEE Transactions on Magnetics, Vol. 53, No. 12, pp. 1-7, Dec. 2017.

[125] G. Lei, T. Wang, J. Zhu, Y. Guo and S. Wang, "System-Level Design Optimization Method for Electrical Drive Systems—Robust Approach," IEEE Transactions on Industrial Electronics, Vol. 62, No. 8, pp. 4702-4713, Aug. 2015.

[126]   G. Lei, J.G. Zhu, C. Liu, B. Ma, "Robust design optimization of electrical machines and drive systems for high quality mass production", In Proceedings of the 6th International Electric Drives Production Conference and Exhibition, Nuremberg, Germany, 30 November–1 December 2016.

[127]   G. Lanza, J. Stoll, A. Krämer, "Assessment of lamination stack production", In Proceedings of the 3rd International Electric Drives Production Conference (EDPC), Nuremberg, Germany, 29–30 October 2013.

[128]   D.W. Zingg, M. Nemec, T.H. Pulliam, "A comparative evaluation of genetic and gradient-based algorithms applied to aerodynamic optimization," European Journal of Computational Mechanics Vol. 17, no. 1-2, 2008.

[129]   China National Institute of Standardization, "Summary report for motor and its energy efficiency standards", CNIS; May 2004.

[130]   De. Almeida, F. Ferreira, A. Duarte, "Technical and Economic Considerations on Super High-Efficiency Three-Phase Motors", IEEE Transactions on Industry Applications, Vol. 50, No. 2, pp.1274-1285, 2014.

[131]   Manual of Maxwell, R2, Ansys., 2019, pp, 1902-1929.

[132]   G. Lei, C. Liu, Y. Guo and J. Zhu, "Multidisciplinary Design Analysis and Optimization of a PM Transverse Flux Machine With Soft Magnetic Composite Core," IEEE Transactions on Magnetics, Vol. 51, No. 11, pp. 1-4, Nov. 2015.

[133]   Z. Huang and J. Fang, "Multiphysics Design and Optimization of High-Speed Permanent-Magnet Electrical Machines for Air Blower Applications," IEEE Transactions on Industrial Electronics, Vol. 63, No. 5, pp. 2766-2774, May 2016.

[134]   Z. Makni, M. Besbes and C. Marchand, "Multiphysics Design Methodology of Permanent-Magnet Synchronous Motors," IEEE Transactions on Vehicular Technology, Vol. 56, No. 4, pp. 1524-1530, July 2007.

[135]   S. Kreuawan, F. Gillon, P. Brochet, "Optimal design of permanent magnet motor using multidisciplinary design optimization", In Proceedings of the 18th International Conference on Electrical Machines, Pattaya, Thailand, pp. 1–6, 25–28 October 2015.

[136]   I. Vese, F. Marignetti and M. M. Radulescu, "Multiphysics Approach to Numerical Modeling of a Permanent-Magnet Tubular Linear Motor," IEEE Transactions on Industrial Electronics, Vol. 57, No. 1, pp. 320-326, Jan. 2010.

[137]   Y. Li, F. Chai, Z. Song, Z. Li, "Analysis of Vibrations in Interior Permanent Magnet Synchronous Motors Considering Air-Gap Deformation", Energies, Vol. 10, No. 1259, 2017.

[138]   X. Sun, L. Chen, Z. Yang, "Overview of bearingless permanent magnet synchronous motors", IEEE Trans.Ind. Electron, Vol. 60, 2013.

[139] P. Pfister and Y. Perriard, "Very-High-Speed Slotless Permanent-Magnet Motors: Analytical Modeling, Optimization, Design, and Torque Measurement Methods," IEEE Transactions on Industrial Electronics, Vol. 57, No. 1, pp. 296-303, Jan. 2010.

[140] E. Schmidt, "Finite Element Analysis of a Novel Design of a Three Phase Transverse Flux Machine With an External Rotor," IEEE Transactions on Magnetics, Vol. 47, No. 5, pp. 982-985, May 2011.

[141] E. M. Barhoumi, F. Wurtz, C. Chillet, B. Ben Salah and O. Chadebec, "Efficient Reluctance Network Formulation for Modeling Design and Optimization of Linear Hybrid Motor," IEEE Transactions on Magnetics, Vol. 52, No. 3, pp. 1-4, March 2016.

[142] S. Wu, X. Zhao, X. Li, P. C. K. Luk and Z. Jiao, "Preliminary Design and Optimization of Toroidally Wound Limited Angle Servo Motor Based on a Generalized Magnetic Circuit Model," IEEE Transactions on Magnetics, Vol. 52, No. 9, pp. 1-9, Sept. 2016.

[143] X. Zhu, Z. Shu, L. Quan, Z. Xiang and X. Pan, "Multi-Objective Optimization of an Outer-Rotor V-Shaped Permanent Magnet Flux Switching Motor Based on Multi-Level Design Method," IEEE Transactions on Magnetics, Vol. 52, No. 10, pp. 1-8, Oct. 2016.

[144] F. Luise et al., "Design Optimization and Testing of High-Performance Motors: Evaluating a Compromise Between Quality Design Development and Production Costs of a Halbach-Array PM Slotless Motor," IEEE Industry Applications Magazine, Vol. 22, No. 6, pp. 19-32, Dec. 2016.

[145] Y. Huang, J. Zhu and Y. Guo, "Thermal Analysis of High-Speed SMC Motor Based on Thermal Network and 3-D FEA With Rotational Core Loss Included," IEEE Transactions on Magnetics, Vol. 45, No. 10, pp. 4680-4683, Oct. 2009.

[146] W. Li, X. Zhang, S. Cheng and J. Cao, "Thermal Optimization for a HSPMG Used for Distributed Generation Systems," IEEE Transactions on Industrial Electronics, Vol. 60, No. 2, pp. 474-482, Feb. 2013.

[147] A. S. Bornschlegell, J. Pelle, S. Harmand, A. Fasquelle and J. Corriou, "Thermal Optimization of a High-Power Salient-Pole Electrical Machine," IEEE Transactions on Industrial Electronics, Vol. 60, No. 5, pp. 1734-1746, May 2013.

[148] W. Hung, S. H. Mao, M. C. Tsai, "Investigation of line start permanent magnet synchronous motors with interior-magnet rotors and surface-magnet rotors," Electrical Machines and Systems, pp. 2888-2893, October 2008.

[149] L. Weili, Z. Xiaochen, C. Skukang, "Study of solid rotor line-start PMSM operating performance," International Conference on Electrical Machines and Systems, 2008, pp. 373-378.

[150] M. Y. Marusina, A. A. Silaev and D. A. Nevmerzhitsky, "Method of Converting an Induction Motor to a Permanent Magnet Synchronous Motor (Ls-Pmsm) with Linear Starting Using FEA for

Mechatronic Systems," 2019 International Conference Quality Management, Transport and Information Security, Information Technologies (IT&QM&IS), Sochi, Russia, pp. 356-358, 2019.

[151]   A. Mahmoudi, S. Kahourzade, N. A. Rahim and W. P. Hew., "Design, Analysis, and Prototyping of an Axial-Flux Permanent Magnet Motor Based on Genetic Algorithm and Finite-Element Analysis," in IEEE Transactions on Magnetics, vol. 49, no. 4, pp. 1479-1492, 2013.

[152]   A. Boglietti, M. Cossale, M. Popescu, and D. A. Staton, "Electrical Machines Thermal Model: Advanced Calibration Techniques", IEEE Transactions on Industry Applications, Vol. 55, No. 3, 2019.

[153]   Y. Wu, H. Gao, "Induction motor stator and rotor winding temperature estimation using signal injection method", Int. IEEE Conf. Electr. Mach. Drives, pp. 615–621, 2005.

[154]   Y. Wu, H. Gao, "Induction motor stator and rotor winding temperature estimation using signal injection method", IEEE Trans. Ind. Appl. Vol. 42, No. 4, pp. 1038–1044, 2006.

[155]   K. Akatsu, A. Kawamura, "Sensorless very low-speed and zero-speed estimations with online rotor resistance estimation of induction motor without signal injection", IEEE Trans. Ind. Appl. Vol. 36, No. 3, pp. 764–771, 2000.

[156]   H. Tajima, G. Guidi, H. Umida, "Consideration about problems and solutions of speed estimation method and parameter tuning for speed sensorless vector control of induction motor drives", IEEE Trans. Ind. Appl. Vol. 38, No. 5, pp. 1282–1289, 2002.

[157]   W. Gao, "A Simple model-based online rotor time constant estimator for an induction machine", IEEE Trans. Energy Convers., Vol. 19, No. 4, pp. 793–794, 2004.

[158]   N. Nait-Said, "Rotor resistance estimation of an induction motor to detect broken bars fault using H-H method", Electr. Power Compon. Syst., Vol. 32, No. 2, pp. 149–161, 2004.

[159]   Ch. Kral, Th. G. Habetler, R.G. Harley, F. Pirker, G. Pascoli, H. Oberguggenberger, C-J M. Fenz, "Rotor temperature estimation of squirrel-cage induction motors by means of a combined scheme of parameter estimation and a thermal equivalent model", IEEE Trans. Ind. Appl., Vol. 40, No. 4, pp. 1049–1057, 2004.

[160]   Zh. Gao, Th. G. Habetler, R. G. Harley, R. S. Colby, "An Adaptive Kalman Filtering Approach to Induction Machine Stator Winding TemperatureEstimation Based on a Hybrid Thermal Model", 14th IEEE Conference ofthe Industry Application, pp. 2-9, 2005.

[161]   Ch. Kral, A. Haumer, S. B. Lee, "Robust Thermal Model for the Estimation of Rotor Cage and Stator Winding Temperatures of Induction Machines", IEEE International Conference on Electrical Machines, pp. 1810–1816, 2012.

[162]   K.M. Sousa, A.A. Hafner, E.G. Carati, H.J. Kalinowski, J.C.C. Silva, "Validation of thermal and electrical model for induction motors using fiber Bragg gratings", Measurement, Vol. 46, No. 6, pp. 1781–1790, 2013.

[163] D. Staton, A. Boglietti, and A. Cavagnino., "Solving the More Difficult Aspects of Electric Motor Thermal Analysis in Small and Medium Size Industrial Induction Motors", IEEE Transactions on Energy Conversion, VOL. 20, NO. 3, pp. 620-628, 2005.

[164] A. Boglietti, A. Cavagnino, D. A. Staton., "Thermal Analysis of TEFC Induction Motors", 38th IAS Annual Meeting on Conference Record of the Industry Applications Conference, October 2003, Salt Lake City, USA.

[165] D.Staton, A.Cavagnino., "Convection Heat Transfer and Flow Calculations Suitable for Electric Machines Thermal Models", IEEE Transactions on Industrial Electronics, Vol. 20, No. 3, pp. 3509-3516, 2005.

[166] C. Ulu, O. Korman, G. Kömürgöz., "Electromagnetic and Thermal Analysis/Design of an Induction Motor for Electric Vehicles", 8th International Conference on Mechanical and Aerospace Engineering (ICMAE), 22-25 July 2017, Prague, Czech Republic.

[167] J. Schützhold, W. Hofmann., "Analysis of the Temperature Dependence of Losses in Electrical Machines", IEEE Energy Conversion Congress and Exposition, October 2013, Denver, CO, USA.

[168] J. Fan, Ch. Zhang, Zh. Wang, Y. Dong, C. E. Nino, A. R. Tariq, and E. G. Strangas., "Thermal Analysis of Permanent Magnet Motor for the Electric Vehicle Application Considering Driving Duty Cycle", IEEE Transactions on Magnetics, Vol. 46, No. 6, pp. 2493-2496 ,2010.

[169] Y. Hu, T. Wu., "Comprehensive Design and Modelling of a Super High-Speed Permanent Magnet Motor", IEEE Workshop on Electrical Machines Design, Control and Diagnosis (WEMDCD), 26-27 March 2015, Torino, Italy.

[170] X. Fan, B. Zhang, R. Qu, D. Li, J. Li, and Y. Huo., "Comparative Thermal Analysis of IPMSMs With Integral-Slot Distributed-Winding (ISDW) and Fractional-Slot Concentrated-Winding (FSCW) for Electric Vehicle Application", IEEE Transactions on Industry Applications, Vol. 55, No. 4, pp. 3577 - 3588 , 2019.

[171] J. G. Lee, H. K. Yeo, H. K. Jung, T. K. Kim, J. S. Ro., "Electromagnetic and thermal analysis and design of a novel-structured surface-mounted permanent magnet motor with high-powerdensity", IET Electric Power Application, Vol. 13, No. 4, pp. 472-478, 2019.

[172] C. Debruyne, M. Polikarpova, S. Derammelaere, P. Sergeant, J Pyrhönen, J.J.M. Desmet, L. Vandevelde, "Evaluation of the Efficiency of Line-Start Permanent-Magnet Machines as a Function of the Operating Temperature", IEEE Transactions on Industrial Electronics, Vol. 61, No. 8, pp. 4443-4454, 2014.

[173] N. Arbab, W. Wang, C. Lin, J. Hearron, B. Fahimi, "Thermal Modeling and Analysis of a Double-Stator Switched Reluctance Motor", IEEE Trans. Energy Convers. Vol. 30, No. 3, pp. 1209–1217, 2015.

[174]   Liwei Song, Zijian Li, Jingyi Gao, Qingchu Zeng, and Fuping Wang, "3D Thermal Analysis of Water-Cooling Induction Motor used for HEV", International Conference on Electrical Machines and Systems, 17-20 Oct. 2008, Wuhan, China.

[175]   A. Kumar., "Electric motor internal heat convection modelling and analysis", Department of Mechanics and Maritime Sciences, Chalmers University of Technology, Gothenburg, Sweden 2018.

[176]   Y. Xie, Ch. Gu, L. Wang., "There-Dimensional Temperature Estimation of Squirrel-Cage Induction Motor Using Finite Element Method", IEEE-International Conference on Electrical Machines and Systems, August 2011, Beijing, China.

[177]   F. Chai, Y. Tang, Y. Pei, P. Liang and H. Gao, "Temperature Field Accurate Modeling and Cooling Performance Evaluation of Direct-Drive Outer-Rotor Air-Cooling In-Wheel Motor", Energies, MDPI, Vol. 9, No. 10, pp. 1-17, October 2016.

[178]   J. Ding, P. Hang, J. Li, "3D Temperature Field Calculation of Mine-used Flame-proof Integrative Variable-speed System", IEEE PEDS June 2015, Sydney, Australia.

[179]   F. Incropera, D. P. Dewitt, Th. Bergman, A. Lavine, "Fundamentals of Heat and Mass Transfer", John Wiley & Sons, Sixth Edition.

[180]   O. Bardran, H. Sarhan, "Thermal Performance Analysis of Induction Motor", International Journal of Heat and Technology Vol. 30, No.1, pp. 75-88, January 2012.

[181]   Qixu Chen, Xi'an jiaotong, Binggang Cao, "Lumped-parameter thermal network model and experimental research of interior pmsm for electric vehicle", CES Transactions on Electrical Machines and Systems, Vol. 1, No. 4, pp. 367 – 374, December 2017.

[182]   L. Popova, J. Nerg and J. Pyrhönen, "Combined Electromagnetic and thermal design platform for totally enclosed induction machines," 8th IEEE Symposium on Diagnostics for Electrical Machines, Power Electronics & Drives, Bologna, 2011, pp. 153-158, doi: 10.1109/DEMPED.2011.6063617.

[183]   J. Nerg, M. Rilla and J. Pyrhonen, "Thermal Analysis of Radial-Flux Electrical Machines With a High Power Density," IEEE Transactions on Industrial Electronics, Vol. 55, No. 10, pp. 3543-3554, Oct. 2008, doi: 10.1109/TIE.2008.927403.

[184]   P. Ghahfarokhi, A. Kallaste, A. Belahcen, T. Vaimann, A. Rassõlkin, "Hybrid thermal model of a synchronous reluctance machine," Case Studies in Thermal Engineering, Vol. 12, pp. 381-389, September 2018, https://doi.org/10.1016/j.csite.2018.05.007.

[185]   G. Dajaku, D. Gerling, "An Improved Lumped Parameter Thermal Model for Electrical Machines", International Conference on Electrical Machines (ICEM), Sept 2006, China.

[186]   Holman J. P., "Heat Transfer", McGraw– Hill Publishing Company, 1990.

[187]   W. Liebe, "Cooling of large machines", Elektrotech. Z (ETZ) A, Vol. 87, pp. 434-442, Jun. 1966.

[188]   A. Boglietti, A. Cavagnino, M. Lazzari and M. Pastorelli, "A simplified thermal model for variable speed self cooled industrial induction motor", IEEE Trans. Ind. Appl., Vol. 39, No. 4, pp. 945-952, Jul./Aug. 2002.

[189]   S. Lipiński and J. Zawilak, "Transient Heat Transfer During the Starting Process of a Line Start Permanent Magnet Synchronous Motor", 2018 International Symposium on Electrical Machines (SME), Andrychów, pp. 1-4, 2018.

[190]   M. Baranski, W. Szelag and C. Jedryczka, "Influence of temperature on partial demagnetization of the permanent magnets during starting process of line start permanent magnet synchronous motor," 2017 International Symposium on Electrical Machines (SME), Naleczow, pp. 1-6, 2017.

[191]   W. Pawlus, J. T. Birkeland, H. Van Khang and M. R. Hansen, "Identification and Experimental Validation of an Induction Motor Thermal Model for Improved Drivetrain Design," IEEE Transactions on Industry Applications, Vol. 53, No. 5, pp. 4288-4297, Sept.-Oct. 2017.

[192]   G. Lv, D. Zeng and T. Zhou, "An Advanced Equivalent Circuit Model for Linear Induction Motors", IEEE Transactions on Industrial Electronics, Vol. 65, No. 9, pp. 7495-7503, Sept. 2018.

[193]   R. Kumar, P. Kumar, T. Kanekawa and K. Oishi, "Stray Loss Model for Induction Motors With Using Equivalent Circuit Parameters", IEEE Transactions on Energy Conversion, Vol. 35, No. 2, pp. 1036-1045, June 2020.

[194]   M. Aminu, P. Barendse and A. Khan, "A Simplified Equivalent Circuit Method for Induction Machine Nonintrusive Field Efficiency Estimation", IEEE Transactions on Industrial Electronics, Vol. 67, No. 9, pp. 7301-7311, Sept. 2020.

[195]   S. Yamamoto, H. Hirahara, A. Tanaka and T. Ara, "A Simple Method to Determine Double-Cage Rotor Equivalent Circuit Parameters of Induction Motors From No-Load and Locked-Rotor Tests", IEEE Transactions on Industry Applications, Vol. 55, No. 1, pp. 273-282, Jan.-Feb. 2019.

[196]   A. Usman and B. S. Rajpurohit, "Comprehensive Analysis of Demagnetization Faults in BLDC Motors Using Novel Hybrid Electrical Equivalent Circuit and Numerical Based Approach", IEEE Access, vol. 7, pp. 147542-147552, 2019.

[197]   X. Ba, Y. Guo, J. Zhu and C. Zhang, "An Equivalent Circuit Model for Predicting the Core Loss in a Claw-Pole Permanent Magnet Motor With Soft Magnetic Composite Core", IEEE Transactions on Magnetics, Vol. 54, No. 11, pp. 1-6, Nov. 2018.

[198]   Saleh A. Al-Jufout, Wasseem H. Al-rousan, and Caisheng Wang, "Optimization of Induction Motor Equivalent Circuit Parameter Estimation Based on Manufacturer's Data", Energies, Vol. 11, pp. 1792-1803, 2018.

[199]   V.F. Sivokobylenko, S.N. Tkachenko, S.V. Derkachev, "Determining the parameters of equivalent circuits and characteristics of induction motors", Elektrichestvo, Vol. 10, pp. 38–44, 2014.

[200]   V.F. Sivokobylenko, "A hybrid equivalent circuit of asynchronous motors with a deep-slot or double-cage rotor", Elektrichestvo, Vol. 4, pp. 34–40, 2016.

[201]   S. J. Chapman, "Electric Machinery Fundamentals", New York :McGraw-Hill, 2012.